UNIVERSITY OF COPENHAGEN

Quantum Correlations Generated by a Soft-Clamped Membrane-in-the-Middle System

PhD Thesis

Junxin Chen

November 2019

Academic supervisor: Prof. Dr. Albert Schliesser

University of Copehagen, 2019
Faculty of Science
Niels Bohr Institute

Acknowledgements

3 years is a short time for PhD study, especially considering the compulsory distractions from research. Getting something done within this time is in no way an easy task, despite how beautiful the works we have accomplished. I still remember how I was like starting my PhD: a student having very little knowledge about optics, and knowing almost nothing about optomechanics. Looking at myself now, it seems like a dream. Without help from others, I can never come to this point. There were many people who played a crucial role during my study. I will try my best to express my thankfulness to everyone of you. In case the list is incomplete, please forgive my carelessness.

First of all, I would like to thank my Lord. It was He who guided me to this journey. During the journey, He strengthened me when I felt weak, healed me when I was hurt, and led my way when I was lost. He was my Shepherd all the way.

The foremost among the people I would like to thank is of course my supervisor Prof. Albert Schließer. He gave me the opportunity to work in his group on the beautiful system. His solid knowledge and creative intuition about optomechanics helped a lot when our projects encountered problem. Despite the tight schedule he always has, he was trying to make himself available, when I need a discussion on the project or suggestion on the career. In my mind, Albert really sets a paragon for a supervisor.

Among my colleagues, I am especially grateful for Massimiliano Rossi, Dr. David Mason, Dr. Yeghishe Tsaturyan, Yannick Seis, Dr. Christoffer Møller and Dr. William Nielsen. I worked closely with Massi and David, and shared all our publications. They are always willing to help and discuss when I encountered problems with patience. I also learned a lot of knowledge, methodology and scientific way of thinking from them. They showed me what a mature researcher is like. In addition to research, they are also nice men, as I do not remember any conflicts among us, but friendship. Yeghishe fabricated almost the membranes used in our experiment. His diligence was always a motivation for me, and it is always amazing to see his rich knowledge in experimental physics, even not related to material. In addition to work, he also gave precious suggestions on various of aspects of life, especially career. He is like a mentor to me. Yannick and Chris were very helpful setting up the early stage of the experiments. In particular, Chris was a main source of knowledge when I was trying my baby steps. Yannick also helped fabricating membranes, when Yeghishe was on exchange. William did a brilliant job in passing on knowledge to me. He found the way of operating a stable membrane-in-the-middle system in cryogenic environment, and the experimental apparatus in this thesis is adapted from William's design. I would like to express my appreciation to other group members in Albert's, Prof. Eugene Polzik's and Prof. Peter Lodahl's group. It was all of you who set up a diligent and helpful environment. To my knowledge, a family like atmosphere is a rare and precious treasure for any research group.

在此，我也想借这个机会感谢我的家人，特别是我的父母，对我的支持。你们可能并不明白我做的研究，但你们相信我所做的是有意义的工作，并且为我所取得的任何进步都感到由衷的高兴。母亲关注我生活中的每一个细节，并且尽她所能地提供帮助和建议。她在我有病痛的时候也用她扎实的专业知识指导我如何用药。父亲虽然没有物理的背景，但是愿意去花时间阅读和量子力学相关的科普知识，尝试了解我的工作。你们对我的支持和关注一直以来都是我继续前行的动力。

我也想感谢 CCiC 的弟兄姊妹们。他们在哥本哈根给了我一个属灵的家，也给我服事神的机会。读 PhD 的过程不可能一帆风顺，生活也会带来各种各样的难处。是他们通过祷告和实际的帮助托住我，帮我渡过各样的难关。他们中的很多人也让我看到神想让我成长的方向。

In the very end of this acknowledgement, I would like to thank my Lord again. You are the Alpha and the Omega, the First and the Last, the Beginning and the End. You are my all in all.

Abstract

Optomechanics is a rapidly developing field, exploring the subtleties of the interaction between light and mechanical oscillators. Thanks to the advances in system design and fabrication, quantum effects have become significant in a range of optomechanical systems. On the mechanical side, mechanical oscillators consisting of billions of atoms have recently been prepared in the motional ground state, squeezed state, single excitation (Fock) state and entangled state, which shows the great potential of massive quantum state preparation and control. By combining mechanical oscillators and qubits, researchers have also achieved complicated manipulation of mechanical quantum states. On the optical side, through the interaction with mechanics, ponderomotive squeezing, and optical-optical entanglement have been realized, which demonstrate the power of optomechanical systems as a quantum media to control optical states.

Apart from preparation of quantum states of light and mechanics, optomechanics provides a platform for ultra-sensitive displacement and force measurements, which is key in many sensing applications like gravitational wave detection and force sensing by magnetic resonance force microscopy (MRFM). A quantum limited measurement with high signal-to-noise ratio is also a prerequisite for measurement-based quantum control of mechanical systems, like feedback cooling to the quantum ground state. To realize this measurement, the experimental apparatus needs to enable high detection efficiency and strong measurement, simultaneously, which is a demanding requirement. Existing optomechanical systems either have strong interaction, but low detection efficiency or a noisy detection chain, or have high detection efficiency, but cannot sustain enough optical power to get strong interaction. Combining these two features is so far a unique advantage of our membrane-in-the-middle system (MIM) with ultra-coherent soft-clamped membrane, which will be introduced in this thesis. With this system, we have acquired displacement measurement record with record breaking quality, only 33% above the Heisenberg Limit, a fundamental limit for displacement measurement. With this high quality measurement record, we achieved the first feedback cooling of a mechanical mode to its quantum ground state, which integral to other measurement-based quantum control protocols.

High detection efficiency and strong measurement is also a key for observing effects of optomechanically induced quantum correlations. Ultilizing this correlation, we demonstrate the first displacement and force sensing below the Standard Quantum Limit (SQL), a milestone in quantum metrology, which opens the gate to the world of sub-SQL sensing. By having two optical fields interacting with the same mechanical oscillator, we also demonstrate ponderomotive entanglement between the two optical fields, which provides a entanglement generator compatible with various condensed matter based quantum systems. This is a necessary building block for optical-microwave entanglement, a useful resource for quantum networks and the quantum internet, eventually.

Sammenfatning

Optomekanik er et forskningsfelt rivende udvilking, som udforsker spidsfindighederne i vekselvirkningen mellem lys og mekaniske oscillatorer. Takket være fremskridt i systemdesign og fabrikation, er kvanteeffekter blevet anselige i en række optomekaniske systemer. På mekaniksiden er mekaniske oscillatorer, bestående af millarder af atomer, for nyligt blevet forberedt i den bevægelsemæssige grundtilstand, klemte tilstande, enkelt-exciterede (Fock) tilstande og sammenfiltrede tilstande, hvilket viser det store potentiale for forberedelse og kontrol af massive kvantetilstande. Ved at kombinere mekaniske oscillatorer og kvantebits har forskere ydermere opnået kompliceret håndtering af mekaniske kvantetilstande. På den optiske side er ponderomotorisk klemning og optisk-optisk sammenfiltring blevet realiseret gennem vekselvirkning med mekanikken, hvilket demontrerer styrken af optomekaniske systemer som et kvantemedie til kontrol af optiske tilstande. Udover forberedelse af kvantetilstande af lys og mekanik giver optomekanik en platform for ultrafølsomme målinger af bevægelser og kræfter, hvilket er centralt for mange sensoranvendelser såsom detektion af tyngdebølger og måling af kræfter med magnetisk resonans kraftmikroskopi. En kvantebegrænset måling med højt signal-til-støj forhold er ligeledes en forudsætning for målingsbaseret kvantekontrol af mekaniske systemer, såsom feedback køling til den kvantemekaniske grundtilstand. Til denne type målinger er både en høj detektionseffektivitet og målingsstyrke samtidigt påkrævet af måleapparatet, hvilket er en udfordrende forudsætning. Eksisterende optomekaniske systemer har enten stærk vekselvirkning, men lav detektionseffektivitet eller støjende detektionskæde, eller en høj detektionseffektivitet, men er ikke i stand til at opretholde tilstrækkelig høj optisk effekt til at opnå stærk vekselvirkning. Kombinationen af disse to egenskaber er på nuværende tidspunkt en unik fordel ved vores mebran-i-midten (MIM) system, med ultrakohærente, blødt-fastspændte membraner, som bliver introduceret i denne afhandling. Med dette system har vi indsamlet bevægelsesmålingsoptegnelser af banebrydende kvalitet; blot 33% over Heisenberggrænsen, der sætter en grundlæggende grænse for bevægelsesmålinger. Med denne høj-kvalitets bevægelsesmålingsoptegnelse har vi som de første opnået feedback-køling af en mekanisk tilstand til sin kvantemekaniske grundstilstand, hvilket er grundlæggende for andre målingsbaserede kvantemekaniske kontrolprotokoller. Høj detektionseffektivitet og målingsstyrke er ligeledes essentielt for observation af effekterne af optomekanisk inducerede kvantekorrelationer. Ved at udnytte disse disse korrelationer har vi påvist den første måling af bevægelse og kraft under standardkvantegrænsen, en milepæl indenfor kvantemetrologi, hvilket åbner dørene til en verden af sub-standardkvantegrænse målinger.Ved at lade to optiske felter vekselvirke med den samme mekaniske oscillator har vi ydermere påvist ponderomotorisk sammenfiltring mellem de to optiske felter, hvilket tilvejebringer en generator af sammenfiltring, der er kompatibel med forskellige faststofbaserede kvantesystemer. Dette er en nødvendig byggesten for optisk-mikrobølge sammenfiltring, hvilket er en nyttig ressource til kvantenetværk og, med tiden, kvanteinternettet.

List of Publications and Preprints

Peer Reviewed Publications

- Massimiliano Rossi, David Mason, **Junxin Chen**, Yeghishe Tsaturyan, and Albert Schliesser. "Measurement-based quantum control of mechanical motion." Nature 563, 53–58 (2018)

  This is the first-ever optomechanical experiment conducted with soft-clamped mechanical resonators. Starting from an empty optical table, I implemented the first version of this setup (see chapter 3), adapting designs by William Nielsen, Yeghishe Tsaturyan and others (see ref [1]). My colleague MR further developed the setup and experimental protocols. For this particular study, I also contributed to characterization of the digital filter electronics, and supporting measurements. MR conducted most of the measurements, and analyzed them together with DM. This study is discussed in Chapter 6.

- David Mason, **Junxin Chen**, Massimiliano Rossi, Yeghishe Tsaturyan, and Albert Schliesser. "Continuous force and displacement measurement below the standard quantum limit." Nature Physics 15, 745–749 (2019)

  This project is discussed in Chapter 4 of this thesis. The project was initiated by postdoc DM, realizing that our system operates in a regime where sub-SQL sensitivity is possible for the first time. I contributed to all aspects of the optical, electronic and optomechanical design of the experiment. I also collected and calibrated most of the data on which this study is based. My colleagues MR and DM did most of the theory and data analysis that is employed to obtain the results discussed in section 4.3 of this thesis.

- Massimiliano Rossi, David Mason, **Junxin Chen**, and Albert Schliesser. "Observing and Verifying the Quantum Trajectory of a Mechanical Resonator" Physical Review Letters 123, 163601 (2019)

  This work is not discussed in this thesis. My contribution consists in setting up the experimental system, and involvement in early discussions on theory.

Preprints

- **Junxin Chen**, Massimiliano Rossi, David Mason, and Albert Schliesser. "Entanglement of Propagating Optical Modes via a Mechanical Interface" arXiv:1911.05729

  This work is discussed in Chapter 5 of this thesis. I realized the optical optical upgrades that enabled this experiment. I also collected and calibrated the data on which this study is based. I made initial contributions to theory and data analysis, which were completed by my colleagues MR and DM.

Conference Presentations

Junxin Chen, Massimiliano Rossi, Yeghishe Tsaturyan, William H. P. Nielsen, Andreas Barg, Christoffer Møller, Eugene S. Polzik, and Albert Schliesser. "Multimode Quantum Optomechanics." Conference on Nanophotonics: Frontiers and Applications (2017), Monte Verita, poster presentation.

Junxin Chen, Massimiliano Rossi, David Mason, Yeghishe Tsaturyan, Yannick Seis, and Albert Schliesser. "Quantum Optomechanics with Ultracoherent Soft–Clamped Resonators." Conference on Lasers and Electro-Optics (2018), San Jose, oral presentation.

Massimiliano Rossi, David Mason, Junxin Chen, Yeghishe Tsaturyan, and Albert Schliesser. "Sub-SQL measurement and single quantum trajectories of a mechanical resonator." The Center for Hybrid Quantum Networks Opening Symposium (2018), Copenhagen, poster presentation.

Junxin Chen, Massimiliano Rossi, David Mason, Yeghishe Tsaturyan, and Albert Schliesser. "Quantum Measurement At and Below the Standard Quantum Limit." The Winter Colloquium on the Physics of Quantum Electronics (2019), Snow Bird, poster presentation

Junxin Chen, David Mason, Massimiliano Rossi, Yeghishe Tsaturyan, and Albert Schliesser. "Measuring Motion Below the Standard Quantum Limit." Quantum Information and Measurement (QIM) V: Quantum Technologies, Rome, oral presentation.

Junxin Chen, Massimiliano Rossi, David Mason, Yeghishe Tsaturyan, and Albert Schliesser. "Quantum otpomechanics with soft-clamped membrane-in-the-middle system." QuaSeRT midterm meeting, Florence, oral presentation.

Contents

Chapter 1

Introduction

Optomechanics is a field studying the interaction between electromagnetic (EM) fields and mechanical oscillators. This field of research was first established by the pioneers of the Laser Interferometer Gravitational-Wave Observatory (LIGO) [2, 3], whose aim was to measure gravitational waves, predicted by the theory of general relativity in 1916 [4]. When a gravitational wave passes through spacetime, the spatial distance between two points along the propagation direction will experience an oscillation. By measuring the relative position between two points in space, one can get information about this oscillation, thus confirming the presence of a gravitational wave.

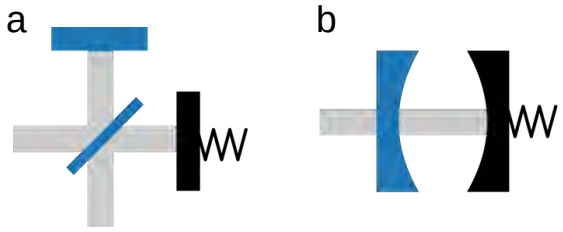

Figure 1.1: Interferometric measurement of displacement A figure from [5]. **a.** Michelson interferometer. **b.** Cavity optomechanics.

The idea of the measurement performed in LIGO is based on a Michelson interferometer, as shown in Fig. 1.1 a, where the movement of the mirror changes the phase of the light of the corresponding arm, and results in intensity change at the output. By detecting this signal, one can infer the displacement of the movable mirror. However, the effect of gravitational wave is extremely weak. The peak strain caused by gravitational wave is of the order 10^{-21} [6], which means one needs to tell a fractional change of only 10^{-21} of the original distance. Considering the fact that the LIGO interferometer arms are of of length 4 km, this demands a displacement measurement of accuracy 10^{-18} m, three orders of magnitudes smaller than the diameter of a proton. Therefore, a simple minded interferometer is not enough for this purpose. One of the key steps in improving the sensitivity is to introduce a cavity in each interferometer arm, as shown in Fig. 1.1 b, which recycles the light and effectively prolongs the arm length. This is the origin of cavity optomechanics, whose primary goal is precise displacement measurement.

Since we measure displacement by looking at change in phase, and a clean laser outputs a coherent state, Fig. 1.2 helps understanding a key point of displacement/phase sensitivity. As there is intrinsic uncertainties in coherent states (represented by the circles), when the phase change caused by displacement is small, the two uncertainty circles may merge together, preventing the measurement from resolving this phase change. This noise is usually referred as imprecision noise. If we increase the amplitude of the coherent state, the uncertainty circles keep the same size as a property of coherent state, the same phase change can result in well separated uncertainty circles, which allows us to resolve the phase change. As the amplitude of a coherent state is given by $|\alpha| = \sqrt{N}$, where N is the average photon number in the state, the phase resolution is given by $1/\sqrt{2N}$, following basic geometry. However, the photons carry some momentum. Upon absorption by or reflection from the object we are measuring, there is momentum transfer to the object, which perturbs the future time evolution of the position of the object. If there is randomness in the momentum or number of

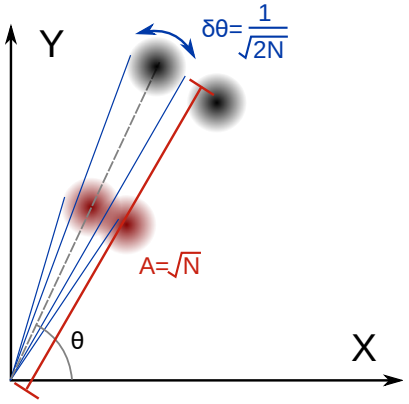

Figure 1.2: Phase resolution of coherent states The horizontal and vertical axis are dimensionless quadratures. θ is the phase of the coherent states. A phase shift is applied to test the phase resolution of coherent states. Here we compare two cases. The red circles represent a coherent state with small amplitude, before and after the phase shift. The black circles represent a coherent state with large amplitude, before and after the same phase shift. In the small amplitude case, the circles have some overlap, which limits the phase resolution. While in the large amplitude case, the circles are separated far apart, which has no problem resolving the phase shift.

photons, this displacement will be random as well, which prevent us from getting an accurate measurement. This effect is called backaction, as it is a result of measurement on the object. Unfortunately, a coherent state has uncertainty in photon number, the standard deviation of which is given by $\sqrt{N}$, following Poisson distribution. This is manifested by the random arrival time of photons on the mirror, usually referred as shot noise. For a general optical state, in phase space, this uncertainty in particle number can be seen as the over lap between the Wigner functions of the state under exam and different Fock states. As Fock states have azimuthal symmetry, the particle number uncertainty only depends on the radial distance between the state and the origin, and the uncertainty in amplitude quadrature of the state. For a coherent state, the amplitude uncertainty is a constant, thus the uncertainty only depends on amplitude $\sqrt{N}$. Now we can see a fundamental trade off between backaction noise and imprecision noise, as a function of photon number, as illustrated in Fig. 1.3. The minimum measurable displacement is called the Standard Quantum Limit (SQL), which was first proposed by Braginsky in 1968 [7].

Mathematically, the Standard Quantum Limit equals the zero point fluctuation of the mechanical oscillator. Therefore, having an imprecision noise lower than the SQL is a necessary condition to resolve zero-point motion, and is a sign of the measurement reaching the quantum regime, when the mechanics is thermalized to a zero-temperature bath. The imprecision noise normalized to the SQL for a measurement is thus treated as a figure of merit of displacement measurement sensitivity. To improve this sensitivity, apart from having more photons by using a stronger laser beam, one can also decrease the cavity linewidth (increases the number of round trips of a photon), decrease the mass of the mechanical oscillator (increases zero-point fluctuation), decrease the effective mechanical linewidth (increases the peak value of zero-point motion), and increase detection efficiency (increases signal-to-noise ratio). Over a century of efforts, displacement imprecision noise has been reduced from tens of orders of magnitude above the SQL to the SQL level and beyond it, as can be seen from a modified figure from Vivishek Sudhir's thesis (Fig. 1.4). Since the first system providing imprecision noise beyond the SQL in 2007, the sensitivity follows a Moore's law like tendency until 2016. Our system continues this tendency and achieved 10^{-7} sensitivity [8], thanks to the membrane-in-the-middle system [9] with ultra-coherent soft-clamped mechanical oscillator [10].

Though optomechanical systems were initially used for precision measurements, during the development of the field, scientists realized that mechanical systems also provide a perfect platform to study massive quantum systems. Usually, quantum systems are tiny and light, from atomic scale such as atoms, ions, molecules and color centers of diamond, to microscale such as quantum dots and superconducting qubits. Massive systems, on the other hand, typically behave in a purely classical fashion, as we know from our daily life. These two worlds behave drastically different. Studying massive quantum systems enables the exploration of the boundary between these two worlds. As the technology in optomechanics advances, mechanical os-

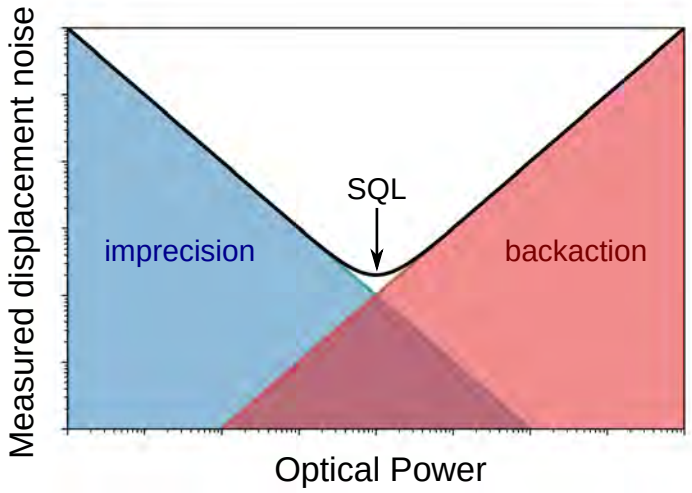

Figure 1.3: The Standard Quantum Limit for displacement measurement Imprecision noise is inversely proportional to optical power, while quantum backaction noise is proportional to it. The Standard Quantum Limit is the minimum noise introduced by measurement, minimized over optical powers.

cillators from meso- to macroscopic scales has enabled the achievement of remarkable goals in preparing massive quantum states, such as motional ground state [8, 12, 13, 14], squeezed state [15, 16, 17], Fock state [18, 19, 20], optical-mechanical entanglement state [21], and mechanical-mechanical entanglement [22, 23]. By applying the cat state preparation proposal for levitated particles [24] or combining microwave cat state preparation techniques [25] and quantum acoustics with superconducting qubits [18, 19], one has the potential of preparing cat states of massive systems with large distance, which is potentially beneficial for exploring new physics beyond standard quantum mechanics and classical mechanics, like low energy signatures of quantum gravity [26, 27, 28, 29].

Quantum mechanical oscillators also find their usage in quantum information processing. Due to the long coherence time compared to many condensed matter based qubits, mechanical oscillators have the potential of acting as quantum memories [30, 31]. Due to orders of magnitudes slower propagation speed of acoustic waves, as compared to microwaves, mechanical device can serve as delay lines, while undertake quantum computing tasks as microwave wave guides [32]. Due to the frequency insensitive interaction between EM wave and mechanical oscillators, electro-opto-mechanical systems are promising candidates for quantum transducers [33, 34, 35], which are of relevance for the quantum internet [36] involving different frequencies.

In this thesis, we focus on the effects of optomechanical quantum correlation, which is a natural consequence of optomechanical interaction in continuous wave regime. During a measurement, the amplitude quadrature of the inputting field pushes the movable mirror (quantum backaction), giving it some random momentum. After a quarter of mechanical period, this random momentum is rotated into displacement, and influence the phase quadrature of the light. Thus the two quadratures of the light field are correlated. To make full use of this quantum correlation, one need to have simultaneously high detection efficiency and strong measurement (in terms of large amount of quantum backaction). This correlation is the mechanism of ponderomotive squeezing of light, which was observed in various of optomechanical systems [1, 37, 38, 39]. Compared to the optical squeezed states generated by optical parametric oscillators (OPO), ponderomotive squeezing has the advantage of working at arbitrary wavelengths. Vyatchanin et al. [40] also proposed a protocol of overcoming the Standard Quantum Limit using this quantum correlation in 1995. Though proposed more than 20 years ago, previous optomechanical systems suffered from either too weak interaction or too low detection efficiency. The amount of measured quantum correlation was not enough to overcome the SQL. Our membrane-in-the-middle system with a soft-clamped mechanical oscillator has the unique feature of satisfying these two demanding conditions simultaneously, which leads to the first experimental realization of sub-SQL measurement [41], which will be introduced in Chapter 4 of this thesis. If we have multiple EM fields interacting with the same mechanical oscillator, this quantum correlation can generate entanglement between different EM fields. This effect was first demonstrated very recently in microwave

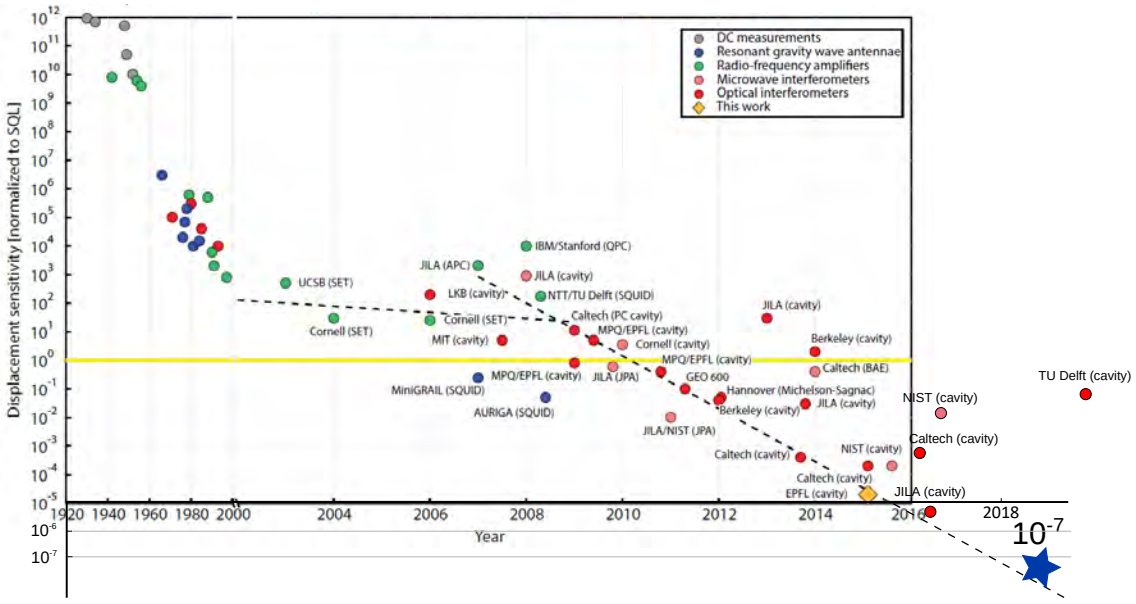

Figure 1.4: Imprecision noise over the last century A modified figure from [11]. The blue star indicates the sensitivity from our work.

regime [42], and in this thesis, we will introduce the first realization in the optical regime. The low noise optical detection allows us to demonstrate the entanglement without assumptions on the noise composition in the detection. The microwave and optical demonstrations of mechanically mediated entanglement pave the way to microwave-optical entanglement, which could find its role in the quantum internet.

Apart from discussing the achievements of our MIM system, another goals of this thesis are to provide a systematic derivation of the theories involved in the projects, to faithfully record the design of the experimental apparatus, the calibration and measurement methods, and to document the operations needed during the experiments. As the thesis is more technical oriented, it may be less self-contained, and may provide a less thorough review of the field of optomechanics compared to other theses. Moreover, some supplementary information is expected to appear in Massimiliano Rossi's thesis. However, I hope this thesis will resolve most of the conceptual, theoretical and technical problems one may encounter when operating an MIM system with a soft-clamped membrane, and be a good introduction to the projects we have done.

In Chapter 2 of this thesis, we introduce the basic theory of optomechanics and some consequences related to the projects introduced in this thesis. In Chapter 3, we introduce the general experimental setup, system characterization techniques and measurement techniques. In Chapter 4, we introduce the theory and experiment of the first displacement and force measurement beyond the Standard Quantum Limit. In Chapter 5, we introduce the theory and experiment for the first mechanics mediated optical-optical entanglement. In Chapter 6, we briefly go through the experiment of the first feedback cooling a mechanical mode to its quantum ground state. In the last chapter, we discuss two outlooks of our membrane-in-the-middle systems with ultra-coherent soft-clamped membranes.

Chapter 2

Basic Theory of Cavity Optomechanics

In this chapter we introduce the optomechanical interaction between one optical mode and one mechanical mode. We begin with quantum harmonic oscillator, then introduce Gaussian optics, and the interaction between the mechanical mode and the optical mode through radiation pressure force. Followed by introducing two consequences of the interaction: the Standard Quantum Limit (SQL) and ponderomotive squeezing. The latter provides a good analogy to both measurement below the SQL and optical-optical entanglement, which will introduce in later chapters.

2.1 Quantum Harmonic Oscillator

An isolated quantum harmonic oscillator can be described by the Hamiltonian:

$$\hat{H} = \frac{k\hat{q}^2}{2} + \frac{\hat{p}^2}{2m}, \tag{2.1}$$

where $\hat{q}$ and $\hat{p}$ are position and momentum operators respectively, while m is the mass of the oscillator and $k \equiv m\Omega_{\rm m}^2$ is the spring constant, where $\Omega_{\rm m}$ the angular resonance frequency of the harmonic oscillator. It is usually more convenient to work with dimensionless position and momentum operators:

$$\hat{Q} = \frac{1}{\sqrt{2}}\frac{\hat{q}}{x_{\rm zpf}} = \frac{1}{\sqrt{2}}\left(\hat{b}^\dagger + \hat{b}\right) \tag{2.2a}$$

$$\hat{P} = \frac{1}{\sqrt{2}}\frac{\hat{p}}{p_{\rm zpf}} = \frac{i}{\sqrt{2}}\left(\hat{b}^\dagger - \hat{b}\right), \tag{2.2b}$$

where $x_{\rm zpf} = \sqrt{\hbar/2m\Omega_{\rm m}}$ and $p_{\rm zpf} = \sqrt{\hbar m\Omega_{\rm m}/2}$ are the standard deviation of the zero point motion and zero point momentum of the oscillator respectively (will be illustrated later), with $\hbar$ the reduced Planck constant, and $\hat{b}$ ($\hat{b}^\dagger$) is the annihilation (creation) operator. The Hamiltonian can also be written in terms of these operators

$$\hat{H} = \frac{\hbar\Omega_{\rm m}}{2}\left(\hat{Q}^2 + \hat{P}^2\right) = \hbar\Omega_{\rm m}\left(\hat{b}^\dagger\hat{b} + \frac{1}{2}\right) = \hbar\Omega_{\rm m}\left(\bar{n} + \frac{1}{2}\right), \tag{2.3}$$

where $\bar{n}$ is the phonon occupancy of the harmonic oscillator. When the oscillator only couples to thermal bath, its occupancy is given by thermal occupancy $\bar{n}_{\rm th} = [e^{\hbar\Omega_{\rm m}/k_{\rm B}T} - 1]^{-1}$, with T the temperature of the oscillator.

It is easy to show the commutation relation of the dimensionless operators:

$$\left[\hat{Q}, \hat{P}\right] = i. \tag{2.4}$$

As a direct consequence of this commutation relation, the product of standard deviations ($\sigma(\hat{O}) = \left(\langle\hat{O}^2\rangle - \langle\hat{O}\rangle^2\right)^{1/2}$) is given by:

$$\sigma(\hat{Q})\sigma(\hat{P}) \geq \frac{1}{2}. \tag{2.5}$$

Therefore, the product is finite even for $T = 0$. When $T = 0$ and $\sigma(\hat{Q}) = \sigma(\hat{P})$, the standard deviations of displacement and momentum are given by $x_{\rm zpf}$ and $p_{\rm zpf}$ respectively. This kind of uncertainty is referred as zero point fluctuation.

2.1.1 Quantum Fluctuation-Dissipation Theorem

In Eqn. 2.3, we mentioned the effect of thermal environment on mechanical Hamiltonian. To describe other effects of thermal noise we need quantum fluctuation-dissipation theorem (more details can be found in [43]), which is typically given in the form of power spectral density (PSD).

For a general quantum operator $\hat{O}$, the PSD is defined by

$$S_{\hat{O}\hat{O}}(\Omega) \equiv \lim_{\tau\to\infty} \frac{1}{\tau}\langle \hat{O}_\tau^\dagger(\Omega)\hat{O}_\tau(\Omega)\rangle, \tag{2.6}$$

where $\hat{O}_\tau(\Omega) \equiv \int_{-\tau/2}^{\tau/2} \hat{O}(t)e^{i\Omega t}dt$ is the Fourier transform of the time domain operator $\hat{O}(t)$ in the time window $-\tau/2 < t < \tau/2$. The Wiener-Khinchin theorem links the PSD of an operator with stationary statistics (i.e. the system is in steady state) to its autocorrelations function by

$$S_{\hat{O}\hat{O}}(\Omega) = \int_{-\infty}^{\infty} d\tau e^{i\Omega t}\langle \hat{O}^\dagger(t+\tau)\hat{O}(t)\rangle_{t=0} = \int_{-\infty}^{\infty} d\Omega' \langle \hat{O}^\dagger(-\Omega)\hat{O}(\Omega')\rangle. \tag{2.7}$$

Please notice that $\hat{O}^\dagger(-\Omega) = [\hat{O}(\Omega)]^\dagger$.

The quantum fluctuation-dissipation theorem states that, in Markovian limit (the thermal bath has no memory), the power spectral density of the Brownian force, caused by exchanging phonon between the harmonic oscillator and thermal environment, is given by

$$S_{\hat{F}\hat{F}}(\Omega) = 2m\Gamma_\mathrm{m}\hbar\Omega\,(\bar{n}(\Omega)+1) \tag{2.8a}$$

$$S_{\hat{F}\hat{F}}(-\Omega) = 2m\Gamma_\mathrm{m}\hbar\Omega\bar{n}(\Omega), \tag{2.8b}$$

where $\bar{n}(\Omega) = 1/(e^{\hbar\Omega/k_\mathrm{B}T} - 1)$ is the thermal phonon occupancy at frequency Ω, and Γ_m is the rate of exchanging energy between mechanics and environment, also referred as mechanical linewidth. The asymmetry between the positive and the negative frequency component can be used as a robust calibration of thermal occupancy, as

$$\bar{n}_\mathrm{th}(\Omega) = \frac{S_{\hat{F}\hat{F}}(-\Omega)}{S_{\hat{F}\hat{F}}(\Omega) - S_{\hat{F}\hat{F}}(-\Omega)}. \tag{2.9}$$

Sometimes, the measurement gives symmetrized spectrum $\bar{S}_{\hat{O}\hat{O}}(\Omega) \equiv \left(S_{\hat{O}\hat{O}}(\Omega) + S_{\hat{O}\hat{O}}(-\Omega)\right)/2$, like in the homodyne measurement described in Section 3.6. In this case, the quantum fluctuation-dissipation theorem gives

$$\bar{S}_{\hat{F}\hat{F}}(\Omega) = m\Gamma_\mathrm{m}\hbar\Omega\,(2\bar{n}(\Omega)+1)\,. \tag{2.10}$$

One can recover the result of classical fluctuation-dissipation theorem $\bar{S}_{\hat{F}\hat{F}}(\Omega) = 2\Gamma_\mathrm{m}mk_\mathrm{B}T$ by taking the high temperature limit $k_\mathrm{B}T \gg \hbar\Omega$.

2.2 Gaussian Optics

Now we introduce some properties of optics. In this thesis, we are always dealing with Gaussian beans, which are beams of monochromatic electromagnetic field whose transverse electric and magnetic field profile is a Gaussian function. As a result, the intensity also has a Gaussian profile. Gaussian optics describes the effects of optical components, which keeps a Gaussian beam Gaussian.

The mathematical form of the electric field of a Gaussian beam is given by

$$\mathbf{E}(r,z) = E_0\hat{x}\frac{w_0}{w(z)}\exp\left(\frac{-r^2}{w(z)^2}\right)\exp\left(-i\left(kz + k\frac{r^2}{2R(z)} + \psi(z)\right)\right), \tag{2.11}$$

where $E_0 = E(0,0)$ is the field amplitude at the focus, r the distance from optical axis (the line $r = 0$), z the coordinate on propagating direction, $w(z)$ the beam width, at which the amplitude drop to $1/e$ compared to optical axis, w_0 the beam waist (the beam width at focus, $z = 0$), $R(z)$ the radius of curvature of the wavefront, and $\psi(z)$ the Gouy phase. The beam width $w(z)$ is a function of z:

$$w(z) = w_0\sqrt{1 + \left(\frac{z}{z_\mathrm{R}}\right)^2}, \tag{2.12}$$

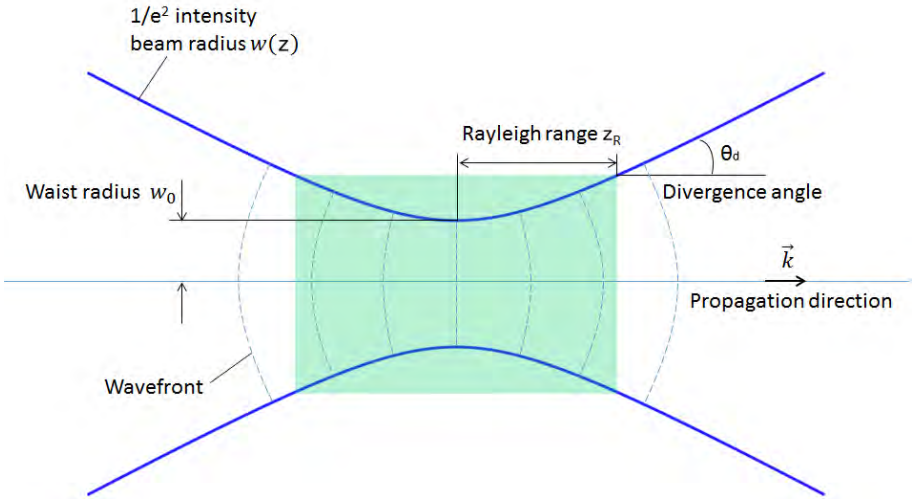

Figure 2.1: Gaussian beam A figure from [44]. The profile of a Gaussian beam around its waist.

where $z_R = \pi w_0^2/\lambda$, with λ the wavelength in the medium, is the Rayleigh range, which quantifies the focusing length. The radius of curvature of wavefront $R(z)$ is also a function of z, which is given by

$$R(z) = z\left[1 + \left(\frac{z_R}{z}\right)^2\right]. \tag{2.13}$$

It is clear that $R(z) = \infty$ at the focus and $z \to \pm\infty$. The Gouy phase $\psi(z)$ is related to z by

$$\psi(z) = \arctan\left(\frac{z}{z_R}\right). \tag{2.14}$$

The divergence angle θ_d is defined as

$$\theta_d \equiv \lim_{z\to\infty} \arctan\left(\frac{w(z)}{z}\right) \approx \frac{\lambda_0}{\pi n w_0}, \tag{2.15}$$

which quantifies how fast the beam width changes with z. The numerical aperture NA is then defined as

$$\mathrm{NA} = n\sin\theta_d = \frac{w_0}{z_R}. \tag{2.16}$$

It is clear from the expressions of $w(z)$, $R(z)$ and $\psi(z)$ that the properties of a freely propagating Gaussian beam is fixed, when w_0 or z_R and λ is known. Therefore, a Gaussian beam can be fully described by a complex beam parameter $q(z)$, which is defined as

$$q(z) = z + \frac{i\pi n w_0^2}{\lambda_0} = z + iz_R, \tag{2.17}$$

where n is the refractive index of the medium, and λ_0 is the wavelength in vacuum. $q(z)$ can also be written in a form closer to lens imaging equation:

$$\frac{1}{q(z)} = \frac{1}{R(z)} - \frac{i\lambda_0}{\pi n w(z)^2}, \tag{2.18}$$

which implies that the propagation of $q(z)$ can be described by ABCD matrix, also known as ray transfer matrix.

ABCD matrix analysis is a method to analyze paraxial rays, the rays close to the optical axis. Each optical elements, including beam travel, interface, lens and mirror, can be described by a 2×2 matrix

$$\begin{pmatrix} A & B \\ C & D \end{pmatrix}. \tag{2.19}$$

Any combination of these optical elements can be described by the matrix-multiplication products of all element matrices. For example the ABCD matrices of propagation in a medium with constant refractive index, refraction at a curved surface, reflection from a flat mirror, and propagation through a thin lens are given by

$$\text{propagation } \begin{pmatrix} 1 & d \\ 0 & 1 \end{pmatrix}, \text{ interface } \begin{pmatrix} 1 & 0 \\ \frac{n_1-n_2}{Rn_1} & \frac{n_1}{n_2} \end{pmatrix}, \text{ mirror } \begin{pmatrix} 1 & 0 \\ 0 & 1 \end{pmatrix}, \text{ lens } \begin{pmatrix} 1 & 0 \\ -\frac{1}{f} & 1 \end{pmatrix}, \tag{2.20}$$

respectively, where d is the propagation distance, n_1 and n_2 are the refractive indices of inputting medium and outputing medium respectively, R is the radius of curvature of the curved surface ($R > 0$ for convex surface, and $R \to \infty$ for flat mirror), and f is the focal length of the lens ($f > 0$ for convex lens). $q(z)$ evolves with ABCD matrix as

$$q_{\mathrm{f}}(z) = \frac{Aq_{\mathrm{i}}(z) + B}{Cq_{\mathrm{i}}(z) + D}, \tag{2.21}$$

where $q_{\mathrm{i}}(z)$ is the complex parameter before the optical element, and $q_{\mathrm{f}}(z)$ after.

2.2.1 Hermite-Gaussian modes

When a cavity is included in an optical path, we might not only encounter Gaussian modes defined above, but also some higher order Hermite-Gaussian modes, which in general do not have axial symmetry along the propagating axis. Then the electric fields of these modes is a function of x, y and z, where x and y are coordinates on a plane perpendicular to the propagating axis:

$$E_{l,m}(x,y,z) = E_0 \frac{w_0}{w(z)} H_l\left(\frac{\sqrt{2}x}{w(z)}\right) H_m\left(\frac{\sqrt{2}y}{w(z)}\right) \exp\left(-\frac{x^2+y^2}{w(z)^2}\right) \exp\left(-i\frac{k(x^2+y^2)}{2R(z)}\right) \exp\left(i\psi(z)\right), \tag{2.22}$$

where H_J, $(J = l, m)$ is the Hermite polynomial of order J. Comparing this expression to Eqn. 2.11, the only differences are the two Hermite polynomial factors, which introduce nodes on the intensity profile. Hermite-Gaussian modes are transverse-electro-magnetic modes (TEM modes). With orders, they are typically referred as TEM_{lm}, where TEM_{00} is the mode described by Eqn. 2.11. Some of the Hermite-Gaussian modes are presented in Fig. 2.2.

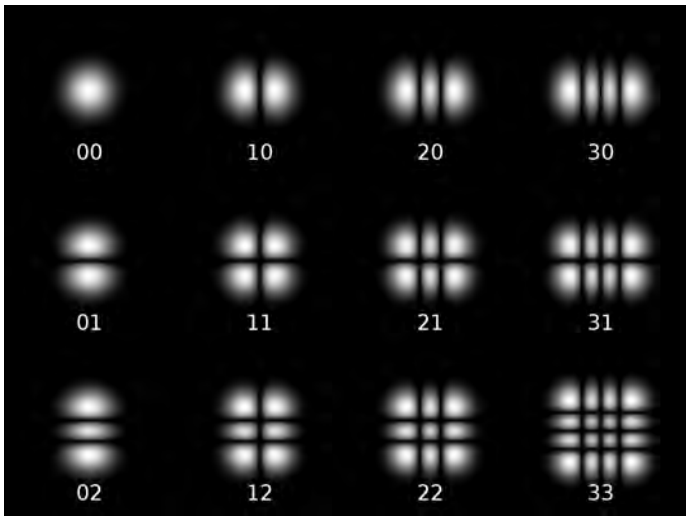

Figure 2.2: Twelve Hermite-Gaussian modes A figure from [45]. The two-digit numbers identify Hermite-Gaussian modes. The first digit represents the number of nodes in the horizontal direction, while the second digit represents that in the vertical direction.

2.3 Radiation Pressure Interaction in Cavity Optomechanics

We now consider a canonical cavity optomechanical system, where one mirror of a Fabry-Pérot cavity is movable and attached to a spring, while the other mirror is fixed, as shown in Fig. 2.3. This model can describe all kinds of cavity optomechanics systems based on radiation pressure interaction, despite their drastical difference in sizes, designs and working conditions.

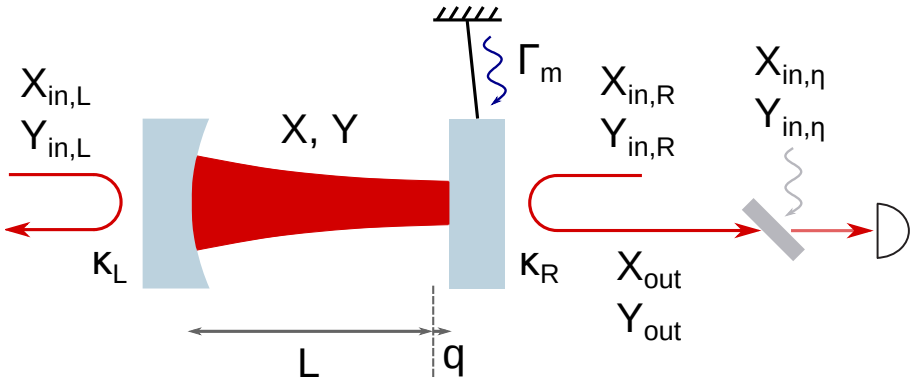

Figure 2.3: Canonical model of cavity optomechanics A Fabre-Pérot cavity with a movable end mirror. In this thesis, we take the convention that input light is always injected from the left side of the cavity.

When there is no interaction, the Hamiltonian of the system is

$$\hat{H}_0 = \frac{\hbar\Omega_{\rm m}}{2}\left(\hat{Q}^2 + \hat{P}^2\right) + \hbar\Omega_{\rm cav}\hat{a}^\dagger\hat{a}, \tag{2.23}$$

where $\Omega_{\rm cav} = 2\pi c/\lambda = \pi c\mathcal{N}/L$ is the cavity resonance frequency, where λ is the wavelength, $\mathcal{N}$ is the mode number, and L is the unmodified cavity length. $\hat{a}$ ($\hat{a}^\dagger$) is the annihilation (creation) operator of the cavity field.

The optomechanical interaction via radiation pressure is based on exchange of momentum between photons and mechanics. This interaction shifts the position of the movable mirror by q from its original equilibium position, thus changes the resonance frequency of the cavity to $\Omega_{\rm cav}(q) = \pi c\mathcal{N}/(L+q)$. If $q \ll L$ holds, we have a linear relation $\Omega_{\rm cav}(q) \approx \Omega_{\rm cav}(1 - q/L)$. Then the cavity hamiltonian becomes:

$$\hat{H}_{\rm cav} = \hbar\Omega_{\rm cav}\hat{a}^\dagger\hat{a}\left(1 - \frac{q}{L}\right) = \hbar\Omega_{\rm cav}\hat{a}^\dagger\hat{a} - \hbar G q\hat{a}^\dagger\hat{a}, \tag{2.24}$$

where $G = \frac{\partial\Omega_{\rm cav}}{\partial q}$ is the optomechanical coupling rate. The second term is the interaction Hamiltonian. One can rewrite it as

$$\hat{H}_{\rm int} = -\sqrt{2}\hbar g_0\hat{a}^\dagger\hat{a}\hat{Q}, \tag{2.25}$$

where $g_0 = G x_{\rm zpf}$ is the vacuum optomechanical coupling rate.

The intra-cavity optical field decays as it leaks out of the cavity. To support constant intra-cavity field, we need a driving laser. Suppose the driving laser is injected from the left mirror, one can model the drive by the Hamiltonian [46]

$$\hat{H}_{\rm drive} = i\hbar\sqrt{\kappa_{\rm L}}\left(\alpha_{\rm in}\hat{a}^\dagger e^{-i\omega t} + c.c.\right), \tag{2.26}$$

where $\kappa_{\rm L}/2\pi = |t_{\rm L}|^2/\tau$, with $t_{\rm L}$ amplitude transmissivity of the left mirror and $\tau = 2L/c$ the round trip time of light in cavity, is the coupling rate of cavity field to the field outside the left mirror, ω is the laser frequency, $c.c.$ stands for complex conjugate, and $\alpha_{\rm in}$ is the laser field amplitude. In principle, this input laser field amplitude is quantum mechanical, and should be described by an operator $\hat{a}_{\rm in}$. However, in practice, clean laser fields can be well described by coherent states, which, in phase space, is composed of a mean field amplitude $\alpha_{\rm in}$ and an uncertainty "bubble" $\delta\hat{a}_{\rm in}$ given by vacuum fluctuation, i.e. $\hat{a}_{\rm in} = \alpha_{\rm in} + \delta\hat{a}_{\rm in}$. When $|\alpha_{\rm in}| \gg \sqrt{\langle\delta\hat{a}_{\rm in}^\dagger\delta\hat{a}_{\rm in}\rangle}$, i.e. the amplitude of the coherent state is large, we can neglect the effect of

the fluctuation part, and treat the field classically in Hamiltonian. For majority of optomechanical systems, including ours, this is a good approximation. Then the total Hamiltonian is given by

$$\hat{H} = \hat{H}_0 + \hat{H}_{\rm int} + \hat{H}_{\rm drive}. \tag{2.27}$$

It is convenient to go to the frame rotating with laser drive frequencies ω, in which we have

$$\hat{H} = \frac{\hbar\Omega_{\rm m}}{2}\left(\hat{Q}^2 + \hat{P}^2\right) - \hbar\tilde{\Delta}\hat{a}^\dagger\hat{a} - \sqrt{2}\hbar g_0\hat{a}^\dagger\hat{a}\hat{Q} + i\hbar\sqrt{\kappa_{\rm L}}\left(\alpha_{\rm in}\hat{a}^\dagger + c.c.\right), \tag{2.28}$$

where $\tilde{\Delta} = \omega - \tilde{\Omega}_{\rm cav}$ is the cavity detuning when optomechanical interaction is turned off, with $\tilde{\Omega}_{\rm cav}$ the cavity frequency with $g_0 = 0$.

Though the quantum fluctuation of the laser drive was neglected in the Hamiltonian, it may have some non-negligible effects. Together with effects from optical noise input from the right mirror and thermal noise acting on the membrane, their time evolutions are given by the Heisenberg-Langevin equations [43]:

$$\dot{\hat{a}} = \frac{i}{\hbar}\left[\hat{H}, \hat{a}\right] - \frac{\kappa}{2}\hat{a} - \sqrt{\kappa_{\rm L}}\hat{a}_{\rm in,L} - \sqrt{\kappa_{\rm R}}\hat{a}_{\rm in,R} \tag{2.29a}$$

$$\dot{\hat{Q}} = \frac{i}{\hbar}\left[\hat{H}, \hat{Q}\right] \tag{2.29b}$$

$$\dot{\hat{P}} = \frac{i}{\hbar}\left[\hat{H}, \hat{P}\right] - \Gamma_{\rm m}\hat{P} + \sqrt{2\Gamma_{\rm m}}\hat{P}_{\rm in}, \tag{2.29c}$$

where $\hat{a}_{{\rm in},L}$ ($\hat{a}_{\rm in,R}$) is the optical noise operator injecting from left (right) mirror (to unify and simplify the notation, we drop the "δ" in $\delta\hat{a}_{{\rm in},L}$), and $\hat{P}_{\rm in}$ is the mechanical momentum noise operator, resulting from the Brownian thermal force noise described in Subsection 2.1.1, $\kappa_R/2\pi = |t_{\rm R}|^2/\tau$ is the coupling rate of cavity field to the field outside the right mirror, and $\kappa = \kappa_{\rm L} + \kappa_{\rm R}$ is the total rate of cavity field coupling to the field outside, i.e. the cavity linewidth (suppose there is no intra-cavity loss mechanism). Here, rotating wave approximation is applied for optical fields, where we neglect the effects of terms rotating at around twice of the laser frequency.

By substituting the Hamiltonian into the Heisenberg-Langevin equations, we have [43]

$$\dot{\hat{a}} = -\left[\frac{\kappa}{2} - i\left(\tilde{\Delta} + \sqrt{2}g_0\hat{Q}\right)\right]\hat{a} - \sqrt{\kappa_{\rm L}}\hat{a}_{\rm in,L} - \sqrt{\kappa_{\rm R}}\hat{a}_{\rm in,R} \tag{2.30a}$$

$$\dot{\hat{Q}} = \Omega_{\rm m}\hat{P} \tag{2.30b}$$

$$\dot{\hat{P}} = -\Omega_{\rm m}\hat{Q} - \Gamma_{\rm m}\hat{P} + \sqrt{2\Gamma_{\rm m}}\hat{P}_{\rm in} + \sqrt{2}g_0\hat{a}^\dagger\hat{a}. \tag{2.30c}$$

Before discussing quantum effects, as we are interested in fluctuations around equilibrium, it is necessary to exam the behavior of the equilibrium case under optomechanical interaction via examining the classical behaviors of these fields. This is done by replacing the field operators with their average values. Then the equations reads

$$\dot{\alpha} = -\left[\frac{\kappa}{2} - i\left(\tilde{\Delta} + \sqrt{2}g_0\langle Q\rangle\right)\right]\alpha - \sqrt{\kappa_{\rm L}}\alpha_{\rm in} \tag{2.31a}$$

$$\langle\dot{Q}\rangle = \Omega_{\rm m}\langle P\rangle \tag{2.31b}$$

$$\langle\dot{P}\rangle = -\Omega_{\rm m}\langle Q\rangle - \Gamma_{\rm m}\langle P\rangle + \sqrt{2}g_0|\alpha|^2, \tag{2.31c}$$

where we have used the fact that vacuum noise injected from the right mirror has zero average amplitude, and the thermal noise is incoherent, such that $\langle P_{\rm in}\rangle = 0$. In the scope of this thesis, we are interested in steady state solutions. Thus, we set all time derivatives on the left hand side to be zero, and get

$$0 = -\left[\frac{\kappa}{2} - i\left(\tilde{\Delta} + \sqrt{2}g_0\langle Q\rangle\right)\right]\alpha - \sqrt{\kappa_{\rm L}}\alpha_{\rm in,L} \tag{2.32a}$$

$$0 = -\Omega_{\rm m}\langle Q\rangle + \sqrt{2}g_0|\alpha|^2, \tag{2.32b}$$

where we have used the second equation $0 = \Omega_{\rm m}\langle P\rangle$ to eliminate $\langle P\rangle$. Then the steady state solutions of

the fields are

$$\alpha_{\mathrm{ss}} = \frac{\sqrt{\kappa_{\mathrm{L}}}}{\frac{\kappa}{2} - i\left(\tilde{\Delta} + \sqrt{2}g_0\langle Q_{\mathrm{ss}}\rangle\right)}\alpha_{\mathrm{in}} \tag{2.33a}$$

$$\langle Q_{\mathrm{ss}}\rangle = \frac{\sqrt{2}g_0|\alpha_{\mathrm{ss}}|^2}{\Omega_{\mathrm{m}}}. \tag{2.33b}$$

The optomechanical coupling is evident in this expression, as $\sqrt{2}g_0\langle Q_{\mathrm{ss}}\rangle$ serves as an additional detuning, which is proportional to mechanical displacement. Thus the new detuning at equilibrium $\Delta = \tilde{\Delta} + \sqrt{2}g_0\langle Q_{\mathrm{ss}}\rangle$. On the other hand, stronger intra-cavity field also results in a new equilibrium position with larger mechanical displacement. The consequences of these classical steady state equations will be discussed in the later sections of this chapter.

Now, we study the quantum behavior by doing some linearization of the interaction Hamiltonian, which can simplify the problem dramatically. We can rewrite the optical field operators $\hat{a}$ in terms of average value $\bar{\alpha} = \sqrt{\bar{n}_{\mathrm{cav}}} = \sqrt{\langle\hat{a}^\dagger\hat{a}\rangle}$, which is the square root of the photon number in the cavity mode, and fluctuation $\delta\hat{a}$, such that $\hat{a} = \bar{\alpha} + \delta\hat{a}$. As $|\bar{\alpha}| \gg \sqrt{\langle\delta\hat{a}^\dagger\delta\hat{a}\rangle}$ holds in our case, we can neglect the second order term of $\delta\hat{a}$, and linearize the interaction Hamiltonian in rotating frame:

$$\hat{H}_{\mathrm{int}}^{\mathrm{lin}} = -\sqrt{2}\hbar g_0\bar{\alpha}\left(\delta\hat{a} + \delta\hat{a}^\dagger\right)\hat{Q}. \tag{2.34}$$

Substituting the linearized Hamiltonian into the Heisenberg-Langevin equation, and focusing on the fluctuation part $\delta\hat{a}$, we have

$$\delta\dot{\hat{a}} = -\frac{\kappa}{2}\delta\hat{a} + i\Delta\delta\hat{a} + \sqrt{2}g\hat{Q} + \sqrt{\kappa_{\mathrm{L}}}\hat{a}_{\mathrm{in,L}} + \sqrt{\kappa_{\mathrm{R}}}\hat{a}_{\mathrm{in,R}} \tag{2.35a}$$

$$\dot{\hat{Q}} = \Omega_{\mathrm{m}}\hat{P} \tag{2.35b}$$

$$\dot{\hat{P}} = -\Omega_{\mathrm{m}}\hat{Q} - \Gamma_{\mathrm{m}}\hat{P} + \sqrt{2\Gamma_{\mathrm{m}}}\hat{P}_{\mathrm{in}} + \sqrt{2}g_0\hat{a}^\dagger\hat{a}. \tag{2.35c}$$

where $g = g_0\bar{\alpha}$ is the multi-photon optomechanical coupling. Please notice that the detuning is the instantaneous detuning at the new equilibrium position Δ in these equations. We notice $\delta\hat{a}$ is not an observable. To get some observable out of this fluctuation, we define optical amplitude quadrature $\hat{X} = \left(\delta\hat{a}^\dagger + \delta\hat{a}\right)/\sqrt{2}$, and phase quadrature $\hat{Y} = i\left(\delta\hat{a}^\dagger - \delta\hat{a}\right)/\sqrt{2}$. Then the Heisenberg-Langevin equation reads:

$$\dot{\hat{X}} = -\frac{\kappa}{2}\hat{X} - \Delta\hat{Y} + \sqrt{\kappa_{\mathrm{L}}}\hat{X}_{\mathrm{in,L}} + \sqrt{\kappa_{\mathrm{R}}}\hat{X}_{\mathrm{in,R}} \tag{2.36a}$$

$$\dot{\hat{Y}} = -\frac{\kappa}{2}\hat{Y} + \Delta\hat{X} + 2g\hat{Q} + \sqrt{\kappa_{\mathrm{L}}}\hat{Y}_{\mathrm{in,L}} + \sqrt{\kappa_{\mathrm{R}}}\hat{Y}_{\mathrm{in,R}} \tag{2.36b}$$

$$\dot{\hat{Q}} = \Omega_{\mathrm{m}}\hat{P} \tag{2.36c}$$

$$\dot{\hat{P}} = -\Omega_{\mathrm{m}}\hat{Q} - \Gamma_{\mathrm{m}}\hat{P} + \sqrt{2\Gamma_{\mathrm{m}}}\hat{P}_{\mathrm{in}} + 2g\hat{X}, \tag{2.36d}$$

where $\hat{X}_{\mathrm{in,L}} = \left(\hat{a}_{\mathrm{in,L}}^\dagger + \hat{a}_{\mathrm{in,L}}\right)/\sqrt{2}$ is the input amplitude noise quadrature, and $\hat{Y}_{\mathrm{in},} = i\left(\hat{a}_{\mathrm{in,L}}^\dagger - \hat{a}_{\mathrm{in,L}}\right)/\sqrt{2}$ is the input phase noise quadrature through the left mirror. Those for the right mirror (labeled with "R") are defined similarly. It is clear from this expression that $\hat{Q}$ only couples to phase quadrature. Thus, if the laser is on resonance with the cavity ($\Delta = 0$), no information about the mechanics is encoded in amplitude quadrature.

The above equation system can be solved relatively easily in frequency domain, where we write $\hat{X}(\Omega) = \int_{-\infty}^{+\infty} dt e^{i\Omega t}\hat{X}(t)$ as the Fourier transform of the corresponding time domain operator, and similarly for other operators. Then the equation system becomes

$$-i\Omega\hat{X}(\Omega) = -\frac{\kappa}{2}\hat{X}(\Omega) - \Delta\hat{Y}(\Omega) + \sqrt{\kappa_{\mathrm{L}}}\hat{X}_{\mathrm{in,L}}(\Omega) + \sqrt{\kappa_{\mathrm{R}}}\hat{X}_{\mathrm{in,R}}(\Omega) \tag{2.37a}$$

$$-i\Omega\hat{Y}(\Omega) = -\frac{\kappa}{2}\hat{Y}(\Omega) + \Delta\hat{X}(\Omega) + 2g\hat{Q}(\Omega) + \sqrt{\kappa_{\mathrm{L}}}\hat{Y}_{\mathrm{in,L}}(\Omega) + \sqrt{\kappa_{\mathrm{R}}}\hat{Y}_{\mathrm{in,R}}(\Omega) \tag{2.37b}$$

$$-i\Omega\hat{Q}(\Omega) = \Omega_{\mathrm{m}}\hat{P}(\Omega) \tag{2.37c}$$

$$-i\Omega\hat{P}(\Omega) = -\Omega_{\mathrm{m}}\hat{Q}(\Omega) - \Gamma_{\mathrm{m}}\hat{P}(\Omega) + \sqrt{2\Gamma_{\mathrm{m}}}\hat{P}_{\mathrm{in}}(\Omega) + 2g\hat{X}(\Omega). \tag{2.37d}$$

Eliminating $\hat{P}(\Omega)$, we have

$$\hat{Q}(\Omega) = \chi_{\mathrm{m}}(\Omega)\left(\sqrt{2\Gamma_{\mathrm{m}}}\hat{P}_{\mathrm{in}}(\Omega) + 2g\hat{X}(\Omega)\right), \tag{2.38}$$

where

$$\chi_{\mathrm{m}}(\Omega) = \Omega_{\mathrm{m}}/((\Omega_{\mathrm{m}}^2 - \Omega^2) - i\Gamma_{\mathrm{m}}\Omega) \tag{2.39}$$

is the mechanical susceptibility, which transduces force into displacement of a harmonic resonator ($\hat{Q}(\Omega) = \chi_{\mathrm{m}}(\Omega)\hat{F}(\Omega)$). In the parenthesis of Eqn. 2.38 is the total noise force acting on the mechanics. The optical quadratures are given by

$$\left(\frac{\kappa}{2} - i\Omega\right)\hat{X}(\Omega) = -\Delta\hat{Y}(\Omega) + \sqrt{\kappa_{\mathrm{L}}}\hat{X}_{\mathrm{in,L}}(\Omega) + \sqrt{\kappa_{\mathrm{R}}}\hat{X}_{\mathrm{in,R}}(\Omega) \tag{2.40a}$$

$$\left(\frac{\kappa}{2} - i\Omega\right)\hat{Y}(\Omega) = \Delta\hat{X}(\Omega) + \sqrt{\kappa_{\mathrm{L}}}\hat{Y}_{\mathrm{in,L}}(\Omega) + \sqrt{\kappa_{\mathrm{R}}}\hat{Y}_{\mathrm{in,R}}(\Omega) + 2g\chi_{\mathrm{m}}(\Omega)\left(\sqrt{2\Gamma_{\mathrm{m}}}\hat{P}_{\mathrm{in}}(\Omega) + 2g\hat{X}(\Omega)\right). \tag{2.40b}$$

Making use of Eqn. 2.38, solving for $\hat{X}$ and $\hat{Y}$, we have

$$\hat{X}(\Omega) = v(\Omega)\left(\sqrt{\kappa_{\mathrm{L}}}\hat{Y}_{\mathrm{in,L}}(\Omega) + \sqrt{\kappa_{\mathrm{R}}}\hat{Y}_{\mathrm{in,R}}(\Omega) + 2g\hat{Q}(\Omega)\right) + u(\Omega)\left(\sqrt{\kappa_{\mathrm{L}}}\hat{X}_{\mathrm{in,L}}(\Omega) + \sqrt{\kappa_{\mathrm{R}}}\hat{X}_{\mathrm{in,R}}(\Omega)\right) \tag{2.41a}$$

$$\hat{Y}(\Omega) = u(\Omega)\left(\sqrt{\kappa_{\mathrm{L}}}\hat{Y}_{\mathrm{in,L}}(\Omega) + \sqrt{\kappa_{\mathrm{R}}}\hat{Y}_{\mathrm{in,R}}(\Omega) + 2g\hat{Q}(\Omega)\right) - v(\Omega)\left(\sqrt{\kappa_{\mathrm{L}}}\hat{X}_{\mathrm{in,L}}(\Omega) + \sqrt{\kappa_{\mathrm{R}}}\hat{X}_{\mathrm{in,R}}(\Omega)\right), \tag{2.41b}$$

where

$$u(\Omega) = \frac{\kappa/2 - i\Omega}{\Delta^2 + (\kappa/2 - i\Omega)^2} \tag{2.42a}$$

$$v(\Omega) = \frac{-\Delta}{\Delta^2 + (\kappa/2 - i\Omega)^2} \tag{2.42b}$$

are the cavity quadratures' susceptibilities.

2.3.1 Output Optical Field and its Spectrum

So far we have only talked about the dynamics of the intra-cavity field. In practice, it is hard to measure the intra-cavity field directly. Instead, one usually measures the field which leaks out of the cavity to extract some information about the intra-cavity field. Let's say we measure the field leaking through the right mirror. The output quadratures are given by the input-output relation:

$$\hat{X}_{\mathrm{out}} = -\hat{X}_{\mathrm{in,R}} + \sqrt{\kappa_{\mathrm{R}}}\hat{X} \tag{2.43a}$$

$$\hat{Y}_{\mathrm{out}} = -\hat{Y}_{\mathrm{in,R}} + \sqrt{\kappa_{\mathrm{R}}}\hat{Y}. \tag{2.43b}$$

In practice, there will be some optical loss from the cavity to the photodetector, which is usually described by a less than unity detection efficiency η. This optical loss will decrease the signal emitted from the cavity, and replace it with vacuum noise. Taking this into consideration, the output quadratures are given by

$$\hat{X}_{\mathrm{out}} = \sqrt{\eta}(-\hat{X}_{\mathrm{in,R}} + \sqrt{\kappa_{\mathrm{R}}}\hat{X}) + \sqrt{1-\eta}\hat{X}_{\mathrm{in},\eta} \tag{2.44a}$$

$$\hat{Y}_{\mathrm{out}} = \sqrt{\eta}(-\hat{Y}_{\mathrm{in,R}} + \sqrt{\kappa_{\mathrm{R}}}\hat{Y}) + \sqrt{1-\eta}\hat{Y}_{\mathrm{in},\eta}, \tag{2.44b}$$

where $\hat{X}_{\mathrm{in},\eta}$ ($\hat{Y}_{\mathrm{in},\eta}$) is the amplitude (phase) noise quadrature of the vacuum getting mixed into the output signal. Substituting Eqn. 2.41 to the above expression we have:

$$\begin{aligned}\hat{X}_{\mathrm{out}}(\Omega) = {} & \sqrt{\eta\kappa_{\mathrm{R}}\kappa_{\mathrm{L}}}\left(u(\Omega)\hat{X}_{\mathrm{in,L}}(\Omega) + v(\Omega)\hat{Y}_{\mathrm{in,L}}(\Omega)\right) + \sqrt{\eta}\kappa_{\mathrm{R}}\left((u(\Omega) - 1/\kappa_{\mathrm{R}})\hat{X}_{\mathrm{in,R}}(\Omega) + v(\Omega)\hat{Y}_{\mathrm{in,R}}(\Omega)\right) \\ & + 2g\sqrt{\eta\kappa_{\mathrm{R}}}v(\Omega)\hat{Q}(\Omega) + \sqrt{1-\eta}\hat{X}_{\mathrm{in},\eta}(\Omega)\end{aligned} \tag{2.45a}$$

$$\begin{aligned}\hat{Y}_{\mathrm{out}}(\Omega) = {} & \sqrt{\eta\kappa_{\mathrm{R}}\kappa_{\mathrm{L}}}\left(-v(\Omega)\hat{X}_{\mathrm{in,L}}(\Omega) + u(\Omega)\hat{Y}_{\mathrm{in,L}}(\Omega)\right) + \sqrt{\eta}\kappa_{\mathrm{R}}\left(-v(\Omega)\hat{X}_{\mathrm{in,R}}(\Omega) + (u(\Omega) - 1/\kappa_{\mathrm{R}})\hat{Y}_{\mathrm{in,R}}(\Omega)\right) \\ & + 2g\sqrt{\eta\kappa_{\mathrm{R}}}u(\Omega)\hat{Q}(\Omega) + \sqrt{1-\eta}\hat{Y}_{\mathrm{in},\eta}(\Omega).\end{aligned} \tag{2.45b}$$

If we only want to detect output amplitude quadrature $\hat{X}_{\rm out}$, we just need to measure the output beam with a photodiode. To get information about output phase quadrature $\hat{Y}_{\rm out}$, one need to exploit interferometric measurement, such as heterodyne and homodyne, to transform phase information to intensity. Then photodiodes can again be used for the detection. In heterodyne, the output field (referred as signal) is beaten with a reference field (local oscillator, LO) at a different frequency. While in homodyne, the LO frequency is the same as the carrier frequency of the signal. In the following, we assume homodyne is performed (a detailed introduction to homodyne can be found in Section 3.6). Suppose the relative phase between LO and signal is θ, then the measured quadrature is given by

$$\hat{X}_\theta(\Omega) = \hat{X}_{\rm out}(\Omega)\cos\theta + \hat{Y}_{\rm out}(\Omega)\sin\theta. \tag{2.46}$$

Suppose our system is in steady state, we can calculate the power spectral density of $\hat{X}_\theta$, and get

$$\bar{S}_{\hat{X}_\theta\hat{X}_\theta}(\Omega) = \frac{1}{2} + f_{\rm imp}(\Omega)\bar{S}_{\hat{Q}\hat{Q}}(\Omega) + \bar{S}_{\rm cor}(\Omega), \tag{2.47}$$

where 1/2 is homodyne imprecision due to shot noise, a result of vacuum noises $\hat{X}_{\rm in}$ and $\hat{Y}_{\rm in}$ of various of origins beating with LO and signal fields. All the vacuum noise operators have the following statistics: $\langle\hat{X}^\dagger_{\rm in,}(\Omega)\hat{X}_{\rm in,}(\Omega')\rangle = \langle\hat{Y}^\dagger_{\rm in,}(\Omega)\hat{Y}_{\rm in,}(\Omega')\rangle = 1/2\,\delta(\Omega-\Omega')$, $\langle\hat{X}^\dagger_{\rm in,}(\Omega)\hat{Y}_{\rm in,}(\Omega')\rangle = -\langle\hat{Y}^\dagger_{\rm in,}(\Omega)\hat{X}_{\rm in,}(\Omega')\rangle = i/2\,\delta(\Omega-\Omega')$. In symmetrized spectral, pure imaginary terms vanish. Collecting all surviving terms, we have 1/2 as in the first term. Imprecision noise serves as a white (frequency independent) background in PSD. If this background is the dominant noise, the measurement of mechanical displacement can hardly be precise. This justifies the name "imprecision noise".

The second term of Eqn. 2.47 reflects the spectrum of the displacement of mechanical oscillator $\bar{S}_{\hat{Q}\hat{Q}}$, which is given by

$$\bar{S}_{\hat{Q}\hat{Q}}(\Omega) = |\chi_{\rm eff}(\Omega)|^2\left(2\Gamma_{\rm qba} + 2\Gamma_{\rm m}(\bar{n}_{\rm th}+1/2)\right), \tag{2.48}$$

where $\chi_{\rm eff}(\Omega)$ is the effective mechanical susceptibility, which determines the shape of mechanical noise spectrum, and $\Gamma_{\rm qba}$ is quantum backaction rate to be defined later. The effective mechanical susceptibility $\chi_{\rm eff}(\Omega)$ is related to the unmodified one by

$$\chi^{-1}_{\rm eff}(\Omega) = \chi^{-1}_{\rm m}(\Omega) - 4g^2 v(\Omega), \tag{2.49}$$

the real and imaginary part of which is given by

$$\mathrm{Re}[\chi^{-1}_{\rm eff}(\Omega)] = \frac{1}{\Omega_{\rm m}}\left(-\Omega^2+\Omega_{\rm m}^2 + \frac{16g^2\Delta\Omega_{\rm m}(4\Delta^2+\kappa^2-4\Omega^2)}{16\Delta^4+8\Delta^2(\kappa^2-4\Omega^2)+(\kappa^2+4\Omega^2)^2}\right) \tag{2.50a}$$

$$\mathrm{Im}[\chi^{-1}_{\rm eff}(\Omega)] = -\frac{\Omega}{\Omega_{\rm m}}\left(\Gamma_{\rm m} - \frac{64g^2\Delta\kappa\Omega}{16\kappa^2\Omega^2+(4\Delta^2+\kappa^2-4\Omega^2)^2}\right). \tag{2.50b}$$

Comparing to the unmodified susceptibility $\mathrm{Re}[\chi^{-1}_{\rm m}(\Omega)] = (-\Omega^2+\Omega_{\rm m}^2)/\Omega_{\rm m}$, and $\mathrm{Im}[\chi^{-1}_{\rm m}(\Omega)] = -\Gamma_{\rm m}\Omega/\Omega_{\rm m}$, the effect of optomechanical interaction can be considered as a modification on mechanical resonance frequency and mechanical linewidth.

$$\delta\Omega_{\rm m} \approx \frac{8g^2\Delta(4\Delta^2+\kappa^2-4\Omega_{\rm m}^2)}{16\Delta^4+8\Delta^2(\kappa^2-4\Omega_{\rm m}^2)+(\kappa^2+4\Omega_{\rm m}^2)^2} = \mathrm{Re}[-2g^2 v(\Omega_{\rm m})] \tag{2.51a}$$

$$\Gamma_{\rm opt} \approx -\frac{64g^2\Delta\kappa\Omega_{\rm m}}{16\kappa^2\Omega_{\rm m}^2+(4\Delta^2+\kappa^2-4\Omega_{\rm m}^2)^2} = g^2\kappa\left(|\chi_{\rm c}(\Omega_{\rm m})|^2 - |\chi_{\rm c}(-\Omega_{\rm m})|^2\right), \tag{2.51b}$$

where

$$\chi_{\rm c}(\Omega) = u(\Omega) - iv(\Omega) = \frac{1}{\kappa/2 - i(\Delta+\Omega)} \tag{2.52}$$

is the cavity susceptibility. In the expressions, both of the shifts are frequency dependent, but we evaluate them at $\Omega_{\rm m}$, which justifies the approximation symbols. Moreover we have used $\Omega+\Omega_{\rm m} \approx 2\Omega_{\rm m}$ in the first equation. The former is referred as optical spring effect, while the latter is referred as optical damping [47]. If the detuning Δ is negative (red detuned), the mechanical resonance frequency is shifted to lower frequency, while mechanical linewidth increases (the oscillator is damped). The opposite happens, if detuning

is positive. If the interaction is strong enough, it is possible to have zero or negative effective mechanical linewidth. In this case, the mechanical oscillator experiences a self-oscillation, until higher order recoil terms (e.g. Duffing nonlinear term [48]) or nonlinear damping terms [49] become significant, and limit the oscillation amplitude. In the high quality factor limit $Q = \Omega_{\rm m}^{\rm eff}/\Gamma_{\rm m}^{\rm eff} \gg 1$, the spectrum around mechanical resonance frequency $\Omega_{\rm m}^{\rm eff}$ can be well approximated by a Lorentzian:

$$\chi_{\rm eff}(\Omega) \approx \frac{1}{2(\Omega_{\rm m}^{\rm eff} - \Omega) - i\Gamma_{\rm m}^{\rm eff}}. \tag{2.53}$$

Therefore, we usually fit the mechanical PSD with a Lorentzian.

The term $2\Gamma_{\rm m}(\bar{n}_{\rm th} + 1/2)$ in Eqn. 2.48 represents the intrinsic noise on the mechanical oscillator (thermal noise plus zero point fluctuation). One can get this result by using Eqn. 2.10. The parameter $\Gamma_{\rm qba} = g^2\kappa(|u(\Omega)|^2 + |v(\Omega)|^2) = g^2\kappa|\chi_{\rm c}(\Omega)|^2$ in Eqn. 2.48 is the so called quantum backaction rate, which is an effect of random arrival of photons on the mirror (shot noise). Just like thermal noise, quantum backaction heats up the mechanical oscillator. For the purpose of measuring the intrinsic motion of the mechanical oscillator, this is a side effect, which affects the measurement record. That is the reason for the name "backaction".

The prefactor before $\bar{S}_{\hat{Q}\hat{Q}}$ in Eqn. 2.47 is the transfer function between displacement and optical quadrature, which has the form

$$f_{\rm imp}(\Omega) = \frac{\Gamma_{\rm meas}}{4}{\rm Re}\left[\zeta(\Omega) - \mu(\Omega)e^{-2i\theta}\right]. \tag{2.54}$$

The last term of Eqn. 2.47 is the correlation between imprecision and displacement noise

$$\bar{S}_{\rm cor}(\Omega) = -\frac{\Gamma_{\rm meas}}{4}\left({\rm Re}[\chi_{\rm eff}(\Omega)]{\rm Im}[\mu(\Omega)e^{-2i\theta}] + {\rm Im}[\chi_{\rm eff}(\Omega)]{\rm Re}[\xi(\Omega)]\right). \tag{2.55}$$

In the above two equations, we introduced the following definitions:

$$\Gamma_{\rm meas} = \eta_{\rm c}\eta\frac{4g^2}{\kappa} \tag{2.56a}$$

$$\zeta(\Omega) = \kappa^2\left(|\chi_{\rm c}(\Omega)|^2 + |\chi_{\rm c}(-\Omega)|^2\right) \tag{2.56b}$$

$$\mu(\Omega) = 2\kappa^2\chi_{\rm c}(\Omega)\chi_{\rm c}(-\Omega) \tag{2.56c}$$

$$\xi(\Omega) = \kappa^2\left(|\chi_{\rm c}(\Omega)|^2 - |\chi_{\rm c}(-\Omega)|^2\right), \tag{2.56d}$$

where $\Gamma_{\rm meas}$ is the rate one can extract information from the mechanical oscillator, $\eta_{\rm c} = \kappa_{\rm R}/\kappa$ is the cavity outcoupling efficiency.

2.4 Bare Cavity

Though we have discussed quite some optomechanics, it is beneficial to step back and have a look at the behavior of a cavity with fixed mirrors – a bare cavity. To get the dynamics of fields related to a bare cavity, we set $g = 0$.

We treat the fields classically, then in steady state the intra-cavity field is given by Eqn. 2.33:

$$\alpha = \frac{\sqrt{\kappa_{\rm L}}}{\kappa/2 - i\Delta}\alpha_{\rm in}. \tag{2.57}$$

Then, from the input-output relation in transmission (setting noise term to be zero, and get $\alpha_{\rm t} = \sqrt{\kappa_{\rm R}}\alpha$), the transmitted field right after the cavity is given by

$$\alpha_{\rm t} = \frac{\sqrt{\kappa_{\rm R}\kappa_{\rm L}}}{\kappa/2 - i\Delta}\alpha_{\rm in}. \tag{2.58}$$

Hence, the transmission power is given by

$$P_{\rm t} = |\alpha_{\rm t}|^2 = \frac{\kappa_{\rm R}\kappa_{\rm L}}{\kappa^2/4 + \Delta^2}P_{\rm in}, \tag{2.59}$$

where $P_{\rm in} = |\alpha_{\rm in}|^2$. We can see the transmission power is the input power times a Lorentzian function of Δ, and κ is the full-width-half-maximum (FWHM) of the peak. The phase difference between input and transmitted field caused by cavity is given by

$$\Delta\theta_{\rm t} = \arctan\frac{2\Delta}{\kappa}. \tag{2.60}$$

We notice, as Δ changes from $-\infty$ to ∞, the phase shift changes from $-\pi/2$ to $\pi/2$. This phase shift can be used to rotate the phase of the input field, especially when the input is not a rotational-invariant state, for instance a squeezed state or with some phase or amplitude modulation.

Both intensity and phase responses from a cavity are shown in Fig. 2.4. As cavity length changes, the resonance frequency will change, which effectively changes the detuning Δ, if the laser frequency stays the same. If the original detuning is around 0, and the frequency change is small, we can see the transmitted amplitude does not change with mirror motion to the first order, while the phase shift is sensitive to this motion. By measuring the phase of the output field, we can infer the mechanical motion. As the phase of the intra-cavity field has the largest slope at $\Delta = 0$, the transduction $f_{\rm imp}$ is maximized on cavity resonance, i.e. at this point, phase measurement is the most sensitive to mechanical motion. Though the transmitted power depends on $\kappa_{\rm L}$ and $\kappa_{\rm R}$, as their roles are exchangeable in Eqn. 2.59, we cannot tell which one is larger from transmission field.

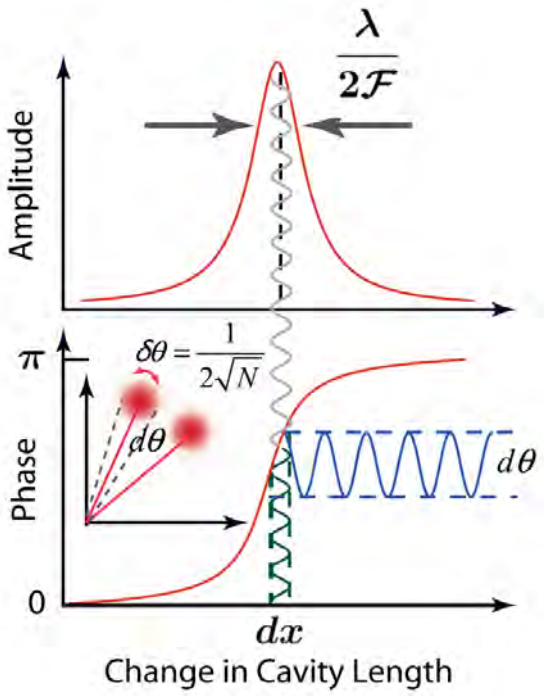

Figure 2.4: Cavity response to mechanical motion in transmission A figure from [47]. When the laser is on resonance with the cavity, the mechanical motion is encoded in phase of the intra-cavity field, but not in amplitude to the first order.

Similarly, we can get the cavity response in reflection. The only difference in derivation is the input-output relation. In reflection, it is given by $\alpha_{\rm r} = -\alpha_{\rm in} + \sqrt{\kappa_L}\alpha$, resulting in reflected field of

$$\alpha_{\rm r} = \left(-1 + \frac{\kappa_L}{\kappa/2 - i\Delta}\right)\alpha_{\rm in}, \tag{2.61}$$

where the factor before $\alpha_{\rm in}$ is referred as reflection coefficient. Then the reflected power is

$$P_{\rm r} = |\alpha_{\rm r}|^2 = \left(1 + \frac{\kappa_{\rm L}^2}{\kappa^2/4 + \Delta^2} - \frac{\kappa\kappa_{\rm L}}{\kappa^2/4 + \Delta^2}\right)P_{\rm in} = \left(1 - \frac{\kappa_{\rm R}\kappa_{\rm L}}{\kappa^2/4 + \Delta^2}\right)P_{\rm in} = P_{\rm in} - P_{\rm t}. \tag{2.62}$$

This result is not surprising, as it follows from the conservation of energy. As a function of detuning Δ, the reflected power is a Lorentzian dip from a constant background given by P_{in}. The phase shift in reflection is given by

$$\tan \Delta\theta_{\text{r}} = -\frac{4\Delta\kappa_{\text{L}}}{4\Delta^2 - \kappa_{\text{L}}^2 + \kappa_{\text{R}}^2}, \tag{2.63}$$

where the second order of Δ appears in the denominator. As a consequence, $\tan \Delta\theta_{\text{r}} = 0$ for both $\Delta = -\infty$ and ∞, which is distinct from the transmission case. We plot the contour traced by the reflection coefficient as Δ changing from $-\infty$ to ∞ in Fig. 2.5. It is not difficult to prove that the contours are circles, and the diameters of the circles are given by $2\kappa_{\text{L}}/\kappa$. When $\kappa_{\text{L}} > \kappa/2$, we say the cavity is over coupled in reflection, in which case, the origin is inside the contour. When $\kappa_{\text{L}} = \kappa/2$, the cavity is critically coupled, and the contour passes through the origin. In this case, the total reflected power can be zero, i.e. the light emitted through input mirror cancels the directly reflected light perfectly. When $\kappa_{\text{L}} < \kappa/2$, the cavity is under coupled, and the origin lies outside the contour. Thus, reflected field contains information about the relation between the mirror reflectivities, which is not available in transmission field.

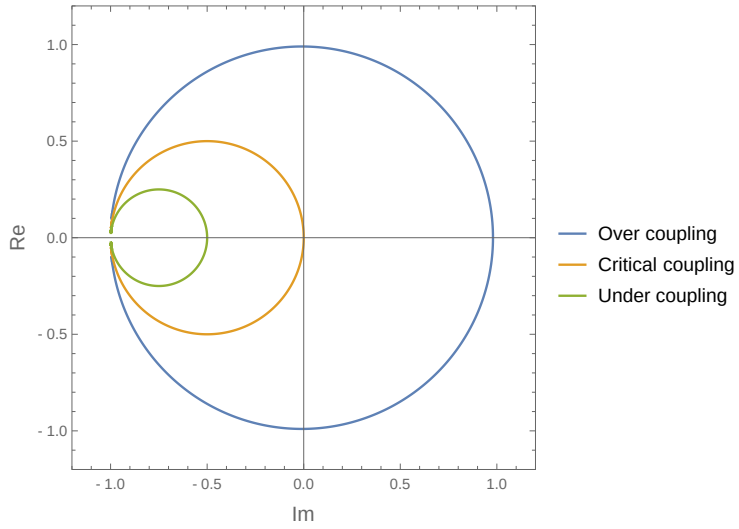

Figure 2.5: Contour plot of the reflection coefficient For a cavity overcoupled in reflection, the contour of reflection coefficient encloses the origin. For a cavity critically coupled in reflection, the contour passes through the origin. While for a cavity undercoupled in reflection, the origin falls out side the contour.

2.5 Static Bistability

Now we introduce the movable mirror. Before talking about quantum effects in optomechanics, we start with two classical phenomena relevant to our experiments. The first one is static bistability, which is introduced in this section. A more detailed introduction can be found in Bowen and Milburn's book [43] and Aspelmeyer et al.'s review [47]. The second one is optomechanically induced transparency, which is covered in the next section.

Static bistability is a result of equation system Eqn. 2.33. Solving for α_{ss}, we get

$$\frac{2i{g_0}^2}{\Omega_{\text{m}}}\alpha_{\text{ss}}|\alpha_{\text{ss}}|^2 - \left(\frac{\kappa}{2} - i\tilde{\Delta}\right)\alpha_{\text{ss}} + \sqrt{\kappa_{\text{L}}}\alpha_{\text{in}} = 0, \tag{2.64}$$

which is a cubic equation, with three solutions in general. When the third order term is small, this equation to a large extend recovers the behavior of a bare cavity, who has a Lorentzian lineshape, and there is only one solution of α_{ss}. However, when the third order term is significant, for a certain system, usually by having large α_{in}, at some detuning, there can be two stable solutions (and one unstable solution). At the same time, the cavity line shape as we scan detuning through the resonance is no more a Lorentzian.

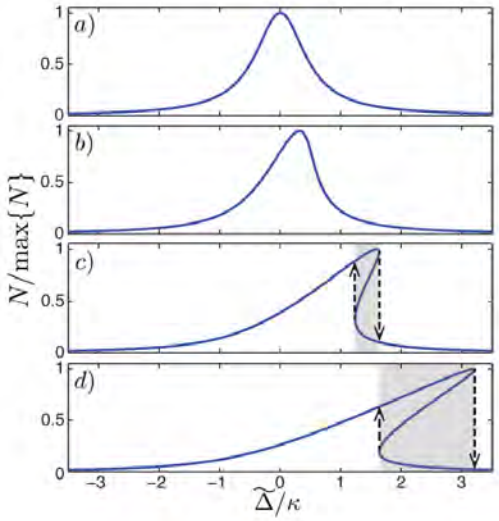

Figure 2.6: Bistability A figure from [43]. From top to bottom: normalized intra-cavity photon number as a function of bare cavity detuning $\tilde{\Delta}$ with increasing input powers. The gray region shows the detuning where bistability exists. The up pointing arrows shows the jump when scanning from blue side to red side of the cavity, while the down pointing arrows shows the jump when scanning from red side to blue side.

Fig. 2.6 shows the cavity lineshapes with increasing input powers from top to bottom. The tilting of the cavity lineshape to positive side of $\tilde{\Delta}$ is a result of radiation pressure pushing the movable mirror. For example, if we scan the laser from the red side of the cavity, as the laser frequency gets closer to cavity resonance, more photons inject into the cavity. These photons push the movable mirror further away from its original equilibrium position, which leads to a longer cavity with lower frequency. This process decreases the instantaneous detuning, and results in a slower increase of intra-cavity photon number compared to the bare cavity case. The argument is similar when scanning from blue side. At some large input power, this tilting is so large, such that more than one solution appears at some detunings as shown in panel c and d. The middle solution is unstable, while the strong field (top trace) and weak field solutions (bottom trace) are stable. This justifies the name bistability. As we scan from the red side, the intra-cavity photon number will follow the strong field solution, until the turning point labelled by the downward pointing arrow, where a jump from strong field to weak field solution happens. While for the scan from the blue side, the intra-cavity photon number will follow the weak field solution, and the jump to strong field solution happens at the detuning marked by the upward pointing arrow.

The lowest intra-cavity photon number required for the onset of bistability $n_{\mathrm{cav}}^{\mathrm{max}}$ sets an upper bound of optical power, if we would like to work in linear regime. In another word, even theoretically (regardless of damaging the system), we cannot increase optomechanical coupling strength g by increasing input power to an arbitrarily large value. In Meystre et al. [50, 47], the authors provided an expression for $n_{\mathrm{cav}}^{\mathrm{max}}$:

$$n_{\mathrm{cav}}^{\mathrm{max}} = \frac{\Omega_{\mathrm{m}}\kappa}{6\sqrt{3}g_0^2} = \frac{\kappa m \Omega_{\mathrm{m}}^2}{3\sqrt{3}\hbar G^2}. \tag{2.65}$$

With this intra-cavity photon number, bistability appears at a single critical detuning at $\tilde{\Delta} = -\sqrt{3}\kappa/2$. From the critical power, if we increase the optical power further, a laser detuning window displaying bistability will open, the width of which is proportional to the power. When the geometric optomechanical coupling G is fixed, narrower cavity linewidth, lower effective mass, and lower mechanical frequency will decrease this upper bound.

2.6 Optomechanically Induced Transparency

Optomechanically induced transparency (OMIT) is an classical optomechanical analogy of EIT in three level systems. In OMIT, a strong laser beam serves as the control beam like in EIT, and the frequency of a weak

tone coherent to the control beam is swept across the mechanical resonance frequency like the probe beam in EIT. Around the mechanical resonance, there will be a dip in transmitted power, which has a linewidth determined by Γ_{m}, analogical to the forbidden transmission rate in EIT. In this sense, optomechanically induced transparency is more accurately called optomechanically induced opacity. OMIT was first proposed in [51], followed by more thorough theoretical analysis in [39] and experimental demonstration in [52]. It finds its application in frequency dependent phase rotation [53, 54] and increasing bandwidth of a cavity based system [55]. In our experiment, we use it as a quick calibration of multi-photon optomechanical coupling g.

The starting point of the derivation of OMIT is Eqn. 2.41. In our case, we suppose the input field has a small but classical pure phase modulation Y_{in}^{ϕ}, and neglect all quantum noises. Please notice that the noise operators in Eqn. 2.41 enter the cavity with a frequency dependent phase rotation described by independent from that described in Eqn. 2.57. When $\kappa \gg \Omega$, the phase rotation in Eqn. 2.41 is negligible, but that in Eqn. 2.57 is still significant. Therefore we should treat these two effects separately. As a result, the phase modulation Y_{in}^{ϕ} is not simply Y_{in} (here we drop the hat, because the fields are classical). In practice, the noises are related to Y_{in}^{ϕ} by

$$X_{\mathrm{in}} = \frac{\Delta}{\sqrt{\Delta^2 + \kappa^2/4}} Y_{\mathrm{in}}^{\phi} \tag{2.66a}$$

$$Y_{\mathrm{in}} = \frac{\kappa/2}{\sqrt{\Delta^2 + \kappa^2/4}} Y_{\mathrm{in}}^{\phi}. \tag{2.66b}$$

Substituting these expressions into the classical version of Eqn. 2.41, we have an expression of intra-cavity field amplitude quadrature caused by the input phase modulation:

$$\begin{aligned} X(\Omega) &= \left(v(\Omega) \frac{\kappa/2}{\sqrt{\kappa^2/4 + \Delta^2}} + u(\Omega) \frac{\Delta}{\sqrt{\kappa^2/4 + \Delta^2}} \right) \sqrt{\kappa_{\mathrm{L}}} Y_{\mathrm{in}}^{\phi}(\Omega) \\ &+ 2g v(\Omega) \chi_{\mathrm{m}}(\Omega) \sqrt{2\Gamma_{\mathrm{m}}} P_{\mathrm{in}} + 4g^2 v(\Omega) \chi_{\mathrm{m}}(\Omega) X(\Omega). \end{aligned} \tag{2.67}$$

The first term is the result of cavity rotation of an input phase modulation, the second term corresponds to thermal motion of the mechanics, whose contribution is typically negligible in our system, and the third term corresponds to the mechanical scattered field. Therefore, OMIT is the interference between the input modulation sideband, and the mechanically scattered sideband. Solving for $X(\Omega)$, and using the input-output relation in transmission, we have

$$X_{\mathrm{out}}(\Omega) = \sqrt{\eta \kappa_{\mathrm{R}}} X(\Omega) = \sqrt{\eta \kappa_{\mathrm{R}} \kappa_{\mathrm{L}}} \frac{C(\Omega)}{1 - M(\Omega)} Y_{\mathrm{in}}^{\phi}, \tag{2.68}$$

where

$$C(\Omega) = v(\Omega) \frac{\kappa/2}{\sqrt{\kappa^2/4 + \Delta^2}} + u(\Omega) \frac{\Delta}{\sqrt{\kappa^2/4 + \Delta^2}} \tag{2.69}$$

is the bare cavity response to the phase modulation signal, and

$$M(\Omega) = 4g^2 v(\Omega) \chi_{\mathrm{m}}(\Omega) \tag{2.70}$$

is the mechanical response. Recall Eqn. 2.49, the definition of effective mechanical susceptibility, we have

$$\frac{1}{1 - M(\Omega)} = \frac{\chi_{\mathrm{eff}}(\Omega)}{\chi_{\mathrm{m}}(\Omega)}. \tag{2.71}$$

When we detect the output field by a direct detection (as we usually do), we measure the absolute square of Eqn 2.68. The absolute square of both $C(\Omega)$ and $1/(1 - M(\Omega))$ at several detunings are plotted in Fig. 2.7. Note that $|C(0)|^2 = 0$, which means at 0 frequency, pure phase modulation has no amplitude component. The tendency of decreasing amplitude, as Δ decreases corresponds to less phase modulation is rotated to amplitude by the cavity. When $\Delta = 0$, cavity response is zero everywhere. The peak and dip structure in $|1/(1 - M(\Omega))|^2$ corresponds to the resonance of χ_{eff} and χ_{m} respectively, as can be seen from Eqn. 2.71. As a result, the peak has a width of the order of optical damped mechanical linewdith Γ_{eff}, while the dip has

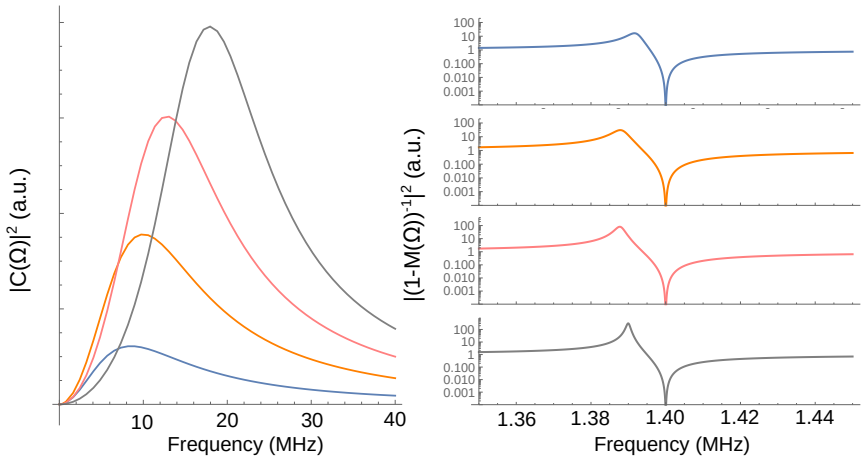

Figure 2.7: Responses as we sweep the frequency of the phase modulation tone OMIT response for $\kappa/2\pi = 16\,\mathrm{MHz}$, $g/2\pi = 100\,\mathrm{kHz}$, and $\Gamma_m/2\pi = 1.2\,\mathrm{mHz}$. These parameters are close to our experimental conditions. Colors corresponds to different detunings $\Delta/2\pi$: blue 3 MHz, orange 6 MHz, pink 10 MHz, and gray 16 MHz. The left panel shows cavity part of response without the effect of mechanics, while the right panel shows mechanical part of OMIT.

a width of Γ_m. Noticing g is contained in $1/(1 - M(\Omega))$, the linewidth features of mechanical response of OMIT provide information about multi-photon optomechanical coupling accurately. However, if we would like to calibrate $g_0 = g/\bar{\alpha}$ from OMIT, we need to know intra-cavity photon number well, which requires knowing η_c accurately, which is typically hard to measure directly in transmission.

As frequency crosses the mechanical resonances, there will be a phase shift, very similar to the case of a cavity, which is shown in Fig. 2.8. This figure is the argument of the total OMIT response $X_{\mathrm{out}}(\Omega)$, but zoomed in to the vicinity of the mechanical response. We can observe two phase jumps due to OMIT. Typically these structures are much narrower than the cavity response. People has proposed to use this feature to get frequency dependent squeezed light using OMIT [54], which finds its application in gravitational wave detectors.

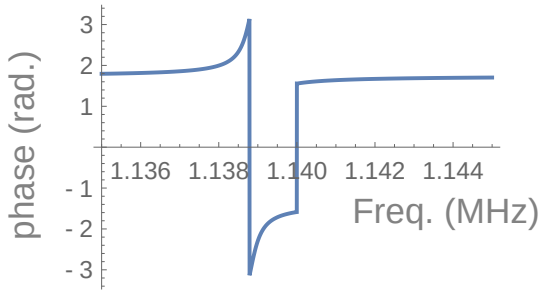

Figure 2.8: OMIT phase Phase shift of the total OMIT response, zoomed in around the mechanical frequency. The parameters are the same as Fig. 2.7, and $\Delta/2\pi = 6\,\mathrm{MHz}$

2.7 Sideband Cooling

In quantum fluctuation dissipation theorem, $S_{\hat{F}\hat{F}}(-\Omega)$ is proportional to the rate, at which a phonon is transferred from the noisy environment (bath) to the mechanical resonator, while $S_{\hat{F}\hat{F}}(\Omega)$ is proportional to the rate of the inverse process [43]. This process has its analogy when the mechanics is interacting with an optical field, the sidebands corresponds to scattering of photons from the carrier frequency. The red sideband (the sideband with frequency lower than the carrier) is a result of creating a pair of a phonon in the mechanics at Ω_m and a red-shifted photon at frequency $\omega - \Omega_m$, where energy is added to the mechanics,

and heats it up. On the contrary, the blue sideband extracts a phonon from the mechanics, and combines it with a carrier photon to create a photon at frequency $\omega + \Omega_m$, which cools the mechanics down. These two processes are embedded in the linearized interaction Hamiltonian, when we write $\hat{Q} = (\hat{b}^\dagger + \hat{b})/\sqrt{2}$:

$$\hat{H}_{\rm int}^{\rm lin} = -\hbar g(\delta\hat{a}^\dagger + \delta\hat{a})(\hat{b}^\dagger + \hat{b}) = -\hbar g(\hat{a}^\dagger\hat{b}^\dagger + \hat{a}^\dagger\hat{b} + \hat{a}\hat{b}^\dagger + \hat{a}\hat{b}), \tag{2.72}$$

where the first and last terms represent the process of red sideband, while the second and third represent the process of blue sideband.

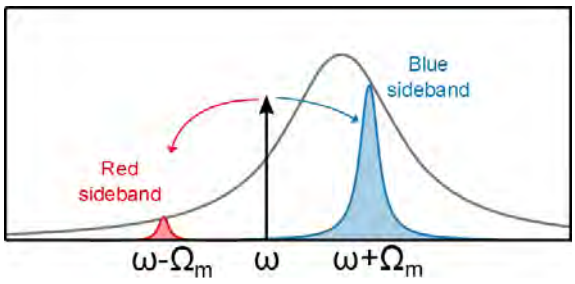

Figure 2.9: Cavity enhancement/suppression of mechanical sidebands A figure from [5]. A case of red detuned laser is shown. The black arrow represents laser, and the Lorentzian curve represents cavity lineshape.

When the interaction is in free space, the two processes are in balance. However, as the intracavity field intensity is proportional to $|\chi_c(\Omega)|^2$, when the input laser is red-detuned ($\Delta < 0$), a cavity can be used to enhance the blue sideband (with an intensity scaling factor $|\chi_c(\Omega_m)|^2$), while suppress the red one (with a scaling factor $|\chi_c(-\Omega_m)|^2$), as shown in Fig. 2.9. This introduces a overall cooling of the mechanical oscillator, with cooling rate $\Gamma_{\rm opt}$, which is called "dynamic cooling" or sideband cooling. On the contrary, if the laser is blue-detuned ($\Delta > 0$), the mechanics will be heated up, due to the enhancement of red sideband. In this case, $\Gamma_{\rm opt}$ is negative. If the interaction is strong enough, such that $\Gamma_{\rm opt} + \Gamma_m < 0$, the mechanical mode will experience an self-oscillation (infinity amplitude in linear regime). The final amplitude will be limited by higher order damping terms essentially.

To have a better idea of sideband cooling, let's suppress the effect of thermal bath by taking $\Gamma_m = 0$. Then the phonon occupancy of the oscillator is solely determined by the optical settings. Recall Eqn. 2.9, the occupancy given by photon bath is then

$$\bar{n}_{\rm opt} = \frac{|\chi_c(-\Omega_m)|^2}{|\chi_c(\Omega_m)|^2 - |\chi_c(-\Omega_m)|^2}. \tag{2.73}$$

Notice that this is never strictly 0, contradicting to the intuition when the unbalance between sidebands are introduced. Intuitively, this unbalance will extract energy from the mechanical oscillator continuously, until it is at quantum ground state. The reason for the finite occupancy lies in the difference between the ability of the mechanics to scatter photons to red and blue sidebands. For the red sideband, the ability for the mechanics to scatter a photon is proportional to $\bar{n} + 1$, while for the blue sideband is $\bar{n}$. As $\bar{n}$ approaches 0, the unbalancing between $\bar{n} + 1$ and $\bar{n}$ will increase, and balance the unbalancing between $|\chi_c(-\Omega_m)|^2$ and $|\chi_c(\Omega_m)|^2$, ending up in a finite occupancy. One can imaging, if $\Omega_m \gg \kappa$, the red sideband can be suppressed better, and the optimal $\bar{n}_{\rm opt}$ can be closer to 0. In fact, in this regime, the optimal $\bar{n}_{\rm opt}$ is given by

$$\bar{n}_{\rm opt}^{\rm min} = \left(\frac{\kappa}{4\Omega_m}\right)^2. \tag{2.74}$$

Now we take the coupling to thermal bath into consideration by taking $\Gamma_m > 0$. In weak coupling regime $g \ll \kappa, \Gamma_m$, the optical bath and thermal bath serve as two independent bathes, competing the effect of each other. Then the final occupancy is the normalized average of thermal occupancy and optical occupancy weighted by their own coupling rates Γ_m and $\Gamma_{\rm opt}$ respectively

$$\bar{n} = \frac{\Gamma_{\rm opt}\bar{n}_{\rm opt} + \Gamma_m\bar{n}_{\rm th}}{\Gamma_{\rm opt} + \Gamma_m}. \tag{2.75}$$

In the limit of $\Gamma_{\rm opt} \gg \Gamma_{\rm m}\bar{n}_{\rm th}$ (i.e. large optomechanical coupling), $\bar{n}$ recovers $\bar{n}_{\rm opt}$. Therefore, $\bar{n}_{\rm opt}$ is also referred as backaction limit (the idea of backaction will be illustrated in the next section).

Sideband cooling of a mechanical oscillator is a technique inherited from laser cooling in atomic physics [13, 56, 57], and it has been used to realize, for the first time, ground state cooling ($\bar{n} < 1$) of a mechanical oscillator [12, 13, 58], due to relatively easy requirements of system parameters, like cavity out coupling efficiency $\eta_{\rm c}$ and detection efficiency η. Moreover, cooling beyond the backaction limit has also been achieved using squeezed light [59]. Other correlated light can also be used for overcoming this limit (e.g. in [60]). We will see later in this thesis that sideband cooling also finds its usage when ground state cooling is not the goal.

2.8 The Standard Quantum Limit

Conventionally, displacement measurement in cavity optomechanics is done under the condition of on resonance laser ($\Delta = 0$) and detects phase quadrature of the output field ($\theta = \pi/2$). It is not hard to see from Eqn. 2.54 that, if the $\bar{S}_{\rm cor}$ is neglected, the conventional measurement gives the largest displacement sensitivity. In this case, $v(\Omega)$ vanishes, $\chi_{\rm c} = u(\Omega) = 1/(\kappa/2 - i\Omega)$, and $\chi_{\rm eff}(\Omega)$ recovers the unmodified $\chi_{\rm m}(\Omega)$. The correlation term in Eqn. 2.47 vanishes, and the spectrum reads

$$\bar{S}_{\hat{X}_{\pi/2}\hat{X}_{\pi/2}}(\Omega) = \frac{1}{2} + \eta_{\rm c}\eta\frac{4g^2\kappa}{\kappa^2/4+\Omega^2}|\chi_{\rm m}(\Omega)|^2\left(\frac{2g^2\kappa}{\kappa^2/4+\Omega^2} + 2\Gamma_{\rm m}(\bar{n}_{\rm th}+1/2)\right). \tag{2.76}$$

This spectrum is normalized to shot noise level. However, to discuss the sensitivity on displacement, we need to compare the measured spectrum to something directly related to mechanical spectrum $\bar{S}_{\hat{Q}\hat{Q}}$. Here we choose the zero-point spectrum $\bar{S}_{\rm zpf}(\Omega) = 2|\chi_{\rm m}(\Omega)|^2\Gamma_{\rm m}$, the mechanical spectrum of zero point motion, which is simply $\bar{S}_{\hat{Q}\hat{Q}}$ with $\Gamma_{\rm qba} = 0$ and $\bar{n}_{\rm th} = 0$. Then the measured displacement spectrum can be written as

$$\begin{aligned}
\bar{S}_{yy}(\Omega) &\equiv \frac{\bar{S}_{\hat{X}_{\pi/2}\hat{X}_{\pi/2}}(\Omega)}{f_{\rm imp}(\Omega)} = \frac{1}{2}\frac{1}{f_{\rm imp}(\Omega)} + \left(\frac{\Gamma_{\rm qba}}{\Gamma_{\rm m}} + \bar{n}_{\rm th} + \frac{1}{2}\right)\bar{S}_{\rm zpf}(\Omega) \\
&= \frac{\kappa^2/4+\Omega^2}{8\eta_{\rm c}\eta g^2\kappa} + \left(\frac{g^2\kappa}{\Gamma_{\rm m}(\kappa^2/4+\Omega^2)} + \bar{n}_{\rm th} + \frac{1}{2}\right)\bar{S}_{\rm zpf}(\Omega) \\
&= \frac{1}{8\eta_{\rm c}\eta\Gamma_{\rm m}C_{\rm c}} + 2\Gamma_{\rm m}|\chi_{\rm m}(\Omega)|^2C_{\rm c} + 2\Gamma_{\rm m}|\chi_{\rm m}(\Omega)|^2\left(\bar{n}_{\rm th}+\frac{1}{2}\right) \qquad (2.77) \\
&= \bar{S}_{\rm imp}(\Omega) + \bar{S}_{\rm qba}(\Omega) + \bar{S}_{\rm th}(\Omega), \qquad (2.78)
\end{aligned}$$

where $C_{\rm c} = g^2\kappa/(\Gamma_{\rm m}(\kappa^2/4+\Omega^2))$ is the classical cooperativity, the ratio between backaction rate and mechanical linewidth. $C_{\rm c}$ has the physical meaning of mechanical phonon occupancy generated by quantum backaction, which is proportional to measurement rate, and can be treated as a measure of measurement strength. The spectra in the last line are imprecision spectrum, quantum backaction spectrum and the spectrum due to intrinsic motion respectively. Imprecision noise and backaction noise sum up to the added noise by the measurement as $\bar{S}_{\rm add}(\Omega) = \bar{S}_{\rm imp}(\Omega) + \bar{S}_{\rm qba}(\Omega)$. As we change measurement strength, we can see a fundamental trade off between imprecision and backaction noise [7]. If we minimize the added noise over $C_{\rm c}$, we have the minimum value when $C_{\rm c} = 1/4\Gamma_{\rm m}|\chi_{\rm m}(\Omega)|$. Notice that $\eta_{\rm c}, \eta < 1$ will increase the imprecision level. To get an optimal limit, we take $\eta_{\rm c}, \eta = 1$, and we have

$$\bar{S}_{\rm SQL}(\Omega) \equiv \bar{S}^{\rm min}_{\rm add}(\Omega) = |\chi_{\rm m}(\Omega)|. \tag{2.79}$$

This limit is called the Standard Quantum Limit (SQL) for displacement measurement. An interesting fact to notice is that the peak value of the SQL spectrum $\bar{S}_{\rm SQL}(\Omega_{\rm m}) = \Gamma_{\rm m}|\chi_{\rm m}(\Omega_{\rm m})|^2 = \bar{S}_{\rm zpf}(\Omega_{\rm m})=1/\Gamma_{\rm m}$, which is exactly the same as the spectrum of zero-point fluctuation.

The SQL can also be defined for force sensing. A frequency dependent force can be transduced into displacement of a mechanical oscillator through mechanical susceptibility by $\hat{Q}_{\hat{F}}(\Omega) = \chi_{\rm m}(\Omega)\hat{F}(\Omega)$. By measuring this displacement, one can get the information about the force. Here, any intrinsic motion of the mechanical oscillator degrades the sensitivity to the displacement caused by the force. Therefore, we treat

it as noise background. Among the intrinsic noise sources, the zero point motion is inevitable. To count for this, we absorb zero point motion into the definition of the SQL in force sensing [41]:

$$\bar{S}^{\mathrm{SQL}}_{\hat{F}\hat{F}} = \frac{1}{|\chi_{\mathrm{m}}(\Omega)|} + \Gamma_{\mathrm{m}}. \tag{2.80}$$

This optimal sensitivity can be achieved when $C_{\mathrm{c}} = 1/4\Gamma_{\mathrm{m}}|\chi_{\mathrm{m}}(\Omega)|$ and bath temperature $T = 0$.

2.9 Ponderomotive Squeezing

Consider the interaction between intra-cavity electromagnetic (EM) field and mechanics as shown in Eqn. 2.36. The amplitude quadrature of EM field changes the momentum of the mechanics, and this change is rotated into displacement of the mechanics through the periodic mechanical motion. The change of displacement in turn, modifies the amplitude quadrature of the intracavity EM field. Thus, the two quadratures of the EM field are correlated. This correlation is the origin of the quantum correlation between imprecision noise and quantum backaction as shown in Eqn. 2.55.

In the discussion of the Standard Quantum Limit, we analyzed a case where the quantum correlation term vanishes. To study the effect of this quantum correlation, we can resume it by having either a homodyne angle θ different from $\pi/2$, or a non-zero cavity detuning ($\Delta \neq 0$), or both. Both of the methods measures a cavity field quadrature other than phase. In the following discussion, for the purpose of simplicity, let's focus on the case of $\theta \neq \pi/2$, while keep $\Delta = 0$. Then the quantum correlation is given by

$$\bar{S}_{\mathrm{cor}}(\Omega) = \frac{\Gamma_{\mathrm{meas}}}{4}\mathrm{Re}[\chi_{\mathrm{m}}(\Omega)]\mu(\Omega)\sin(2\theta) = \frac{\Gamma_{\mathrm{meas}}}{4}\mathrm{Re}[\chi_{\mathrm{m}}(\Omega)]\frac{2\kappa^2}{\kappa^2/4+\Omega^2}\sin(2\theta) \tag{2.81}$$

At the same time $f_{\mathrm{imp}}(\Omega)$ has the form

$$f_{\mathrm{imp}}(\Omega) = \frac{\Gamma_{\mathrm{meas}}}{4}\frac{2\kappa^2}{\kappa^2/4+\Omega^2}(1-\cos(2\theta)). \tag{2.82}$$

From this we can see the effect of θ on the transduction factor: θ other than $\pi/2$ degrades $f_{\mathrm{imp}}(\Omega)$, making the sensitivity to mechanical motion worse. When $\theta = 0$ or π, the homodyne detects purely amplitude quadrature, and no mechanical information is left in the measured spectrum. Now the measured spectrum is given by

$$\begin{aligned}\bar{S}_{\hat{X}_\theta\hat{X}_\theta}(\Omega) = \frac{1}{2} + \frac{\Gamma_{\mathrm{meas}}}{4}\frac{2\kappa^2}{\kappa^2/4+\Omega^2}|\chi_{\mathrm{m}}(\Omega)|^2\left(2\Gamma_{\mathrm{qba}} + 2\Gamma_{\mathrm{m}}(\bar{n}_{\mathrm{th}}+1/2)\right)(1-\cos(2\theta)) \\ + \frac{\Gamma_{\mathrm{meas}}}{4}\frac{2\kappa^2}{\kappa^2/4+\Omega^2}\mathrm{Re}[\chi_{\mathrm{m}}(\Omega)]\sin(2\theta).\end{aligned} \tag{2.83}$$

On mechanical resonance ($\Omega = \Omega_{\mathrm{m}}$), the quantum correlation $\bar{S}_{\mathrm{cor}}(\Omega)$ vanishes, because $\mathrm{Re}[\chi_{\mathrm{m}}(\Omega)] = \Omega_{\mathrm{m}}(\Omega_{\mathrm{m}}^2-\Omega^2)/((\Omega_{\mathrm{m}}^2-\Omega^2)^2+\Gamma_{\mathrm{m}}^2\Omega^2) = 0$. When $\Omega \neq \Omega_{\mathrm{m}}$, the quantum correlation can be negative. If at a frequency the sum of the second and third terms is negative, making the total spectrum smaller than shot noise level, we say the optical field is squeezed. Because this squeezing comes from interaction of light with a movable object, it is named ponderomotive squeezing. Fig. 2.10 shows typical squeezing spectra at different θ's.

Suppose $\theta \in (0, \pi)$, ponderomotive squeezing happens, when

$$\frac{\Gamma_{\mathrm{qba}}}{\Gamma_{\mathrm{m}}} + \bar{n}_{\mathrm{th}} + \frac{1}{2} < \frac{\Omega^2-\Omega_{\mathrm{m}}^2}{2\Gamma_{\mathrm{m}}\Omega_{\mathrm{m}}}\cot\theta. \tag{2.84}$$

As $\Omega \neq \Omega_{\mathrm{m}}$, there is always a θ in the above specified interval satisfying the condition. It is the exactly same case, when $\theta \in (-\pi, 0)$. The homodyne angle for optimal squeezing is given by

$$\tan(2\theta_{\mathrm{opt}}) = \frac{\Omega_{\mathrm{m}}^2-\Omega^2}{2\Gamma_{\mathrm{m}}\Omega_{\mathrm{m}}(\Gamma_{\mathrm{qba}}/\Gamma_{\mathrm{m}}+\bar{n}_{\mathrm{th}}+1/2)}. \tag{2.85}$$

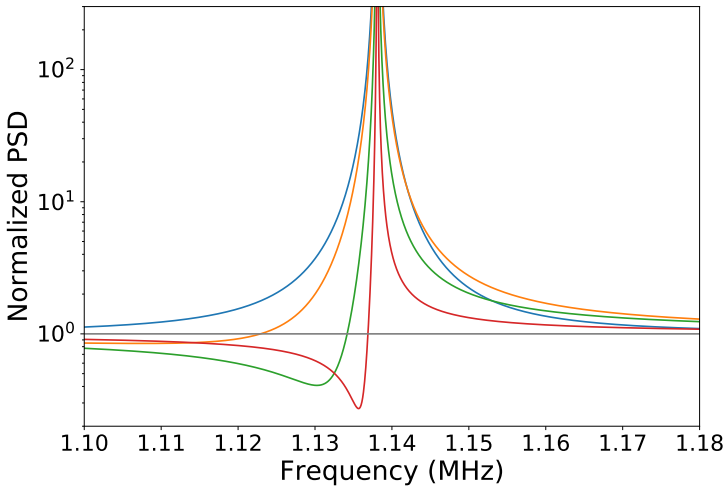

Figure 2.10: Ponderomotive squeezing Typical spectra of ponderomotive squeezing. The blue, orange, green and red spectra correspond to homodyne angles $\theta = \pi/2, 0.7\pi/2, 0.3\pi/2, 0.1\pi/2$ respectively. The spectra are in a Fano shape, as a result of quantum correlation. The tall tips are truncated to emphasis on the squeezing part.

Ponderomotive squeezing was first proposed in [61, 62], and the first experimental realization was demonstrated in 2013 [37, 38]. In contrast to squeezed light generated by optical parametric oscillators (OPO), which strongly depends on the material of the oscillator and the optical frequency, ponderomotive squeezing relies on radiation pressure, an effect available for EM fields at any frequency. This freedom provides the opportunity for less engineering problem, when developing a squeezer at a new wavelength. This feature may find its application, for example, in gravitational wave detection [63]. Moreover, ponderomotive squeezing shares the same principle as measurement beyond the Standard Quantum Limit and optomechanical entanglement of optical fields, which will be discussed in detail in the corresponding chapters. Thus, it provides a good analogy for understanding these effects.

2.9.1 Squeezing Bound in Toy Model

In general, the lower bound for squeezed spectrum is pretty complicated. Instead, we study the limit where $\kappa \gg \Omega_{\mathrm{m}}$, and $\Delta = 0$. In this limit, the measured spectrum is given by

$$\bar{S}_{\hat{X}_\theta \hat{X}_\theta}(\Omega) \approx \frac{1}{2} + 4\Gamma_{\mathrm{meas}} |\chi_{\mathrm{m}}(\Omega)|^2 \left(\Gamma_{\mathrm{qba}} + \Gamma_{\mathrm{m}}(\bar{n}_{\mathrm{th}} + 1/2)\right)(1 - \cos(2\theta)) + 2\Gamma_{\mathrm{meas}} \mathrm{Re}[\chi_{\mathrm{m}}(\Omega)] \sin(2\theta). \quad (2.86)$$

To simplify the problem, we define quantum cooperativity $C_{\mathrm{q}} \equiv 4g^2/(\kappa_i \Gamma_{\mathrm{m}}(\bar{n}_{\mathrm{th}}+1/2))) = \Gamma_{\mathrm{qba}}/(\Gamma_{\mathrm{m}}(\bar{n}_{\mathrm{th}}+1/2))$, the ratio between backaction rate and intrinsic decoherence rate. C_{q} serves as a figure of merit of strength of optomechanical interaction. Express Eqn. 2.86 in terms of C_{q}:

$$\bar{S}_{\hat{X}_\theta \hat{X}_\theta}(\Omega) \approx \frac{1}{2} + 2\eta_{\mathrm{c}}\eta \left[2\Gamma_{\mathrm{qba}}^2 |\chi_{\mathrm{m}}(\Omega)|^2 (1 + \frac{1}{C_{\mathrm{q}}})(1 - \cos(2\theta)) + \Gamma_{\mathrm{qba}} \mathrm{Re}[\chi_{\mathrm{m}}(\Omega)] \sin(2\theta)\right]. \quad (2.87)$$

Focus on frequency components off mechanical resonance $|\Omega^2 - \Omega_{\mathrm{m}}^2| \gg \Gamma_{\mathrm{m}}\Omega$, where the correlation term is significant, and the contribution from mechanical motion is small. We can neglect imaginary part of $\chi_{\mathrm{m}}(\Omega)$, such that $\chi_{\mathrm{m}}(\Omega) \approx \Omega_{\mathrm{m}}/(\Omega_{\mathrm{m}}^2 - \Omega^2)$, and $\chi_{\mathrm{m}}(\Omega) = \mathrm{Re}[\chi_{\mathrm{m}}(\Omega)]$. Thus, the spectrum is a quadratic function of $\chi_{\mathrm{m}}(\Omega)$, and takes the minimum value when

$$\chi_{\mathrm{m}}^{\mathrm{min}}(\Omega) = -\frac{\sin(2\theta)}{4\Gamma_{\mathrm{qba}}(1 + 1/C_{\mathrm{q}})(1 - \cos(2\theta))}, \quad (2.88)$$

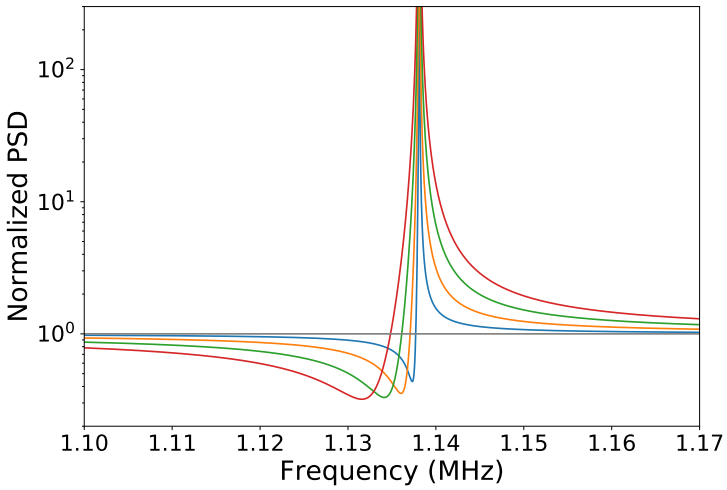

Figure 2.11: Ponderomotive squeezing at different quantum backaction rates The blue, orange, green and red spectra correspond to $\Gamma_{\mathrm{qba}}/2\pi = 1, 3, 6, 10\,\mathrm{kHz}$ respectively, and the other parameters like homodyne angles are the same.

and the minimum value is

$$\bar{S}^{\mathrm{min}}_{\hat{X}_\theta \hat{X}_\theta}(\Omega) = \frac{1}{2} - \frac{\eta_c \eta \sin^2(2\theta)}{4(1 + 1/C_{\mathrm{q}})(1 - \cos(2\theta))}. \tag{2.89}$$

The expression is minimized when $\theta \to 0$:

$$\bar{S}^{\mathrm{min}}_{\hat{X}_\theta \hat{X}_\theta}(\Omega) = \frac{1}{2}\left(1 - \frac{\eta_c \eta}{1 + 1/C_{\mathrm{q}}}\right) = \frac{1}{2}\left(1 - \eta_{\mathrm{meas}}\right), \tag{2.90}$$

where $\eta_{\mathrm{meas}} = \Gamma_{\mathrm{meas}}/(\Gamma_{\mathrm{qba}} + \Gamma_{\mathrm{m}}(\bar{n}_{\mathrm{th}} + 1/2))$ is the overall measurement efficiency [8], the ratio between rate of collecting information and total decoherence rate. From this equation, it is clear that to detect more ponderomotive squeezing, one needs to have simultaneously high detection efficiency and measurement strength. Suppose there is no upper limit for C_{q}, infinity squeezing is achievable with $\eta_c \eta = 1$ and $C_{\mathrm{q}} \to \infty$. In practice, C_{q} is limited by static bistability. Strong and efficient measurement is a key for all other experiments discussed in this thesis as well.

In addition to increasing the amount of squeezing, increasing Γ_{qba} also has the effect of increasing the characteristic bandwidth of the squeezed light. This effect can be extracted from Eqn. 2.87. As we increase Γ_{qba}, there is more quantum correlation available for squeezing. Though the mechanical peak grows as a quadratic function of Γ_{qba}, we can always find a frequency away from the mechanical resonance, where the contribution from mechanical peak is small. In this region, the increased amount of quantum correlation can influence wider bandwidth of imprecision noise. As a result, we observe broader characteristic bandwidth of squeezed light, and the squeezed part is pushed further away from the resonance as we increase Γ_{qba}, as shown in Fig. 2.11.

Chapter 3

Experimental Setup

In this chapter, we introduce the crucial components of the experimental setup, including the cryostat, the mechanical oscillator, the optomechanical cavity, the homodyne detector and cavity mirrors, together with their characterizations. In addition, we provide knowledge about feedback control, which is required in experiments.

3.1 Cryostat

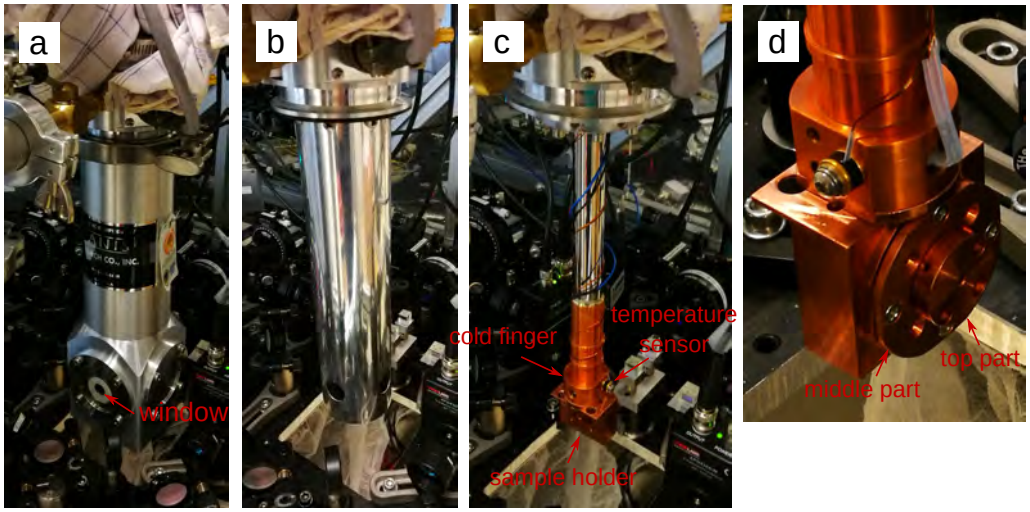

Figure 3.1: Cryostat a. The outer shell of cryostat. On the outer shell of the cryostat, there are a pair of windows for optical access. **b.** Inside the shell is a radiation shield. **c.** Inside the shield is the guiding tube of transfer tube. At the end of the guiding tube is the cold finger, where liquid helium evaporates, and provides cryogenic temperature. Sample holder is mounted on the cold finger. **d.** Zoom-in to the cold finger and sample holder.

Apart from interacting with photons, the mechanical oscillator in an optomechanical system can also interact with the gas molecules through collisions. In this interaction, the energy stored in the mechanical motion is dissipated into kinetic energy of the surrounding gas in the form of sound wave, leading to a broadening of the mechanical linewidth Γ_m, and results in a additional decoherence channel [64]. This process is referred as "gas damping". Our mechanical system is a 2D membrane, which has large cross section (3 mm × 3 mm) on the vibrating direction and low mass (of the order of 2 ng). This fact makes the gas damping effect more pronounced. An common approach to reduce gas damping is to put the mechanical part in vacuum.

As shown in Section 2.3, lower temperature means lower thermal occupancy of the environment, thus lower thermal decoherence rate $\Gamma_{th} = \Gamma_m(\bar{n}_{th} + 1/2)$, which describes the decoherence caused by coupling be-

tween the mechanics and the thermal environment. Moreover, the intrinsic loss of amorphous materials (e.g. Si_3N_4 used for our membranes) decrease as temperature goes down, which further decreases decoherence rate, mainly due to the suppression of effects of two-level systems [65, 66, 67, 68]. In addition to reducing thermal decoherence, the thermal motion of the mirror substrates provides a noise background in addition to shot noise (will be illustrated further in Section 3.7), which effectively increases the imprecision level. Cryogenic environment can suppress this mirror motion by reducing phonon occupancy, just as cooling the mechanics. In a word, cryogenic environment is beneficial.

A cryostat is a device providing both vacuum and low temperature environment. Depending on the working principle, cryostats can be classified into many types. For a wet cryostat, the part intended to be cooled down is just immersed in cooling agent, such as liquid helium. For a flow cryostat, cooling agent constantly flows through a tube to cool a part of the cryostat called the cold finger, where typically the sample is attached. In these two types of cyrostats, continuous consumption of cooling agent is required. If liquid helium is used (to get a temperature around 4 K), cryogenic experiment could be very expensive. Close cycle cryostats provide a helium conservation alternative, where a certain amount of liquid helium is recycled in the system. A compressor is used to compress the evaporated helium back to liquid phase. This operation introduces strong vibrations to the experimental apparatus, which can be a big issue for precise mechanical measurement, like in our case.

In practice, we choose a flow cryostat from Janis, as shown in Fig. 3.1. A transfer tube is used to send liquid helium from a pressurized dewar to the cold finger. The outer shell and the KF flange defines the vacuum volume, and a turbo pump is used to reduce the vacuum down to 10^{-5} mbar at the pressure gauge at room temperature. When the cryostat is at liquid helium temperature, the pressure at the gauge is of the order 10^{-6} mbar, due to condensation of gas molecule and slower molecule speed. However, as the gauge is far away from the sample, and the mechanics is enclosed in a sample holder as shown in Fig. 3.14, the real pressure at the membrane is not known accurately. At room temperature, we observe strong gas damping in optomechanical cavity. While at liquid helium temperature, though we do not know the proportion of gas damping in the total damping effect, the total damping is so small, such that it does not keep us from achieving the project goals. To reduce the vibration from the turbo pump, we pour a concrete block around the vacuum pipe coming out of the pump, as shown in Fig. 3.2. Inside the outer shell is a radiation shield, with optical access as well. When the cryostat is cold, the radiation shield is thermalized to a temperature significantly lower than room temperature, which provides a cold radiation environment for the sample. This helps to thermalize the sample to liquid helium temperature. The cold finger and sample holder are made of copper, in order to maximize the thermal conductivity and, then the thermalization. A temperature sensor is attached to the cold finger as close to the sample holder as possible to get the information about temperature.

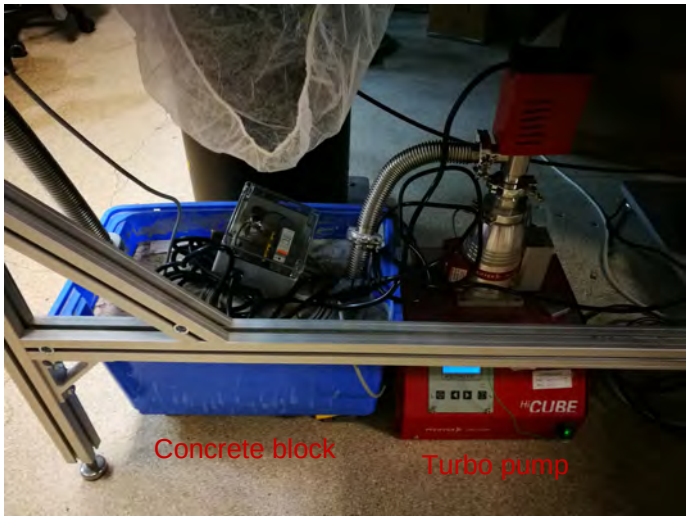

Figure 3.2: Turbo pump and concrete block The concrete block is used to reduce vibration from the turbo pump, such that it has less influence on the experimental apparatus.

3.2 Soft-Clamped Membranes

Our mechanical oscillator is based on a Si_3N_4 membrane. $C_q > 1$ is a sign for an optomechanical system to reach quantum regime. To make C_q large, increasing intra-cavity photon number by increasing the input power is the most convenient way. However, effects like static bistability limit the amount of optical power (see Section 2.5). Alternatively, we can try to decrease thermal decoherence rate $\Gamma_m(\bar{n}_{th}+1/2)$. As mentioned in the previous section, putting the mechanical system into cryogenic environment directly decreases $\bar{n}_{th}$, and decreases Γ_m. Both of the effects help achieving large C_q. However, liquid helium temperature is still not enough to reach the regime of $C_q \gg 1$ for a conventional Si_3N_4 membrane based optomechanical system [9, 14, 69]. Instead, dilution refrigerators can be used to reduce environment temperature further. However, this device is extraordinarily expensive. Moreover optical experiments at temperature of the order 10 mK is not trivial. As the heat conductivity of materials are poor at this temperature, any absorption of photons can cause dramatic heating. Another way of decreasing thermal decoherence rate is to engineer the mechanical oscillator, such that Γ_m is smaller than the conventional design under the same condition. "Soft-clamping" is a design aiming at this target [10]. With this design, an membrane-based optomechanical system can reach $C_q > 1$ at liquid helium temperature or even at room temperature.

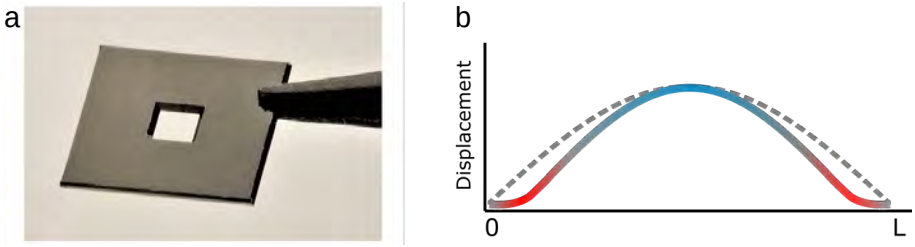

Figure 3.3: Conventional Si_3N_4 membranes a. a picture of a conventional square Si_3N_4 membrane, from [70]. **b.** A figure from [5]. The profile of the fundamental mode of a conventional square membrane. The redder the color indicates more local curvature.

It is beneficial to introduce some basic concepts of mechanical loss of membrane oscillator before we introduce soft-clamping in detail. Quality factor (Q factor) is a commonly used parameter to characterize the energy loss rate of a harmonic oscillator. In the case of mechanics, Q factor is defined as

$$Q = \frac{\Omega_m}{\Gamma_m} = \frac{W}{\Delta W}, \tag{3.1}$$

where W is the energy stored in mechanical motion, while ΔW is the energy loss per cycle of harmonic motion. Recall mechanical energy stored in an oscillator decays as $E_0 e^{\Gamma_m t/2\pi}$. Therefore, Q factor quantifies the number of motion cycles a oscillator can oscillates before the energy drop to $1/e$ of the original level. For a membrane mechanical oscillator, most energy is stored in the elongation of the membrane (W_{elong}), while energy loss is dominant by bending of the membrane (ΔW_{bend}), which leads to mechanical loss through the imaginary part of Young's modulus of the material [71].

Now we focus on square Si_3N_4 membranes. Typically, very high stress is built in the square Si_3N_4 membrane during the fabrication, this increases W_{elong} without changing ΔW_{bend}. Thus, the Q factor of the modes of a square membrane is boosted compared to the intrinsic value of the material, according to [72, 73]

$$Q_{mem}^{-1} = (\Lambda + \frac{\pi^2(N^2+M^2)}{4}\Lambda^2)Q_{int}^{-1}, \tag{3.2}$$

where Q_{mem} is the Q factor of the square membrane, Q_{int} is the intrinsic Q factor of Si_3N_4 [74, 75, 76], N and M are integer mode indices representing the number of antinodes, and the dimensionless parameter Λ is given by [73]

$$\Lambda = \sqrt{\frac{E}{3\bar{\sigma}}}\frac{h}{l}, \tag{3.3}$$

with E the Young's modulus, $\bar{\sigma}$ the stress, h the thickness, and l the length of the mechanical mode. In the case of a square membrane l is simply the edge length of the membrane. The Young's modulus of Si_3N_4

is around 200 GPa, the typical stress in the Si_3N_4 membrane is up to 1.3 GPa, and the aspect ratio h/l for a membrane with edge length of the order of 200 μm (giving $\Omega_m \approx 1$ MHz) and thickness of dozens of nano meter is extremely small. Therefore $\Lambda \approx 10^{-3}$ is a small number. In this case, $Q_{mem} \gg Q_{int}$. This decrease of dissipation rate is referred as "dissipation dilution". The term proportional to the second order of Λ in the dissipation dilution factor corresponds to the sinusoidal motion of the membrane, as indicated by the dashed line in Fig. 3.3 b, which is inevitable. However, the term proportional to the first order of Λ is a result of clamping of the membrane to the solid silicon frame. At the edge of the membrane, the mechanics tends to moving out of the plane to follow the sinusoidal shape, while the clamping tends to keep the mechanics in plane. This competition results in large curvature at the edge of membrane, which is the dominant source of mechanical energy loss.

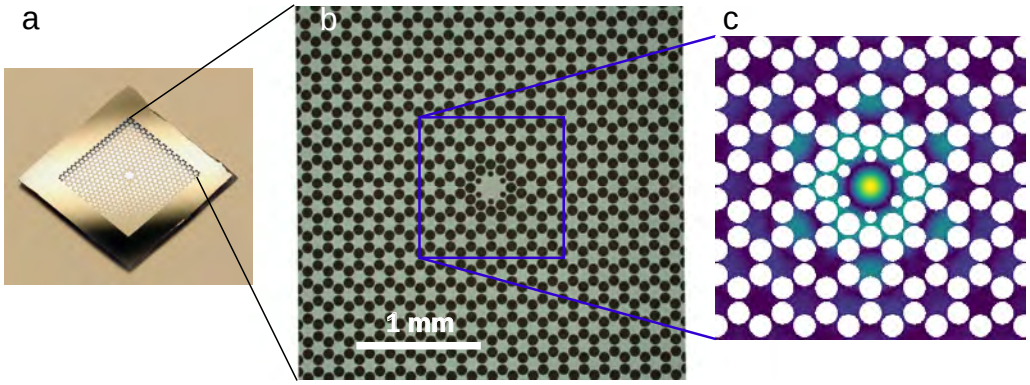

Figure 3.4: Soft-clamped Si_3N_4 membranes a. a photo of a soft-clamped membrane. **b.** Zoom in of **a.** from COMSOL. **c.** the defect mode we are interested in, zoomed in around the defect.

With the introduction of soft-clamping, one can reduce by order of magnitude the high curvature at the clamping point In a soft-clamped membrane, a honeycomb pattern of holes is etched on a Si_3N_4 membrane, forming a phononic crystal, as shown in Fig. 3.4. In the middle of the membrane, there is a defect, which can support mechanical vibrations localized around it. It is one of them the mode of interest in the following experiments, as shown in Fig. 3.4 **c**, whose largest vibration amplitude is located at the center of the defect. The defect modes are not directly clamped to a hard frame. Instead, its shape decays exponentially into the phononic crystal structure, with negligible amplitude at the membrane edge. Thus this design strongly suppresses the clamping contribution of the mechanical energy dissipation. In addition, phononic crystal opens a bandgap, where no whole membrane mode but defect mode exists. Phonons at frequencies falling in the bandgap are not allowed to propagate in the phononic crystal. Therefore, mechanical energy stored in the defect mode cannot radiate through the membrane and get lost in the silicon frame. This shielding helps boosting the Q factor of the membrane further, and helps isolating the mode of interest from other modes. The mechanical spectrum of the soft-clamped membrane, used in this thesis, close to the first bandgap, is shown in Fig. 3.5.

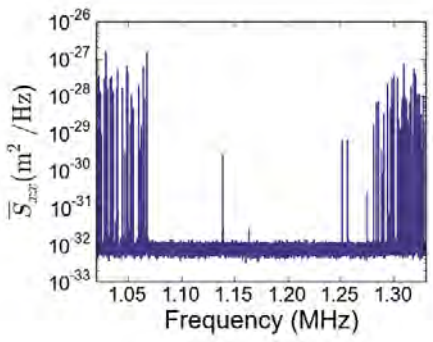

Figure 3.5: Mechanical spectrum close to bandgap the mode around 1.14 MHz is the mode of interest.

3.2.1 Cryogenic Ringdown

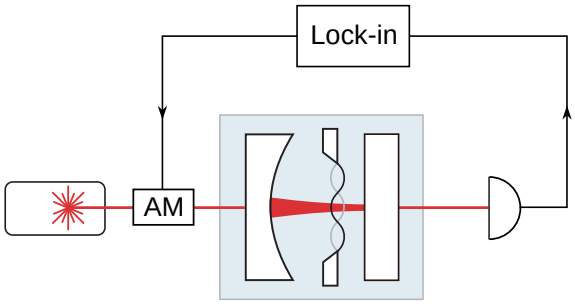

Figure 3.6: Setup of ringdown experiment AM is amplitude modulator, used to excite the membrane, and lock-in is lock-in amplifier, used for membrane excitation and signal processing. The interference between the injecting laser and reflected fields from the mirrors and the membrane causes a membrane position dependent intensity modulation. This is directly detected by a photodiode, and analyzed by a lock-in amplifier.

Ringdown is a widely used method to extract the Q factor of a mechanical oscillator, in which the oscillator is firstly excited to a relatively large amplitude compared to the thermal motion, then the excitation is terminated, and the amplitude of the excited oscillator decays freely. By monitoring the amplitude decreasing, one can extract the Q factor.

Experimentally, we use the same laser for excitation and readout of the membrane. We tune the laser to a wavelength, where the cavity mirrors have very low reflectivities (refer to Fig. 3.16). This choice of wavelength reduces the effect of optical damping to a negligible level, which allows measurement of the bare mechanical property. Though the reflectivities of the mirrors are low, they still form reflecting surfaces, which form an interferometer with the reflecting surface of the membrane. In this way, membrane motion can be transferred into intensity modulation of the output laser from the cavity, which is subsequently directly detected by a photodiode. The voltage signal from the photodiode is fed to a lock-in amplifier. In general, the output of a lock-in amplifier at demodulation frequency Ω_d, with a low-pass filter $h(\Omega)$, is given by (see Appendix B for more detail)

$$X + iY = h(\Omega_\mathrm{S} - \Omega_\mathrm{d}) \frac{A_\mathrm{S}}{\sqrt{2}} e^{i((\Omega_\mathrm{S}-\Omega_\mathrm{d})t+\Phi)}, \tag{3.4}$$

where Ω_S is the frequency of the signal, A_S is the amplitude of the demodulated signal (different from but proportional to the amplitude of the signal), and Φ is the phase of the signal. For ringdowm measurement, we set $\Omega_\mathrm{d} = \Omega_\mathrm{S} = \Omega_\mathrm{m}$ to obtain a DC signal, whose amplitude $R = \sqrt{X^2 + Y^2}$ is proportional to the amplitude of the demodulated signal A_S, which reflects the amplitude of the mechanics.

To excite the membrane, we output a tone from the lock-in amplifier around frequency Ω_m, and feed it to an amplitude modulator. The radiation pressure of the amplitude modulated light insert a sinusoidal force $F \sin \Omega_\mathrm{d} t$ on the mechanical oscillator, with F proportional to the light intensity and modulation depth. Then the equation of motion of the mechanics is given by

$$\ddot{q} + \Gamma_\mathrm{m} \dot{q} + \Omega_\mathrm{m}^2 q = \frac{F}{m} \sin \Omega_\mathrm{d} t, \tag{3.5}$$

the steady state solution of which is

$$q(t) = \frac{F}{m \Omega_\mathrm{d} Z_\mathrm{m}} \sin(\Omega_\mathrm{d} t + \phi), \tag{3.6}$$

where ϕ is the phase lag of the mechanics relative to the driving force, and

$$Z_\mathrm{m} = \sqrt{\Gamma_\mathrm{m}^2 + \frac{(\Omega_\mathrm{m}^2 - \Omega_\mathrm{d}^2)^2}{\Omega_\mathrm{d}^2}}. \tag{3.7}$$

Aparently, we need $\Omega_m^2 \approx \Omega_d^2$ to excite the mechanics to large amplitude. Larger driving force also corresponds to larger steady state mechanical amplitude.

In practice, the mean power at the output of the amplitude modulator may drift in time, which can cause undesirable change in lock-in signal. Splitting part of the output light, shining on a photodetector with much narrower bandwidth than the drive frequency provides information about the mean power, which can be used to stabilize the output by a PID controller (see Section A.3 for more information).

When the amplitude modulation drive is turned off, the excited mechanical mode starts to ringdown. One way to get the mechanical information is to continuously monitor the mechanical motion in time, and fit the ringdown time trace with an exponential Ae^{-t/τ_c}. The fitted time constant $\tau_c = 2\pi/\Gamma_m$ gives mechanical linewidth, from which we can get $Q = \Omega_m/\Gamma_m$. This continuous monitoring method may be affected by laser heating and residual optical damping (though cavity linewidth is extremely large), making the result not accurate. Both of the effects are caused by the presence of probe laser. A straightforward way to eliminate these potential artifacts is to let the mechanical mode ringdown "in the darkness", while only send light to it when needed. This is called stroboscopic ringdown, where we use the amplitude modulator to block the light most of the time, and let the light through occasionally. The result is "stroboscopic" ringdown time trace, which can be fitted by an exponential function just as the continuous case.

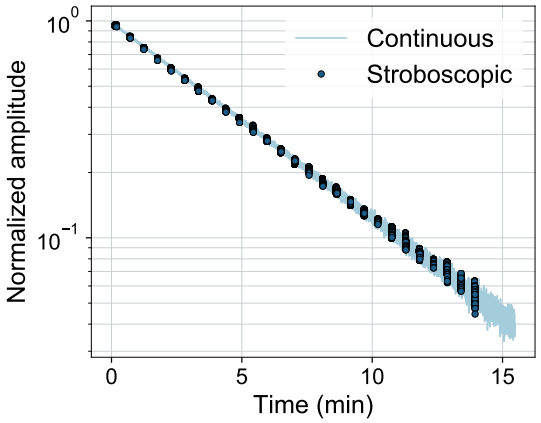

Figure 3.7: Ringdown A figure from [8]. Both continuous and stroboscopic results are shown.

In practice, we did ringdown experiment in cryogenic environment at a temperature around 11 K (due to thermalization issue, this temperature is higher than 4.2 K provided by liquid helium). The results of continuous and stroboscopic ringdown are shown in Fig. 3.7. The stroboscopic ringdown gives $Q = 1.02 \times 10^9$, and the continuous one gives $Q = 1.03 \times 10^9$. The good agreement shows no presence of significant contribution from laser heating or optical spring. The Q factor corresponding to $\Gamma_m/2\pi = 1.1$ mHz.

3.2.2 Frequency Noise

Q factor determines the energy dissipation rate of the mechanics, which is only one of the decoherence channels of the mechanical quantum state. Apart from energy dissipation, phase decoherence (dephasing) can also degrade the mechanical quantum state. Though energy dissipation causes dephasing at a rate of Γ_m, which explains partially the dephasing process, process like pure dephasing cannot be characterized by Q factor. For mechanical oscillators, dephasing can be a result of thermal fluctuations [77], absorption and de-absorption of molecules on the oscillator surface [78, 79], diffusion of molecules along the device [80], and excitation and relaxation of two-level systems on the surface [30, 81, 48]. For high Q mechanical oscillators, there is evidence showing that the main contribution of dephasing comes from the two-level systems [30, 48]. To quantify the potential of soft-clamped membranes to be used as quantum memories, measurement of overall dephasing is necessary. Dephasing process results in phase noise sidebands of the mechanical carrier frequency, which can be inferred from frequency noise spectrum of the mechanical mode according to

$$\bar{S}_{\phi\phi}(\omega) = \bar{S}_{\omega\omega}(\omega)/\omega^2, \tag{3.8}$$

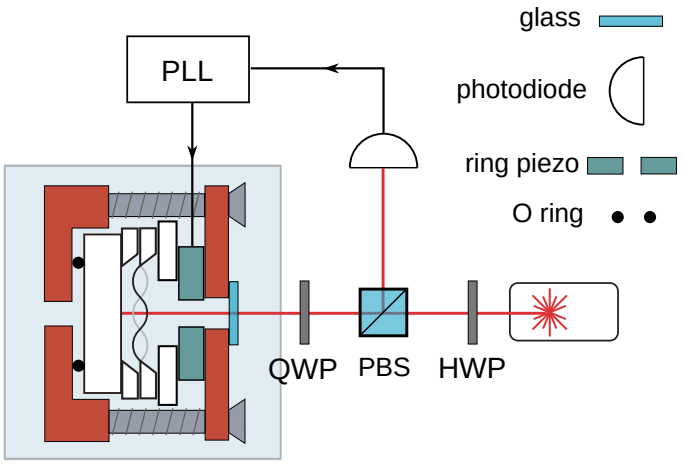

Figure 3.8: Setup of frequency noise measurement PLL stands for phase lock loop.

where $\omega = \Omega - \Omega_m$ is the sideband frequency of the mechanical carrier.

We follow the procedure introduced in Fong et al. [48] to measure frequency noise of our device. Though the experimental setup of frequency noise experiment could, in principle, be the same as ringdown, due to historical reason, this measurement is conducted with a mirror-membrane-glass interferometer, and the drive is provided by a piezo, as shown in Fig. 3.8. In this setup, a flat mirror, spacers, the membrane and a piezo are clamped together. An O ring is put between sample holder and the mirror to protect the mirror from cracking during the clamping, and provide clamping force to the entire structure, when the top copper piece is pressed against the piezo. A piece of glass is glued at the opening of this copper piece. This glass and the mirror form a very low finesse cavity, which gives mechanical motion information as the ringdown case. This glass also prevents the gas molecules in the cryostat from condensing on the membrane during cool down. Otherwise, the mechanical property of the membrane may degrade. The laser light first passes through a half waveplate (HWP) to adjust its polarization, which determines the amount of light transmitting through the polarizing beam splitter (PBS). Then the transmitted light from the PBS passes through a quarter waveplate (QWP), which can change the polarization of light from linear to circular. The reflected light from the mirror interferes with the reflected light from membrane. The membrane motion thus modulates the intensity of the total reflected light at mechanical frequency. The polarization of the reflected light carrying mechanical information is changed from circular to linear by the QWP. However, due to the opposite propagation direction, the polarization is perpendicular to that at the input of the PBS this time. Then, the light is reflected by the PBS to a photodetector, whose output is input to a phase locked loop (PLL). The PLL outputs a drive to the Piezo at Ω_m to excite the membrane. From the evolution of the PLL reference frequency, we can extract the information of membrane frequency noise.

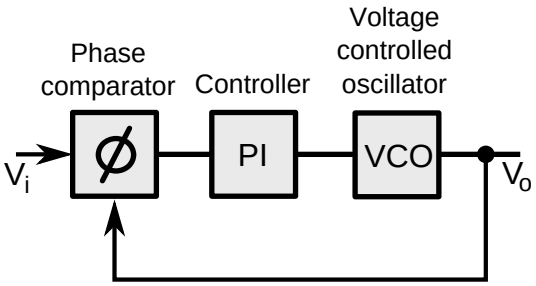

Figure 3.9: Phase locked loop

A phase locked loop is typically used to excite a resonating system with time dependent resonance fre-

quency. During the process, the drive frequency follows the resonance frequency tightly with the help of PLL, which allows us to excite the resonating system always maximally with the same driving power. A phase locked loop is typically composed of 3 components: a phase comparator, a proportional-integral (PI) controller (see Subsection 3.4.1 for more detail), and a voltage controlled oscillator (VCO). The phase of the input signal V_i containing the frequency information of the mechanical oscillator is compared to the phase of a reference signal V_o. The difference is treated as a error signal of a PI controller, which subsequently changes the voltage to the VCO to update the frequency of the reference signal. If the frequencies of the input and reference are different, the phase difference will evolve like $(\omega_\mathrm{i} - \omega_\mathrm{r})t$, where ω_i and ω_o are frequencies of input and reference respectively. Therefore, matching the two phases also matches the frequencies. By monitoring the time evolution of the reference frequency, we can get directly the information of the frequency noise of the membrane up to the bandwidth of the PLL. In real experiment, the PLL is provided by a module of a HF2 Zürich Instrument lock-in amplifier, which converts analog input to a digital signal at a certain sampling rate. To avoid excess noise called aliasing, the bandwidth of the PLL loop should be less than half of the sampling rate. This is also a general rule for any analog to digital spectrum analysis.

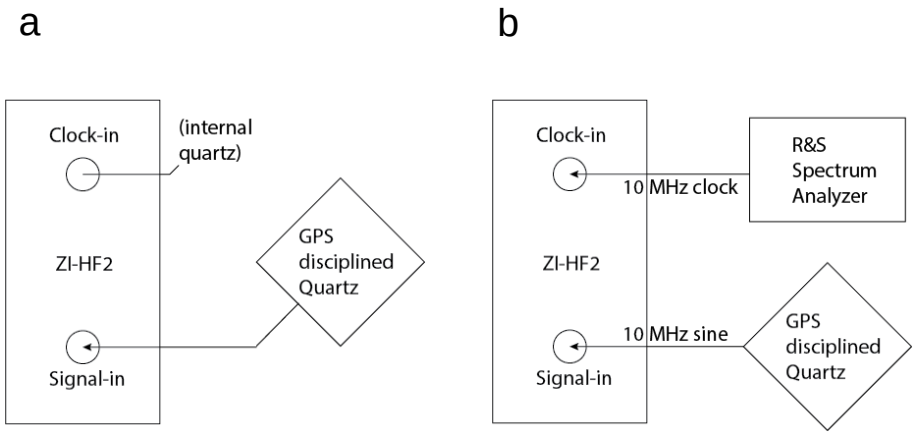

Figure 3.10: Frequency noises of clocks a. b. the measurement setups of the HF2 internal quartz noise and Rohde&Schwarz spectral analyzer clock noise respectively.

Measurement of frequency noise using PLL only reliably reflects the noise of the input signal, if the noise of the reference is small compared to the signal. When the opposite happens, we are effectively measuring the the noise of the reference, which is undesirable. To have an idea of the frequency noise of the internal clock of HF2 (provided by a quartz, and serves as the reference in PLL), we "measure" the 10 MHz output of the quietest clock we can find at hand, a GPS disciplined quartz, as shown in Fig. 3.10 **a**. We conduct fast Fourier transformation on the time traces of the reference frequency in PLL, and get a frequency noise spectrum as shown in Fig. 3.11 **a**. This noise performance is even above the level of membrane at liquid helium temperature. To find a proper reference clock source (the GPS disciplined quartz is not portable, and is not placed in our lab), we measured the noise performance of the 10 MHz output of a Rohde&Schwarz spectral analyzer, by inputting the output to the external clock input of the HF2, and conducting the same measurement on the GPS disciplined quartz, as shown in Fig. 3.10 **b**. The result is displayed in Fig. 3.11 **a**. It is clear that the noise performance of the spectral analyzer clock is better than that of the internal quartz of HF2. Actually, the noise performance is also better than that of the membrane at liquid helium temperature (measured with spectral analyzer clock), as shown in Fig. 3.11 **b**. Recall Eqn. 3.8, we notice that when the phase noises are the same, frequency noises at high frequencies are larger than frequency noises at lower frequencies. This explains the level difference between the spectral analyzer clock in Fig. 3.11 **a** and **b**, as the former is at 10 MHz and the latter is at 700 kHz.

Using the output of the R&S spectral analyzer as the clock of reference, we measured frequency noise performance of membrane at room temperature and liquid helium temperature, by resonantly driving the membrane to a large amplitude. The results are shown in Fig. 3.12, which can be divided into three regions from low frequency to high frequency. The performance from very low frequency to around 0.3 Hz could be a consequence of energy dissipation related to Γ_m and a slow drift in time, which has a frequency dependence of $1/f^2$, where f is the sideband frequency. However, due to lacking of points (i.e. too short measurement

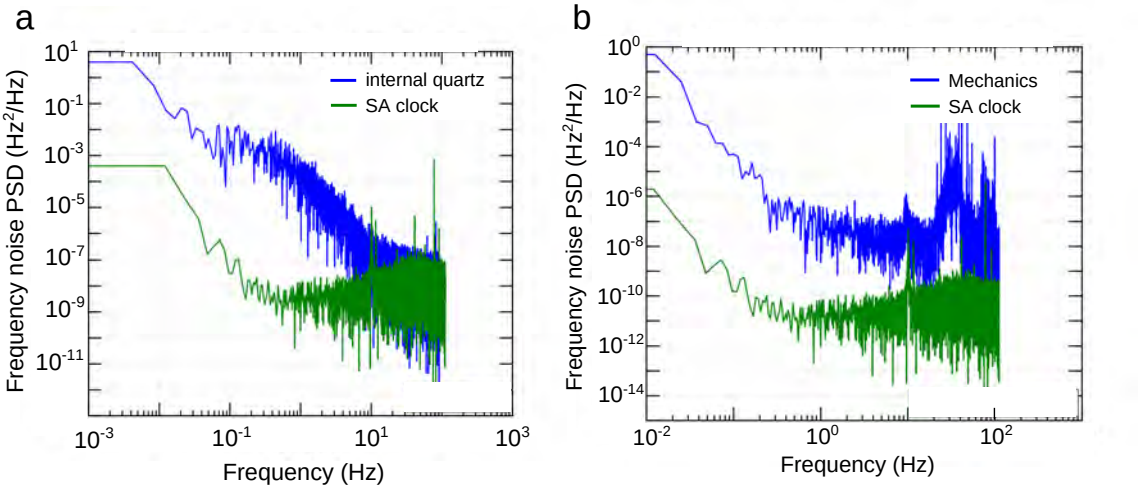

Figure 3.11: Frequency noises of clocks a. The frequency noise spectral of the internal quartz of HF2 and the 10 MHz output of a Rohde&Schwarz spectral analyzer. **b.** The frequency noise of the spectral analyzer output and the membrane at liquid helium temperature.

time), the conclusion in this region is not certain. In the region from 0.3 Hz to 20 Hz, the frequency noise has a $1/f$ dependence, which is classified as flicker noise. Above 20 Hz, the noise is dominant by some sharp and broad peaks, whose origin is not clear yet. One suspicion is the pendulum motion of the cold finger, as the frequency lies in this range. More research is required to exam the potential of soft-clamped membranes as quantum memory. Indeed, in the quantum trajectory experiment, my colleague Massimiliano Rossi and David Mason evaluate the phase noise of the membrane, and find negligible decoherence contribution from pure dephasing [82]. However, this experiment is out of the scope of this thesis.

3.3 Membrane-in-the-Middle Cavity

3.3.1 Optomechanical coupling

A membrane-in-the-middle (MIM) system is a Fabry-Pérot cavity with a membrane in between two mirrors. Though the moving part is a membrane, instead of one of the mirrors, this is still a optomechanical system. The membrane couples to the cavity dispersively, which can be illustrated in a regime where the reflectivity of the membrane is low. In this case, the standing wave supported by the mirrors is not strongly disturbed by the membrane. As the material of membrane (Si_3N_4 in this case) has higher refractive index than vacuum, a membrane makes the optical path length longer in the cavity compared to a bare cavity case. Consequentially, the cavity resonance frequency decreases, as shown in Fig. 3.13. However, this frequency shift depends on the position of the membrane relative to the intensity profile of the intra-cavity mode. When the membrane is located at the node of the standing wave, effectively photon does not "see" the membrane, and there is no frequency shift in this case. In the same spirit, the frequency shift is the largest when the membrane is at anti-node. Recall that optomechanical coupling $G = \partial\Omega_{\mathrm{cav}}/\partial q$ is position dependent cavity frequency shift. To get finite first derivative, we need to move away from the node and anti-node. The maximum G appears at the position with the largest slope of intensity, which is also our working point. When the optomechanical cavity itself does not have any degree of freedom, the relative position of membrane to standing wave can be tuned by hopping between different free spectra ranges (FSR). A free spectra range is defined as c/nL, where c is speed of light in vacuum, L is the cavity length. The physical meaning of FSR is the frequency spacing between adjacent cavity modes (i.e. number of anti-nodes differs by 1).

3.3.2 Cavity Assembly

In principle, there are large numbers of ways the mirrors and the membrane are put together. However, a general rule of thumb is that more tunability leads to less stability. To maximize the stability of the system,

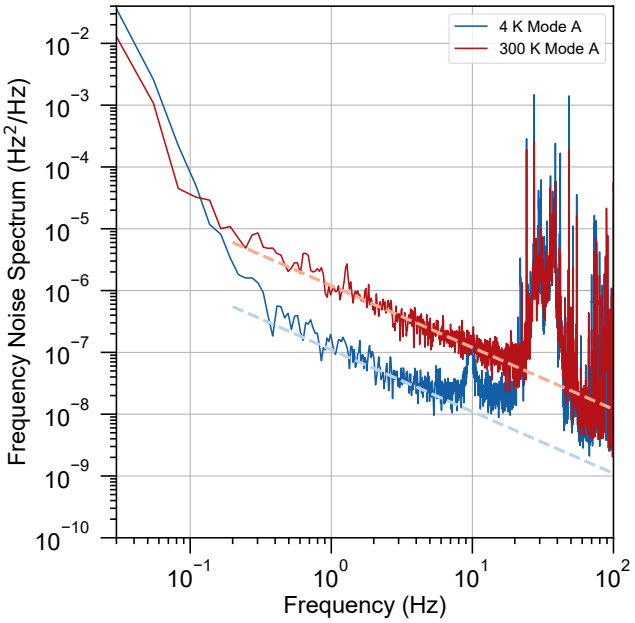

Figure 3.12: Frequency noises of a soft-clamped membrane The dashed lines are guides to the eyes of $1/f$ dependence. The low frequency cut off is determined by the length of the time trace, while the high frequency cut off is determined by sampling frequency.

we chose a monolithic way of assembling, as shown in Fig. 3.14. An O ring is firstly placed in the groove in the bottom part of the copper sample holder, then a flat mirror is placed on top of the O ring. The role of the O ring is to provide clamping force on the mirror, while protecting it from cracking under pressure. Introducing a rubber ring in the system right beside the mirror may sounds unstable, as it results in a movable mirror. However, as the frequency of this rubber-mirror system is very low compared to the frequency of the membrane, this is not problematic in practice. Subsequently, a spacer-membrane-spacer sandwich is placed on top of the flat mirror, where the first spacer falls in the groove carved in the bottom part. As the spacers are fabricated from silicon wafers, just like the membrane, the flat surfaces of silicon wafers and the flat mirror guarantee that the membrane and the flat mirror are parallel. This is crucial for reducing scattering of photons into undesirable cavity modes, which is a source of cavity internal loss. Then the sandwich is clamped down by the middle part of the sample holder. At the end of this clamping, the lowest spacer touches the surface of the bottom part, which stabilizes the system yet further.

The alignment of the top mirror to the defect of the soft-clamped membrane is the key step of cavity assembly, because the horizontal direction of the cavity mode is defined by the position of the curved mirror, and the overlapping between the optical and the mechanical modes contributes to g_0. If the cavity TEM_{00} mode does not fall on the center of the defect, g_0 will suffer. Moreover, if the optical mode is clipped by any holes on the soft-clamped membrane, light scattering to other modes will happen, and will significantly broaden the cavity linewidth, thus will decrease η_c. In the alignment process, we first set up the camera and lens after the cavity, such that a sharp magnified image of the membrane appears on the camera, when the membrane is illuminated by flash light. Subsequently, by adjusting the orientations of the two mirrors before the cavity, we adjust the injecting angle and position of the laser such that it is perpendicular to the flat mirror and passing through the center of the defect on the membrane. Please notice that, curved mirror is not in the assembly yet. Then we focus the light on the flat mirror, by changing the distance between the collimation lens and the fiber head. Up to this step, the laser beam defines the optical axis of the cavity. The rest is to put the curved mirror on the top spacer, move it horizontally to align the center to the laser beam defined axis, such that the TEM_{00} mode falls on the center of the defect, and fix its position by clamping with another O ring and the top part of sample holder. The final image should look like Fig. 3.15. Scanning the laser through the resonances helps seeing TEM_{00} mode, and makes alignment easier.

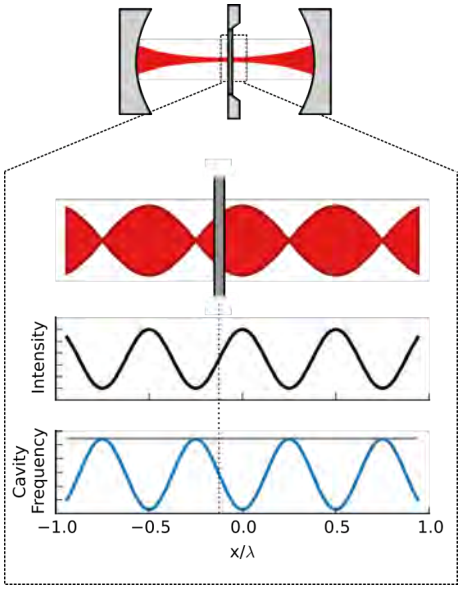

Figure 3.13: Optomechanical coupling A figure from [83]. Illustration of optomechanical coupling in a MIM system.

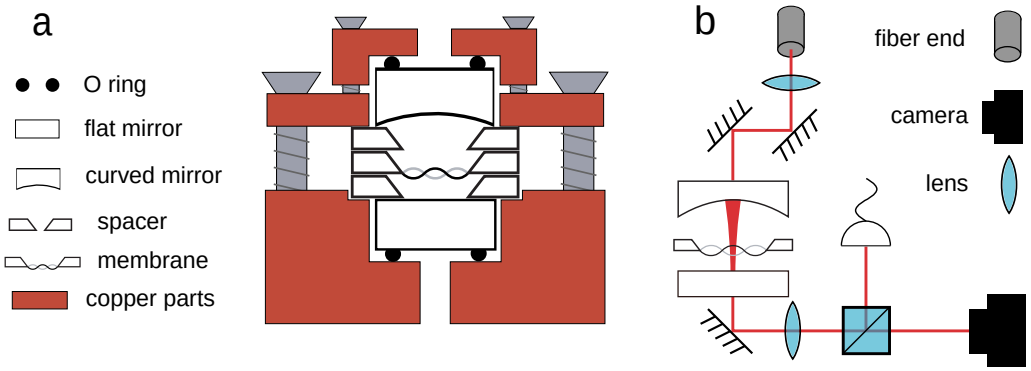

Figure 3.14: Membrane-in-the-middle system a. The assembly of membrane-in-the-middle system. **b.** The setup of curved mirror and cavity alignment.

The O ring, mirrors, silicon chips and stainless steel screws do not have very good thermal conductivity, especially at low temperatures. Moreover, the phononic structure of the soft-clamped membrane reduces the cross section for heat exchange between the defect and the silicon frame. Therefore, the defect mode is not thermalized to liquid helium temperature, but a temperature around 10 K.

3.3.3 Alignment to cavity mode

An input light beam can only be well coupled to the cavity mode, if the spatial and temporal properties of the two match. Temporally, the frequency of the injecting laser has to match the cavity resonance frequency up to an order of cavity linewidth, this part will be taken care of in the next section. Matching of spatial mode is equivalent to matching the propagating axis and the complex parameter $q(z)$ of the input beam and the cavity for Gaussian optics.

As shown in Fig. 3.14 **a**, the cavity mirrors we use is a flat mirror and a curved mirror with radius 25 mm. The cavity mode defined by this composition has beam waist at the flat mirror, while the radius of curvature of the wave front should match that of the curved mirror at its reflecting surface. The thickness of the spacer contacting flat mirror is 350 μm, the thicknesses of the membrane chip and the top spacer are 500 μm, and the diameter of the curved mirror is 7 mm. Then the cavity length is 1.6 mm. By plugging $z = 1.6$ mm and

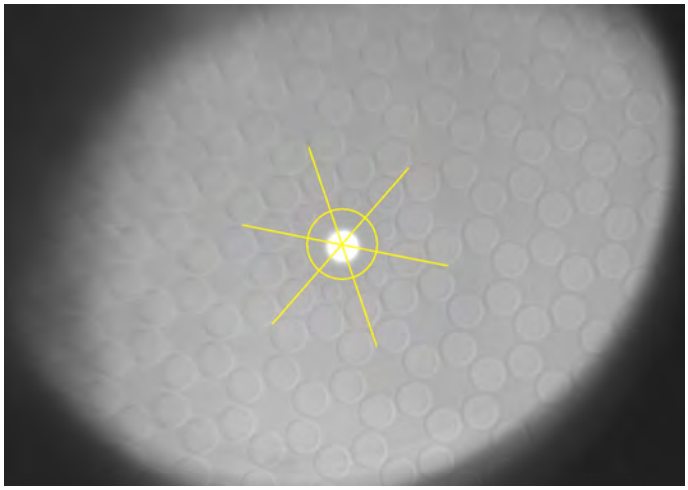

Figure 3.15: Camera image of a membrane and a TEM_{00} mode The yellow lines are guides to the eyes for the center of the defect.

$R(z) = 25\,\text{mm}$ into Eqn. 2.13, we get $z_R = 6.2\,\text{mm}$. Provided $\lambda \approx 800\,\text{nm}$, the cavity mode is uniquely determined, and the beam waist $w_0 = 39\,\mu\text{m}$ (i.e. the light spot size on defect), which is much smaller than the typical defect size of $210\,\mu m$. This hierarchy helps avoiding clipping of cavity mode. If w_0 is comparable to defect size, even if the mode axis is placed exactly at the centered of the defect, the tail of the Gaussian profile will still be clipped, and will result in optical loss.

The setup of cavity alignment is show in Fig. 3.14 **b**. We can design a suitable optical path from fiber to the cavity to optimally couple the laser to cavity mode, the parameters of which we just figured out. As the properties of a Gaussian beam depend only on one parameter, if the wavelength is fixed, we can relatively freely choose the distance between the fiber head and the curved mirror, and the focal length of the lens after fiber (the collimation lens). We fix the focal length of the collimation lens to be 11 mm. Then the only adjustable parameter to shape the profile properties of the beam in the system is the distance between the fiber head and the collimation lens, which can be finely tuned with a collimator without changing optical axis. The single-mode fiber outputs a Gaussian mode with numerical aperture (NA) specified by the producer. From this data, and the distance between fiber head and curved mirror, we can calculate the required distance between fiber head and lens using ABCD matrix analysis, introduced in Section 2.2, and put the lens roughly at this distance away from the fiber head.

Apart from shaping the Gaussian profile, another aspect of alignment is to match the propagation axis of the laser to the optical axis of the cavity. As illustrated in Fig. 2.2, TEM_{00} (the mode of interest) has the most confined profile around propagation axis. If the axes do not match, by either finite offset or angle between the axes, the coupling to TEM_{00} mode will decrease, and the coupling to higher order Hermite-Gaussian modes may increase. These modes can be identified from the camera image. Bright high order modes compared to the fundamental one is a signature of poor alignment. This part of alignment is done with two adjustable mirrors, as in the case of top mirror alignment. Firstly, the laser is tuned to a wavelength, where the mirrors have low reflectivity (refer to Fig. 3.16), such that considerable amount of light can transmit through the cavity. From the image on the camera, one can tell if the beam is straightly passing through the holes on the sample holder. After this step, we go to a higher reflectivity wavelength, and find the fundamental mode by fine tuning the wavelength. Due to path length difference, higher order Hermite-Gaussian modes appears at a different frequency from the fundamental one. We sweep laser frequency across the resonance of the fundamental mode, such that transmission peaks appear on the photo detector. The alignment is finalized by maximizing the transmission peaks by adjusting 4 degrees of freedom on the mirrors and 1 degree of freedom at the collimation lens.

3.3.4 Looking for the Working Laser Wavelength

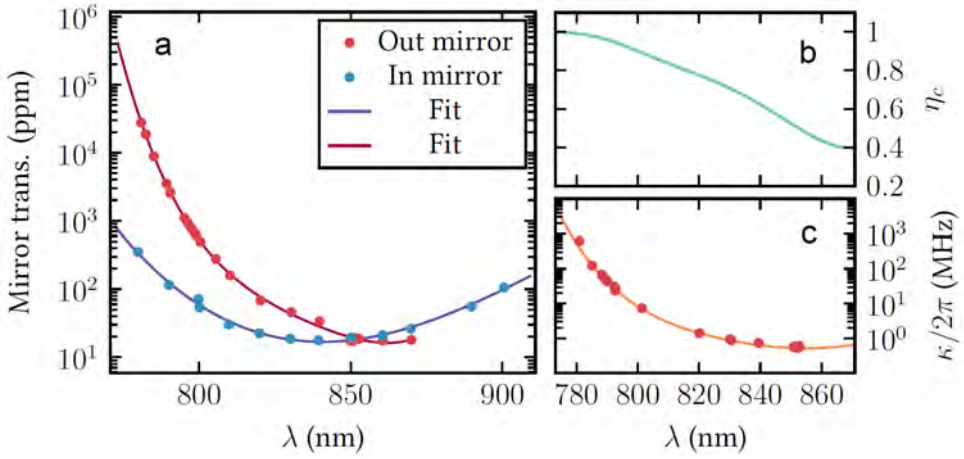

Figure 3.16: Cavity mirror coatings Measurements and figure from [46], the same pair of mirrors are used in this theses. **a.** Transmissions of cavity mirrors at different wavelengths. The unit ppm stands for parts per million, i.e. 10^{-6}. **b.** cavity out-coupling efficiency as a function of wavelength. **c.** Cavity linewidth of a 1.7 mm-long bare cavity as a function of wavelength.

As mentioned in Chapter 2, close to unity cavity out-coupling efficiency η_c and reasonably narrow cavity linewidth κ (corresponding to large measurement rate Γ_{meas}) is preferred to be satisfied simultaneously by our system. For a bare cavity, its linewidth κ is related to transmission coefficients of the input and output mirrors by

$$\frac{\kappa}{2\pi} = \frac{\kappa_L}{2\pi} + \frac{\kappa_R}{2\pi} = \frac{c}{2L}(|t_L|^2 + |t_R|^2). \tag{3.9}$$

The cavity out-coupling efficiency is given by

$$\eta_c = \frac{\kappa_R}{\kappa} = \frac{|t_R|^2}{|t_L|^2 + |t_R|^2}. \tag{3.10}$$

Thus, both of the parameters are a function of transmission of the mirrors. As the reflectivity of the membrane is low, thus the modification from a bare cavity case is small, it is not exaggerated to say mirror coatings determines the performance of the cavity. As coatings are making use of interference to generate high reflectivities (therefore low transmission), the mirror transmissions are always a function of wavelength. For our mirrors, this dependence is shown in Fig. 3.16 a. We can also calculate η_c and κ approximately using mirror coating data. It is clear that there is a trade off between high η_c and high κ in wavelength. Our choice is to work around wavelength $\lambda = 796\,\text{nm}$, where $\eta_c = 0.9$ and $\kappa/2\pi \approx 10\,\text{MHz}$ for a bare cavity. This wavelength gives both reasonably high η_c and narrow enough κ to see strong quantum backaction, and $\kappa \gg \Omega_m$ to keep us in the so called unresolved-sideband regime.

3.3.5 Transfer Matrix Model

So far, we only considered the effects of a bare cavity. After knowning the rough range of working wavelength, we need to find optical modes giving good optomechanical couplings.

Though the optomechanical coupling of a membrane-in-the-middle system can be modelled by a moving end mirror setting. There are some differences between the dispersive coupling and the moving end mirror coupling. The most significant difference is that, in dispersive coupling, system parameters including vacuum optomechanical coupling rate g_0 is a period function of membrane position relative to the cavity mirrors [84]. Thus, understanding this dependence is a necessary step for us to find the optimal working condition. To do so, one need to apply the transfer matrix model (TMM). The following contents in this subsection are based on Jayich et al. [84], Dumont et al. [85] and William Nielsen's thesis [46].

The related system parameters are shown in Fig. 3.17, where t's and r's are amplitude transmission and reflection coefficient respectively for cavity mirrors and the membrane, L stands for the cavity length,

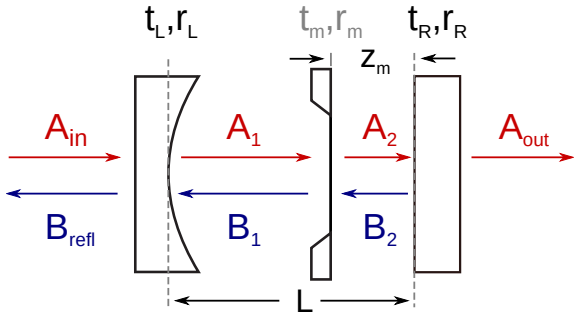

Figure 3.17: Fields amplitudes and system parameters Right propagating fields are labelled by A's, while left propagating fields are labelled by B's. For the consideration of field propagation, the starting point of intra-cavity fields are labelled by the starting points of the arrows. For instance, the starting point of field A_1 is at the right surface of the left mirror. As membrane thickness is small compared to the cavity length, we neglect its thickness in the transfer matrix model.

z_m stands for the distance between the membrane and the right mirror. As light only passes through the mirror substrates once, and the coated surfaces are super polished, we can neglect the mirror optical loss at the mirrors, such that $|t_L|^2 + |r_L|^2 = |t_R|^2 + |r_R|^2 = 1$. Then, these coefficients can be extracted from mirror transmission in Fig. 3.16. The membrane transmission and reflection coefficients can be calculated by treating it as a thin dielectric plate, and gives [86, 84]

$$r_m = \frac{(n^2-1)\sin(knd)}{2in\cos(knd) + (n^2+1)\sin(knd)} \tag{3.11a}$$

$$t_m = \frac{2n}{2in\cos(knd) + (n^2+1)\sin(knd)}, \tag{3.11b}$$

where d is membrane thickness. Please notice that n is in general complex, with the imaginary part describing absorption of light. For Si_3N_4, the real part of n is around 2.0 [87, 88], and the imaginary part is negligibly small, even inside a cavity with light passing through large amount of times [46]. As the optomechanical coupling is due to radiation pressure, higher r_m means larger coupling strength. From this expression, we can see r_m is modulated by membrane thickness due an etalon effect between two surfaces of the membrane. For our membrane thickness of around 20 nm, the reflectivity increases linearly with membrane thickness, up to around 50 nm.

Now we have thorough understanding of the system parameters, which allow us to calcualtes the fields [46]

$$A_1 = it_L A_{in} + r_m B_1 e^{ik(L-z_m)} \tag{3.12a}$$

$$B_1 = r_m A_1 e^{ik(L-z_m)} + it_m B_2 e^{ikz_m} \tag{3.12b}$$

$$A_2 = it_m A_1 e^{ik(L-z_m)} + r_m B_2 e^{ikz_m} \tag{3.12c}$$

$$B_2 = r_R A_2 e^{ikz_m} \tag{3.12d}$$

$$B_{refl} = r_L A_{in} + it_L B_1 e^{ik(L-z_m)} \tag{3.12e}$$

$$A_{out} = it_R A_2 e^{ikz_m} \tag{3.12f}$$

Without loss of generality, we can set $A_{in} = 1$, and solve for A_j and B_j, with $j = 1, 2$ under arbitrary condition. However, of course, what is of interest is the case close to cavity resonance, and the resonance condition, in high cavity finesse ($r_L = r_R = 1$) and low membrane absorption limit, can be described by [84, 46]

$$|r_m|\cos(2k_{res}z_m) = \cos(k_{res}L + \arg(r_m)), \tag{3.13}$$

where k_{res} is the resonance wavevector, which is related to resonance frequency by $\Omega_{res} = k_{res}c$, with c the speed of light in vacuum, and $\arg(r_m) \approx 0$. From the left handside, we can see a periodicity in $2k_{res}z_m$. To have a better view of this periodicity, we can assume $|r_m| \ll 1$, which to a large extend holds in our experimental condition. Under this assumption, the resonance condition is not far from the bare cavity case,

such that $k_{\mathrm{res}} \approx k_{0,\mathrm{n}}$, where $k_{0,\mathrm{n}}$ is the nth cavity resonance without a membrane. Then the expression can be written as

$$k_{\mathrm{res}} \approx \frac{1}{L}|r_{\mathrm{m}}| \sin\left(2k_{0,\mathrm{n}} z_{\mathrm{m}}\right) + k_{0,\mathrm{n}}, \tag{3.14}$$

where the modulation of cavity resonance frequency is evident. If we treat $k_{0,\mathrm{n}}$ as a continuous variable, the argument of the sin function $2kz_{\mathrm{m}}$ has 2π periodicity, and the resonance frequency shift is shown in Fig. 3.18. As $|r_{\mathrm{m}}|$ increases, the modulated cavity resonance is distorted away from a simple sinusoidal curve, when membrane is not placed exactly in the center of the cavity [85].

This period in $2kz_{\mathrm{m}}$ space can be understood as follows. The optomechanical coupling is the same if the ratio of the distance from membrane to the closest standing wave nodes on the left (right) side and the half wavelength is kept the same. Thus if we change k to $k + nT_k$, where n is an interger, and $T_k = \pi/z_{\mathrm{m}}$, the coupling does not change. To get a 2π period, we work with $2kz_{\mathrm{m}}$ instead of T_k.

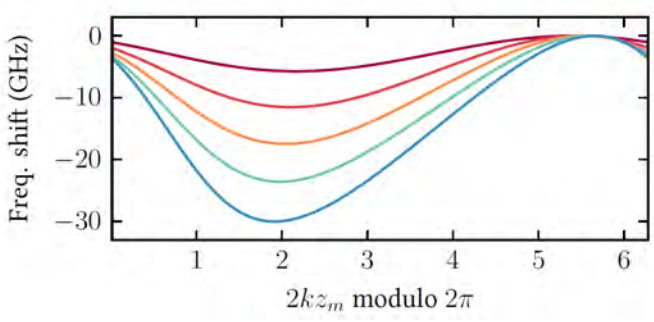

Figure 3.18: Membrane position modulation of cavity resonance frequency A figure from [46]. From top to bottom, $|r_{\mathrm{m}}| = \{0.1, 0.2, 0.3, 0.4, 0.5\}$.

Apart from cavity resonance frequency, other important system parameters, such as cavity linewidth κ, cavity out-coupling efficiency, and vacuum optomechanical coupling rate g_0, are also modulated by membrane position. It is beneficial to have a look at these dependences closely, and acquire a physical intuition.

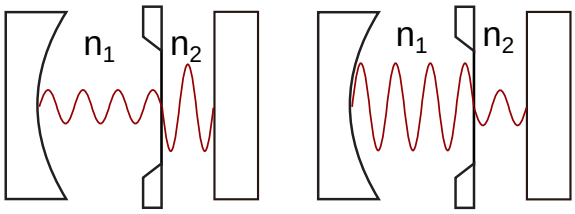

Figure 3.19: Illustration of subcavities

Cavity linewidth There is no analytical expression for cavity linewidth for an MIM system. However, we can solve the problem numerically, and make sense out of it by comparing it with the case of a bare cavity. κ_0, the cavity linewidth for a bare cavity, is given by

$$\frac{\kappa_0}{2\pi} = \frac{|t_{\mathrm{L}}|^2 + |t_{\mathrm{R}}|^2}{\tau} = \frac{c(|t_{\mathrm{L}}|^2 + |t_{\mathrm{R}}|^2)}{2L}, \tag{3.15}$$

with τ the cavity round trip time. The meaning behind this equation is the intra-cavity field gets lost whenever it reaches cavity mirrors. For one mirror, let's say the left mirror, the rate of energy loss is given by

$$\frac{\kappa_{\mathrm{L}}}{2\pi} = \frac{|t_{\mathrm{L}}|^2}{\tau}, \tag{3.16}$$

where $1/\tau$ determines the rate of light reaching this mirror, and $|t_{\mathrm{L}}|^2$ determines the ratio of energy loss. It is the same case for the right mirror. When there is a membrane between two mirrors, it divide the cavity

into two subcavities (illustrated in Fig. 3.19), with energy loss rates

$$\frac{\kappa_{\mathrm{L}}}{2\pi} = \frac{c|t_{\mathrm{L}}|^2}{2(L - z_{\mathrm{m}})} \text{ and } \frac{\kappa_{\mathrm{R}}}{2\pi} = \frac{c|t_{\mathrm{R}}|^2}{2z_{\mathrm{m}}}. \tag{3.17}$$

The total κ then should be a convex combination of κ_{L} and κ_{R}, with the weight determined by the relative power circulating in the subcavities (proportional to n_j), which can be modulated by membrane position.

Cavity out-coupling efficiency This is straightforwardly given by rate of field exceeding the right mirror divided by the total rate of field exceeding the cavity

$$\eta_{\mathrm{c}} = \frac{|t_{\mathrm{R}}|^2|A_2|^2}{|t_{\mathrm{L}}|^2|B_1|^2 + |t_{\mathrm{R}}|^2|A_2|^2}. \tag{3.18}$$

The modulation can again be viewed as a result of distribution of optical power between two sub-cavities. When more power is concentrated in the right subcavity, more light is exceeding through the right mirror, and can be collected by the detection chain, thus results in higher η_{c}.

Vacuum optomechanical coupling rate The optomechanical coupling rate $G = \frac{\partial \Omega_{\mathrm{cav}}}{\partial z_{\mathrm{m}}}$ is simply the first order derivative of the modulation of cavity resonance frequency. g_0 is then given by Gx_{zpf}. Noticing that $x_{\mathrm{zpf}} = \sqrt{\hbar/2m\Omega_{\mathrm{m}}}$ is not well known due to unknown effective mass of the mechanical mode, we cannot determine g_0 accurately from TMM. However, it authentically reflects the tendency as $2kz_{\mathrm{m}}$ changes.

The subcavity picture also provides a physical intuition on the modulation of optomechanical coupling in $2kz_{\mathrm{m}}$ space, which works even when r_{m} is not small. Recall the moving end mirror model of optomechanics, where the radiation pressure force is given by

$$F_{\mathrm{rad}} = \frac{2\hbar k\bar{n}_{\mathrm{cav}}}{\tau} = \hbar G\bar{n}_{\mathrm{cav}}, \tag{3.19}$$

which is a straightforward consequence of $F = \partial p/\partial t$, where p and t are momentum and time respectively. In this case, all intra-cavity photons contributes to the radiation pressure force, and thus G. On the contrary, a membrane in the middle of a cavity experience radiation pressure force from both sides. Moreover, because of the high cavity finesse, these radiation pressure are caused by approximately the same photons, thus they are nearly perfectly correlated, and can cancel each other if they are in opposite directions. In this case, the total radiation pressure force is given by

$$F_{\mathrm{rad}} = F_1 - F_2 = 2\hbar k\left(\frac{\bar{n}_1}{\tau_1} - \frac{\bar{n}_2}{\tau_2}\right) = \hbar G\bar{n}_{\mathrm{cav}}, \tag{3.20}$$

where $\tau_1 = 2(L - z_{\mathrm{m}})/c$ and $\tau_2 = 2z_{\mathrm{m}}/c$ are round trip times of the subcavities, and $\bar{n}_1$ and $\bar{n}_2$ are the corresponding photon numbers, which sum up to $\bar{n}_{\mathrm{cav}}$. Therefore, G is given by

$$G = 2k\frac{\bar{n}_1/\tau_1 - \bar{n}_2/\tau_2}{\bar{n}_1 + \bar{n}_2}, \tag{3.21}$$

which depends on the photon distribution in the subcavities, which is modulated by $2kz_{\mathrm{m}}$. One can express this expression in terms of fields calculated before as

$$G = \frac{2k(|A_1|^2 + |B_1|^2 - |A_2|^2 - |B_2|^2)}{\tau_1(|A_1|^2 + |B_1|^2) + \tau_2(|A_2|^2 + |B_2|^2)}. \tag{3.22}$$

Notice that the A_j and B_j are fluxes, the round trip time is used to convert them to photon numbers, such that $\bar{n}_j = \tau_j(|A_j|^2 + |B_j|^2)$.

An example of $2kz_{\mathrm{m}}$ modulated system parameters are shown in Fig. 3.20.

3.3.6 Determining Membrane Position in $2kz_{\mathrm{m}}$ Space

For stability reason, we choose a monolithic design of membrane-in-the-middle cavity. As a consequence, the position of membrane relative to standing wave, therefore the system parameters cannot be tuned continuously. Instead of changing membrane position continuously by using piezo electrics, we change standing wave position discretely relative to membrane by hopping between different TEM_{00} modes.

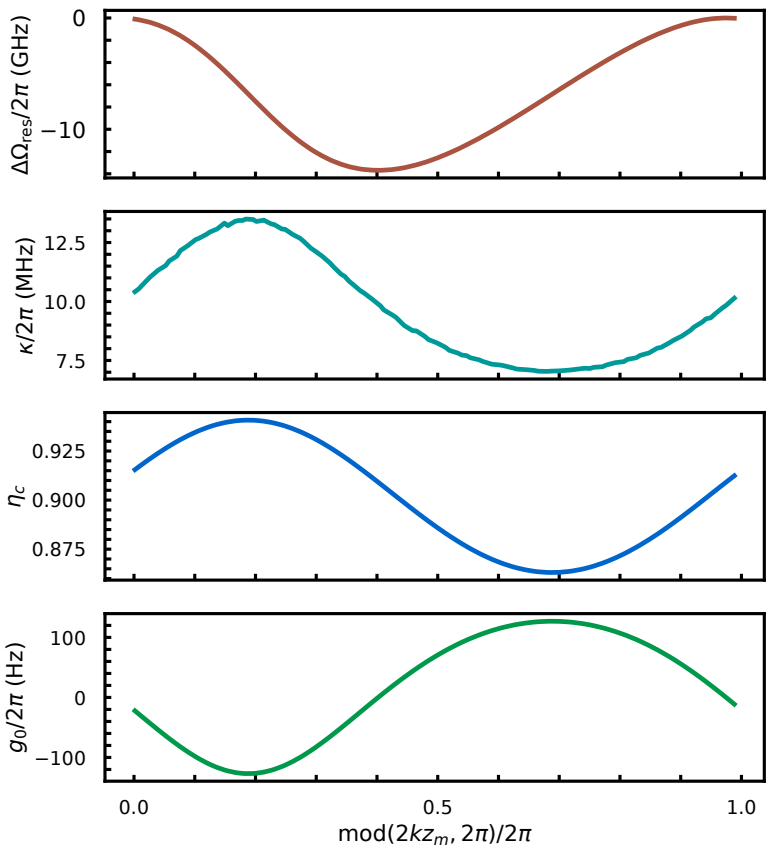

Figure 3.20: $2kz_{\mathrm{m}}$ **modulation of system parameters** The following system parameters are used $T_1 = 60\,\mathrm{ppm}$, $T_2 = 600\,\mathrm{ppm}$, $z_{\mathrm{m}} = 302\,\mu m$, $L = 1.595\,\mathrm{mm}$, $d = 20\,\mathrm{nm}$, $\lambda = 796\,\mathrm{nm}$, $m = 2\,\mathrm{ng}$, $\Omega_{\mathrm{m}}/2\pi = 1.137\,\mathrm{MHz}$, $n = 2.0$.

Hopping from one mode to an adjacent one (i.e. changing frequency by one FSR) means changing the number of nodes in cavity by 1, which is equivalent to changing wave number k of the light by π/L. Thus, we move our position in $2kz_{\mathrm{m}}$ by $2\pi z_{\mathrm{m}}/L$. In another words, in one period in k space, we have L/z_{m} number of modes. To get an idea of coupling landscape in $2kz_{\mathrm{m}}$, we need to exam at least L/z_{m} modes. More than L/z_{m} modes typically means better coverage on different coupling points. However, if we rewrite the ratio L/z_{m} in the form of $integer1/integer2$, with the integers $integer1$ and $integer2$ relatively prime to each other. Then $integer1$ sets a period of modes in $2kz_{\mathrm{m}}$ space by hopping between resonances. Sampling more modes than this number just results in the same coupling as one of the first $integer1$ modes. For example, if $L/z_{\mathrm{m}} = 5/2$, one can get at most 5 points in $2kz_{\mathrm{m}}$ space by changing laser frequency to hop between resonances.

To get coupling information, we find typically 7 to 9 adjacent TEM_{00} modes around the target wavelength, and record their wavelengths. Comparing these wavelengths to the ones expected by a bare cavity, we can get the frequency shifts, as shown in Fig. 3.21. In frequency domain, the points fall on a sinusoidal curve. When represent this frequency domain picture in k space, the resonances fall on a modulation curve with changed order. If $z_{\mathrm{m}} = L/2$, the k space picture will be a sinusoidal curve as well. The point at largest slope in $2kz_{\mathrm{m}}$ picture is our working point. Going to zero-coupling point is also helpful for some specific purposes.

For other system parameters, at the maximum coupling point in our case, η_{c} increases from 0.90 to 0.95,

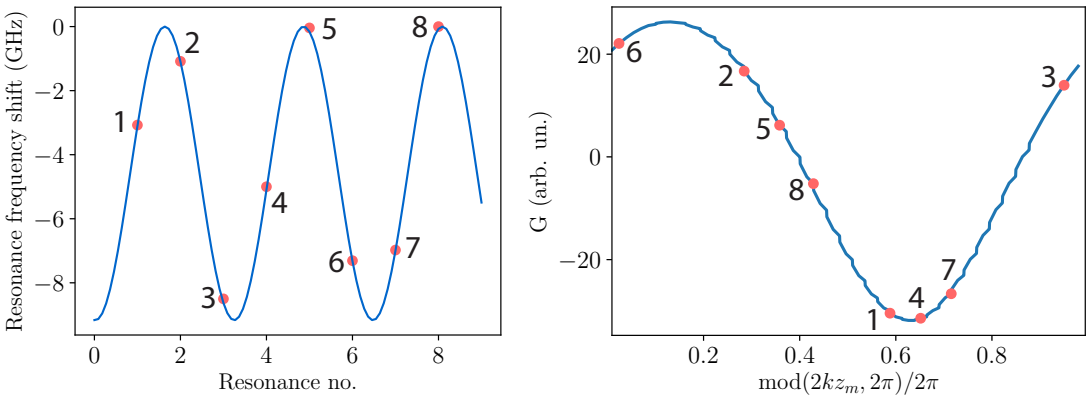

Figure 3.21: Optomechanical coupling of different modes left: in frequency domain, marked as resonance number; right: in $2kz_m$ domain.

and κ increases from around $2\pi \times 10\,\mathrm{MHz}$ to around $15\,\mathrm{MHz}$. The increasing in η_c is beneficial, and the increasing of κ is tolerable for our experiments.

3.3.7 Cavity Linewidth Measurement

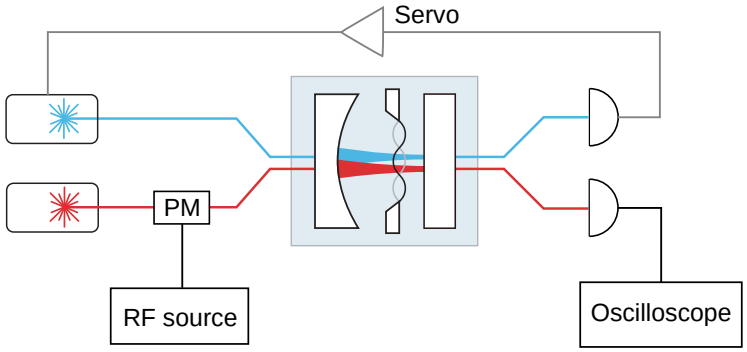

Figure 3.22: Setup of cavity linewidth measurement PM stands for phase modulator. The blue laser is used to provide sideband cooling in order to stabilize the system.

Cavity linewidth κ is a crucial parameter for any optomechanical experiments. An accurate way of measuring κ is sideband calibration, where a phase modulation of light at a known frequency is used as an reference to measure cavity linewidth.

The phase modulation of light is provided by an Electro-optical modulator, which contains some material exhibiting electro-optic effect. Suppose the original light field is given by $Ae^{i\omega t}$. If we apply a phase modulation with depth β and frequency Ω_{mod}, the modulated field is given by

$$A \exp\left(i\omega t + i\beta \sin\left(\Omega_{\mathrm{mod}} t\right)\right). \tag{3.23}$$

This expression can be expanded using Jacobi-Anger expansion, and reads [89]

$$Ae^{i\omega t}\left(J_0(\beta) + \sum_{n=1}^{\infty} J_n(\beta) e^{in\Omega_{\mathrm{mod}}} + \sum_{n=1}^{\infty} (-1)^n J_n(\beta) e^{-in\Omega_{\mathrm{mod}}}\right), \tag{3.24}$$

where J_n, $n \in \mathbf{Z}$ is nth order Bessel's function of first kind. The first term in bracket determines the residual amplitude at the original (carrier) frequency, the second term represents sidebands at frequencies $n\Omega_{\mathrm{mod}}$

higher than the carrier, and the third term represents sidebands at frequencies lower than the carrier, distributed symmetrically against higher frequency sidebands. If $\beta \ll 1$, Eqn. 3.24 can be simplified to

$$Ae^{i\omega t}\left(1 + i\beta \sin\left(\Omega_{\text{mod}} t\right)\right) = Ae^{i\omega t}\left(1 + \frac{\beta}{2}e^{i\Omega_{\text{mod}}} - \frac{\beta}{2}e^{-i\Omega_{\text{mod}}}\right), \tag{3.25}$$

where only a the first order red sideband and the first order blue sideband are important.

When we scan the carrier frequency by more than $2\Omega_{\text{mod}}$, and cross a cavity resonance, we will observe three Lorentzian peaks in the transmission intensity in frequency domain. We observe these peaks using a photodiode and an oscilloscope, as shown in Fig. 3.22. As laser scanning to the blue side of the optomechanical cavity, the membrane will be excited, which distorts the cavity line shape. To suppress this effect, we use an auxiliary laser to sideband cool the mechanics during the process. In this way, we have both cavity response and a reference frequency Ω_{mod}. Then we can extract κ by fitting the three Lorentzians and assign a corresponding frequency to these fitted linewidths. An experimental result of sideband calibration is shown in Fig. 3.23. To reduce the effect of noises, we typically average the linewidth data over 20 to 30 repetitions. This method can measure a $\kappa \approx 10\,\text{MHz}$ down to 100 kHz precision.

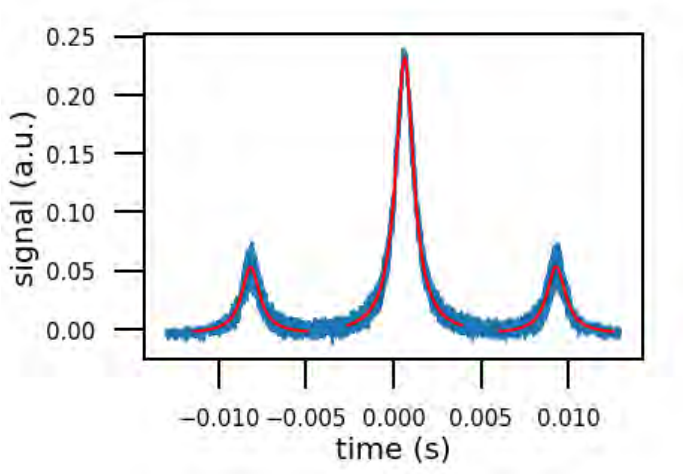

Figure 3.23: Sideband calibration Signal appearing on oscilloscope during sideband calibration of cavity linewidth, with lorentzian fitting of each peak. The horizontal axis is time, as appears on the oscilloscope.

3.4 Cavity Lock

At working wavelength, cavity mirrors are highly reflective. Only of the order of 0.001% of injecting power is transmitted through the input mirror. If there is only one mirror, the transmission port will be almost dark. However, as the two mirrors form a cavity, when the injecting light matches the cavity resonance, the tiny amount of transmitted light through the first mirror can be captured and accumulate in the cavity, ending up in a significant intra-cavity field. As this intra-cavity field leaks out the cavity, in transmission, there could be considerable field. While in reflection, the field leaking out from cavity interferes with the field directly reflecting off the input mirror destructively, resulting in a weaker reflection field. Thus, keeping the laser frequency around the cavity resonance frequency is crucial for experiments involving high finesse cavities.

In practice, the relative frequency between laser and cavity resonance is not a constant. Fluctuation and drifting due to reasons such as mechanical motion of the whole experimental apparatus and thermal fluctuation can cause undesirable frequency change of either cavity resonance or laser frequency. As the cavity linewidth is narrow compared to the frequency fluctuation and drifting, we need to do some active control to cancel these effects. This control is typically implemented in feedback scheme.

3.4.1 Basics of Feedback Control

Feedback control is a controlling scheme, where the output of a system is "fed back" to the input, in order to modify the system dynamics. This subsection only introduces the ideas and techniques used in our experiment. For more information, a pedagogic review can be found in Bechhoefer et al. [90].

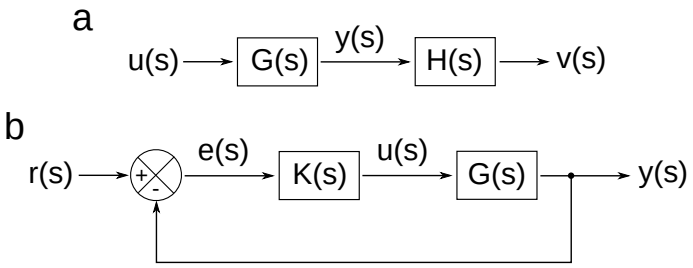

Figure 3.24: System dynamics in control theory a. Compound system. **b.** Feedback scheme.

We start with a general description of the dynamics of a linear system, whose state is described by an n-element vector $\vec{x}$:

$$\dot{\vec{x}} = \boldsymbol{A}\vec{x} + \boldsymbol{B}\vec{u} \tag{3.26a}$$

$$\vec{y} = \boldsymbol{C}\vec{x} + \boldsymbol{D}\vec{u}, \tag{3.26b}$$

where $\vec{u}$ is the input vector with m elements, and $\vec{y}$ is the output vector with p elements.

Most of the time, it is easier to work in frequency domain. In control theory, this is typically done through Laplace transformation

$$\mathcal{L}(y(t)) \equiv y(s) = \int_0^\infty y(t)e^{st}dt. \tag{3.27}$$

If $s = i\Omega$ and the lower bound of integration is extended to $-\infty$, Laplace transformation is equivalent to Fourier transformation. Comparing to Fourier transformation, Laplace transformation has the advantage of taking initial condition into account. Laplace transformation transforms a differential equation problem into polynomial problem of parameter s. It is typically hard to access the system state $\vec{x}$ directly, so the ratio between input and output $G \equiv \vec{y}/\vec{u}$ is widely used for description of the system dynamics. Even it is possible to access $\vec{x}$, we can just set the corresponding elements in $\boldsymbol{C}$ to be zero or one to transfer it to $\vec{y}$. For a compound system composed of cascaded system as shown in Fig. 3.24 a, the total dynamics is described by convolution $H * G(t) \equiv \int_0^\infty H(\tau)G(t-\tau)d\tau$, which is simply $\mathcal{L}(H * G(t)) = H(s)G(s)$ in frequency domain, i.e. $v(s) = H(s)G(s)u(s)$ (Here we focus on a one-dimension input and output, and drop the arrows and bold symbols for simplicity).

In a feedback control, a reference signal $r(s)$ is input to the system, and one would like to have an output $y(s)$ as close to the reference as possible, i.e. the error signal $e(s) = r(s) - y(s)$ close to zero. The scheme is a loop, as shown in Fig. 3.24 b, which gives the dynamics

$$y(s) = K(s)G(s)e(s). \tag{3.28}$$

Substituting $e(s) = r(s) - y(s)$, we have

$$y(s) = \frac{K(s)G(s)}{1 + K(s)G(s)}r(s) = \frac{L(s)}{1 + L(s)}r(s), \tag{3.29}$$

where $L(s) = K(s)G(s)$ is the loop gain. The negative sign in the feedback node says when $y(s) > r(s)$, the error is negative. If we have a simple proportional control law as

$$u(s) = K_\mathrm{p}(s)e(s),\ K_\mathrm{p} > 0, \tag{3.30}$$

we can compensate this error. Similar argument applies for the case where $y(s) < r(s)$. When the error is a constant, we need infinity proportional gain to keep $L(s)/(1+L(s)) = 1$. In practice, there is always an upper bound for the available proportional gain. Then the error will accumulate. When the error is caused by a

short time perturbation, the proportional control is probably enough to keep the error zero, as in average no error accumulation happens. To solve the problem of the need of infinity DC gain, we introduce the integral control:

$$u(t) = \frac{K_\mathrm{i}}{\tau} \int_{-\infty}^{t} e(t')dt', \tag{3.31}$$

where τ of dimension of time is to keep K_i dimensionless. This control law is simply

$$u(s) = \frac{K_\mathrm{i}}{\tau s} e(s) \tag{3.32}$$

in frequency domain. As $s \to 0$ the gain $K_\mathrm{i}/\tau s \to \infty$, which meets the requirement of infinity DC gain. The cost of infinity DC gain is the dramatic decreasing of gain as frequency increases. Therefore, proportional and integral controls are typically used simultaneously, to form a PI controller:

$$u(s) = \left(K_\mathrm{p}(s) + \frac{K_\mathrm{i}}{\tau s} \right) e(s). \tag{3.33}$$

Another commonly used controller is the differential controller, which count for the case of large $\dot{e}(t)$. But for our system, PI controllers are sufficient.

3.4.2 Slope Lock

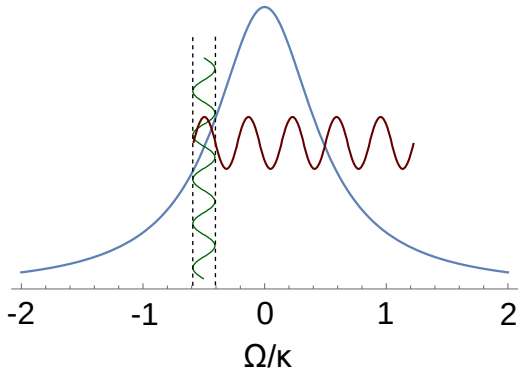

Figure 3.25: Transferring jitters in frequency into amplitude

Slope lock is a simple way of locking laser to cavity. When a laser is detuned from the resonance of the cavity, frequency jitters will be translated to amplitude jitters in the transmitted or reflected light of the cavity, as shown in Fig. 3.25. The Lorentzian represents the cavity lineshape. When the frequency moves closer to resonance, we have more transmission (less reflection), and vise versa. By detecting this change of field amplitude, thus intensity, we can get the information of relative frequency fluctuation between cavity and laser, and correct it. Notice that the scheme of getting error signal is the same as that to get mechanical information by detecting field amplitude. If the lock bandwidth is as large as mechanical frequency, mechanical information will be wiped out as if it is an error to be corrected. Therefore, there is a low pass filter to limit the feedback bandwidth.

The setup of slope lock is plotted in the upper half of Fig. 3.22, the part only involving the "blue" laser. The transmitted laser is directly detected by a photodetector, and the output is fed to a servo, which is a PI controller. The output of the servo goes to a piezo on the laser cavity, which can tune the laser frequency by changing the laser cavity length. The intended DC voltage (set point), which corresponds to the optical power falling on the detector, is the reference signal in control theory. When the input power to the cavity is stable, this set point corresponds to a unique detuning value on the red side of the cavity (blue detuning leads to instability). Thus, we can keep the relative frequency between laser and cavity at a desired frequency. The advantages of slope lock are simple implementation and possibility to lock at large detunings. However, when approaching resonance, the error signal gets smaller, and can be essentially zero on resonance. Therefore, if we want to lock the laser on resonance, as what is required for many experiments, slope lock is not a good choice. Moreover, slope lock cannot tell the difference between frequency jitter and intensity fluctuation. Therefore, if the input power is fluctuating, the frequency will not be stable.

3.4.3 Pound-Drever-Hall Lock

To solve the problem of on resonance locking, a common approach is Pound-Drever-Hall (PDH) lock. This subsection is only a short introduction. Black et al. [91] is a good resource for more detailed information.

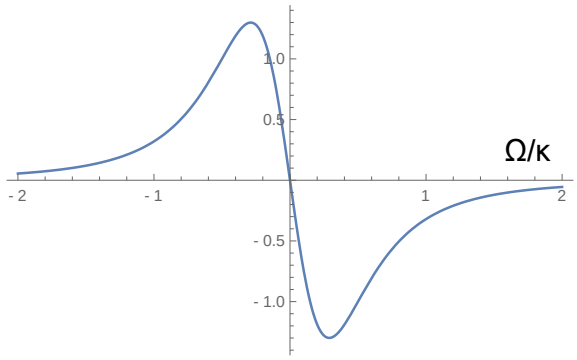

Figure 3.26: Derivative of Lorentzian lineshape

We have noticed that slope lock does not have descent error signal on cavity resonance. However, if we have a look at the derivative of a Lorentzian around resonance, we can observe a sign difference above and below the resonance, and a sharp slope. This provides a good error signal. To get this derivative signal, we modulate the phase of the laser at a known frequency, for example using a phase modulator as shown in Fig. 3.27. When the demodulation frequency $\Omega_{\text{mod}} < \kappa$, demodulating the reflected/transmitted intensity signal, we can get an error signal showing the derivative lineshape around DC (as dipicted in Fig. 3.26). Notice that the mixer will give both sum (at frequency around $2\Omega_{\text{mod}}$) and difference frequency (at around DC) of LO and signal, the lowpass filter is used to select the low frequency component.

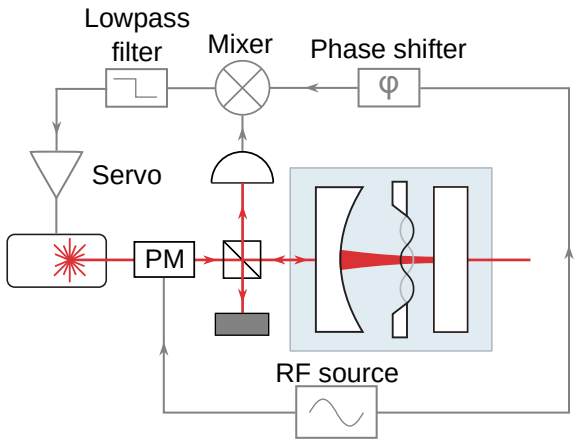

Figure 3.27: PDH setup The beams splitter is a non-polarizing one. The first reflected beam is blocked by a beam dump, and the reflected beam from the cavity is detected by a photodetector. This arrangement leads to loss of half of the input power in transmission signal, but this can be easily compensated by increasing the input power. The advantange of this arrangement is saving precious space before the cavity.

When the modulation frequency $\Omega_{\text{mod}} \gg \kappa$, error signal in reflection is given by Fig. 3.28, where the sharp features have characteristic width of κ. In the meanwhile, the error signal in transmission is strongly suppressed. As the modulation frequency is too large, there is not enough time for sideband light to build up in and transmit through the cavity. Thus, the phase modulation in transmission is negligible, and we do not have strong PDH signal. The central feature of the reflected signal at zero frequency is the part of the error signal we should focus on, if we aiming at locking on resonance, i.e. the set point in PI control. At this point, the lock is also insensitive to input power. If the set point is deviating from zero, the lock is slightly detuned, but it cannot go to a detuning beyond $\pm\kappa/2$. When the lock point is detuned, the input power dependence of lock frequency also recovers.

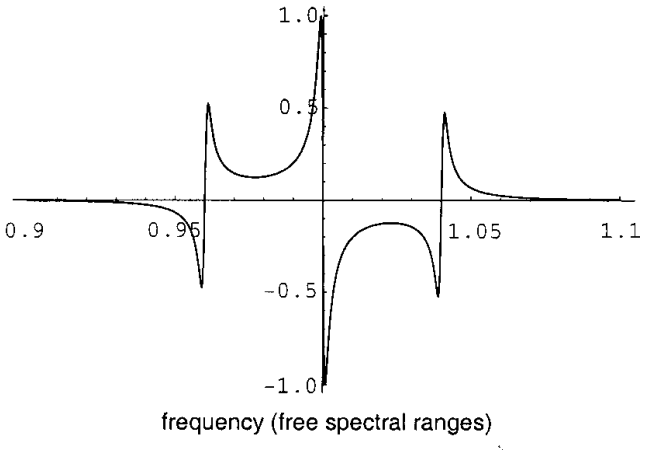

Figure 3.28: PDH signal for fast modulation A figure from [91]. The frequency unit is a bit arbitrary. The actual width of the feature is proportional to the cavity linewidth.

3.5 OMIT

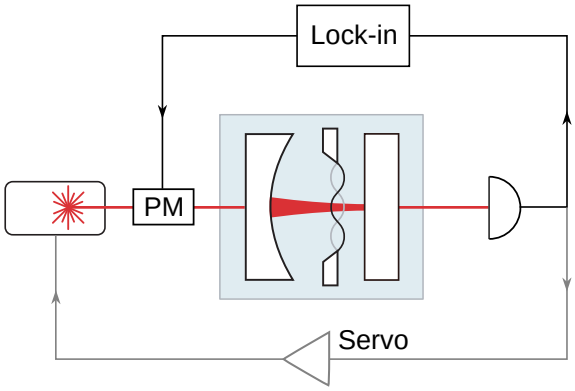

Figure 3.29: Set up for OMIT A tone from a lock-in amplifier is used to drive the phase modulator. The photo current from the diode is demodulated by the lock-in amplifier at the same frequency as the drive.

As mentioned in Section 2.6, optomechanically induced transparency can be used to calibrate multi-photon optomechanical coupling g accurately. In this section, we introduce this g calibration.

The experimental setup is shown in Fig. 3.29. A strong laser beam is locked to the optomechanical cavity with a red detuning, which can be accurately measured by comparing locking position and maximum transmission power, and making use of the Lorentzian cavity response. The transmission of this laser beam is directly detected by a photodetector. The output of the photodetector is input to a lock-in amplifier, which generates a tone at the same frequency as the demodulation frequency, to an electro-optical phase modulator to generate a pair of weak phase modulation sidebands of the input laser beam. As we sweep the phase modulation frequency, the lock-in amplifier records the OMIT response. From this response, we can extract g by fitting.

For the largest power we can input before effects like bistability happens, the OMIT response at the vicinity of Ω_m is shown in Fig. 3.30. Fitting the curve gives $g/2\pi = 329\,\mathrm{kHz}$, which corresponds to a $C_q = 4g^2/(\kappa\Gamma_m(\bar{n}_{th} + 1/2)) = 119$ for thermal bath temperature $T = 11\,\mathrm{K}$. This means our quantum backaction rate can be 119 times the thermal decoherence rate, which is the record for any optomechanical systems in optical domain.

We can also estimate the vacuum optomechanical coupling rate g_0 from OMIT response. The DC voltage output by the photodetector can be transferred to the optical power falling on the detector P_{det} by the conversion gain of the detector (in unit V/W, available from specification and verified by measurement). We

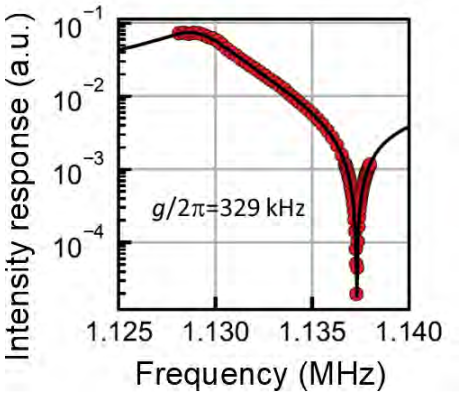

Figure 3.30: OMIT response with large input power A figure from [8]. The fitting of data gives a $g/2\pi = 329\,\mathrm{kHz}$.

take $\eta_c = 0.95$ from the transfer matrix model, and plug in the measured detection efficiency from cavity to photodiode $\eta_d = 0.97$, and the intra-cavity optical energy is given by

$$E_{cav} = \frac{P_{det}}{\eta_d \eta_c \kappa}. \tag{3.34}$$

Then the intra-cavity photon number is calculated to be

$$\bar{n}_{cav} = \frac{E_{cav}\lambda}{2\pi\hbar c} = \frac{P_{det}\lambda}{2\pi\hbar\eta_d\eta_c c\kappa}. \tag{3.35}$$

Essentially, the vacuum optomechanical coupling is given by

$$g_0 = g/\sqrt{\bar{n}_{cav}}. \tag{3.36}$$

Please notice that this value of g_0 is based on assumptions like cavity out-coupling efficiency, which is a source of uncertainty.

3.6 Balanced Homodyne

Balanced homodyne is a common way of frequency reference measurement, which allows measurement of arbitrary quadrature, including phase. In homodyne measurement, reference frequency is the same as signal carrier frequency. Balancing helps removing the effect of common noise between reference and signal. We implement this measurement in all projects introduced in this thesis.

3.6.1 Theory of Balanced Homodyne

The scheme of balanced homodyne measurement is shown in Fig. 3.31. For a simple case, the combination of polarizing beam splitters (PBS) and half waveplate (HWP) can be replaced by a 50:50 non-polarizing beam splitter. However, it is not easy to find a commercial non-polarizing beam splitter with perfect balancing of transmission and reflection. As an alternative, we combine signal and local oscillator (LO) with orthogonal polarization at the first PBS, and subsequently rotate their polarization by $\pi/4$, using the HWP. Thus, the powers of the signal and LO are split evenly after the second PBS. This approach is effectively the same as a single non-polarizing beam splitter, but provides more control on the splitting, allowing us to compensating imperfection of the optics. The optics and diodes are carefully chosen, such that they introduce as low optical loss as possible. The bottle neck on this part of detection efficiency are the quantum efficiencies of the diodes, which are around 90%.

Both a single non-polarizing 50:50 beam splitter and the PBS-HWP complex can be described by the 50:50 beam splitter matrix

$$\frac{1}{\sqrt{2}}\begin{pmatrix} 1 & 1 \\ -1 & 1 \end{pmatrix}. \tag{3.37}$$

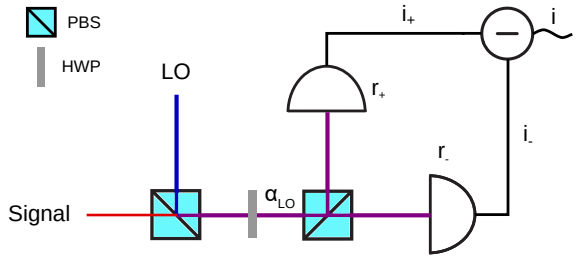

Figure 3.31: Balanced Homodyne The scheme of balanced homodyne in experiment. PBS refers to polarizing beam splitter, HWP refers to half waveplate.

We describe the signal and LO with classical fields $\alpha_S\,(1+n(t)+i\phi(t))$ and $\alpha_{LO}e^{i\theta}\,(1+n(t)+i\phi(t))$ respectively, where θ is the relative phase between signal and LO, and $n(t)$ and $\phi(t)$ are the common classical amplitude and phase noise respectively. Without loss of generality, we can discard the irrelevant common phase between the fields to make α_S and α_{LO} real. Then the fields at photodiodes are given by

$$\frac{\alpha_{LO}}{\sqrt{2}}\,(1+n(t)+i\phi(t))\,e^{-i\theta} \pm \frac{\alpha_S}{\sqrt{2}}\,(1+n(t)+i\phi(t)) + \hat{a}_{\pm,\mathrm{vac}}(t)\rceil \tag{3.38}$$

where $\hat{a}_{\pm,\mathrm{vac}}$ is the annihilation operator of vacuum field at photodiode $\pm$. Beating of this vacuum noise with classical field carrier results in shot noise in spectrum. Here we assumed phase fluctuation $\phi(t) \ll 1$, thus $e^{i\phi(t)} \approx i\phi(t)$. As the vacuum fluctuation is invariant under rotation of phase, the photocurrent spectrum is completely determined by the classical field amplitude:

$$\sqrt{\frac{(1+n(t))^2-\phi^2(t)}{2}(\alpha_{LO}^2+\alpha_S^2\pm 2\alpha_{LO}\alpha_S\cos\theta)} \approx \frac{1+n(t)}{\sqrt{2}}\sqrt{\alpha_{LO}^2+\alpha_S^2\pm 2\alpha_{LO}\alpha_S\cos\theta}, \tag{3.39}$$

where the approximation $\phi(t) \ll 1$ is used again. In this limit, common classical phase noise between signal and LO does not contribute to the homodyne result. The photocurrent generated by the diodes are proportional to the field intensity:

$$i_\pm = r_\pm\left((1+2n(t))\left(\frac{\alpha_{LO}^2}{2}+\frac{\alpha_S^2}{2}\pm\alpha_{LO}\alpha_S\cos\theta\right)+(1+n(t))\hat{a}_{\pm,\mathrm{vac}}(t)\sqrt{\frac{\alpha_{LO}^2}{2}+\frac{\alpha_S^2}{2}\pm\alpha_{LO}\alpha_S\cos\theta}\right), \tag{3.40}$$

where $r_\pm$ are the responsivity of the diodes, and we have used the fact $n(t) \ll 1$, thus $(1+n(t))^2 \approx 1+2n(t)$. The difference current $i = i_+ - i_-$ is subsequently transferred into voltage by a resistor, and then amplified by amplifiers. Therefore, the information is encoded in the voltage output of the photodetector. It is composed of DC and AC parts, where the DC voltage is given by

$$V_{DC} = (g_+ - g_-)\left(\frac{\alpha_{LO}^2}{2}+\frac{\alpha_S^2}{2}\right)+(g_+ + g_-)\alpha_{LO}\alpha_S\cos\theta, \tag{3.41}$$

where $g_\pm = r_\pm G$ is the transfer factor from field intensity to voltage, with G the electronic gain of the detector. If we treat V_{DC} as a function of θ, the first term serves as an offset, which vanishes when $g_+ = g_-$. The second term oscillates as θ changes, as a consequence of interference between LO and signal. The AC part of the voltage is composed of classical and quantum noises (represented by $n(t)$ and $\hat{a}_{\pm,vac}$ respectively). The spectrum of the voltage noise is given by

$$\bar{S}_{VV}(\Omega) = \frac{1}{2}g_+g_-(\alpha_{LO}^2+\alpha_S^2)+\frac{1}{2}(g_+-g_-)V_{DC}+2V_{DC}^2\bar{S}_{nn}(\Omega), \tag{3.42}$$

where we normalize the spectrum to vacuum noise, and take the convention where vacuum noise is 1/2. The first two terms correspond to shot noise, while the last term corresponds to classical amplitude noise.

It is clear that when $V_{\mathrm{DC}} = 0$, the contribution of classical amplitude noise vanishes in the BHD spectrum. In this case, neither classical phase noise or amplitude noise contributes to the final result, which is a desired property of BHD. However, when measuring quadrature other than phase ($\theta \neq \pi/2$), it is necessary to have finite V_{DC}. The cancellation of amplitude noise is not perfect anymore. In addition, as g_+ and g_- are usually slightly different, the finite V_{DC} will also cause difference in shot noise level. As shot noise is a commonly used reference, especially when considering squeezing, these effects needs to be carefully calibrated to make sure the measured "shot noise" is truly shot noise.

3.6.2 Balanced Homodyne Calibration

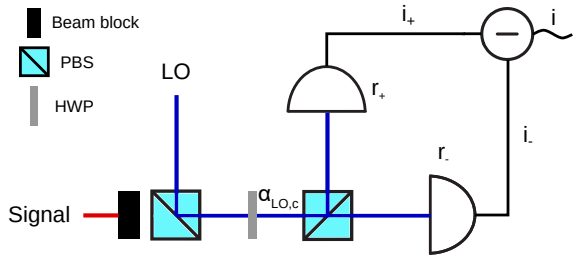

Figure 3.32: Balanced Homodyne Calibration The scheme of balanced homodyne calibration.

In the calibration, as shown in Fig. 3.32, we block the signal beam, and introduce a power imbalance δ between + and − path, such that the field classical amplitudes are given by

$$(1 + n(t))\alpha_{\mathrm{LO},c}\sqrt{(1 \pm \delta)/2} \tag{3.43}$$

We adjust $\alpha_{\mathrm{LO},c} = \sqrt{\alpha_{\mathrm{LO}}^2 + \alpha_{\mathrm{S}}^2}$. As $\alpha_{\mathrm{LO}} \gg \alpha_{\mathrm{S}}$, this is a small adjustment. Comparing to Eqn. 3.39, we notice, when $\delta = 2\alpha_{\mathrm{LO}}\alpha_{\mathrm{S}}\cos\theta$, the two cases are identical, as the DC voltage and spectrum are completely determined by classical field amplitude. Thus, the voltage noise spectrum is given by

$$\bar{S}_{VV}(\Omega) = \frac{1}{2}g_+g_-\alpha_{\mathrm{LO},c}^2 + \frac{1}{2}(g_+ - g_-)V_{\mathrm{DC}} + 2V_{\mathrm{DC}}^2\bar{S}_{nn}(\Omega), \tag{3.44}$$

with $V_{\mathrm{DC}} = \alpha_{\mathrm{LO},c}^2((g_+ - g_-) + (g_+ + g_-)\delta)/2$. Therefore, we can reproducing all effects in balanced homodyne with LO alone by adjusting the imbalancing, simulating the power difference caused by interference in BHD. In this way, we can calibrate the BHD background, without removing the optomechanical cavity from the signal path. This demonstrates another advantage of the tunability given by the PBS-HWP complex.

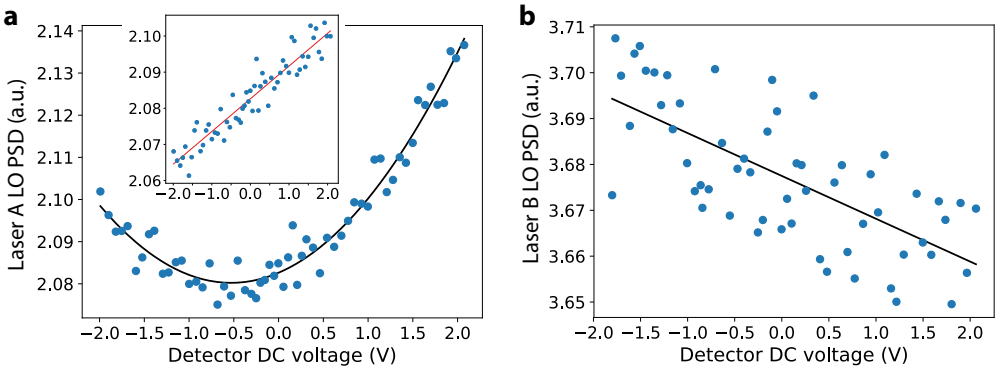

Figure 3.33: Balanced homodyne systematic error The result of BHD calibration for two lasers. The insert in **a** is the same function with quadratic part removed.

In practice, we measure the average value of $\bar{S}_{VV}(\Omega)$ over a interesting frequency range as a function of V_{DC}. The result is shown in Fig. 3.33. We name the two Ti-Saphire lasers used in the experiment A and B. Laser A is used for reading out the mechanical information, while Laser B is mostly used for cooling and actuation. Laser A spectrum shows a clear quadratic dependence on V_{DC}, which is a signature of contribution from classical amplitude noise. The lowest point of the parabola has a negative offset in V_{DC}, indicating $g_+ > g_-$. This contribution is more clear when the quadratic contribution is subtracted from all data points, as shown in the insert of Fig. 3.33 **a**. The spectrum of laser B does not show clear quadratic dependence, inferring low classical noise. The dominating deviation from the shot noise at $V_{\mathrm{DC}} = 0$ comes from $g_+ < g_-$. With this calibration result, we claim that the correction of background level is negligible in BHD experiments when $V_{\mathrm{DC}} \in (-1\,\mathrm{V}, 1\,\mathrm{V})$.

3.6.3 Mode Matching of Signal and Local Oscillator

The discussion in Subsection 3.6.1 is based on an assumption that LO and signal share the same optical mode after combination and polarization rotation. However, in practice, the two modes might be different. Let $\alpha_{\mathrm{LO},\parallel}$ with amplitude $\sqrt{1-\epsilon}\alpha_{\mathrm{LO}}$ representing the overlapped part between LO and signal modes, where ϵ is mode mismatch factor. It follows naturally that $\alpha_{\mathrm{LO},\perp}$ with amplitude $\sqrt{\epsilon}\alpha_{\mathrm{LO}}$ is the part of LO orthogonal to the signal mode. Then the Eqn. 3.38, the field at photodiode, should be rewritten as

$$\frac{\alpha_{\mathrm{LO},\parallel}}{\sqrt{2}}\left(1+n(t)+i\phi(t)\right)e^{-i\theta} \pm \frac{\alpha_{\mathrm{S}}}{\sqrt{2}}\left(1+n(t)+i\phi(t)\right) + \frac{\alpha_{\mathrm{LO},\perp}}{\sqrt{2}}\left(1+n(t)+i\phi(t)\right)e^{-i\theta} + \hat{a}_{\pm,\mathrm{vac}}(t)\Big| \tag{3.45}$$

As the orthogonal part does not interfere with the signal, the phase of this term has no effect, can be dropped for simplicity. Then the mode matched coherent amplitude reads

$$\frac{1+n(t)}{\sqrt{2}}\sqrt{\alpha_{\mathrm{LO}}^2(1-\epsilon)+\alpha_{\mathrm{S}}^2 \pm 2\sqrt{1-\epsilon}\alpha_{\mathrm{LO}}\alpha_{\mathrm{S}}\cos\theta}, \tag{3.46}$$

which determines how the signal beam is transferred into photocurrent. In the meanwhile the orthogonal part reads

$$(1+n(t))\alpha_{\mathrm{LO}}\sqrt{\frac{\epsilon}{2}}. \tag{3.47}$$

Though the orthogonal part does not interfere with the mode matched part, it still contributes to the total intensity shining on the photodiode, and classical and shot noise. In the case $\alpha_{\mathrm{S}} \ll \alpha_{\mathrm{LO},\parallel}$ and $\epsilon \ll 1$, we can see the mode matched coherent amplitude is approximately given by $(1+n(t))\sqrt{\alpha_{\mathrm{LO}}^2(1-\epsilon)}$, which is weaker than the completely mode matched case by multiplying a factor $\sqrt{1-\epsilon}$. While the orthogonal part introduces uncorrelated shot noise with a strength $\sqrt{\epsilon}$. We can see the role of non-zero ϵ is exactly the same as non-unity η. Therefore, having the modes of LO and signal as close to each other as possible is a crucial task to optimize detection efficiency.

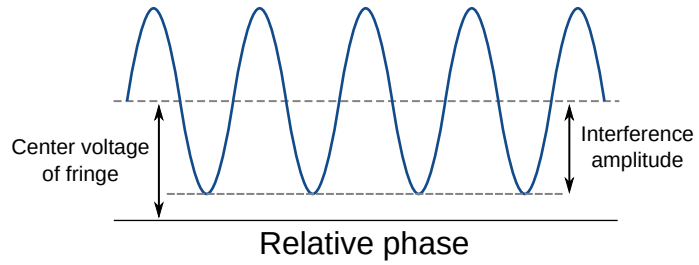

Figure 3.34: Interference fringe from DC output of the photodetector One of the diode is blocked, and the signal and LO powers are balanced. In this case, visibility is defined as the ratio between the amplitude of fringe and the center voltage.

The way to check ϵ is to block one diode on the balanced homodyne detector, adjust the power of LO and signal to be the same, and sweep the path length between signal and LO, which changes θ in Eqn. 3.46.

From the DC output of the photodetector, we can observe a interference fringe, as illustrated in Fig. 3.34. The visibility of this fringe is defined by

$$vis \equiv \frac{2\sqrt{1-\epsilon}\alpha_{\mathrm{LO}}\alpha_{\mathrm{S}}}{\alpha_{\mathrm{LO}}^2+\alpha_{\mathrm{S}}^2} = \sqrt{1-\epsilon} = \frac{V_{\mathrm{max}}-V_{\mathrm{min}}}{V_{\mathrm{max}}+V_{\mathrm{min}}}, \tag{3.48}$$

where V_{max} and V_{min} are the maximum and minimum voltage of the interference fringe respectively. From this expression, we can calculate ϵ, and can add a factor $1-\epsilon$ to the detection efficiency η. Please notice that, here, we have used the fact $V_{\mathrm{DC}} \propto \alpha_{\mathrm{LO}}^2 + \alpha_{\mathrm{S}}^2$ at $\theta = \pi/2$, where the LO amplitude is the summation of mode matched and mismatched part.

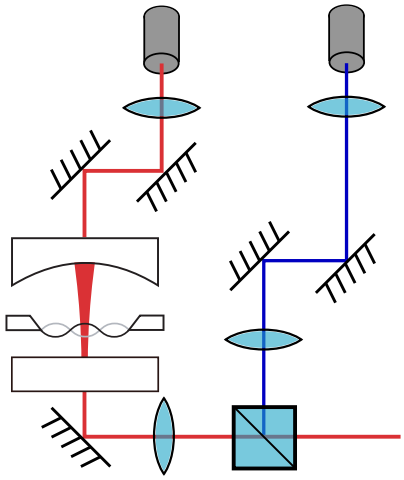

Figure 3.35: Mode matching between signal and LO

The idea of mode matching LO and signal is to build a LO optical path mimicking the signal path as shown in Fig. 3.35. Ideally, the distances between fiber heads and collimations, the distances between collimation lens and the lens before the combining PBS (recollimation lens), and the distances between the recollimation lens and the PBS are the same in LO and signal. The positions of the collimation and recollimation lens are adjustable along the propagation axis, and the collimator complex is place on a translational stage to adjust its position without messing up alignment too much. These degrees of freedoms help fine adjust the LO properties. In practice, the signal beam is PDH-locked around working wavelength, and we change the lens positions, the collimator position and the beam position and orientation (beam walk) to maximize the visibility. For Laser A, we can achieve a fringe visibility of 98%, and for Laser B 94%.

3.6.4 Path Length Lock

As can be expected from the scheme of homodyne, the stability of the relative phase between LO and signal is important. If the relative path length changes, there will be a random phase $\omega\Delta L/c$ in addition to the desired homodyne angle θ, where ω is the laser frequency, and ΔL is the path length fluctuation. In practice, mechanical vibration of the optical table and mirror mounts, as well as thermal expansion/contraction of fiber, can result in path length fluctuation. Therefore, stabilizing the relative path length by a lock is necessary. As there are many possible causes of path length fluctuation, it is unfeasible to counteract all of the sources. The typical approach is introducing a movable element (or an element with changeable refractive index) in the path of LO, to adjust the optical path length of LO. By feedback controlling the motion of this element, we can stabilize the relative path length.

The setup of path length lock around the movable part is illustrated in Fig. 3.36. The movable part is a mirror glued on a piezo. By changing the voltage applied on the piezo, we can tune the mirror position over a range of the order of 10 μm, corresponding to 10 wavelengths (i.e. 10 resonances). Before injecting into the fiber leading to LO of BHD, the laser is first reflected to the piezo controlled mirror by a PBS. The quarter waveplate ensures the reflected light from the mirror can transmit through the PBS. This double-pass setup

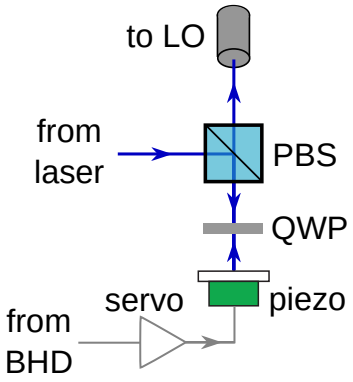

Figure 3.36: Path length lock of BHD PBS stands for polarizing beamsplitter, QWP stands for quarter waveplate. Changing the length of the piezo modifies optical path length of LO, thus changing the relative phase between LO and signal.

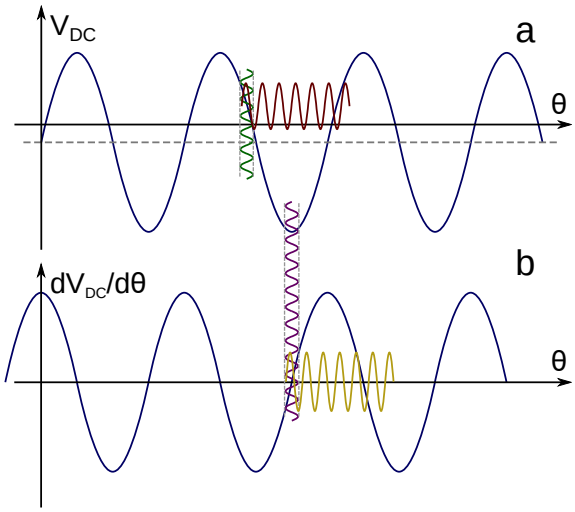

Figure 3.37: Balanced homodyne fringe a. Excursion in relative phase between signal and LO results in fluctuation in V_{DC}, which can be used as error signal for path length lock. **b.** The derivative of V_{DC}, for illustration of jitter lock.

reduces the possible intensity change of LO as the mirror changes its position, due to change of coupling to fiber.

The homodyne phase is determined by the locking voltage compared to the balanced homodyne interference fringe, which is shown in Fig. 3.37. As illustrated in Eqn. 3.41 a, the interference fringe has an offset, when the responsivities of the positive and negative diodes are not the same. With the correction of the offset, the homodyne angle is given by

$$\cos\theta = \frac{2(V_{\mathrm{DC}} - \mathrm{offset})}{V_{\mathrm{pp}}}, \tag{3.49}$$

where V_{pp} is the peak-to-peak voltage in the fringe, and V_{DC} the DC voltage of the balanced homodyne. If the relative phase changes due to some undesirable excursion, the DC voltage output from the balanced homodyne detector will change accordingly, providing a lock error signal in a very similar way to slope cavity lock (illustrated in Fig. 3.37). Similar to the cavity lock case, this simple lock scheme does not provide descent error signal around peaks of the fringe, i.e. around $\theta = 0$ and π. To lock there, a technique of providing jitters in path length (therefore voltage to the piezo) can be applied, the mechanism of which is essentially the same as PDH lock. As shown in Fig. 3.37 b, the jitters result in a derivative of V_{DC}, which has the largest slope at the peaks of the fringe. This slope caused signal can then be used as error signal for

path length lock.

3.7 Thermal Motion of Mirrors

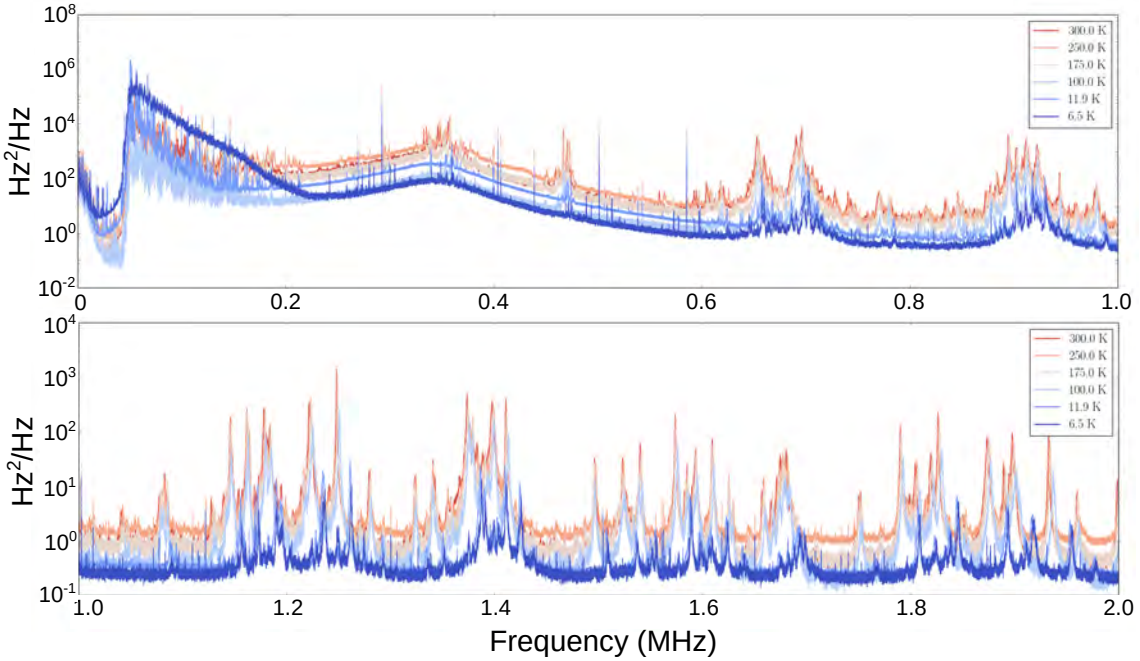

Figure 3.38: Mirror thermal noise [46, 92] from 0 to 2 MHz. The spectra from red to blue are measured at cryostat temperature at 300.0 K, 250.0 K, 175.0 K, 100.0 K, 11.9 K and 6.5 K respectively.

In membrane-in-the-middle system, the mechanics is considered to be the membrane. However, the mechanical motion of the cavity mirrors can also be encoded in the probe light. This coupling is exactly the conventional optomechanical coupling introduced in Section 2.3. Due to the dramatic mismatching in mode effective mass between mirror modes and membrane defect modes (a factor of 10^8), the zero point motion of mirror modes $x_{\mathrm{zpf,mirror}} = \sqrt{\hbar/2m_{\mathrm{mirror}}\Omega_{\mathrm{mirror}}}$ are 4 orders of magnitude smaller than that of defect modes. As a result, though the direct optomechanical coupling of mirror modes is indeed more efficient than the dispersive coupling of membrane, the vacuum optomechanical coupling rates of mirror modes are much smaller than those of defect modes at optimal coupling points. This small coupling together with low Q factor prevent the mirror modes from being an interesting object to study scientifically.

Though not interesting for science, we can still measure the thermal motion of the mirror modes in our experiments, as they introduce phase modulations. The result is some mechanical spectrum in addition to the one given by membrane modes, serving as a additional imprecision noise. As the mirror motion is incoherent with the membrane motion, the light scattered by these mechanical modes cannot interfere. Moreover, the optomechanical coupling is small for the mirror modes, causing almost no correlation between the quadratures of the light. These two facts make mirror noise a "hard" floor in spectrum, i.e. a lower bound cannot be overcome by correlations. Therefore, having mirror noise as low as possible, especially lower than imprecision noise is a crucial task in experiment.

To know the way to avoid mirror motion in spectrum, one needs to know the features of mirror motion through measurement. My colleague Dr. William Nielsen and Dr. Christoffer Møller assembled a cavity without membrane using the same mirror as ours, lock laser on resonance with the cavity with PDH lock, and measure the phase quadrature of the transmitted light using balanced homodyne receiver. The output of homodyne detector is fed to a DAQ card for spectrum analysis. To get a higher sensitivity to the mirror modes, they move the laser wavelength closer to 850 nm, where the cavity linewidth is narrower. They repeat the same measurement at different temperatures, to study temperature dependence of the mirror motion behavior. The results of the measurement from 0 MHz to 2 MHz is shown in Fig. 3.38. The mirror

modes spectra are not flat, where the peaked structures indicates normal modes of the mirror-sample holder assembly. Between these sharp features, there are some relatively quite region such as around 0.8 MHz and 1.05 MHz. These "valleys" are good region to place the defect mode of interest. This can be achieved by changing the size of the membrane defect. The mirror modes have smaller amplitudes as temperature decreases. This illustrates the reason to go to cryogenic temperature. In fact, for the pair of cavity mirror we use, the mirror noise level is one to two orders of magnitude higher than shot noise level at room temperature, which prevents us from doing quantum limited experiment at room temperature, even though the system parameter can achieve $C_{\mathrm{q}} > 1$.

Chapter 4

Mechanical Sensing Below the Standard Quantum Limit

In Section 2.8, we have seen that the measured noise of a conventional continuous wave interferometric displacement measurement is subjected to the Standard Quantum Limit (SQL). This limit has its origin in Heisenberg uncertainty principle and rotation of mechanical noises. Heisenberg uncertainty principle states

$$\sigma(\hat{Q})\sigma(\hat{P}) \geq 1. \tag{4.1}$$

Recall that $\hat{Q}$ and $\hat{P}$ are dimensionless displacement and momentum operators respectively. As a displacement measurement decreases the uncertainty of $\hat{Q}$, there must be backaction in $\hat{P}$ to increase its uncertainty. As we are monitoring the mechanical oscillator continuously, after a quarter mechanical period, this backaction caused uncertainty in $\hat{P}$ rotates into displacement, and is encoded in the signal. Effectively, in this way, we are trying to measuring a pair of conjugate variables simultaneously. Then Heisenberg uncertainty principle inevitably plays a role in the measurement precision. The concept of the Standard Quantum Limit was first proposed in a pioneer article of LIGO 50 years ago [7]. Out of both interest in fundamentals of quantum physics and application like gravitational wave detection, scientists put remarkable efforts in approaching and even overcoming the SQL. The closest approach to date is the one introduced in Section 4.2.

Though one cannot violate Heisenberg uncertainty, for a measurement smarter than the conventional one, the measurement precision can go beyond the SQL in principle. The first category of methods enabling measurement below the SQL is to only measure one quadrature of the mechanical oscillator, and decouple the other. In this way, the measurement is not subjected to Heisenberg uncertainty principle, and thus no backaction appears in the measurement record. This sort of backaction evading measurements mainly includes pulsed measurement introduced in Section 7.1, two tone reservoir engineering scheme [93], coupling to speed of a free mass [94], and coupling to a "negative mass oscillator" provided by atomic ensembles [95]. So far, backaction evading measurements of the displacement of a mechanical oscillator have only be demonstrated using reservoir engineering [15, 16, 17, 96] and negative mass [97] approaches. However, all of these demonstrations suffered from some technical weaknesses, keeping them from overcoming the SQL. For instance, the two tone demonstrations in microwave regime suffered from excess noise introduced by amplifiers, making the noise background significantly higher than shot noise [15, 16, 17], the two tone trial in optical domain suffered from low detection efficiency (thus high imprecision noise) and laser heating [96], and the negative mass approach suffered from excess noise coming from the atoms, and low C_{q}'s of atoms and mechanical oscillator [97]. If these technical challenges are addressed properly, sub-SQL measurement using backaction evading measurement will still be feasible.

The second category of approaches aiming at overcoming the SQL is making use of quantum correlations between backaction noise and imprecision noise. These methods include inputting a squeezed light as probe, injecting squeezed vacuum in the dark port of an interferometer [98], and making use of the optomechanically induced quantum correlations (i.e. ponderomotive squeezing introduced in Section 2.9) [40]. The former approach has already been implemented in the Advanced LIGO [99, 100], and is planned on VIRGO. However, the sensitivity is still above the SQL due to classical noise sources like thermal noise of mirror coating. The second approach is also referred as variational readout, and the simplest way of getting this correlation is to measure a quadrature other than phase [40]. Recently, a proof of principle experiment

was conducted by the Regal group using this approach [101], where they achieved broadband displacement sensitivity boosting. However, due to too low detection efficiency, their demonstration failed to beat the SQL.

As will be shown in the first section of this chapter, the key condition for overcoming the SQL using variational readout is $\eta_{\rm meas} \to 1$. In Chapter 3, we introduced the efforts to increase cavity out-coupling efficiency, the mode matching between signal and LO, and the efficiency of the optics. These give a total detection efficiency of around 77%. In addition, the ultra-narrow mechanical linewidth makes it easy to achieve $C_{\rm q} \gg 1$. Being able to satisfy these two conditions simultaneously is a unique feature of our system, which gives high quality mechanical measurement. The overall measurement efficiency of our system can reach $\eta_{\rm meas} = 56\%$, above the threshold of 45%.

In this chapter, we will introduce the theory of sub-SQL measurement using variational readout, the performance of our measurement under the condition of continuous wave phase quadrature measurement, and the first demonstration of sub-SQL measurement.

4.1 Theory

In the discussion in Section 2.8, we forced ourselves in a condition where quantum correlations between imprecision and backaction noise vanish. However, in practice, this term is a crucial recipe for displacement and force sensing below the SQL in variational readout approach. To illustrate the idea, we consider a case the same as the toy model discussed in Subsection 2.9.1, where $\kappa \gg \Omega_{\rm m}$, and $\Delta = 0$. Recall Eqn. 2.77, the measured displacement noise with correlation is given by:

$$\begin{aligned} \bar{S}_{\rm yy}(\Omega) &= \bar{S}_{\rm imp} + \bar{S}_{\rm qba}(\Omega) + \bar{S}_{\rm th}(\Omega) + \bar{S}_{\rm cor}(\Omega) \\ &= \frac{1}{8\eta_c\eta\Gamma_{\rm meas}(1-\cos(2\theta))} + |\chi_{\rm m}(\Omega)|^2\Gamma_{\rm qba} + |\chi_{\rm m}(\Omega)|^2\Gamma_{\rm m}(\bar{n}_{\rm th}+1/2) + \frac{{\rm Re}[\chi_{\rm m}(\Omega)]\sin(2\theta)}{2(1-\cos(2\theta))}. \end{aligned} \tag{4.2}$$

The displacement measurement sensitivity is below the SQL if the added noise ($\bar{S}_{\rm add}(\Omega) = \bar{S}_{yy}(\Omega) - \bar{S}_{\rm th}(\Omega)$) is below $\bar{S}_{\rm SQL}$. However, in practice, we measure spectrum with intrinsic noise. It is typical to compare $\bar{S}_{yy}(\Omega)$ and $\bar{S}_{\rm SQL}(\Omega)$ directly. Then the signature of overcoming the SQL is $\bar{S}_{yy}(\Omega)/\bar{S}_{\rm SQL}(\Omega) < 1$. As in the case of ponderomotive squeezing, if the correlation term is negative, it can cancel the effect of backaction and imprecision noise. This makes it possible to have a better sensitivity than the SQL.

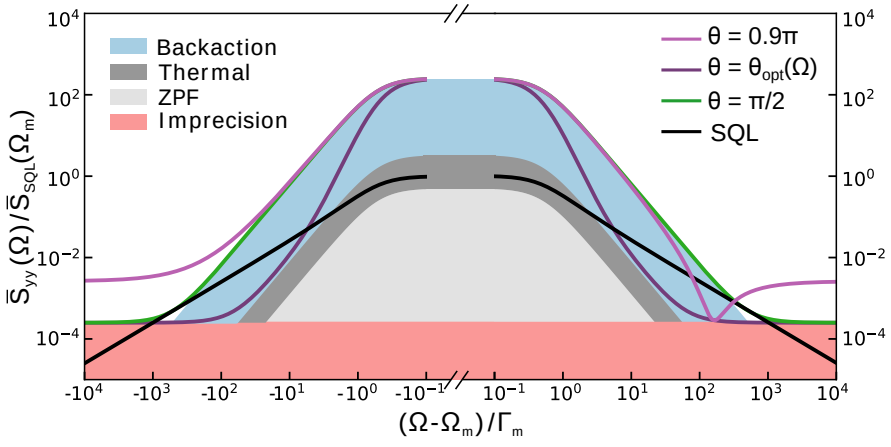

Figure 4.1: Sub-SQL Mechanical Spectrum A figure from [41]. The horizontal axis is logarithmic with zero the mechanical resonance frequency.

Fig. 4.1 shows the noise composition of a measured mechanical spectrum and the spectrum when variational readout is applied. From the figure, we can see several features of variational readout. The quantum correlations only exist between imprecision and backaction noise, which means the intrinsic noise cannot be affected by the correlation (as the optimal line never touches the gray part). As intrinsic noise is always

above the SQL level in the vicinity of mechanical resonance, sub-SQL sensitivity cannot happen in this region. However, as the intrinsic noise decreases as second order of $\chi_{\mathrm{m}}(\Omega)$ away from the mechanical resonance, while the quantum correlations decrease as the first order, there is always a frequency away from resonance, such that the only quantum noises are significant, and quantum correlations dominate over the intrinsic noise. Therefore, sub-SQL sensitivity only exists on the wings of the mechanical peak.

Now let's explore the parameter requirements for sub-SQL displacement measurement. Following the frequency argument above, we focus on frequency components where $|\Omega^2 - \Omega_{\mathrm{m}}^2| \gg \Gamma_{\mathrm{m}}\Omega$. Similar to the process in Subsection 2.9.1, we minimize the ratio $\bar{S}_{yy}(\Omega)/\bar{S}_{\mathrm{SQL}}(\Omega)$ over $\chi_{\mathrm{m}}(\Omega)$ (for the convenience of discussion, let's take $\Omega_{\mathrm{m}} < \Omega$), and have

$$\min \frac{\bar{S}_{yy}(\Omega)}{\bar{S}_{\mathrm{SQL}}(\Omega)} = \sqrt{\frac{1+1/C_{\mathrm{q}}}{\eta_{\mathrm{c}}\eta}}\frac{1}{2|\sin\theta|} - \frac{1}{2\tan\theta} = \frac{1}{\sqrt{\eta_{\mathrm{meas}}}}\frac{1}{2|\sin\theta|} - \frac{1}{2\tan\theta}. \tag{4.3}$$

The first term is the collection of imprecision noise and mechanical motion, and the second term is the quantum correlations. When $\theta \in (0, \pi)$, we have negative correlation, as requested. The minimum value occurs when

$$\theta_{\mathrm{min}} = \arccos\sqrt{\eta_{\mathrm{meas}}} \tag{4.4}$$

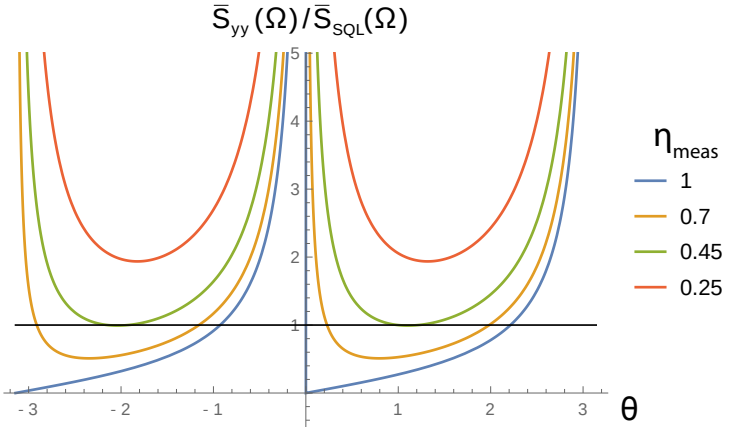

Figure 4.2: Minimum Ratio the minimum ratio between $\bar{S}_{yy}(\Omega)$ and $\bar{S}_{\mathrm{SQL}}(\Omega)$ at different η_{meas}'s.

Fig. 4.2 shows the dependence of the ratio in Eqn. 4.3 on both homodyne angle θ and measurement efficiency η_{meas}. The higher η_{meas} is, the more sensitivity below the SQL can be achieved. There is also a lower bound of $\eta_{\mathrm{meas}} \approx 0.45$ to observe any sub-SQL sensitivity, despite the choice of θ. This requirement of high measurement efficiency is exactly what our system can meet.

4.2 Quantum Limited Continuous Field Phase Quadrature Measurement

The most conventional measurement of mechanical displacement is using a continuous beam on resonance with the optomechanical cavity, and monitoring the phase quadrature of the light on a homodyne detector. This measurement gives the best sensitivity of displacement on resonance with the mechanical peak. Before introducing sub-SQL measurement, we confirm our ability to measure displacement near the SQL in the conventional way, which is a prerequisite of sub-SQL measurement.

In principle, one laser locked to the cavity with PDH lock is enough for the measurement. In practice, however, if we only have one laser beam, it is difficult to lock the laser exactly on cavity resonance. Because any fluctuation to the blue side of the cavity will cause excitation of the mechanics, which decays slowly due to high Q factors of the modes. For worse case, instability might happen. Moreover, light scattered from some low frequency mechanical mode can be very strong, where the mechanical modes are the eigenmodes

of the whole membrane instead of the defect. These sidebands of the laser carrier can serve as carriers themselves, and acquire their own sidebands. In spectrum, these second order sidebands can appear even in band gap, making the spectrum around the mode of interest noisy. Introducing an auxiliary laser to sideband cool all mechanical modes is a solution beneficial for solving both locking instability problem and second order sideband problem. For the latter issue, sideband cooling decreases "carrier" and "sideband" simultaneously, which is an efficient way of reducing these second order sidebands. However, as the auxiliary laser should be kept weak to reducing backaction, sideband cooling is usually not enough to suppress all these sidebands. To further suppress them, we also feedback cool (see Subsection 6.1 for more information) some of the low frequency mechanical modes providing these second order sidebands, which is effectively reducing carrier strength.

The experimental setup of this continuous wave conventional measurement is shown in Fig. 4.5. The auxiliary beam has the orthogonal polarization to that of the probe beam, and it occupies a different TEM_{00} mode. The orthogonal polarizations allow us to separate the probe and the auxiliary cleanly with a PBS in transmission. The frequency difference accounts for the imperfections of the polarizing optics, and avoids cross talk between these lasers. Otherwise, the field leaking through the PBS may appear in the homodyne spectrum. Just as the probe laser, the auxiliary laser introduces decoherence, which should be taken into account when calculating total decoherence rate. For this reason, to get high C_q, we need to use as weak auxiliary laser as possible. When calculating C_q of the probe, decoherence rate caused by the auxiliary laser should also be added into total decoherence rate in the denominator.

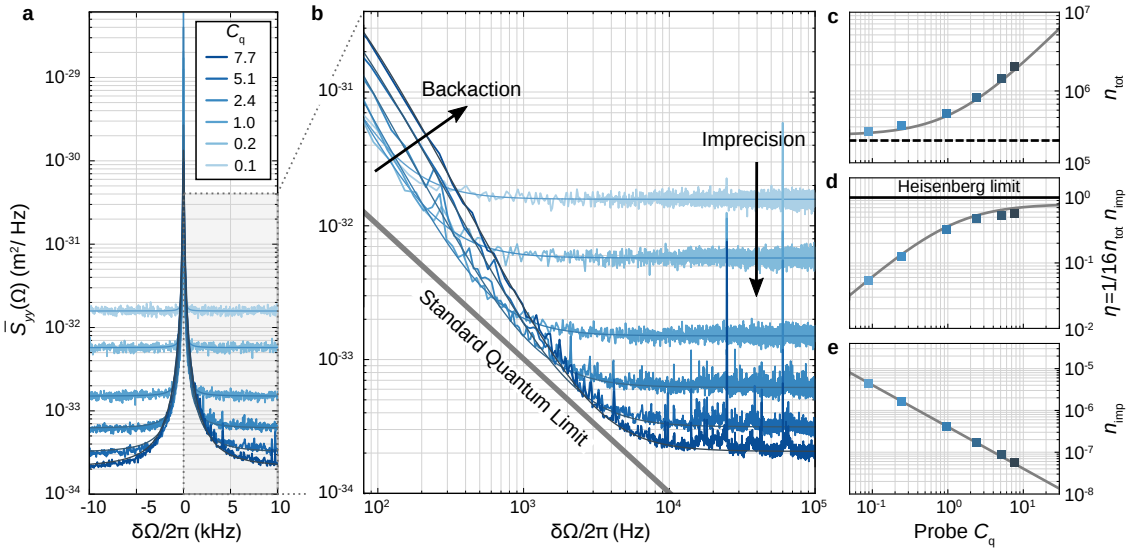

Figure 4.3: Quantum limited measurement A figure from [8]. **a.** Measured displacement spectrum of the defect mode of interest at different C_q's. **b.** Zoom-in to the blue sideband of the displacement spectrum in a log-log plot. **c, d, e.** total phonon occupancy, $1/16\bar{n}_{tot}\bar{n}_{imp}$, and $\bar{n}_{imp}$ of the spectra in **a** as a function of C_q.

Fig. 4.3 presents a result of CW conventional measurement. In this measurement, the cavity linewidth of the probe $\kappa/2\pi = 15.9\,\mathrm{MHz}$. The auxiliary laser has a cavity linewidth of $\kappa_{aux}/2\pi = 12.9\,\mathrm{MHz}$, a detuning of $\Delta_{aux}/2\pi = -4.2\,\mathrm{MHz}$, and a $C_{q,aux} = 0.08$ when the auxiliary is the only laser beam. The experimental results of spectra of the mode of interest at different C_q's are shown in Fig. 4.3 a and b, where b is a zoom-in of the high frequency side of the peak in a. We change C_q of probe from well below 1 to of the order of 10, by increasing probe laser intensity. As C_q increases, it is clear that the imprecision noise decreases as expected. In b, we can also see the increase of total phonon occupancy due to stronger backaction at higher C_q. When C_q is large, we can observe some structures on top of imprecision noise. The broader peaks are due to the mirror modes as introduced in Section 3.7, while the sharp peaks are the residual second order sidebands discussed above. To get an idea of the quality of the measurement, we can compare the spectral with that of the Standard Quantum Limit. At a frequency off mechanical resonance, we can find the spectra approaching the SQL. The closest point on the Lorentzian fit of the mechanical peak is only 35% above the SQL level, which is the closest ever achieved with conventional displacement measurement. To have a fair

comparison between the measurement record and a fundamental limit, we also compare with Heisenberg limit, which is defined as

$$\sqrt{16\bar{n}_{\mathrm{qba}}\bar{n}_{\mathrm{imp}}} \geq 1, \tag{4.5}$$

where $\bar{n}_{\mathrm{qba}} = C_{\mathrm{c}}$ is the occupancy of quantum backaction induced phonon, and $\bar{n}_{\mathrm{imp}} \equiv \bar{S}_{\mathrm{imp}}(\Omega_{\mathrm{m}})/2\bar{S}_{\mathrm{zpf}}(\Omega_{\mathrm{m}})$ is the imprecision noise occupation. Then according to Eqn. 2.77, the Heisenberg limit can be simplified to

$$\frac{1}{\sqrt{\eta_{\mathrm{c}}\eta}} \geq 1, \tag{4.6}$$

which is clearly satisfied by any optomechanical system. The physical meaning of Heisenberg limit lies directly in Heisenberg microscope type of experiment: observation of a particle using photon will perturb the original state. The stronger the probe is, the more information we can get, but also cause more perturbation on the system. The information acquired lies in $\bar{n}_{\mathrm{imp}}$, while the perturbation is described by $\bar{n}_{\mathrm{qba}}$ for the case of a harmonic oscillator.

In practice, it is not easy to measure $\bar{n}_{\mathrm{qba}}$ directly, the standard benchmark is to use the total occupancy $\bar{n}_{\mathrm{tot}} = \bar{n}_{\mathrm{qba}} + \bar{n}_{\mathrm{th}}$ instead, and the expression reads

$$\sqrt{16\bar{n}_{\mathrm{tot}}\bar{n}_{\mathrm{imp}}} = \sqrt{16\bar{n}_{\mathrm{imp}}\bar{n}_{\mathrm{qba}}\left(1+\frac{1}{C_{\mathrm{q}}}\right)} = \frac{1}{\sqrt{\eta_{\mathrm{c}}\eta}}\sqrt{1+\frac{1}{C_{\mathrm{q}}}} = \frac{1}{\sqrt{\eta_{\mathrm{meas}}}} \geq 1, \tag{4.7}$$

where C_{q} is also involved, and the whole expression can be summarized into a function of η_{meas}. Figure 4.3 c to e show the total phonon occupancy $\bar{n}_{\mathrm{tot}}$, $1/\eta_{\mathrm{meas}}$ and $\bar{n}_{\mathrm{imp}}$ at different C_{q}'s respectively. When C_{q} is small, $\bar{n}_{\mathrm{tot}}$ is dominant by thermal occupancy, which is indicated by the dashed line, and $\bar{n}_{\mathrm{imp}}$ is large. As the C_{q} increases, $\bar{n}_{\mathrm{tot}}$ starts to be dominant by quantum backaction, and $\bar{n}_{\mathrm{imp}}$ decreases linearly. As a result, $1/\eta_{\mathrm{meas}}$ approaches 1, the upper bound set by the Heisenberg limit. The highest value in these spectra of overall measurement efficiency is $\eta_{\mathrm{meas}} = 56\%$, leading to $1/\sqrt{\eta_{\mathrm{meas}}} = 1.34$, which is only 34% above the Heisenberg limit. Again, this is the record for any displacement measurement to-date.

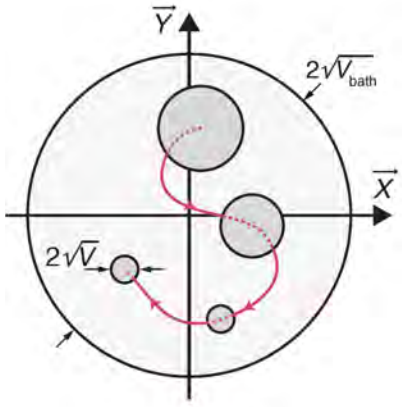

Figure 4.4: Evolution of conditional state of a mechanical mode A figure from [82]. The trajectory of the conditional state is stochastic, as indicated by the red line. The variance of the conditional state decays exponentially, as indicated by the diameter of the circles.

High η_{meas} is not only helpful for the measurement result approaching some limit, but also plays a significant role in the state estimation. For a mechanical mode under continuous monitoring, when the measured information is discarded (i.e. no conditioning), the state can be best described by a thermal state of occupancy $\bar{n}_{\mathrm{tot}}$ centered at $(0,0)$ in the phase space as shown in Fig. 4.4. When the measurement result is used to update the mechanical state, it will collapse from the big thermal state to a conditional displaced thermal state deterministically, while the displacement from the origin is a random vector governed by the stochastic process of quantum backaction and thermal noise. The final occupancy of this conditional state in the limit of $C_{\mathrm{q}} \gg 1$ is given by [8, 43, 102]

$$\bar{n}_{\mathrm{est}} \approx \frac{1}{2}\left(\sqrt{\frac{1}{\eta_{\mathrm{meas}}}} - 1\right). \tag{4.8}$$

The purity of the state is given by $(1 + 2\bar{n}_{\mathrm{est}})^{-1}$. Thus, the conditional state occupation is a monotonically decreasing function of η_{meas}, while the state purity is a monotonically increasing function. When $\eta_{\mathrm{meas}} = 1$, the conditional state is a pure coherent state. This high quality state estimation finds its direct application in measurement-based quantum control of mechanical motion, which is introduced in Chapter 6.

4.3 Mechanical Sensing Below the Standard Quantum Limit

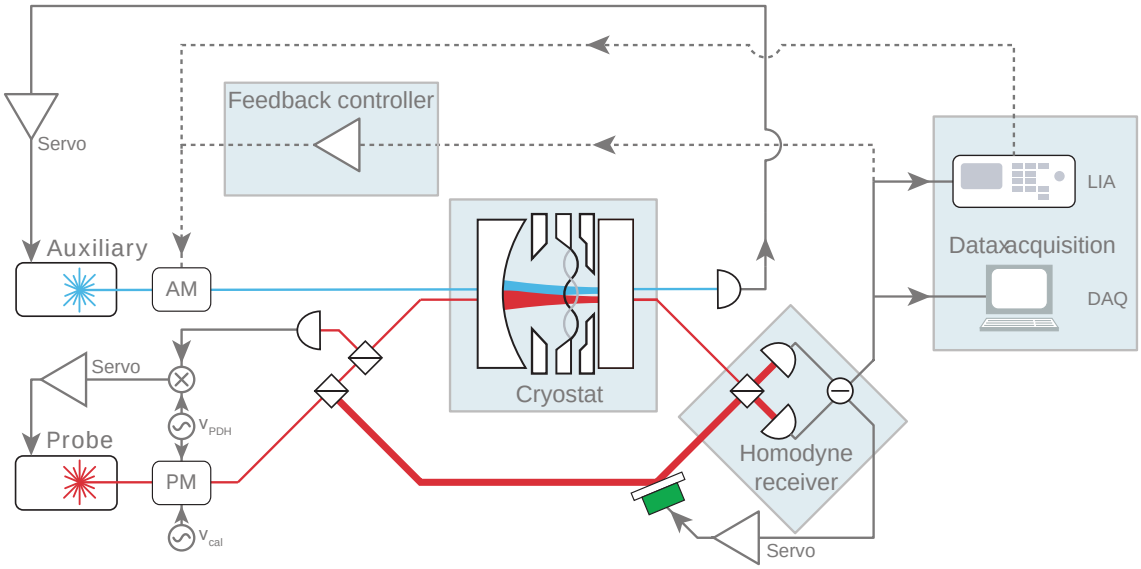

Figure 4.5: Experimental setup of sub-SQL measurement In the laser beams, AM stands for a fiber based amplitude modulator, while PM stands for a phase modulator based on electro-optical effect (an EOM).

The experimental setup for sub-SQL measurement is shown in Fig. 4.5. The probe laser passes through a phase modulator, before it is splitted into a probe beam with $C_{\mathrm{q}} \gg 1$ and the local oscillator. The phase modulator generates the phase modulation tone needed for system parameter calibration (refer to Subsection 4.3.1). The probe beam measures the displacement of the membrane, and the probe field transmitted through the cavity is measured by a balanced homodyne detector, where the probe beam and local oscillator recombine. An auxiliary laser provides some sideband and feedback cooling to suppress the second order mechanical sidebands around the mode of interest. A lock-in amplifier has the option of outputting a tone to the amplitude modulator to generate a coherent force for force sensing experiment (to be introduced in Subsection 4.3.5). For different cooldowns of the crystat, the parameters of the membrane-in-the-middle cavity do not stay at exactly the same number, due to some force distribution change in the ensemble during a thermal cycle from room temperature to liquid Helium temperature and back. Therefore, a full system characterization is needed at the beginning of each cooldown. In fact, this change may degrade the optomechanical coupling by changing the relative position of membrane defect and the cavity mode. If the cavity mode is too off the center of the defect, we may have to re-align the cavity curved mirror. For the thermal cycle providing data for measurement sensitivity exceeding the SQL, the cavity linewidth of the maximum optomechanical coupling mode is $\kappa/2\pi = 16.2\,\mathrm{MHz}$, the Q factor of the membrane is 1.03×10^9 and the vacuum optomechanical coupling rate from backaction calibration is $g_0/2\pi = 120.7\,\mathrm{Hz}$ (refer to Subsection 4.3.1 for backaction calibration).

Due to the existence of the auxiliary beam and the slightly detuned probe beam, we do not have a mechanical peak with linewidth as narrow as $\Gamma_{\mathrm{m}}/2\pi = 1.1\,\mathrm{mHz}$. Instead, we have an optically broadened mechanical mode with mechanical linewidth $\Gamma_{\mathrm{eff}}/2\pi \approx 32\,\mathrm{Hz}$, frequency $\Omega_{\mathrm{eff}}/2\pi = 1.35\,\mathrm{MHz}$ and thermal occupancy $\bar{n}_{\mathrm{th}} \approx 8$. The Standard Quantum Limit for comparison is the one given by this effective mechanical oscillator $|\chi_{\mathrm{eff}}(\Omega)|$. As the detuning of the probe beam is only around 0.12κ, the behavior of sub-SQL measurement does not deviate too much from the one presented in Section 4.1.

In variational readout, we need to measure a quadrature other than phase. To do so, we adjust the relative phase by changing the position of the movable mirror in the local oscillator path of the balanced homodyne

setup, as mentioned in Subsection 3.6.4. The homodyne phase is determined by the locking voltage compared to the balanced homodyne interference fringe. By changing this lock point, we can measure arbitrary quadrature. In the sub-SQL measurement, slope lock is sufficient, while in the optical entanglement project will be introduced in the next chapter, the jitter lock also plays a role.

In real experiment, we measured a series of spectra with different homodyne angles. In this way, we can scan through the optimal homodyne angle, get the phase quadrature measurement for comparison and study the quadrature angle dependence of the sensitivity improvement. Before presenting the results, we will introduce several calibration techniques and imperfections in the experiment.

4.3.1 Backaction Calibration

The spectra we measure through homodyne detector are directly fluctuations in voltage, which is proportional to photocurrents of the photodiodes, and directly proportional to quadrature fluctuations in the signal. However, we need to know the optomechanical coupling information to transfer this phase fluctuation into an accurate (dimensionless) mechanical displacement for the purpose of comparing to the SQL. Recall that g_0 relates phonon occupancy and frequency shift of the optomechanical cavity according to

$$\langle \delta\Omega_{\mathrm{cav}}^2 \rangle = g_0^2(2\bar{n}+1). \tag{4.9}$$

Therefore, calibration of g_0 is a necessary step to get phonon occupancy and displacement. Conventional calibrations include optomechanically induced transparancy (OMIT) [52], measuring optical spring and damping effects (sideband cooling method), and phase calibration tone [103]. The first two methods requires knowing total detection efficiency $\eta_c\eta$ and environment temperature accurately, while the last one requires knowing environment temperature and the phase modulation depth accurately. Measuring mechanical sideband asymmetry can serve as a direct calibration of occupancy, but it requires heterodyne detection, because in homodyne, only symmetrized spectrum is available.

In our system, measuring environment temperature with a thermalmeter is not trivial due to bad thermalization through elements like O rings and mirrors, and determining cavity outcoupling η_c is not easy either. To eliminate the dependency of g_0 calibration on these two quantities, we make use of the fact that our system can reach the regime $\Gamma_{\mathrm{qba}} \gg \Gamma_{\mathrm{th}}$, and develop a novel calibration method by combining calibration tone and sideband cooling methods.

In the calibration, we apply a very weak probe laser (the laser we are determining g_0 for), whose backaction is small compared to thermal decoherence rate. This signal is detected in phase quadrature at homodyne detector. At the same time, a strong red detuned auxiliary beam is applied to sideband cool the mechanics close to backaction limit $\bar{n}_{\mathrm{opt}}$ mentioned in Section 2.7. Typically, a series of measurement at different cooling beam power is conducted, as shown in Fig. 4.6. The plateau level in variance corresponds to $\bar{n}_{\mathrm{opt}}$. When the cooling power is maximum, the phonon occupancy of the mechanical mode is so close to $\bar{n}_{\mathrm{opt}}$, such that the fraction of the contribution of intrinsic noise to the total mechanical noise is only around 4%. Therefore, this method provides a well-defined temperature reference, as $\bar{n}_{\mathrm{opt}}$ only depends on Ω_{m}, κ and Δ, which can be directly and accurately measured. In the meanwhile, the low cooling power end provides a good estimation of thermal occupancy of the bath, the temperature of which is fitted to be 11 ± 2 K. The optical decoherence rate increases linearly with auxiliary laser power, indicating the absence of classical noises in the auxiliary laser.

To get the information of g_0, we apply a phase modulation tone common to probe and LO, with a known phase modulation depth ϕ at a frequency $\Omega_{\mathrm{cal}} \approx \Omega_{\mathrm{m}}$ by an electro-optical modulator (EOM), as shown in Fig. 4.5 without electronic feedback loop. (More information about phase modulation of EOM can be found in Section A.1.) According to Gorodetksy et al. [103], the phase modulation caused by this calibration tone is transferred to homodyne signal in the exactly same way as the phase modulation caused by mechanics, robust against changing in conditions such as homodyne angle, detuning, and probe strength. Then we can define a transduction factor from phase modulation to variance in voltage

$$K = \frac{\langle \delta V^2 \rangle_{\mathrm{cal}}^{\mathrm{QBA}}}{\langle \delta\phi^2 \rangle_{\mathrm{cal}}^{\mathrm{QBA}}} = \frac{\langle \delta V^2 \rangle_{\mathrm{cal}}^{\mathrm{QBA}}}{\phi^2/2}, \tag{4.10}$$

where $\langle \delta V^2 \rangle_{\mathrm{cal}}^{\mathrm{QBA}}$ is the voltage fluctuation in spectrum caused by the calibration tone. Then the voltage

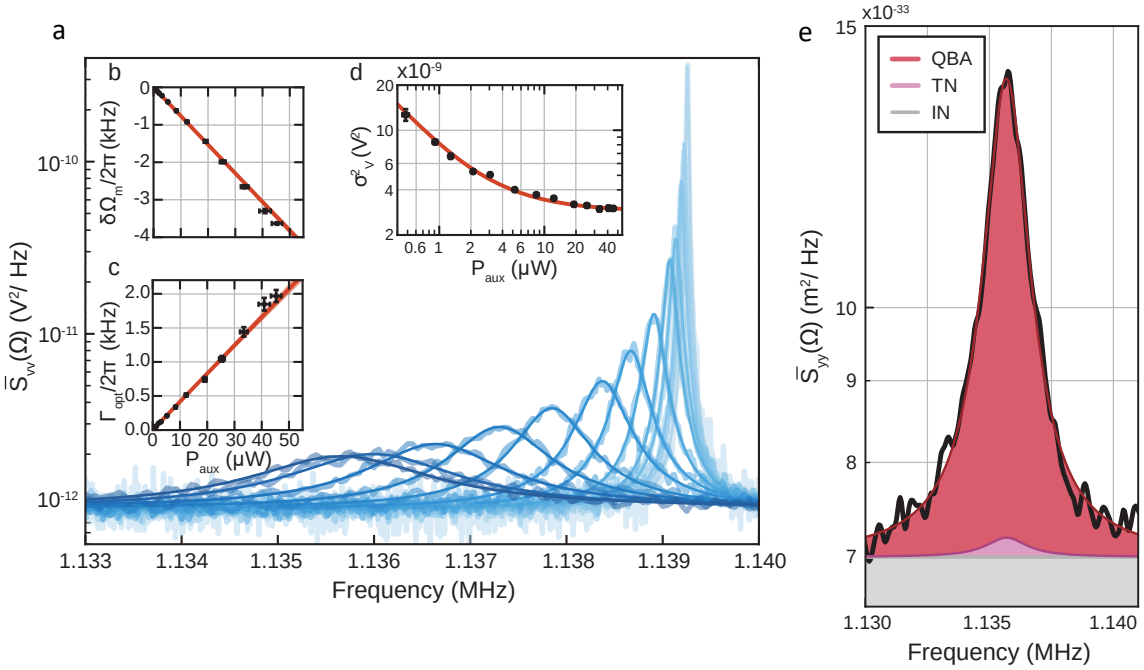

Figure 4.6: Backaction calibration A figure from the supplementary information of [8]. **a.** The sideband cooling spectrum at different cooling powers. The power increases from right to left. **b. c. d.** Optical spring effect, optical damping and spectrum area respectively. **e.** Noise breakdown of the mechanical spectrum at largest sideband cooling power, where QBA stands for quantum backaction, TN for thermal and zero fluctuation noises, and IN for imprecision noise.

variance caused by mechanical motion can be transduced into frequency modulation of cavity according to

$$\langle \delta V^2 \rangle_{\text{mech}}^{\text{QBA}} = K \langle \delta\phi^2 \rangle_{\text{mech}}^{\text{QBA}} = K \frac{\langle \delta\Omega_{\text{cav}}^2 \rangle_{\text{mech}}^{\text{QBA}}}{\Omega_{\text{m}}^2} = \frac{K 2 g_0^2}{\Omega_{\text{m}}^2} \left(\bar{n}_{\text{opt}} + \frac{1}{2} \right) \tag{4.11}$$

Substituting Eqn. 4.10 in, we have an expression of g_0:

$$g_0 = \sqrt{\frac{\langle \delta V^2 \rangle_{\text{mech}}^{\text{QBA}}}{\langle \delta V^2 \rangle_{\text{cal}}^{\text{QBA}}} \frac{\Omega_{\text{m}}^2 \phi^2/2}{2(\bar{n}_{\text{opt}} + \frac{1}{2})}}. \tag{4.12}$$

From this expression, we can see that, when there is uncertainty in EOM calibration, there will be uncertainty in the phase modulation depth ϕ, and g_0 will inhere this uncertainty.

To verify the backaction calibration of g_0, we also conduct OMIT calibration. The former gives $g_0/2\pi = (127 \pm 2)$ Hz, and the latter gives $g_0/2\pi = 129^{+2}_{-3}$ Hz, which match very well within uncertainty. As the two methods are sensitive to different parameters of the system, the good matching between the results demonstrate our thorough understanding of our system. Moreover, if there is significant heating of the mechanics due to absorption (a linear effect with respect to P_{aux}), it will lead to different results of the two calibration methods. The absence of this difference rules out significant undesirable heating.

Apart from getting g_0, we can use backaction calibration to convert an arbitrary measured voltage spectrum into dimensionless displacement spectrum [103]

$$\bar{S}_{yy}(\Omega) = \frac{\Omega_{\text{m}}^2 \phi^2/2}{2 g_0^2 \langle \delta V^2 \rangle_{\text{cal}}^{\text{meas}}} \bar{S}_{VV}(\Omega), \tag{4.13}$$

where $\langle \delta V^2 \rangle_{\text{cal}}^{\text{meas}}$ is the voltage fluctuation caused by the calibration tone in the measurement run, which can

in general be different from $\langle \delta V^2 \rangle_{\mathrm{cal}}^{\mathrm{QBA}}$. Substituting Eqn. 4.12 into this expression, we have

$$\bar{S}_{yy}(\Omega) = \frac{\langle \delta V^2 \rangle_{\mathrm{cal}}^{\mathrm{QBA}} (\bar{n}_{\mathrm{opt}} + 1/2)}{\langle \delta V^2 \rangle_{\mathrm{cal}}^{\mathrm{meas}} \langle \delta V^2 \rangle_{\mathrm{mech}}^{\mathrm{QBA}}} \bar{S}_{VV}(\Omega). \tag{4.14}$$

Notice that all parameters in this calibration factor is known with small uncertainty, even the phase modulation depth ϕ is cancelled. $\bar{n}_{\mathrm{opt}}$ only depends on κ_{aux}, Δ_{aux} and Ω_{m}, which can be measured to high accuracy. The idea of this calibration is using phase modulation tones as intermediators to compare the measured spectrum with a well understood backaction calibration spectrum. This robust calibration finds its application whenever an accurate comparison to dimensionless displacement related quantity is required, for instance in phonon occupancy calibration.

To compare the measurement result to the Standard Quantum Limit, one of the most important points is to guarantee that the comparison is fair. As the SQL is defined in dimensionless mechanical spectrum, the powerful backaction calibration of arbitrary spectrum to dimensionless mechanical spectrum plays a pivot role in this experiment. To compare the measured spectrum with the SQL, please recall the SQL is given by $|\chi_{\mathrm{eff}}(\Omega)| = \sqrt{\Omega_{\mathrm{eff}}} / \sqrt{(\Omega_{\mathrm{eff}}^2 - \Omega^2)^2 + \Gamma_{\mathrm{eff}}^2 \Omega^2}$, which is fully determined by the mechanical frequency under optical spring effect and the optically damped mechanical linewidth. These parameters can be extracted accurately from the fitting of the spectrum. Then the ratio between calibrated dimensionless displacement spectrum and the SQL is given by

$$\frac{\bar{S}_{yy}(\Omega)}{\bar{S}_{\mathrm{SQL}}(\Omega)} = \frac{\langle \delta V^2 \rangle_{\mathrm{cal}}^{\mathrm{QBA}} (\bar{n}_{\mathrm{opt}} + 1/2) \sqrt{(\Omega_{\mathrm{eff}}^2 - \Omega^2)^2 + \Gamma_{\mathrm{eff}}^2 \Omega^2}}{\langle \delta V^2 \rangle_{\mathrm{cal}}^{\mathrm{meas}} \langle \delta V^2 \rangle_{\mathrm{mech}}^{\mathrm{QBA}} \sqrt{\Omega_{\mathrm{eff}}}} \bar{S}_{VV}(\Omega), \tag{4.15}$$

which only depends on accurately known parameters. Thus this comparison of measured spectrum and the SQL is robust.

4.3.2 Calibration of Imprecision Noise

In the same way as transducing mechanical mode induced voltage fluctuation into displacement spectrum, one can also convert the imprecision noise in voltage into effective dimensionless displacement.

$$\frac{\langle \delta V^2 \rangle_{\mathrm{cal}}^{\mathrm{QBA}} (\bar{n}_{\mathrm{opt}} + 1/2)}{\langle \delta V^2 \rangle_{\mathrm{cal}}^{\mathrm{meas}} \langle \delta V^2 \rangle_{\mathrm{mech}}^{\mathrm{QBA}}} \bar{S}_{VV}^{\mathrm{imp}}(\Omega) = \bar{S}_{\mathrm{imp}}(\Omega) = \frac{1}{2 f_{\mathrm{imp}}(\Omega)}. \tag{4.16}$$

Recall that

$$f_{\mathrm{imp}}(\Omega) = \eta_{\mathrm{c}} \eta \frac{g^2}{\kappa} \mathrm{Re}\left[\zeta(\Omega) - \mu(\Omega) e^{-2i\theta}\right], \tag{4.17}$$

which is a function of $\eta_{\mathrm{c}}\eta$, θ and Δ, where Δ dependence is hidden in the cavity susceptibility dependent functions $\zeta(\Omega)$ and $\mu(\Omega)$. Therefore, a series of converted imprecision noise at different homodyne angles can provide information about the detuning of the probe. This could be particularly useful when detuning is small. Typically, the method of measuring detuning is to compare the transmission power at the lock point P_{lock} with the maximum value when scanning through the cavity resonance P_{max}:

$$\Delta = \frac{\kappa}{2} \sqrt{1 - \frac{P_{\mathrm{lock}}}{P_{\mathrm{max}}}}. \tag{4.18}$$

When detuning is small, the uncertainties in P_{lock} and P_{max} result in large uncertainty in Δ. On the contrary, the imprecision noise calibration does not suffer from this. Moreover, this calibration also provides a measure of the usually hard to access total detection efficiency $\eta_{\mathrm{c}}\eta$.

From the spectra series at different homodyne angles, we extract displacement imprecision, and the result is shown in Fig. 4.7. If there is no detuning for the probe, the curve should be centered at $\theta = \pi/2$. The finite red detuning rotates the detected quadrature, and shifts the whole curve to the right. From this shift, we can extract the detuning $\Delta \approx 1.2\kappa$. If we change detection efficiency $\eta_{\mathrm{c}}\eta$, the level of calibrated imprecision noise will shift up or down accordingly. From the vertical position of this curve, we can extract

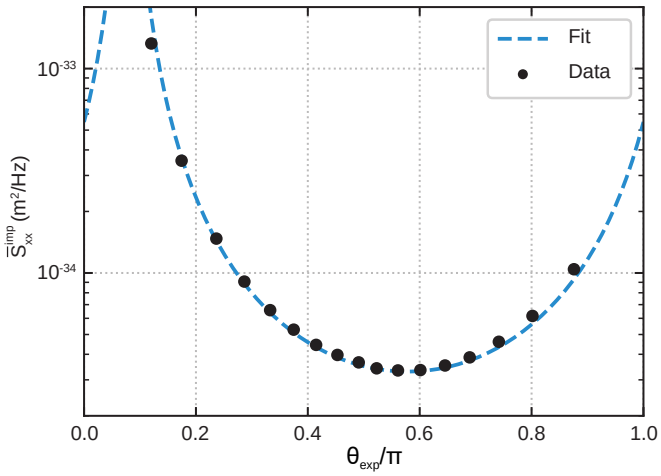

Figure 4.7: Calibrated imprecision noise A figure from the supplementary information of [41]. Notice that the dimension of the imprecision noise spectra is in m^2/Hz, which is the dimensionless displacement in main text multiplied by $2x_{zpf}^2 = \hbar/m\Omega_m$.

total detection efficiency $\eta_c\eta = 77\%$. Comparing the fit and data, we can also observe some systematic error of the measurement, as the data points lie below the fit on the left while above on the right. This systematic error goes hand in hand with drifts in g and Δ, which will be discussed in more detail in Subsection 4.3.3. As f_{imp} is a function of g^2, uncertainties in g will degrade the reliability of detection efficiency calibration.

4.3.3 Model Fit of Displacement Spectra

Whenever a theoretical model is available, comparing theoretical model to the experimental data is always a key step when presenting the experiment results. Ideally, all parameters in the theory are available with low uncertainties through independent measurements, and one can plot independent theoretical predictions against experimental data. However, in many cases, some parameters have to be determined from the experimental data to be compared to the theory, either due to lacking of independent characterization approach or parameter fluctuations in experiments. In this case, a model fit of the data is useful. In the sub-SQL displacement measurement, the systematic error in imprecision noise calibration infers the existence of drifts in experimental conditions during the series of measurement, which makes it necessary to model fit every spectrum.

During the experiment, we notice the drifting parameter is the probe power, which is a result of polarization drifting of light in fibers. Between different parts of the experiment (e.g. homodyne lock and the detection part), we use polarization-maintaining (PM) fibers as an optical link. If the input polarization of the light aligns with one of the two axes of the built-in birefringence in a PM fiber, the cross talk between orthogonal polarization modes will be strongly suppressed. Consequently, the input polarization will be maintained in the output of the fiber, as indicated by the name "polarization-maintaining". However, if the alignment is not perfect, cross talk still exists, and the output polarization will change with the conditions of the fiber, such as temperature and stress. As we are using polarizing optics before and after the optomechanical cavity to separate probe and auxiliary beams, this polarization drift will be converted into power fluctuation in the laser beams. In practice, we use a combination of a polarizer and a half waveplate to adjust the input polarization and maximize optical power before every fiber. During the alignment process, we observe the transmitted optical power after a polarizing beam splitter, while introduce perturbation on the fiber, such as heating and bending. The input polarization is adjusted such that smallest change in transmitted power is observed upon perturbation. However, the accuracy of this alignment is limited to a few degrees, which leaves residual power fluctuation.

The consequence of this power fluctuation is directly changing optomechanical coupling rate g. In addition, due to the slightly red detuned PDH lock of the probe, the fluctuation also affects the detuning (recall that PDH lock is only robust against power fluctuation when locked exactly on resonance). The power fluctuation in LO can also change the homodyne angle θ slightly. Therefore, in the model fit of displacement

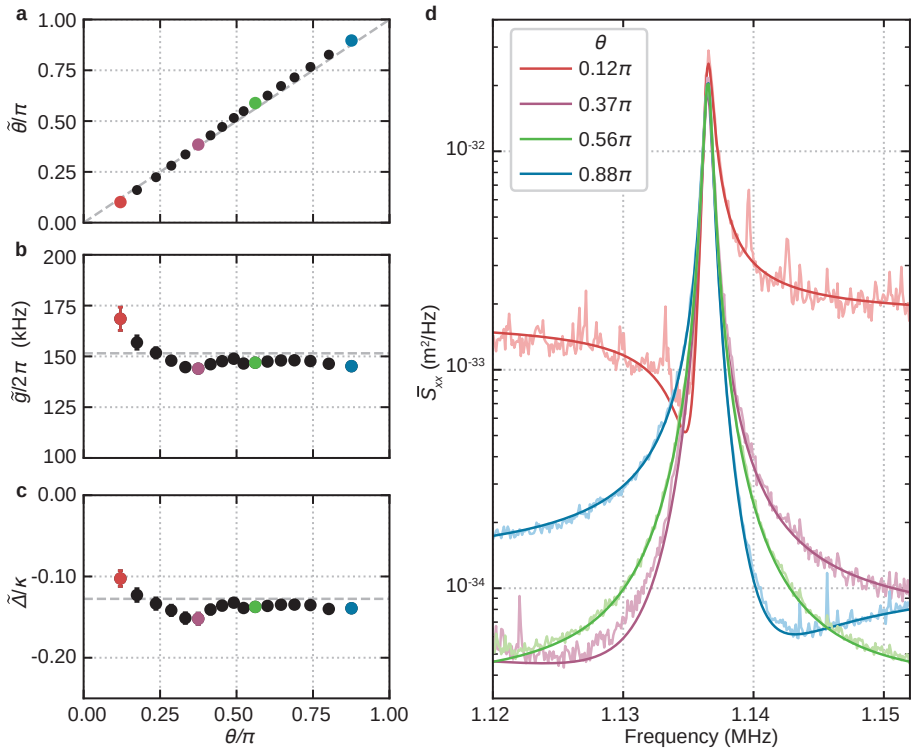

Figure 4.8: Model fit of spectra A figure from the supplementary information of [41]. **a-c.** Fitted homodyne angle $\tilde{\theta}$, fitted optomechanical coupling strength $\tilde{g}$ and fitted probe detuning $\tilde{\Delta}$ as a function of homodyne angle (extracted from lock point). **d.** Four sample spectra and their fits, calibrated into absolute displacement unit.

spectra, we choose to vary θ, g and Δ. The result is shown in Fig. 4.8. We first notice the fitting curves match the spectra in panel d very well, which demonstrates the explanation power of the theory. The increasing imprecision level as the measured quadrature approaching amplitude quadrature reflects the reduction of displacement transduction in balanced homodyne. The strong correlation between fitted detuning $\tilde{\Delta}$ and optomechanical coupling $\tilde{g}$ confirms the argument of PDH lock. The fitted homodyne angle $\tilde{\theta}$ follows expectation well, indicating low power fluctuation in LO. To compute the SQL, we use the average value of $\tilde{\Delta}$ and $\tilde{g}$. This choice may sound random, but its validity will be illustrated in the following subsection. With g from fitting and $\eta_c\eta$ from imprecision noise calibration, we calculate an overall measurement efficiency $\eta_{\text{meas}} = 58\%$, which is larger than the threshold value of 45%. Thus, sub-SQL sensitivity for displacement measurement is expected when the detection homodyne angle is optimal.

4.3.4 Sub-SQL Displacement Measurement

Fig. 4.9 presents the measured displacement spectra at around phase quadrature and two quadratures giving most sub-SQL results above and below the mechanical resonance, and the SQL. Due to the difference in detuning and coupling strength, the mechanical responses actually have slightly different peak frequencies. In this plot, we shift the peaks horizontally, such that their peaks align, making it easier to compare with the SQL. Notice that when $\Delta, \Omega_m \ll \kappa$, quantum correlations on mechanical resonance is negligible, making the tip of the mechanical peaks a good indicator of Ω_{eff}. The SQL is calculated using the average values of fitting results $\tilde{\Delta}$ and $\tilde{g}$, as mentioned in the previous subsection. Though the choice of parameters is relatively random, as the sub-SQL sensitivity only happens at the wings of the mechanical resonance, the difference in effective mechanical linewidth Γ_{eff} does not affect the SQL in this region. This can be understood by

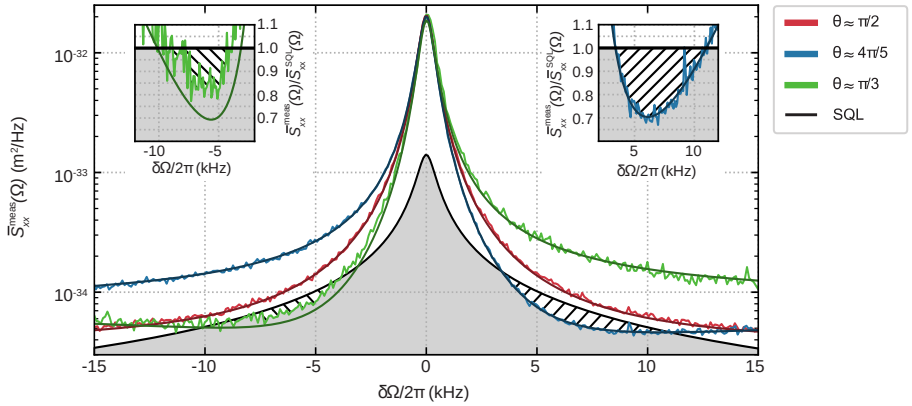

Figure 4.9: Sub-SQL displacement measurement A figure from [41]. The measured displacement spectra in absolute displacement unit. The horizontal axis is the frequency relative to mechanical resonance. The two inserts are the ratio between displacement spectra and SQL around the sub-SQL region.

looking at the expression of SQL

$$\bar{S}_{\mathrm{SQL}}(\Omega) = |\chi_{\mathrm{eff}}| = \frac{\Omega_{\mathrm{eff}}}{\sqrt{(\Omega_{\mathrm{eff}}^2 - \Omega^2)^2 + \Gamma_{\mathrm{eff}}^2 \Omega^2}}. \tag{4.19}$$

When $|\delta\Omega| \equiv |\Omega_{\mathrm{eff}} - \Omega| \gg \Gamma_{\mathrm{eff}}$ and $\Omega \approx \Omega_{\mathrm{eff}}$, the SQL is approximately given by

$$\bar{S}_{\mathrm{SQL}}(\Omega) \approx \frac{1}{2|\delta\Omega|}, \tag{4.20}$$

which is independent of parameters can be influenced by g and Δ. Fig. 4.10 plots the SQL at $\Gamma_{\mathrm{eff}} = 10, 30, 100\,\mathrm{Hz}$. The tails are very insensitive to the choice of the effective mechanical linewdith. Comparing the frequency scales in this plot and Fig. 4.9, we can conclude that the choice of parameters in SQL calculation is reasonable.

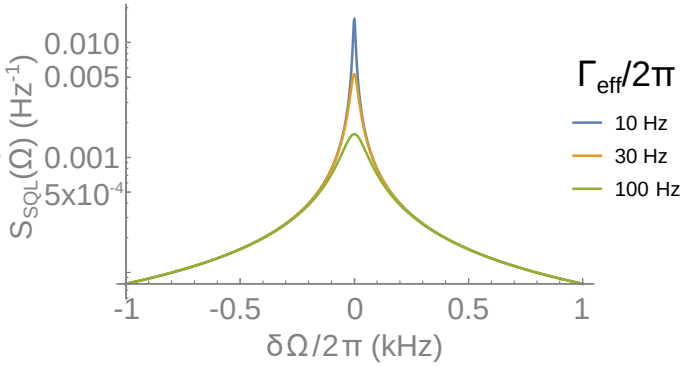

Figure 4.10: The SQL at different Γ_{eff} Around mechanical resonance, smaller Γ_{eff} leads to larger SQL. Away from mechanical resonance, the SQLs are the similar at different Γ_{eff}.

From Fig. 4.9, it is evident that the blue and green displacement spectra can dive below the SQL on both sides of the mechanical resonance. The insert shows the ratio between the displacement spectra and the SQL, with the best sensitivity 1.5 dB below the SQL. The deviation between fit and the spectrum at $\theta \approx \pi/3$ is probably an effect of mirror noise, as it is asymmetric on the two sides of the mechanical resonance.

The bandwidth of the sensitivity improvement by variational readout is proportional to the backaction rate of the probe beam, for the exactly the same reason as that for ponderomotive squeezing (see Section 2.9). To demonstrate this dependence, we plot the ratio of displacement spectrum and the SQL as a function of both frequency and homodyne angles in Fig. 4.11 at three different probe C_{q}'s. It is evident that

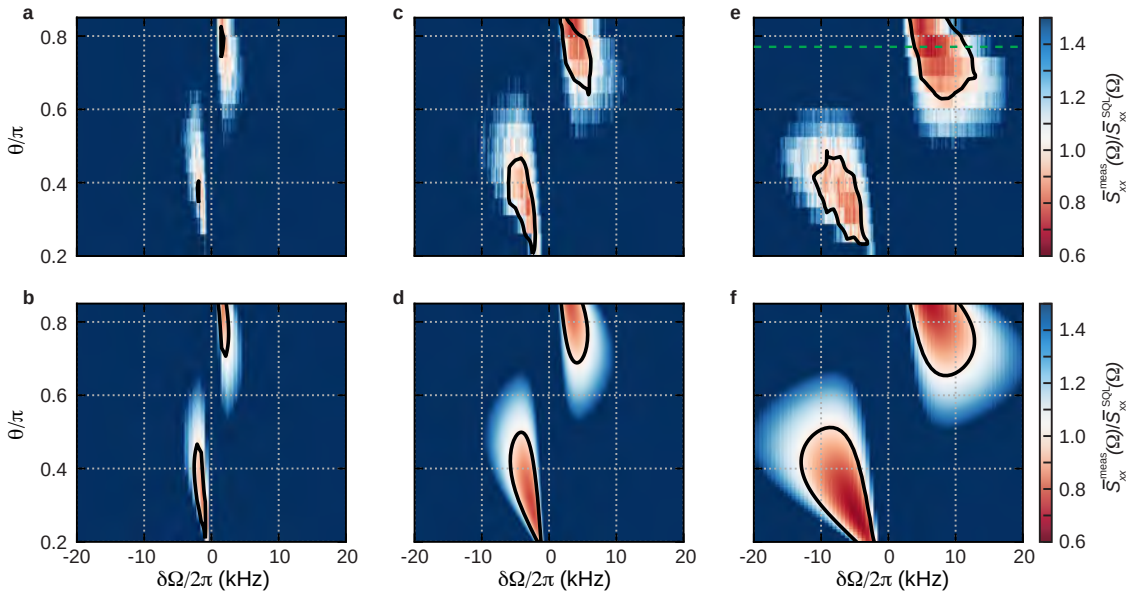

Figure 4.11: Broadband sub-SQL sensitivity A figure from [41]. **a,c,e.** measured ratio between displacement spectra and the SQL at $C_q = \{5.3, 10.2, 20.7\}$ respectively. The black line highlights the contour of ratio 1. **b,d,f.** The corresponding independent theoretical prediction.

as C_q increases, the bandwidth of the sensitivity improved region increases as well. The experimental data matches theoretical prediction well. The relatively large deviation at high C_q is a result of more prominent mirror noise, which can be inferred from the asymmetric behavior between high frequency and low frequency branches. This study demonstrates one of the easiest way to get broadband sensitivity improvement, increasing probe power.

In this subsection, the experimental result demonstrates the first displacement measurement overcoming the Standard Quantum Limit ever achieved.

4.3.5 Sub-SQL Force Measurement

We also demonstrate sub-SQL force sensitivity using the same system. As mentioned in Section 4.1, the force measurement is based on measurement of force induced displacement. Therefore, the experiment presented here is essentially the same story as the one for displacement. In force sensing case, if the signal-to-noise ratio (SNR) of the force sensing in a measurement exploiting variational readout is better than that given by the SQL, sub-SQL force sensitivity is achieved.

To generate a force to measure, we output a tone from a lock-in amplifier, and input it to the amplitude modulator. The radiation pressure force from the auxiliary beam then serves as a classical coherent force to measure. We scan the frequency of this tone through the mechanical resonance, and measure the response of the mechanical mode using the same homodyne setup as displacement sensing case, and analyze the AC voltage output from the detector using the lock-in amplifier. We conduct this scanning measurement twice with two different homodyne angles, where one is $\theta \approx \pi/2$, and the other is $\theta \approx 4\pi/5$. The latter corresponds to the best sub-SQL angle. The raw voltage responses are presented in Fig. 4.12 a, as light lines. The noise in force sensing experiment is given by the displacement noise without driving force, acquired in a similar way as displacement sensing. The raw voltage background noise spectra are plotted as dark lines. We can see from the figure that the force responses are parallel to each other, highlighting the same mechanical susceptibilities in these two cases. The lower response for $\theta \approx 4\pi/5$ case is a result of less sensitive displacement-to-optical-quadrature convertion factor $f_{\mathrm{imp}}(\Omega)$. The same conversion difference appears in the noise backgrounds, thus it has no effect on the signal-to-noise ratio. The quantum correlations suppress the displacement noise in the $\theta \approx 4\pi/5$ case, resulting in better signal to noise ratio.

Using the calibration tone technique, we can transduce the force response into displacement (absolute displacement unit in this case). By further dividing the calibrated displacement by the modulus square of the

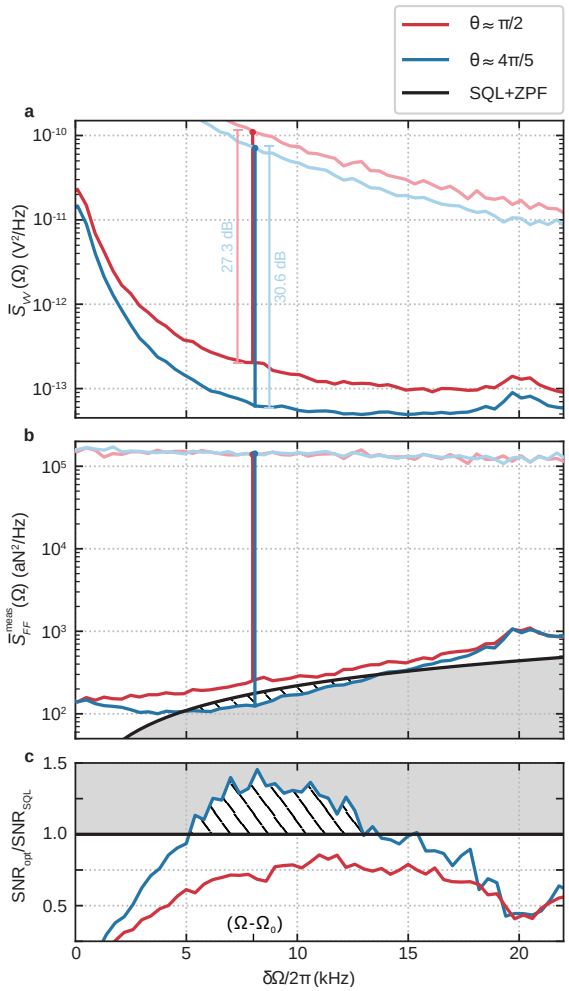

Figure 4.12: sub-SQL force sensing A figure from [41]. **a.** Raw force response (light lines) and raw displacement noise background (dark lines). The vertical lines highlights the signal-to-noise ratio of a sample frequency. **b.** Calibrated force spectra from a and the SQL for force sensing. **c.** The ratio between measured signal-to-noise ratios and the one given by the SQL.

effective mechanical susceptibility in absolute displacement unit $m^{-2}((\Omega_{\rm eff}^2-\Omega^2)^2+\Gamma_{\rm eff}^2\Omega^2)^{-2}$, we calibrate the mechanical responses into force spectra, as shown in Fig. 4.12 b. In the same panel, we also plot the calculated SQL for force sensing, as defined by Eqn. 2.80, but in absolute displacement unit. In this case, the transduction difference is countered perfectly by the calibration, such that the force spectra of the two homodyne angles overlap. This level authentically represents the spectrum of the applied force. We can see that the force noise background (converted from displacement noise background) of the $\theta \approx 4\pi/5$ case can be below the SQL (converted from the SQL in displacement case) in some frequency range. As the force signal is the same, and the noise background is below the SQL, the SNR in this range is better than the one given by the SQL. To illustrate this point more clearly, we plot the ratio between the measured SNR and the one given by the SQL in Fig. 4.12 c. Clearly, the blue trance can overcome the SQL for force sensing in some frequency range.

4.4 Conclusion

In this project, we demonstrate the first displacement and force measurement below the Standard Quantum Limit by exploiting the quantum correlations generated by the optomechanical interaction. This is a remarkable achievement half a century after the concept was proposed. Apart from the significance in fundamental

physics, the technique used in our work can be applied to gravitational detectors to enhance the sensitivity [40], and be used to decrease the final phonon occupancy in feedback cooling [104]. Variational readout is also compatible to the state of the art force sensing application [105], which can help improving the sensitivity as we have demonstrated. Moreover, as the force sensitivity is governed by the thermal force noise power spectral density [105]

$$S_{FF} = \frac{4mk_{\mathrm{B}}T\Omega_{\mathrm{m}}}{Q}, \tag{4.21}$$

the low mass (around 7 ng) and high quality factor provided by our soft-clamped membrane help getting high sensitivity. However, as we have emphasised, the sensitivity improvement in variational readout is off mechanical resonance, where the force sensitivity is lower than that on resonance. To make full use of the force sensitivity provided by the mechanical oscillator, we would like to have negative quantum correlations on mechanical resonance, which are not significant even with detuned probe beam for conventional interferometric measurement like homodyne and heterodyne. Fortunately, the synodyne detection introduced in Buchmann et al. [106] can unveil on mechanical resonance quantum correlations. In synodyne detection the local oscillator should contain two frequency components, one at $\omega - \Omega_{\mathrm{m}}$, and the other at $\omega + \Omega_{\mathrm{m}}$. Then the mechanical information is encoded in DC photocurrent. This has already been realized in microwave regime by Ockeloen-Korppi et al. [107]. However, due to difficulties like extracting information from DC photocurrent, synodyne has not been realized in optical regime yet. If we can solve the technical challenges, the high detection efficiency and large quantum backaction provided by our system can significantly enhance the force sensitivity on mechanical resonance, even below the Standard Quantum Limit.

Chapter 5

Optical-Optical Entanglement via Optomechanical Interaction

Quantum information processing in microwave regime is a rapid developing field, led by the advances of technology in superconducting qubits. However, propagation of microwave in cables or waveguides is very lossy, preventing distant quantum computation nodes in microwave regime communicating efficiently, as required by quantum network. One of the most realistic methods to extend the communication distance of MW quantum nodes is bi-directional conversion between quantum information in microwave frequency and optical frequency, preferably telecom frequency, where low loss optical fibers are available. As electromagnetic (EM) field at any frequency has radiation pressure, optomechanical interaction is insensitive to the frequency of the EM fields. This fact makes mechanical resonators a good candidate for the quantum transducer between MW frequency and optical frequency [108], which can convert quantum information between these two frequencies. In particular, membrane-in-the-middle cavity based system is one of the most advanced transducers [33, 34], though they still suffer from transducing efficiency and excess noises. Quantum transducer is still an outstanding goal for the community.

Apart from converting quantum states between microwave and optical frequencies, it is also interesting to have entanglement between them. By doing entanglement swapping operation on the optical part [109, 110], the distant microwave nodes can be entangled. This entanglement is important quantum information processing resource. Again, due to the interaction independent from EM frequency, mechanical oscillators are a good candidate for the purpose. Optomechanical interaction mediated entanglement was first proposed around 20 years ago [111]. In this chapter, we present a demonstration of mechanics mediated optical-optical entanglement, a solid step towards the vision of microwave-optical entanglement. Together with the recent report on mechanics mediated microwave-microwave entanglement [42], we pave the way to the entanglement between two EM fields at drastically different frequencies. In the microwave experiment, the entanglement is confined in the fridge [42]. When the entangled field is amplified by the detection chain, excess thermal noise introduced by the amplifiers destroys the entanglement. Therefore, the entanglement in the fridge has to be inferred from the room temperature detection record, with careful calibration. In contrast to its microwave counter part, the optical-optical entanglement demonstrated here survives until the detector, due to the high detection efficiency and the low noise detection chain in optical domain. Thus no assumption is needed to conclude the existence of entanglement.

5.1 Theory

In this section, we first introduce the criteria used to determine the existence of entanglement of continuous variables. Then we will discuss how a mode in these criteria can be extracted from a freely propagating optical field. Last, we will study how two optical modes can be entangled by optomechanical interaction to the same mechanical mode.

5.1.1 Inseparability

An inseparability criterion is usually a necessary condition for a multi-partite quantum state to be separable. In another words, violation of an inseparability criterion is a clear signature of quantum entanglement. Through out this thesis, we are dealing with continuous variables (CV). For CVs, typical inseparability criteria are defined with joint EPR type variable $\hat{X}_{\pm} = \hat{X}_A \pm \hat{X}_B$ and $\hat{Y}_{\pm} = \hat{X}_A \pm \hat{Y}_B$ [112, 113], with $\hat{X}_j$ and $\hat{Y}_j$ the amplitude and phase quadratures of mode j respectively.

Among the criteria, the first proposed and the most widely used one is DGCZ inseparability criterion introduced in Duan et al. [112]. The criteria states that a bipartite separable state must satisfy

$$\mathcal{I} = \frac{V(\hat{X}_+) + V(\hat{Y}_-)}{2} \geq 1, \tag{5.1}$$

where $V(\hat{O})$ represents the variance of the operator $\hat{O}$. To prove the existence of CV entanglement, one needs to find modes such that $\mathcal{I} < 1$.

5.1.2 Covariance Matrices

Though inseparability criterion indicates the existence of entanglement, the amount of violating the criterion is not necessarily proportional the amount of entanglement between the two parts of the system. To quantify the amount of entanglement, one needs an entanglement measure. An entanglement measure is a variable showing monotonic behavior as a function of amount of entanglement, preferably valid for both pure and mixed state.

For a Gaussian state, where all its quadratures follow Gaussian statistics, it is straight forward to extract an entanglement measure from its covariance matrix $\boldsymbol{\sigma}$. A covariance matrix is a matrix collecting all the covariances like

$$\sigma_{ij} = \frac{1}{2}\langle x_i x_j + x_j x_i \rangle - \langle x_i \rangle \langle x_j \rangle \tag{5.2}$$

of a bipartite state, where the vector $\mathbf{x} = \left(\hat{X}_A, \hat{Y}_A, \hat{X}_B, \hat{Y}_B\right)^{\mathrm{T}}$. This matrix can characterize all features of a Gaussian bipartite state. We can write the 4×4 matrix in a block form with three 2×2 matrices as

$$\boldsymbol{\sigma} = \begin{pmatrix} \boldsymbol{\alpha} & \boldsymbol{\gamma} \\ \boldsymbol{\gamma}^T & \boldsymbol{\beta} \end{pmatrix}. \tag{5.3}$$

$\boldsymbol{\alpha}$ and $\boldsymbol{\beta}$ describes individual subsystems, while $\boldsymbol{\gamma}$ describes correlations between them.

Entanglement information can be characterized by a single parameter $\tilde{\nu}_-$ related to the covariance matrix, which is the smaller symplectic eigenvalue of the partial transposed covariance matrix [114]. When $\tilde{\nu}_- < 1/2$, the quantum state is entangled. Moreover, smaller $\tilde{\nu}_-$ below 1/2 corresponds to larger amount of entanglement. In this sense, $\tilde{\nu}_-$ is a kind of entanglement measure, which is defined by

$$\tilde{\nu}_- = \sqrt{\frac{\Delta(\boldsymbol{\sigma}) - \sqrt{\Delta(\boldsymbol{\sigma})^2 - 4\mathrm{Det}\boldsymbol{\sigma}}}{2}}, \tag{5.4}$$

where $\Delta(\boldsymbol{\sigma}) = \mathrm{Det} + \mathrm{Det} - 2\mathrm{Det}$. This seemly complicated parameter has the physical meaning related to minimum value of DGCZ inseparability [115]:

$$\tilde{\nu}_- = \min \frac{\mathcal{I}}{2}, \tag{5.5}$$

where the minimization is over all local operations (such as rotation, squeezing on an individual subsystem). $\tilde{\nu}_-$ as a relatively unconventional entanglement measure is also related to the famous entanglement measure logarithmic negativity E_N [116] by $E_N = \max[0, -\ln(2\tilde{\nu}_-)]$.

5.1.3 Optical Modes from Propagating Fields

As shown in the above subsections, both inseparability $\mathcal{I}$ and symplectic eigenvalues of the partial transposed covariance matrix $\tilde{\nu}_-$ are dimensionless quantities, which infers the quadratures we are dealing with in these criteria are dimensionless as well. This is true for intracavity and mechanical modes. However, we do not

have direct access to these modes, but the output optical field. Due to input-output relation $\hat{a}_{\text{out}} = -\hat{a}_{\text{in}} + \sqrt{\kappa}\hat{a}$, the output field annihilation operator, thus so do amplitude and phase quadratures, has a dimension $\sqrt{\text{Hz}}$. This indicates that the output field should be treated properly to extract a well-defined optical mode. In this subsection, we are going to tackle this problem. More details of this discussion can be found in Zippilli et al. [115].

In general, a freely propagating continuous field $\hat{E}(z,t)$ with z the coordinator along the propagating axis and t the time, just as our output optical field, can be decomposed into the positive and negative frequency components $\hat{E}(z,t) = \hat{E}_+(z,t) + \hat{E}_-(z,t)$. In most of the cases, the interesting bandwidth of quantum field and the bandwidth of the detection aperture is much smaller than the laser frequency ω, thus we can approximate the frequency with the laser carrier frequency ω. Then the positive frequency component is given by

$$\hat{E}_+(z,t) = i\sqrt{\frac{\hbar\omega}{2\epsilon_0 c S}}e^{ikz}\hat{a}(t), \tag{5.6}$$

where ϵ_0 is the vacuum permittivity, c is the speed of light in vacuum, S is the mode cross section area, $k = \omega/c$ is the wave vector at laser frequency, and $\hat{a}(t)$ is the annihilation operator in time domain with commutation relation $[\hat{a}(t), \hat{a}^\dagger(t')] = \delta(t-t')$.

In practice, measurement only has access to a finite time interval of the continuous field, which defines a temporal mode. This time interval can be determined by pulsing the measurement beam, pulsing the local oscillator, cutting off the measurement, or filtering the measured record in post processing. Despite the physical implementation, all these processes can be described by applying a filter function $h_\tau(t)$ with time constant τ (therefore bandwidth $2\pi/\tau$) to the field, such that the mode is given by

$$\bar{a}_\tau(\Omega,t) = \int_{-\infty}^{\infty} e^{i\Omega s}h_\tau(t-s)\hat{a}_{\text{out}}(s)ds, \tag{5.7}$$

with $\{\bar{a}_\tau(\Omega,t)\}^\dagger = \bar{a}_\tau^\dagger(-\Omega,t)$.This temporal mode should be dimensionless as required by the motivation of this subsection. Therefore, $h_\tau(t)$ has the dimension of $\sqrt{\text{Hz}}$, as $\hat{a}_{\text{out}}(t)$ has the dimension $\sqrt{\text{Hz}}$ and ds has the dimension second. Moreover, normalization requires

$$\int_{-\infty}^{\infty} h_\tau^2(s)ds = 1. \tag{5.8}$$

Alternatively, one can express the filter function in frequency domain

$$\tilde{a}_\tau(\Omega,t) = \int_{-\infty}^{\infty} e^{-i(\Omega'-\Omega)t}\tilde{h}_\tau(\Omega'-\Omega)\tilde{a}(\Omega')d\Omega', \tag{5.9}$$

where $\tilde{O}(\Omega')$ represents the Fourier transformation of $\hat{O}(s)$.

An example of filter function $h_\tau(t)$ is when we turn on the measurement suddenly and completely at time t and turn it off suddenly and completely after a duration τ. The filter function is given by

$$h_\tau^{\text{step}}(t) = \frac{\Theta(t)-\Theta(\tau-t)}{\sqrt{\tau}},\ h_\tau^{\text{step}}(\Omega) = \sqrt{\frac{2\pi}{\tau}}e^{i\Omega\tau/2}\frac{\sin(\Omega\tau/2)}{\pi\Omega}, \tag{5.10}$$

where $\Theta(s)$ is Heaviside function.

This filter function is also the default window function of a Discrete Fourier Transformation (DFT), a method commonly used to get spectrum from a discrete string of data. The definition of which is as follows:

$$F_k = \sum_{n=0}^{N-1} f_n e^{-i2\pi kn/N}, k = 1,2,3,...,N-1 \tag{5.11}$$

where f_n is complex number, n is "time index" (suppose the data is taken in time domain), k is "frequency index". As DFT is not applied on an infinity length string, there is a cut off at Nth data point, represented by a window function. With the window function, one can extend the sum limit from $-\infty$ to $+\infty$:

$$F_k = \sum_{n=-\infty}^{\infty} f_n e^{-i2\pi kn/N}h(N-n), k = 1,2,3,...,N-1 \tag{5.12}$$

where we choose the notation of the window function to be h on purpose. If the number of data points is large, we can approximate the sum with a integral:

$$F(k) = \int_{-\infty}^{\infty} e^{ikt} h_\tau(\tau - t) f(t) dt, \tag{5.13}$$

which is exactly the same as Eqn. 5.7. Therefore, DFT of the propagating field defines a filtered optical mode. By default, this filter has a sudden cut off, which is described by $h_\tau^{\text{step}}(t)$.

So far, the temporal modes of propagation field is expressed in terms of annihilation operator, which is not an observable. Similar to the cavity mode case, we can define field quadratures as

$$\bar{X}_\tau(\Omega) = \frac{1}{\sqrt{2}} \left(\{\bar{a}_\tau(\Omega, t)\}^\dagger + \bar{a}_\tau(\Omega, t) \right) = \frac{1}{\sqrt{2}} \left(\bar{a}_\tau^\dagger(-\Omega, t) + \bar{a}_\tau(\Omega, t) \right) \tag{5.14a}$$

$$\bar{Y}_\tau(\Omega) = \frac{i}{\sqrt{2}} \left(\{\bar{a}_\tau(\Omega, t)\}^\dagger - \bar{a}_\tau(\Omega, t) \right) / \sqrt{2} = \frac{i}{\sqrt{2}} \left(\bar{a}_\tau^\dagger(-\Omega, t) - \bar{a}_\tau(\Omega, t) \right) / \sqrt{2}, \tag{5.14b}$$

which can be measured by homodyne detection. It is evident that each temporal mode quadrature contains two frequency components, one at Ω and the other at $-\Omega$, symmetrically opposite to DC. Each of these components can be treated as a mode itself. Therefore, a temporal mode quadrature of propagation field treated here is a composition of two sideband modes.

5.1.4 Three-Mode Optomechanics

Now, it is time to study the physical system. The three-mode model (two optical and one mechanical modes) is an easy generalization of the two mode version introduced in Section 2.3. The Hamiltonian in the frames rotating with the input laser frequencies is given by

$$\hat{H} = \frac{\hbar \Omega_{\text{m}}}{2} \left(\hat{Q}^2 + \hat{P}^2 \right) - \sum_j \hbar \Delta_j \hat{a}_j^\dagger \hat{a}_j - \sum_j \sqrt{2} \hbar g_{0j} \hat{a}_j^\dagger \hat{a}_j \hat{Q} + \sum_j i\hbar \sqrt{\kappa_{j,\text{L}}} \left(\alpha_{j,\text{in}} \hat{a}_j^\dagger + c.c. \right), \tag{5.15}$$

where $j = A, B$, representing optical modes A and B. In general, the vacuum optomechanical coupling rate g_{0j}, the cavity coupling rates $\kappa_{j,\text{L}}, \kappa_{j,\text{R}}, \kappa_j$ are different between mode A and B. Similar to the one optical mode case, the output fields of laser j is given by

$$\hat{X}_j^{\text{out}}(\Omega) = \sqrt{\eta_j \kappa_{j,\text{R}} \kappa_{j,\text{L}}} \left(u_j(\Omega) \hat{X}_j^{\text{in,L}}(\Omega) + v_j(\Omega) \hat{Y}_j^{\text{in,L}}(\Omega) \right) \tag{5.16a}$$

$$+ \sqrt{\eta_j} \kappa_{j,\text{R}} \left((u_j(\Omega) - 1/\kappa_{j,\text{R}}) \hat{X}_j^{\text{in,R}}(\Omega) + v_j(\Omega) \hat{Y}_j^{\text{in,R}}(\Omega) \right) + 2g \sqrt{\eta_j \kappa_{j,\text{R}}} v_j(\Omega) \hat{Q}(\Omega) + \sqrt{1 - \eta_j} \hat{X}_j^{\text{in},\eta}(\Omega)$$

$$\hat{Y}_j^{\text{out}}(\Omega) = \sqrt{\eta_j \kappa_{j,\text{R}} \kappa_{j,\text{L}}} \left(-v_j(\Omega) \hat{X}_j^{\text{in,L}}(\Omega) + u(\Omega) \hat{Y}_j^{\text{in,L}}(\Omega) \right) \tag{5.16b}$$

$$+ \sqrt{\eta_j} \kappa_{j,\text{R}} \left(-v_j(\Omega) \hat{X}_j^{\text{in,R}}(\Omega) + (u_j(\Omega) - 1/\kappa_{j,\text{R}}) \hat{Y}_j^{\text{in,R}}(\Omega) \right) + 2g \sqrt{\eta_j \kappa_{j,\text{R}}} u_j(\Omega) \hat{Q}(\Omega) + \sqrt{1 - \eta_j} \hat{Y}_j^{\text{in},\eta}(\Omega),$$

where η_j is the detection efficiency of mode j, $\hat{X}_j^{\text{in}}$ and $\hat{Y}_j^{\text{in}}$ are the corresponding vacuum noise operators, $\hat{Q}(\Omega)$ is given by

$$\hat{Q}(\Omega) = \chi_{\text{m}}(\Omega) \left(\sqrt{2\Gamma_{\text{m}}} \hat{P}_{\text{in}}(\Omega) + \sum_j 2 g_j \hat{X}_j(\Omega) \right), \tag{5.17}$$

where $\hat{X}_j$ is the intracavity amplitude quadrature of mode j, and the cavity quadrature susceptibilities are defined as

$$u_j(\Omega) = \frac{\kappa_j/2 - i\Omega}{\Delta_j^2 + (\kappa_j/2 - i\Omega)^2} \tag{5.18a}$$

$$v_j(\Omega) = \frac{-\Delta_j}{\Delta_j^2 + (\kappa_j/2 - i\Omega)^2}. \tag{5.18b}$$

The definition of homodyne in two mode case is the same as the one mode one, such that the detected propagating field is defined as

$$\hat{X}_j^{\theta_j}(\Omega) \equiv \hat{X}_j^{\text{out}}(\Omega)\cos\theta_j + \hat{Y}_j^{\text{out}}(\Omega)\sin\theta_j \tag{5.19a}$$

$$\hat{Y}_j^{\theta_j}(\Omega) = \hat{X}_j^{\theta_j+\pi/2}(\Omega) \tag{5.19b}$$

Optical Spectral

As discussed in Subsection 5.1.3, DFT defines filtered optical modes; thus we can extract the entanglement information of the modes by studying their spectra, which directly provide covariances.

The homodyne spectral of the detected fields can be written as

$$\bar{S}^{\text{out}}_{\hat{X}_j^{\theta_j}\hat{X}_k^{\theta_k}}(\Omega) = \frac{1}{2}\delta_{jk} + f_{jk}^{\text{imp}}(\Omega)\bar{S}_{\hat{Q}\hat{Q}}(\Omega) + \bar{S}_{jk}^{\text{cor}}(\Omega). \tag{5.20}$$

When $j = k$, the spectrum represents self correlation within an optical mode; while for $j \neq k$, the spectrum represents the cross correlation between two modes. The delta function δ_{jk} shows that shot noise only exists in self correlations. As an analogy to the single optical mode case, the mechanical spectrum is given by

$$\bar{S}_{\hat{Q}\hat{Q}}(\Omega) = |\chi_{\text{eff}}|^2(\Omega)\left(2\Gamma_A^{\text{qba}} + 2\Gamma_B^{\text{qba}} + 2\Gamma_{\text{m}}(\bar{n}_{\text{th}} + 1/2)\right), \tag{5.21}$$

where $\Gamma_j^{\text{qba}} = g_j^2\kappa_j(|u_j(\Omega)|^2 + |v_j(\Omega)|^2)$, and the effective susceptibility is

$$\chi_{\text{eff}}^{-1}(\Omega) = \chi_{\text{m}}^{-1}(\Omega) + \sum_j 4g_j^2 v_j(\Omega). \tag{5.22}$$

The transduction function is given by

$$f_{jk}^{\text{imp}} = \frac{\sqrt{\Gamma_j^{\text{meas}}\Gamma_k^{\text{meas}}}}{4}\text{Re}\left[e^{-i(\theta_j-\theta_k)}\zeta_{jk}(\Omega) - e^{-i(\theta_j+\theta_k)}\mu_{jk}(\Omega)\right], \tag{5.23}$$

and the quantum correlation term is given by

$$\bar{S}_{jk}^{\text{cor}}(\Omega) = -\frac{\sqrt{\Gamma_j^{\text{meas}}\Gamma_k^{\text{meas}}}}{4}\left(\text{Re}\left[\chi_{\text{eff}}(\Omega)\right]\text{Im}\left[e^{-i(\theta_j+\theta_k)}\mu_{jk}(\Omega)\right] + \text{Im}\left[\chi_{\text{eff}}(\Omega)\right]\text{Re}\left[e^{-i(\theta_j-\theta_k)}\xi_{jk}(\Omega)\right]\right). \tag{5.24}$$

The corresponding variables are

$$\Gamma_j^{\text{meas}} = \frac{4g_j^2}{\kappa_j}\eta_j\eta_{\text{c},j} \tag{5.25a}$$

$$\zeta_{jk}(\Omega) = \kappa_j\kappa_k\left(\chi_{\text{c},j}(\Omega)\chi_{\text{c},k}(\Omega)^* + \chi_{\text{c},j}(-\Omega)\chi_{\text{c},k}(-\Omega)^*\right) = \zeta_{kj}(\Omega)^* \tag{5.25b}$$

$$\mu_{jk}(\Omega) = \kappa_j\kappa_k\left(\chi_{\text{c},j}(\Omega)\chi_{\text{c},k}(-\Omega) + \chi_{\text{c},k}(\Omega)\chi_{\text{c},j}(-\Omega)\right) = \mu_{kj}(\Omega) \tag{5.25c}$$

$$\xi_{jk}(\Omega) = \kappa_j\kappa_k\left(\chi_{\text{c},j}(\Omega)\chi_{\text{c},k}(\Omega)^* - \chi_{\text{c},j}(-\Omega)\chi_{\text{c},k}(-\Omega)^*\right) = \xi_{kj}(\Omega)^*, \tag{5.25d}$$

where $\chi_{\text{c},j}(\Omega) = u_j(\Omega) - iv_j(\Omega)$ is the cavity field susceptibility, and $\eta_{\text{c},j}$ is the cavity outcoupling of mode j.

Now we can define the DGCZ inseparability spectrum as

$$\mathcal{I}(\Omega) = \frac{\bar{S}_{\hat{X}_+\hat{X}_+}(\Omega) + \bar{S}_{\hat{Y}_-\hat{Y}_-}(\Omega)}{2} = 1 + f_{\hat{Q}\mathcal{I}}(\Omega)\bar{S}_{\hat{Q}\hat{Q}}(\Omega) + \mathcal{I}_{\text{cor}}(\Omega), \tag{5.26}$$

where the EPR variables $\hat{X}_{\pm}(\Omega) = \hat{X}_A^{\theta_A}(\Omega) \pm \hat{X}_B^{\theta_B}(\Omega)$ and $\hat{Y}_{\pm}(\Omega) = \hat{Y}_A^{\theta_A}(\Omega) \pm \hat{Y}_B^{\theta_B}(\Omega)$, and

$$f_{\hat{Q}\mathcal{I}}(\Omega) = \frac{1}{4}\mathrm{Re}\left[\Gamma_A^{\mathrm{meas}}\zeta_{AA}(\Omega) + \Gamma_B^{\mathrm{meas}}\zeta_{BB}(\Omega) + 2\sqrt{\Gamma_A^{\mathrm{meas}}\Gamma_B^{\mathrm{meas}}}\mu_{AB}(\Omega)e^{-\imath 2\Theta}\right], \tag{5.27a}$$

$$\begin{aligned}\mathcal{I}_{\mathrm{cor}}(\Omega) =& -\mathrm{Im}[\chi_{\mathrm{eff}}(\Omega)]\mathrm{Re}\left[\frac{\Gamma_A^{\mathrm{meas}}\xi_{AA}(\Omega) + \Gamma_B^{\mathrm{meas}}\xi_{BB}(\Omega)}{4}\right] \\ &+ \mathrm{Re}[\chi_{\mathrm{eff}}(\Omega)]\mathrm{Im}\left[\frac{\sqrt{\Gamma_A^{\mathrm{meas}}\Gamma_B^{\mathrm{meas}}}\mu_{AB}(\Omega)e^{-\imath 2\Theta}}{2}\right],\end{aligned} \tag{5.27b}$$

where $\Theta = (\theta_A + \theta_B)/2$. The criterion of entanglement then follows as $\mathcal{I}(\Omega) < 1$.

Toy Model

To capture the physical feature of this inseparability spectrum, it is easier to go to the limit where $\kappa_j \gg \Omega_{\mathrm{m}}$ and on resonance lasers $\Delta_j = 0$ as in Subsection 2.9.1. To simplify the case furthermore, we assume $\Gamma_A^{\mathrm{meas}} = \Gamma_B^{\mathrm{meas}}$. Then the inseparability is given by

$$\begin{aligned}\mathcal{I}(\Omega) \approx \quad & 1 + 4\Gamma_{\mathrm{meas}}|\chi_{\mathrm{m}}(\Omega)|^2\left(2\Gamma_A^{\mathrm{qba}} + 2\Gamma_B^{\mathrm{qba}} + 2\Gamma_{\mathrm{m}}(\bar{n}_{\mathrm{th}} + 1/2)\right)(1 + \cos(2\Theta)) \\ & -4\Gamma_{\mathrm{meas}}\mathrm{Re}[\chi_{\mathrm{m}}(\Omega)]\sin(2\Theta).\end{aligned} \tag{5.28}$$

This form is highly similar to the squeezing spectrum Eqn. 2.87. Following the derivation in Subsection 2.9.1, it is not hard to show that the lower bound of this inseparability spectrum is

$$\mathcal{I}_{\mathrm{min}}(\Omega) = 1 - \frac{\eta_{\mathrm{meas}}^{\mathrm{tot}}}{2}, \tag{5.29}$$

where $\eta_{\mathrm{meas}}^{\mathrm{tot}}$ is the *total* measurement efficiency $\eta_{\mathrm{meas}}^{\mathrm{tot}} = 2\Gamma_{\mathrm{meas}}/\Gamma_{\mathrm{dec}}$. The 2 in denominator reflects the fact that we have two lasers, and the quantum backaction from one appears as an effective thermal noise for the other. This limits the lower bound of $\mathcal{I}(\Omega)$ to 1/2. Just like ponderomotive squeezing case, larger Γ_{meas} helps getting more prominent violation of DGCZ criterion.

We can also evaluate symplectic eigenvalue of partial transposed covariance matrix relatively easily in toy model, where the covariance matrix is given by

$$\mathbf{V} = \begin{pmatrix} \frac{1}{2} & 2\Gamma_{\mathrm{meas}}\mathrm{Re}[\chi_m(\Omega)] & 0 & 2\Gamma_{\mathrm{meas}}\mathrm{Re}[\chi_m(\Omega)] \\ 2\Gamma_{\mathrm{meas}}\mathrm{Re}[\chi_m(\Omega)] & \frac{1}{2} + 8\Gamma_{\mathrm{meas}}|\chi_m(\Omega)|^2\Gamma_{\mathrm{dec}} & 2\Gamma_{\mathrm{meas}}\mathrm{Re}[\chi_m(\Omega)] & 8\Gamma_{\mathrm{meas}}|\chi_m(\Omega)|^2\Gamma_{\mathrm{dec}} \\ 0 & 2\Gamma_{\mathrm{meas}}\mathrm{Re}[\chi_m(\Omega)] & \frac{1}{2} & 2\Gamma_{\mathrm{meas}}\mathrm{Re}[\chi_m(\Omega)] \\ 2\Gamma_{\mathrm{meas}}\mathrm{Re}[\chi_m(\Omega)] & 8\Gamma_{\mathrm{meas}}|\chi_m(\Omega)|^2\Gamma_{\mathrm{dec}} & 2\Gamma_{\mathrm{meas}}\mathrm{Re}[\chi_m(\Omega)] & \frac{1}{2} + 8\Gamma_{\mathrm{meas}}|\chi_m(\Omega)|^2\Gamma_{\mathrm{dec}} \end{pmatrix}, \tag{5.30}$$

where $\Gamma_{\mathrm{dec}} = \Gamma_A^{\mathrm{qba}} + \Gamma_B^{\mathrm{qba}} + \Gamma_{\mathrm{m}}(\bar{n}_{\mathrm{th}} + 1/2)$. Then $\tilde{\nu}_-(\Omega)$ can be calculated to be

$$2\tilde{\nu}_-(\Omega) = \sqrt{1 + 16\Gamma_{\mathrm{meas}}|\chi_{\mathrm{m}}(\Omega)|^2\Gamma_{\mathrm{dec}}\left(1 - \sqrt{1 + \frac{\mathrm{Re}[\chi_{\mathrm{m}}(\Omega)]^2}{4|\chi_{\mathrm{m}}(\Omega)|^4\Gamma_{\mathrm{dec}}^2}}\right)}. \tag{5.31}$$

To ensure significant effect from mechanics, it is reasonable for us to focus the vicinity of Ω_{m} such that $|\delta_{\mathrm{m}}| = |\Omega_{\mathrm{m}} - \Omega| \ll \Omega_{\mathrm{m}}$. Then the ratio in the inner square root $\mathrm{Re}[\chi_{\mathrm{m}}(\Omega)]^2/4|\chi_{\mathrm{m}}(\Omega)|^4\Gamma_{\mathrm{dec}}^2 \approx \delta_{\mathrm{m}}^2/\Gamma_{\mathrm{dec}}^2$. If $\Gamma_{\mathrm{dec}} \gg |\delta_{\mathrm{m}}|$, as can be routinely achieved in our system, we have $\sqrt{1 + \delta_{\mathrm{m}}^2/\Gamma_{\mathrm{dec}}^2} \approx 1 + \delta_{\mathrm{m}}^2/(2\Gamma_{\mathrm{dec}}^2)$. At the same time, for the same argument as in Subsection 2.9.1, we focus on $|\delta_{\mathrm{m}}| \gg \Gamma_{\mathrm{m}}$, such that we have the hierarchy $\Gamma_{\mathrm{m}} \ll |\delta_{\mathrm{m}}| \ll \Gamma_{\mathrm{dec}}$, we have the approximation $4|\chi_{\mathrm{m}}(\Omega)|^2 \approx 1/\delta_{\mathrm{m}}^2$. With all these approximations, $\tilde{\nu}_-(\Omega)$ can be simplified to

$$2\tilde{\nu}_-(\Omega) \approx \sqrt{1 - \frac{2\Gamma_{\mathrm{meas}}}{\Gamma_{\mathrm{dec}}}} = \sqrt{1 - \eta_{\mathrm{meas}}^{\mathrm{tot}}}. \tag{5.32}$$

The fact that $\tilde{\nu}_-(\Omega) = 0$ when $\eta_{\mathrm{meas}}^{\mathrm{tot}} \to 1$ shows arbitrary amount of entanglement is achievable when the measurement is highly efficient and strong.

5.1.5 Physical Interpretations of the Optical-Optical Entanglement

Generally speaking, entanglement is a consequence of quantum correlations. As illustrated in the beginning of Section 2.9, optomechanical interaction correlates the amplitude and phase quadratures of the intra-cavity field, which leads to ponderomotive squeezing. The optomechanical entanglement discussed above is a direct analogy to ponderomotive squeezing. Just in the latter case, the amplitude fluctuation of one field induced motion will not only modify the phase quadrature of itself, but also the phase quadrature of the other optical field. In this way, cross correlation is generated between the optical fields.

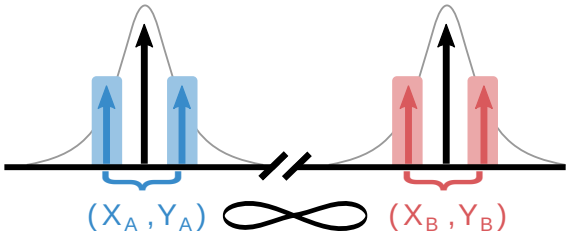

Figure 5.1: Optical modes in frequency domain A figure from [117]. Two mechanical sidebands of each laser form four initial optical modes, at different frequencies in spectrum. Homodyne measurement combines a pair of sidebands of one laser into a single optical mode. This work shows the entanglement between these combined modes, shown in blue and red for laser A and B respectively.

Firstly, let's summarize the composition of the entangled modes in frequency domain. Figure 5.1 provides an illustration. Recall Eqn. 5.14, each optical mode we are dealing with contains two sidebands of a laser frequency, which together gives a pair of amplitude and phase quadrature of the mode of interest. The two pairs of sideband modes at different laser frequencies are illustrated with blue and red colors respectively. Optomechanical interaction then mediates entanglement between these blue and red compound modes. Therefore, this interaction is a close analogy to the four-mode squeezing from Kerr non-linearity [118] but with delayed response function χ_{m}, which is distinct from the resolved-sideband treatment in the microwave paper [42]. This scenario was first studied in Giovannetti et al. [111], but at DC frequency. Later, a general case was discussed in Giannini et al. [119, 120].

The intensive mathematical discussion in the theory papers may hide the essential physics behind this optomechanical entanglement phenomenon. To further interpret this entanglement, we move to a simplified model. On the basis of the toy model used in Subsection 5.1.4, we further assume a one-sided cavity, where $\kappa_{j,\mathrm{L}} = 0$ and $\kappa_{j,\mathrm{R}} = \kappa_j$. In addition, we assume $\kappa_A = \kappa_B = \kappa$, then the output fields are given by

$$\hat{X}_j^{\mathrm{out}}(\Omega) = \hat{X}_j^{\mathrm{in}}(\Omega), \tag{5.33a}$$

$$\hat{Y}_j^{\mathrm{out}}(\Omega) = \hat{Y}_j^{\mathrm{in}}(\Omega) + 2\sqrt{\Gamma_{\mathrm{qba}}}\chi_{\mathrm{m}}(\Omega)\left(\sqrt{2\Gamma_{\mathrm{m}}}\hat{P}_{\mathrm{in}}(\Omega) + \sqrt{4\Gamma_{\mathrm{qba}}}(\hat{X}_A^{\mathrm{in}}(\Omega) + \hat{X}_B^{\mathrm{in}}(\Omega))\right). \tag{5.33b}$$

It is clear that self-correlation exists between amplitude and phase quadratures of the same mode, therefore we have ponderomotive squeezing in each mode. In this case, the amplitude fluctuation of the other mode serves as an effective thermal noise, which degrades the ponderomotive squeezing. At the same time, cross-correlation exists between amplitude quadrature of one mode (let's say mode A) and phase of the other (let's say mode B), and amplitude fluctuation from mode B serves as an effective thermal bath for this cross correlation. Fig. 5.2 **a** illustrates this dynamics.

Fig. 5.3 shows diagrams of quadratures in phase spaces of different basis. If we stay at local basis of cavity as illustrated in the first row of Fig. 5.3, which plot amplitude quadrature of one optical mode against its own phase quadrature, we can see clearly self-squeezing. However, cross correlation is hidden in this basis (e.g. correlation between $\hat{X}_A$ and $\hat{X}_B$). To get cross-correlations between $\hat{X}_A$ and $\hat{X}_B$, we measure these two quadratures simultaneously. The same applies for phase quadratures. To compare with DGCZ inseparability criterion, we can plot $\hat{X}_A$ against $\hat{X}_B$, and $\hat{Y}_A$ against $\hat{Y}_B$, in the so-called measurement basis, as shown in the third row of Fig. 5.3. The the variance along the diagonal direction is the variance of sum of the quadratures, while that along the anti-diagonal direction is the variance of difference. If we measure straight amplitude and phase quadratures, we do not get any squeezing, as can be expected from an analogy to one optical mode case. However, if we rotate to the optimal measurement basis, we can see the squeezing of the "X" sum quadrature variance below vacuum level, while the "Y" difference quadrature variance at

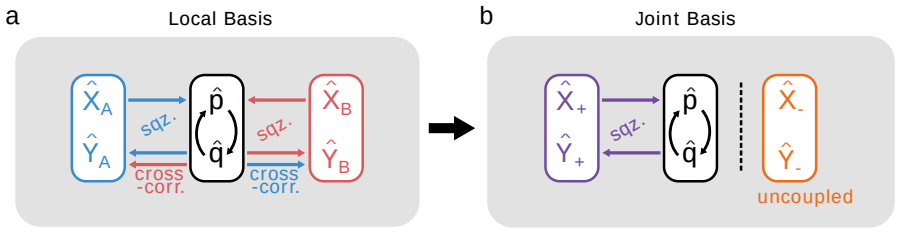

Figure 5.2: Dynamics in the Joint Mode Basis. A figure from [117] **a**, Schematic illustration of the couplings between the optical quadratures $(\hat{X}_A, \hat{Y}_A, \hat{X}_B, \hat{Y}_B)$ and mechanical position/momentum (q, p). Each laser generates self-squeezing as well as cross-correlations. **b**, Schematic illustration of the couplings after moving to the (non-local) joint basis $(\hat{X}_\pm = \hat{X}_A \pm \hat{X}_B, \hat{Y}_\pm = \hat{Y}_A \pm \hat{Y}_B)$. Here, there is only a self-squeezing of the sum-mode, while the difference-mode remains uncoupled from all system dynamics.

vacuum level, which gives $\mathcal{I} < 1$, indicating entanglement. If we keep rotating the measurement basis, we will observe breathing of both "X" sum quadrature and "Y" sum quadrature.

In the spirit of EPR variables, we can also interpret the entanglement in terms of joint quadratures $\hat{X}_\pm = \hat{X}_A \pm \hat{X}_B$ and $\hat{Y}_\pm = \hat{Y}_A \pm \hat{Y}_B$. Similar quadratures can be defined for noise operators and output fields. Then we can rewrite the dynamics as

$$\hat{X}_+^{\mathrm{out}}(\Omega) = \hat{X}_+^{\mathrm{in}}(\Omega), \tag{5.34a}$$

$$\hat{Y}_+^{\mathrm{out}}(\Omega) = \hat{Y}_+^{\mathrm{in}}(\Omega) + 4\sqrt{\Gamma_{\mathrm{qba}}}\chi_{\mathrm{m}}(\Omega)\left(\sqrt{2\Gamma_{\mathrm{m}}}\hat{P}_{\mathrm{in}}(\Omega) + \sqrt{4\Gamma_{\mathrm{qba}}}\hat{X}_+^{\mathrm{in}}(\Omega)\right), \tag{5.34b}$$

$$\hat{X}_-^{\mathrm{out}}(\Omega) = \hat{X}_-^{\mathrm{in}}(\Omega), \tag{5.34c}$$

$$\hat{Y}_-^{\mathrm{out}}(\Omega) = \hat{Y}_-^{\mathrm{in}}(\Omega). \tag{5.34d}$$

In this expression, only joint sum phase quadratures $\hat{Y}_+^{\mathrm{out}}(\Omega)$ and $\hat{Y}_+^{\mathrm{in}}(\Omega)$ are coupled to the mechanics. This leads to the ponderomotive squeezing of the joint sum mode. Please notice that this squeezing strength is twice of that of self-squeezing of individual modes. In the meanwhile, the joint difference mode is completely decoupled from the mechanics. This reproduces the dynamics of EPR variables [95], and is illustrated in the second row of Fig. 5.3. In the rotated joint basis, $\hat{X}_+$ has variance below vacuum, while $\hat{Y}_-$ has variance at vacuum level. Then the DGCZ inseparability $\mathcal{I} = (V(\hat{X}_+) + V(\hat{Y}_-))/2$ is clearly below 1, which demonstrates entanglement. In this way, the entanglement can be understood as ponderomotive squeezing of a joint mode.

5.2 Experiment

In the previous experiments, only one of the lasers was used for measuring the mechanical motion. In optical-optical entanglement, the transmitted fields of both of the lasers are detected with balanced homodyne setup, as shown in Fig. 5.4. To suppress second order mechanical sidebands, the lasers are slightly red detuned, which requires PDH lock. As we only have one fiber based phase modulator, we exploit the built-in EOMs of the lasers (see Section A.2 for more information) to apply the required phase modulation for PDH lock. The fiber based phase modulator is only used for cavity linewith measurement, optomechanically induced transparency calibration, and a benchmark for calibration tones generated by the laser EOMs. Feedback cooling is employed to suppress second order mechanical sidebands further, as in previous experiments. The feedback motional signal comes from Laser B, while the actuation force comes from radiation pressure of Laser A, through an amplitude modulator. In principle, this intensity modulation will appear in the homodyne spectrum of Laser A, acquire its own mechanical sidebands, and result in noise peaks in the band gap. However, in practice, this modulation is weak. Even the amplitude modulation tone itself is hard to be observed in the spectrum of Laser A, despite its mechanical sidebands. Therefore, the feedback cooling of low frequency modes is essentially the same as previous experiments.

We use the same membrane, but a slightly longer cavity (1.75 mm long, due to changing the broken 350 μm thick flat mirror spacer to a 500 μm thick one), compared to the previous experiments. As usual, a full system characterization is conducted to keep track of system parameter change. For the thermal cycle for

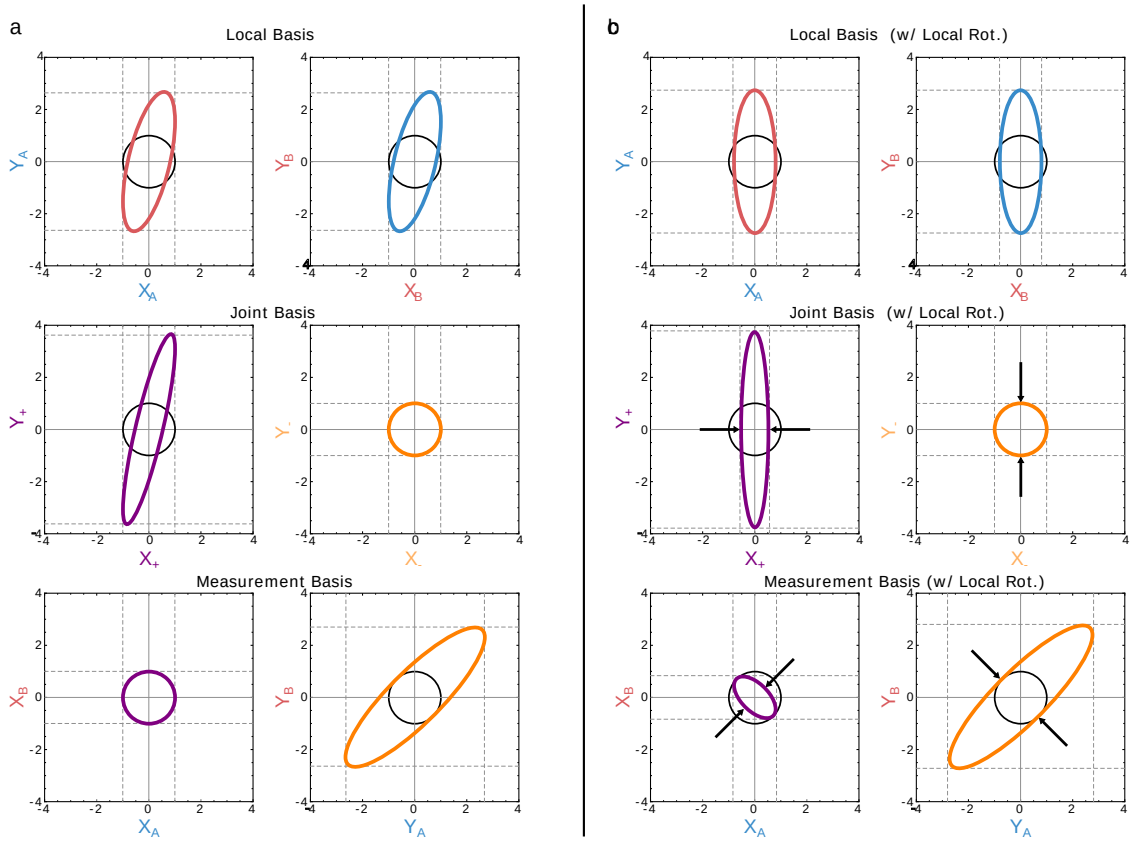

Figure 5.3: Entanglement in Phase Space. A figure from [117]. **a**, Different phase space portraits of the system correlations (i.e. different cuts of the 4-dimensional covariance ellipsoid). In all subplots, the black circle indicates vacuum noise, and the dashed lines indicate the marginal variances along each axis. The top row is in the (local) cavity quadrature basis, where each system simply exhibits self-squeezing. The middle row moves to the joint bases, where we see that the difference mode remain in vacuum, while the sum-mode displays self-squeezing (with a non-zero squeezing angle). We note that the squeezing of this joint quadrature is stronger than the sub-system self-squeezing. The bottom row corresponds to the ellipses we are able to directly measure in our system (i.e. simultaneous $\{\hat{X}_A, \hat{X}_B\}$ or $\{\hat{Y}_A, \hat{Y}_B\}$). **b**, Similar noise ellipses as in **a**, but with a local rotation of the A,B subsystems (i.e. $\theta_A = \theta_B \neq 0$). As a result, the joint-basis ellipses (middle row) are aligned such that we now see $V(X_+) + V(Y_-)$ will violate the DGCZ criterion, as indicated by the black arrows. In measurement basis, these variances are extracted from the diagonal/anti-diagonal variances (bottom row).

entanglement experiment, we have $\Omega_m/2\pi = 1.39\,\text{MHz}$, and $Q = 1.04\times10^9$. To get simultaneously high cavity out-coupling and relatively narrow cavity linewidth, we choose to work with wavelengths around 796 nm for both of the lasers. Laser A is at a wavelength 796.750 nm, and Laser B at 796.154 nm, corresponding to maximum coupling points in two adjacent 2kz periods. At these wavelengths, we have $\kappa_A/2\pi = 13.3\,\text{MHz}$ and $\kappa_B/2\pi = 12.6\,\text{MHz}$, narrower than previous experiments due to longer cavity. These cavity linewidths allow us to achieve quantum backaction rates of $\Gamma_A^{\text{qba}}/2\pi \approx 1.35\,\text{kHz}$ and $\Gamma_B^{\text{qba}}/2\pi \approx 0.89\,\text{kHz}$, which are much larger than the thermal decoherence rate $\Gamma_m(\bar{n}_{\text{th}}+1/2)/2\pi \approx 0.20\,\text{kHz}$ at 10 K, as required by significant entanglement.

To automize the measurement, we use the PI controller module of RedPitaya for homodyne path length lock, which also records V_{DC} of each lock. This voltage record is not influenced by the AC noises, therefore more accurate than reading from oscilloscope. By utilizing slope lock for most homodyne angles and dither lock for homodyne angles close to 0 and π, we can lock the homodyne angles at arbitrary values. Before each measurement run, we lock the homodyne angles at 0 and π to get peak-to-peak voltage. Together with the locking DC voltage, we can extract homodyne angles accurately. The photocurrents from homodyne detectors are low-pass filtered to suppress noise aliasing, and subsequently measured by a DAQ card, which

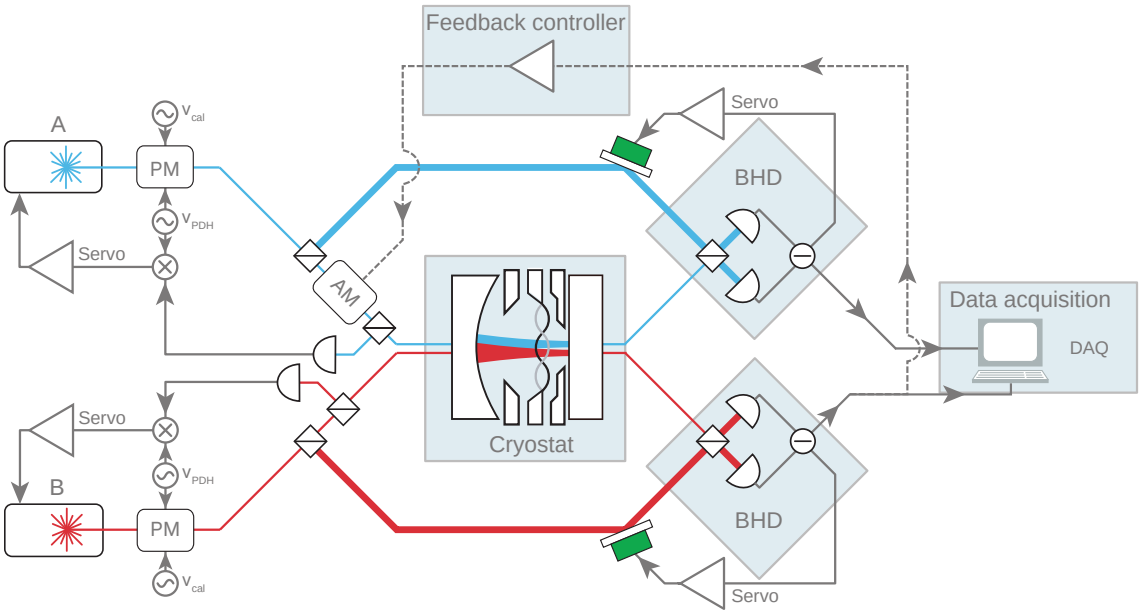

Figure 5.4: Setup for optical-optical entanglement The transmitted field of the two lasers are measured simultaneously via two homodyne detectors.

digitizes the voltage signal at a rate 15MSa/s using an analog-to-digital converter (ADC). Unlike in previous experiments, where the digital signal is directly fast Fourier transformed to get voltage spectrum, the photo current signals are recorded in the form of 140 chunks of 70-ms-long time traces in entanglement experiment, where the total measurement time sums up to around 10 s. As bandwidth as narrow as 14 Hz is not required, and we need more averages of a steady state spectrum, we divide the 70-ms-long time trace further into 9-ms-long chunks in post-processing.

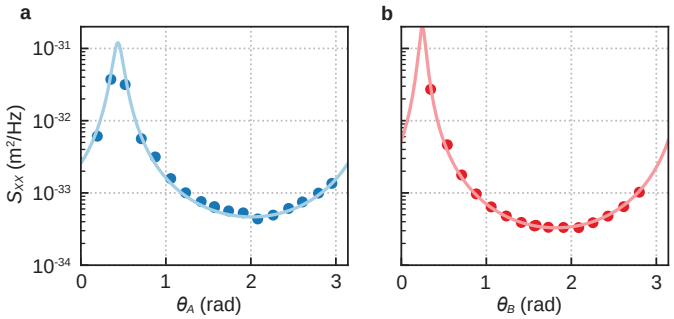

Figure 5.5: Imprecision displacement noise calibrations A figure from [117]. **a.** for Laser A. **b.** for Laser B.

Though the entanglement only depends on the sum of the homodyne angles of Laser A and Laser B, for conceptual simplicity, we choose a common basis of the two lasers in experiment, i.e. always having $\theta_A \approx \theta_B$. In an experimental run, we first measure time traces with $\theta_A \approx \theta_B \approx \Theta$, and then the orthogonal quadrature $\theta_A + \pi/2 \approx \theta_B + \pi/2 \approx \Theta + \pi/2$. After measuring the signal from optomechanical cavity, we block the signal beams and record shot noise for comparison. (When measure shot noise, path length lock has to be deactivated. Otherwise, the lock will try to compensate the voltage change by outputing maximum voltage to the piezo with mirror. The deformation of the piezo will mis-align the beam to the fiber, and cause a drop in LO power.) We scan the common first homodyne angle Θ from $-\pi/2$ to $\pi/2$, correspondingly the second common homodyne angle from 0 to π, and get 20 time traces equally spaced in phase. Applying fast Fourier transformation on each time traces, we can get self-correlation spectra as in sub-SQL experiment. From the calibration tones in these spectra and imprecision noise, we calibrate total

detection efficiencies to be $\eta_A^c \eta_A = 60\%$ and $\eta_A^c \eta_A = 77\%$, using the same technique presented in Subsection 4.3.2. We attribute he lower detection efficiency for Laser A to worse homodyne mode matching. The sum or difference between the time traces of the Laser A and Laser B photocurrents gives the cross correlations. The Fourier transformation of this sum or difference gives correlation spectra. To count the laser power drift happening during the measurement as mentioned in Subsection 4.3.3, we fit self and correlation spectra separately with free parameters optomechanical coupling rate g_j and detuning Δ_j, where $j = A, B$. An example of spectra in an experimental run is shown in Fig. 5.6, where fit and data match well, showing the explanation power of the model. The parameters for each experimental run is shown in Fig. 5.7. As all entanglement results will be compared to shot noise, to determine the existence of entanglement or declare the amount, the uncertainties in these parameters is not very crucial. In the meanwhile, noise background is calibrated to be shot noise limited with less than 1% uncertainty (see Subsection 3.6.2).

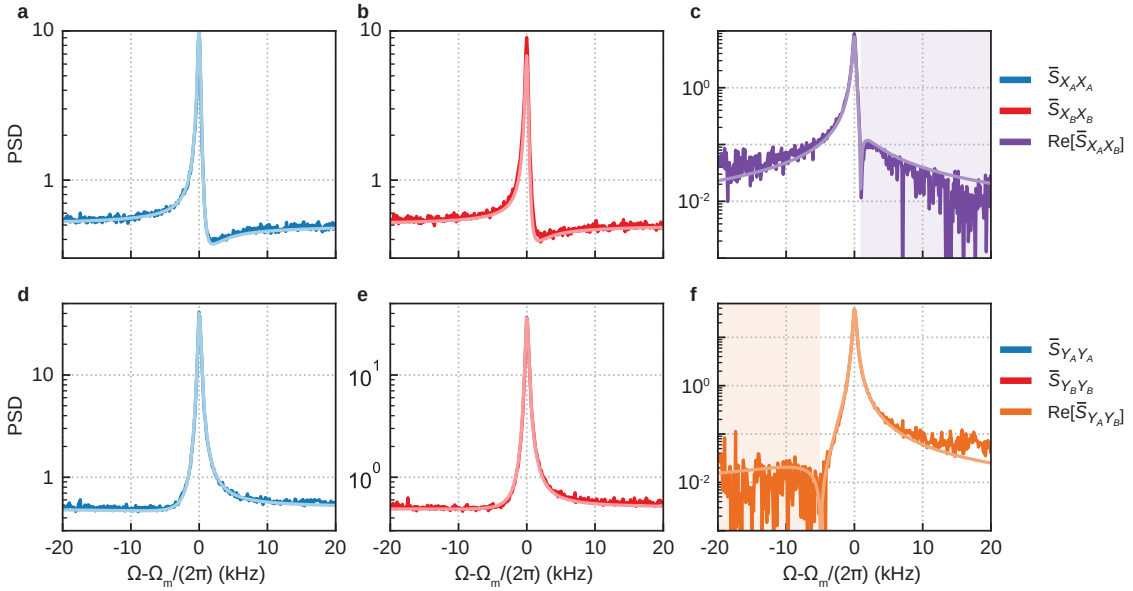

Figure 5.6: Spectra and fit A figure from [117]. **a,b,c** Normalized power spectral density at $\Theta \approx 0$ for Laser A, Laser B and cross correlation respectively. In this convention, vacuum noise is 1/2. The shadowed area in cross correlation PSD corresponds to negative value **a,b,c** The corresponding PSDs for orthogonal quadratures.

Now we are ready to calculate inseparability. To get a well-defined temporal optical mode as discussed in Subsection 5.1.3, we demodulate the time traces at a frequency $\Omega_{\text{mod}}/2\pi = 1.1416\,\text{MHz}$ with a low-pass filter with bandwidth 200 Hz. The choice of the demodulation frequency is to maximize the observed entanglement, and the low-pass filter bandwidth is much smaller than the mechanical features of bandwidth around $\Gamma_{\text{A}}^{\text{qba}}$ and $\Gamma_{\text{B}}^{\text{qba}}$, such that the modes do not smear important structures in frequency. From demodulation of time traces of Laser A and B in the first measurement, we get X_j^Θ quadratures, while from the second measurement Y_j^Θ quadratures. Inseparability is simply given by $\mathcal{I} = V(X_A^\Theta + X_B^\Theta) + V(Y_A^\Theta - Y_B^\Theta)$, which can be calculated straightforwardly. In Fig. 5.8 a, b, we plot 2D histograms of X_j^Θ quadratures and Y_j^Θ quadratures for $\Theta \approx 0$, the measurement displaying the minimum inseparability. In the histogram of X quadratures, we can see the squeezing below the vacuum noise level in diagonal direction, which represents the summation of the two quadratures $(X_A^\Theta + X_B^\Theta)/\sqrt{2}$. While in the histogram of Y quadratures, the variance in diagonal direction shows anti-squeezing. The variance in anti-diagonal directions of both histograms stays at vacuum fluctuation level. This direction represents the difference between the quadratures $(X_A^\Theta - X_B^\Theta)/\sqrt{2}$. As the two lasers share the same mechanical information, subtraction of the quadratures cancels the common mechanical information and left only vacuum fluctuation. Noticing that the inseparability is calculated by the summation of the sum of X quadratures and difference bewteen Y quadratures, inseparability is thus smaller than 1 for $\Theta \approx 0$, a clear indication of entanglement between two optical modes. Fig. 5.8 c shows the homodyne angle Θ dependence of the variances and the inseparability. The

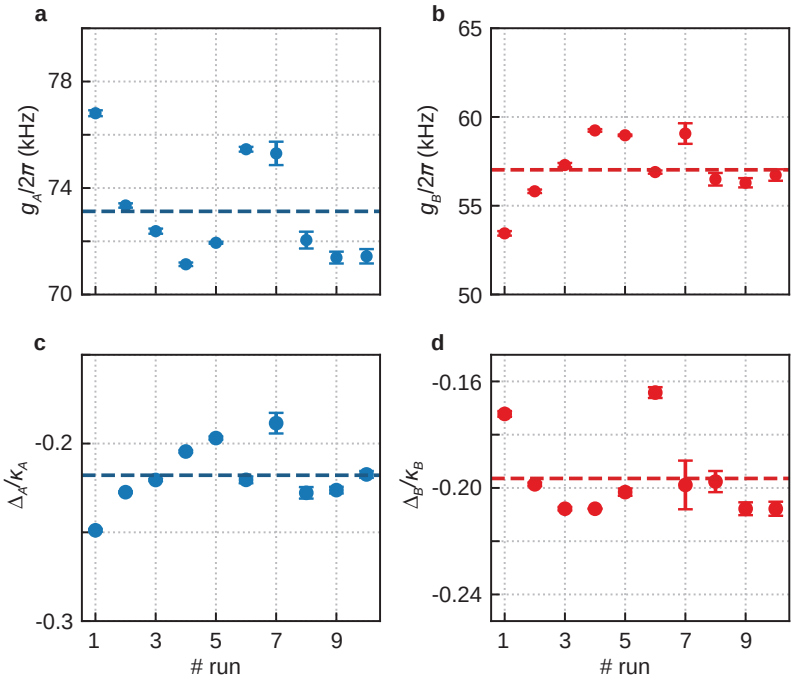

Figure 5.7: Fitted parameters A figure from [117]. **a,b** fitted optomechanical couplings for Laser A and B respectively. **c,b** fitted detunings for Laser A and B respectively. The error bars are a single standard deviation from the fits. The dashed lines are mean value of the parameters over all measurements.

difference variance, represented by the difference quadrature Y_- discussed in Subsection 5.1.5, is always at vacuum noise level, due to the perfect cancellation of common mechanical noise. While the sum variance experiences an oscillation, which represents the squeezing of the joint sum quadrature X_+. As we change Θ, we change the projection axis in the joint basis phase space diagram, and the variance oscillates as a result of squeezing. Because of constant difference quadrature and an oscillating sum quadrature, the observed inseparability also oscillates with Θ.

The minimum inseparability from this measurement is $\mathcal{I} = 0.83$, which is significantly below 1. As the measurement ensembles contain $\sim 10^4$ samples, the statistic error of $\mathcal{I}$ is confined to 1% level. Together with the less than 1% systematic error in vacuum noise calibration, our claim of entanglement has more than 7 standard deviations significance. This concludes the first observation of optical-optical entanglement through optomechanical interaction.

To extract the amount of entanglement, we need to reconstruct the covariance matrix using Gaussian homodyne tomography. In the tomography, we measure five pairs of homodyne angles $\{\theta_A, \theta_B\} = \{0,0\}, \{\pi/2, \pi/2\}, \{0, \pi/2\}, \{\pi/2, 0\}, \{\pi/4, \pi/4\}$ (notice that $\theta_A \neq \theta_B$ in general). The diagonal entries can be fully determined by the first two pairs. For the cross correlations, $\{0,0\}$ gives $\langle X_A X_B \rangle$ and its complex conjugate, $\{\pi/2, \pi/2\}$ gives $\langle Y_A Y_B \rangle$ and its complex conjugate, $\{0, \pi/2\}$ gives $\langle X_A Y_B \rangle$ and its complex conjugate, $\{\pi/2, 0\}$ gives $\langle Y_A X_B \rangle$ and its complex conjugate, $\{\pi/4, \pi/4\}$ gives $\langle X_A Y_A \rangle$ and $\langle X_B Y_B \rangle$ and their complex conjugates. Thus this measurement can fully characterize all co- and self-variances.

The independent entries of the covariance matrix is shown in Fig. 5.9 a, where data and theoretical prediction match reasonably well. The deviation mainly comes from optical power fluctuation as explained in the spectra fit. The matrix form of the covariance matrix is shown in Fig. 5.9. From these covariances, and using Eqn. 5.4, we can calculate the minimum simplectic eigenvalue of partial tranposed covariance matrix $2\tilde{\nu} = 0.79$, corresponding to a logarithmic negativity $E_N = 0.35$.

5.2.1 Frequency dependent entanglement

In the previous discussion, we ignored the frequency dependence of entanglement by focusing on optical modes at a certain frequency. However, as can be inferred from, for instance, Eqn. 5.26, entanglement has frequency dependence, mainly due to mechanical and optical susceptibilities. To study this frequency depen-

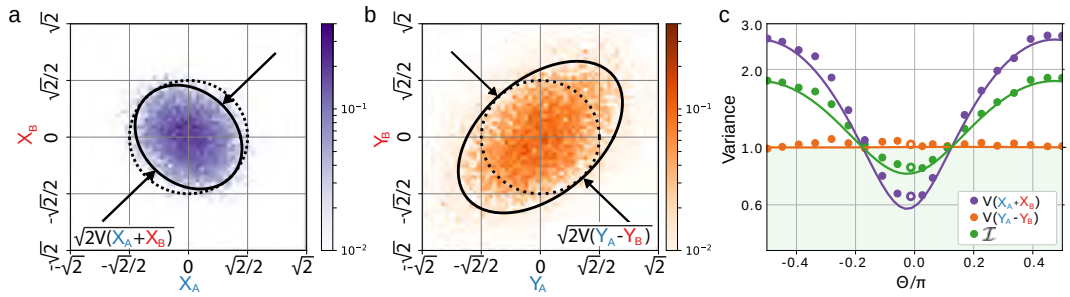

Figure 5.8: Inseparability A figure from [117]. **a,b.** 2D histograms for the first and second quadratures respectively for $\Theta \approx 0$. The dashed circles has the diameter $\sqrt{2}$, twice of the vacuum noise standard deviation. The solid elipses represent twice of the covariance ellipses. The scaling factor of 2 is aimed at having 95% of the points falling into the circles/ellipses. The arrows indicate the diagonal/anti-diagonal directions, which correspond to the sum and difference of quadratures respectively. Histogram variances along these directions are used to calculate inseparability directly. **c.** Variances of quadrature sum and difference, and inseparability as functions of homodyne angle Θ.

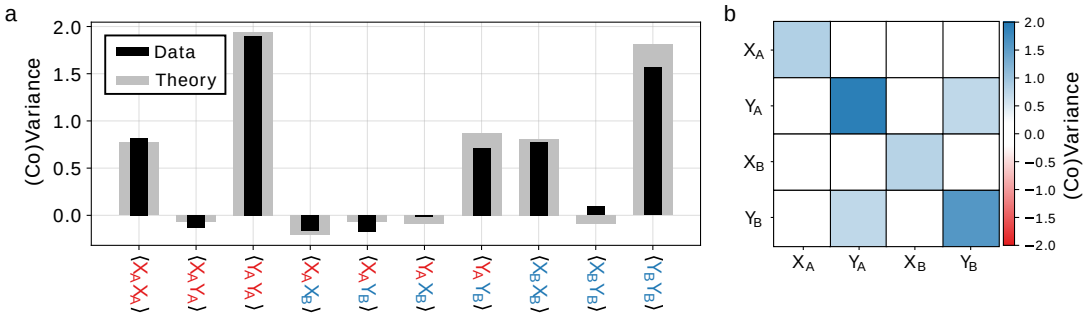

Figure 5.9: Covariance matrix A figure from [117]. **a.** Measured (black) and predicted (gray) entries of covariance matrix. **b.** Measured data in matrix form. The color coding is aimed at emphasis significant non-zero entries.

dence, we can continue with the demodulation analysis, and sweep the demodulation frequency. However, this task can be computing resource heavy. Alternatively, we can simply take DFT of the sum and difference time traces, which is equivalent to the demodulation method in defining optical mode, as illustrated in Subsection 5.1.3. In the latter case, the filter function $h(t) = (\Theta(t) - \Theta(\tau - t))/\sqrt{\tau}$, where $\Theta(t)$ is Heaviside function, and $\tau = 9$ ms is the measurement time.

The frequency dependence of entanglement is shown in Fig. 5.10. Panel a shows the spectra of X_+^Θ and Y_-^Θ at $\Theta \approx 0$, as an example. The average of these spectra gives the inseparability spectrum in panel b. In the same sub-figure, we also plot $2\tilde{\nu}$ extracted from experimental data. This quantity highlights a lower bound of inseparability, as expected. The full model fits in these panels show good match between model and data. Panel c and d show Θ and frequency dependence of inseparability. As the quantity has a period of π in Θ, we only plot Θ from $\pi/2$ to $\pi/2$. We observe good agreement between theory and experiment in this contour plot. The asymmetric inseparability between high frequency and low frequency parts in the experimental data is again a result of mirror noise. We do not explicitly display the dependence of entanglement bandwidth as a function of optical power, but the case is the same as sub-SQL: entanglement bandwidth is proportional to optical power.

Notice that the total bandwidth of entanglement is much larger than the demodulation bandwidth used in frequency independent entanglement study, the covariance matrix in that case does not contain all entanglement information. To quantify the total amount of entanglement achieved in the experiment, we calculate the entanglement of formation over a bandwidth containing all entanglement feature. The entanglement of formation has the physical meaning of number of entangled bits (ebits) needed to generate an entangled

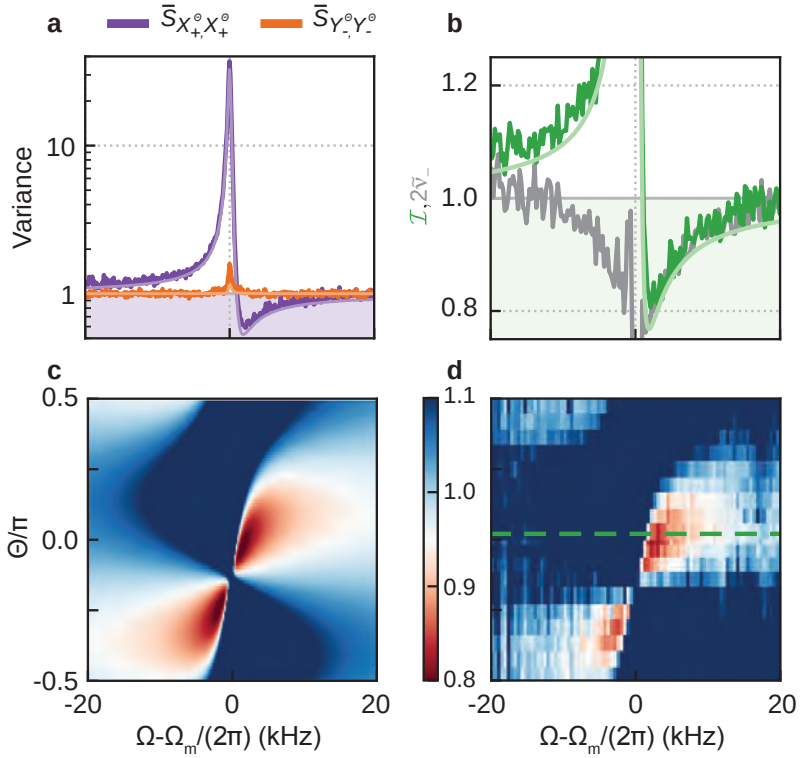

Figure 5.10: Frequency dependent entanglement A figure from [117]. **a.** normalized power spectral density of X_+^Θ and Y_-^Θ with $\Theta \approx 0$. **b.** Inseparability (green) at $\Theta \approx 0$ and $2\tilde{\nu}$ (gray). The solid lines in a and b are fits to the full model. **c,d.** Theoretical and experimental contour plots of inseparability respectively. The frequency axis is relative to the mechanical frequency. The green dashed line in d indicates the slice displayed in a and b.

state, where one ebit is defined by a maximally entangled two-qubit state (e.g. $|\Psi^-\rangle = (|01\rangle - |10\rangle)/\sqrt{2}$). This quantity is considered as a "proper measure of quantum correlations" [121]. For a symmetric Gaussian bipartite state, entanglement of formation is defined by [42, 122]

$$E_\mathrm{f} = c_+ log_2 c_+ - c_- log_2 c_-, \tag{5.35}$$

where $c_\pm = \left(\pm\sqrt{R} + 1/\sqrt{R}\right)^2/4$, with $R = 2^{-E_\mathrm{N}}$. We integrate E_f in a bandwidth of 30 kHz, and get an entanglement distribution rate of 753 ebits/s. The choice of the integration bandwidth is aiming at covering all frequencies showing $2\tilde{\nu} < 1$ in spectrum. Though the choice is a bit arbitrary, having a too wide bandwidth does not influence the result, as E_f in these frequency range is zero.

5.2.2 Entanglement between Highly Non-Degenerate Laser Beams

In the introduction of this chapter, we mentioned that the main selling point of this optical-optical entanglement through optomechanical interaction is the EM frequency independence. In the almost degenerate experiment, we demonstrate entanglement between two fields separated by 0.3 THz in frequency. To further demonstrate the frequency independence, we repeat the same experiment as shown in Fig. 5.10, but with Laser A at 912.024 nm (within the wavelength range of TiSaphire laser) and Laser B at 796.750 nm. The choice of 912 nm is a trade off between reasonably narrow cavity linewidth, high cavity out-coupling efficiency and large separation in laser frequencies. The wavelengths of the two lasers are separated by more than 120 nm. At 912.024 nm, the cavity linewidth is calibrated to be $\kappa_A/2\pi = 3.797$ MHz, which is comparable to mechanical frequency. In this case, toy model does not hold anymore, but the full model is still valid. This narrow cavity linewidth also decreases the optical power needed to achieve the same backaction rate dramatically. In this experiment, we keep $\Gamma_A^{\mathrm{qba}} \approx \Gamma_B^{\mathrm{qba}} \approx 2\pi \times 1$ kHz. The inseparability spectrum of the

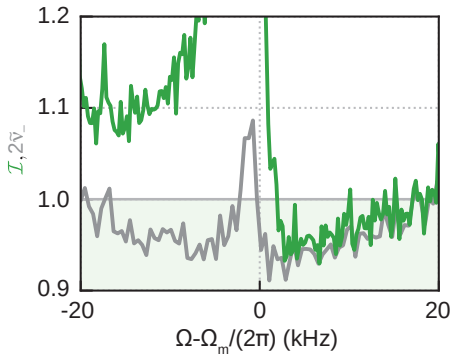

Figure 5.11: Highly non-degenerate entanglement A figure from [117]. The inseparability (green) and minimum symplectic eigenvalue $2\tilde{\nu}$ for two lasers separated by more than 120 nm in wavelength. The inseparability is at the best combination of homodyne angles.

best homodyne angle and reconstructed $2\tilde{\nu}$ are shown in Fig. 5.11, with the lowest value of $2\tilde{\nu} = 0.92 < 1$. Again, this measurement has a statistic error of around 1%, while systematic error due to deviation of noise background from vacuum is below 1% even further than the almost degenerate case, due to the low optical power used. Thus, this entanglement is statistically significant. One may notice that the amount of observed entanglement is less than the almost degenerate case, mainly due to worse cavity out-coupling efficiency, as a consequence of mirror coating. Please notice that, the reduced entanglement is at the detector, due to mixing in uncorrelated vacuum. The intra-cavity entanglement is not degraded significantly. To improve the detected entanglement at these wavelengths, one can exploit a mirror coating with two optimal reflectivities at the intended wavelengths. Nevertheless, this experiment demonstrates the EM frequency insensitive entanglement between EM fields.

5.3 Conclusion

In conclusion, we demonstrated the first optical-optical entanglement via optomechanical interaction. In contrast to the demonstration in microwave regime, the entanglement survives until the room temperature. In contrast to the traditional way of generating optical entanglement by optical parametric oscillators, the system demonstrating the first optical-optical entanglement [123, 124], mechanical oscillator can be integrated as a part of hybrid quantum system [18, 19, 32, 125], and can provide a coherent link between microwave and optical frequencies [33, 126]. By combining the technologies in microwave and optical regimes, we pave the way to microwave-optical entanglement.

Chapter 6

Feedback Cooling to Quantum Ground State

Strong and efficient measurement does not only allow us to overcome the Standard Quantum Limit and generating entanglement between two lasers, it also enables the first feedback cooling a mechanical oscillator to its quantum ground state, even only when conventional displacement measurement is implemented.

Cooling the mechanical oscillator to its quantum ground state is a prerequisite for many quantum protocols such as mechanical Fork state preparation [18, 20] and mechanical entanglement [22]. The ground state cooling methods fall in three categories. The first category employs a high frequency mechanical oscillator, usually in GHz range, and a fridge (for instance a dilution fridge) enabling temperature lower than 100 mK. This setting allows the mechanics to be cooled down to motional ground state passively [127]. However, dilution fridge is extremely pricy, and operating optics at such a low temperature is in no way trivial. The second category exploits sideband cooling introduced in Section 2.7, and ground state cooling using this approach has been achieved almost 10 years ago [12, 13, 58]. The final occupancy is limited by the backaction, thus, sideband resolution $\Omega_{\mathrm{m}} \gg \kappa$ is required to achieve low occupancy, which is hard for many optomechanical systems. Moreover, if the reflectivities of the cavity mirrors are kept the same, the only way to decrease κ is to make the cavity longer, which sacrifices the vacuum optomechanical coupling g_0. The third category is feedback cooling, which does not require sideband resolution. Feedback cooling of a mechanical oscillator is a cooling procedure where the measured displacement is treated as error signal, and a feedback loop is used to cancel the displacement to achieve the goal of cooling the mechanics. Over the past 20 years, feedback cooling has been implemented on systems from as small as trapped atoms [128] and ions [129], to larger ones like nano- and micro-particles [130, 131], cantilevers [132, 133], nanomechanical resonators [134, 135], to as large as test masses of gravitational wave detectors [136, 137]. However, none of them has reached occupancy smaller than 1, a widely accepted condition for successful ground state cooling. (In this case, the mechanical mode spend more than half of the time in ground state.) The closest attempt was described in Wilson et al. [135], where they achieved a final occupancy of 5 phonons. The failure of reaching ground state can be summarized as too low overall measurement efficiency η_{meas}. Because the ultimate limit of feedback cooling is given by the conditional state occupancy $\bar{n}_{\mathrm{est}}$ [43, 102]. As illustrated in the end of Section 4.2, the high quality measurement provided by our system can solve this problem, by providing a close-to-zero conditional state occupancy.

6.1 Theory

The scheme of feedback cooling is shown in Fig. 6.1. There are two stochastic forces thermal force F_{th} and quantum backaction force F_{ba} acting on the mechanics. As their roles are the same, we note their sum as F_{bath} for simplicity. These forces are transduced into dimensionless mechanical motion Q through mechanical susceptibility $\chi_{\mathrm{m}}(\Omega)$. The dimensionless detected motion is described by $y = Q + Q_{\mathrm{imp}}$, where Q_{imp} is the imprecision displacement, as quantum correlation is absent when we detect the optical phase quadrature. The controller takes y as error signal and output a feedback force $F_{\mathrm{fb}}(\Omega) = h_{\mathrm{fb}}(\Omega)y(\Omega)$ to try to make $y = 0$, where h_{fb} is the transfer function from y to feedback force. This function is proportional to a feedback gain g_{fb} with dimension Hz (proportional to dimensionless proportional gain), and typically

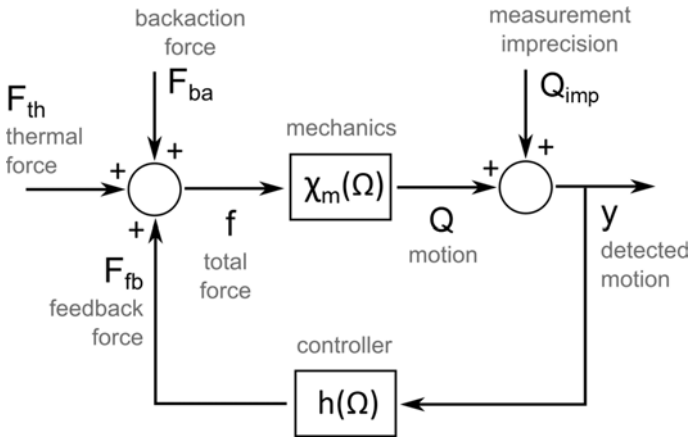

Figure 6.1: Scheme of feedback cooling

contains a low-pass/band-pass filter to limit the feedback bandwidth. Then the dynamics of this closed cycle system is given by

$$Q(\Omega) = \chi_{\mathrm{m}}(\Omega)(F_{\mathrm{bath}} + h_{\mathrm{fb}}(\Omega)y(\Omega)) \tag{6.1a}$$

$$y(\Omega) = Q(\Omega) + Q_{\mathrm{imp}}(\Omega). \tag{6.1b}$$

Solving for Q and y, we have

$$Q(\Omega) = \frac{\chi_{\mathrm{m}}(\Omega)}{1 - h_{\mathrm{fb}}(\Omega)\chi_{\mathrm{m}}(\Omega)}(F_{\mathrm{bath}}(\Omega) + h_{\mathrm{fb}}(\Omega)Q_{\mathrm{imp}}(\Omega)) \tag{6.2a}$$

$$y(\Omega) = \frac{\chi_{\mathrm{m}}(\Omega)F_{\mathrm{bath}}(\Omega) + Q_{\mathrm{imp}}(\Omega)}{1 - h_{\mathrm{fb}}(\Omega)\chi_{\mathrm{m}}(\Omega)}. \tag{6.2b}$$

Comparing this expression of Q to $Q(\Omega) = \chi_{\mathrm{m}}(\Omega)F(\Omega)$, we notice that the feedback process changes the mechanical susceptibility to an effective one

$$\chi_{\mathrm{fb}}(\Omega) = \frac{\chi_{\mathrm{m}}(\Omega)}{1 - h_{\mathrm{fb}}(\Omega)\chi_{\mathrm{m}}(\Omega)}. \tag{6.3}$$

For some proper choice of h_{fb}, this effective susceptibility can be broader and lower than the original one, which damps the mechanics and cools it down. For example, if we introduce a $\pi/2$ phase delay in the feedback transfer function, we can have $h_{\mathrm{fb}}(\Omega) = -ig_{\mathrm{fb}}\Gamma_{\mathrm{m}}\Omega/\Omega_{\mathrm{m}}$ [135], which provides a damping force inversely proportional to the velocity of the oscillator. As a result, the effective susceptibility will be given by

$$\chi_{\mathrm{fb}}(\Omega) = \frac{\Omega_{\mathrm{m}}}{\Omega_{\mathrm{m}}^2 - \Omega^2 - i\Gamma_{\mathrm{m}}(1 + g_{\mathrm{fb}})\Gamma_{\mathrm{m}}\Omega}, \tag{6.4}$$

which is simply mechanical susceptibility with mechanical linewidth $(1 + g_{\mathrm{fb}})\Gamma_{\mathrm{m}}$, a factor of $1 + g_{\mathrm{fb}}$ broader than the case without feedback. In the low gain limit, i.e. $h_{\mathrm{fb}} \ll F_{\mathrm{bath}}/Q_{\mathrm{imp}}$, this broadening effect is exactly the same as that the optical damping caused by sideband cooling, which decreases phonon occupancy. However, increasing gain does not always mean lower occupancy. If we have a look at Eqn. 6.2a, the imprecision displacement, uncorrelated to the real mechanical motion, will also be transduced into feedback force, resulting in heating. When $h_{\mathrm{fb}} \gg F_{\mathrm{bath}}/Q_{\mathrm{imp}}$, this heating could be the dominant source of mechanical motion, and essentially leads to higher occupancy. In the meanwhile, the detected displacement y decreases monotonically with feedback gain, which can even be below the imprecision level. This effect is called noise squashing. Cooling the detected spectrum down to imprecision level corresponds to the coolest mechanical mode.

The phonon occupancy should in principle be calculated based on the variances of displacement and momentum and their zero point fluctuations

$$\bar{n} = \frac{1}{2}\left(\langle \delta P^2 \rangle + \langle \delta Q^2 \rangle - 1\right), \tag{6.5}$$

because the equipartition condition does not hold for feedback cooling in general. However, when the feedback bandwidth is limited, the equipartition condition can be considered valid, and we can calculate phonon occupancy by

$$\bar{n} \approx \int_0^\infty \bar{S}_{QQ}(\Omega)\frac{d\Omega}{2\pi} - \frac{1}{2}, \tag{6.6}$$

which can be inferred from the in loop spectrum $\bar{S}_{yy}(\Omega)$.

6.2 Experiment

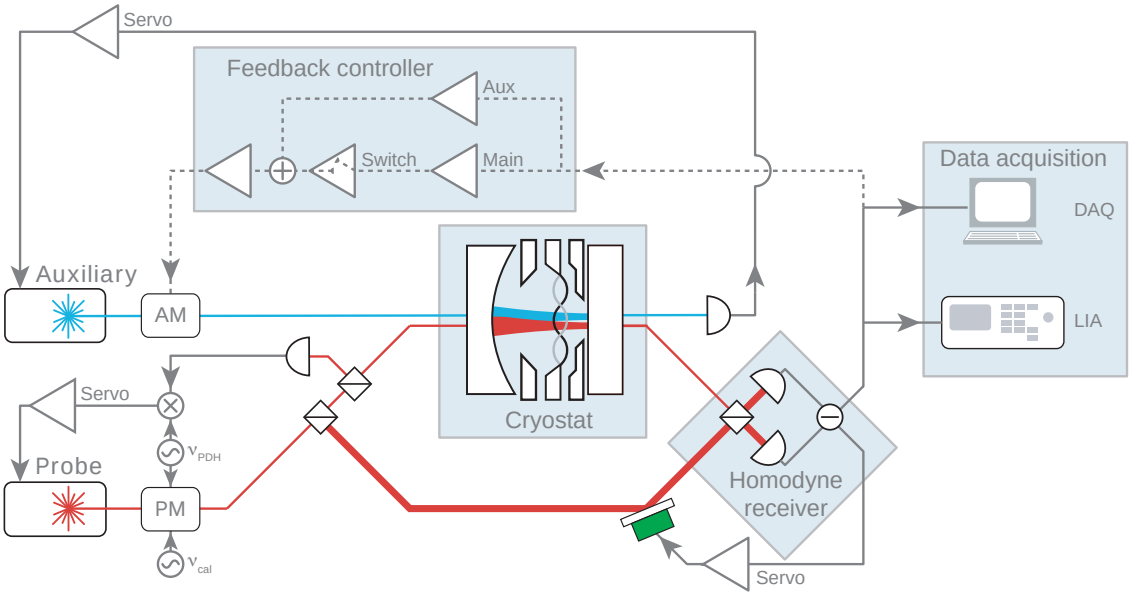

Figure 6.2: Experimental setup for feedback cooling A figure from the supplementary information of [8].

The experimental setup is shown in Fig. 6.2. The optical parameters are the same as those presented in Section 4.2. The probe laser is locked to the cavity on resonance using a PDH lock setup, and the auxiliary laser is slope locked to the red side of the cavity. The transmitted probe field is detected by a banlanced homoyne detector. This output is fed to a data acquisition card for spectral analysis (FFT in this case) and an FPGA (RedPitaya) for generating feedback cooling signal. We use the built-in IQ module in an open source software module (PyRPL) to conduct this analysis. The output of the FPGA is input to an amplitude modulator, which modulates the amplitude of the auxiliary laser. Thus the radiation pressure of this beam can serve as actuation force in feedback cooling on the membrane.

As can be noticed from Subsection 6.1, the choice of feedback transfer function h_{bf} is crucial for the purpose of feedback cooling. In practice, as we have multiple modes in our system, this choice is even more subtle. As mentioned in Section 4.2, we need to feedback cool some of the low frequency modes of the whole membrane in addition to the mode of interest. Therefore, the total transfer function is a summation of the main transfer function and 8 auxiliary ones, each at a different center frequency. The number of feedback channel is limited by that available in 3 RedPitayas. In principle, there is no upper bound for this number. In our case, the transfer function is chosen to be [8]

$$h_{\mathrm{fb}}(\Omega) = h_{\mathrm{main}}(\Omega) + h_{\mathrm{aux}}(\Omega) = g_{\mathrm{fb}} e^{i\Omega\tau - i\phi}\left(\frac{\Gamma_{\mathrm{fb}}\Omega}{\Omega_{\mathrm{fb}}^2 - \Omega^2 - i\Gamma_{\mathrm{fb}}\Omega}\right)^2 + h_{\mathrm{aux}}(\Omega), \tag{6.7}$$

where the main transfer function is generated by demodulation at Ω_{fb}, low-pass filter the demodulated signal with a forth order low pass filter with bandwidth Γ_{fb}, and remodulate the signal. The propagation of RF signal in cables, the processing time of the FPGA, and the response time of the cavity introduce a time delay τ

between the feedback force and displacement signal, which introduces a frequency dependent phase $e^{i\Omega\tau}$ to the transfer functions. In the spirit of providing damping force, we choose the demodulation phase ϕ, such that the argument of the main filter around mechanical frequency $\arg(h_{\rm main}(\Omega_{\rm m})) \approx \pi/2$. Any total phase from 0 to π leads to cooling of the mechanical mode, while phase from π to 2π leads to excitation. Due to the existence of time delay, a good phase for cooling the defect mode of interest is always an excitation phase for some other modes probably outside the band gap. To limit the gain at these frequencies, such that they do not experience self-oscillation, the low-pass filter in FPGA is necessary. In real experiment, the bandwidth of this filter is $\Gamma_{\rm fb}/2\pi = 77.78\,$kHz. As the filter phase changes dramatically around the resonance of the band-pass filter, to get a nearly homogeneous feedback phase over the mechanical mode, we choose the center frequency of the main filter to be $\Omega_{\rm fb}/2\pi = 1.195\,$MHz, which is higher than the mechanical frequency $\Omega_{\rm m}/2\pi = 1.14\,$MHz. The idea of choosing auxiliary filters is the same as the main one.

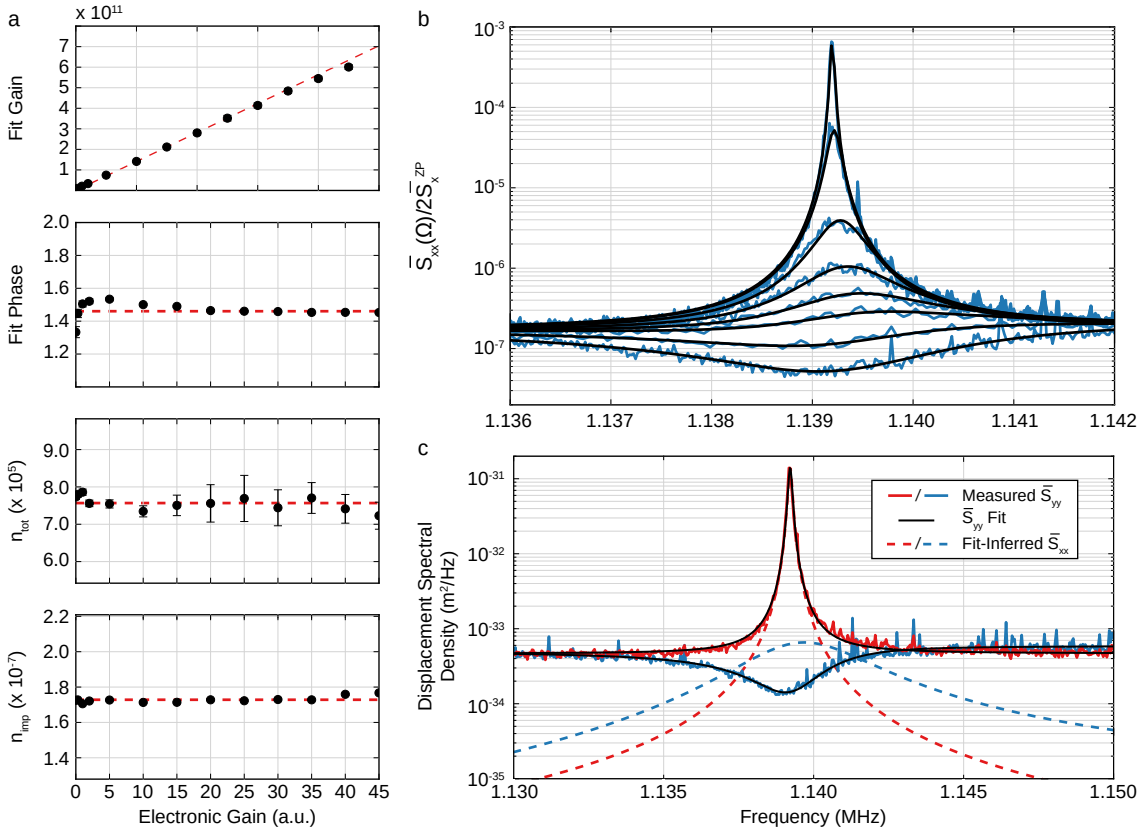

Figure 6.3: Fitting of feedback results A figure from the supplementary information of [8]. **a.** Fitted feedback gain $g_{\rm fb}$, fitted demodulation phase ϕ, fitted total bath occupancy $\bar{n}_{\rm tot}$, and fitted imprecision occupancy $\bar{n}_{\rm imp}$ as a function of electronic gain set by the FPGA. **b.** The detected mechanical spectra and their fits at different electronic gain. From top to bottom, the electronic gain increases. **c.** The spectra and fits at minimum and maximum electronic gain in this series (solid lines), plot together with the fit inferred real displacement spectra (dashed lines).

The spectra of detected displacement and their fitting during feedback cooling is shown in Fig. 6.3 b, where spectra with different feedback gains are plot together. When the gain is low, the mechanical spectrum is sharp and tall, corresponding to large occupancy. As we increase the feedback gain, the mechanical peak becomes broader, shorter and cooler. The coolest mechanical mode is available when the spectrum is cooled down to the imprecision level. Increasing feedback gain further, the spectrum goes into squash regime, corresponding to hotter mechanical mode. The real mechanical spectrum inferred from the fit of the detected spectrum is displayed in Fig. 6.3 c as dashed lines. In squashing regime, the tails of the real mechanical motion peak are significantly higher than those of low gain case, due to feeding back uncorrelated imprecision noise. This illustrates visually the heating in squashing regime. The fitted feedback gain $g_{\rm fb}$,

demodulation phase ϕ, total bath occupancy $\bar{n}_{\mathrm{tot}}$, and imprecision occupancy $\bar{n}_{\mathrm{imp}}$ are shown in Fig. 6.3 a, as a function of electronic gain set by the FPGA. Among which, g_{fb} is expected to have a linear increasing as electronic gain increases, whose behavior matches the expectation well. All other parameters are expected to keep constant as electronic gain changes. They follow the expectation as well. Though we do not check the phonon occupancy independently using a separate beam, and only infer it from the model, the good agreement between fitting and experiment provides confidence on the results.

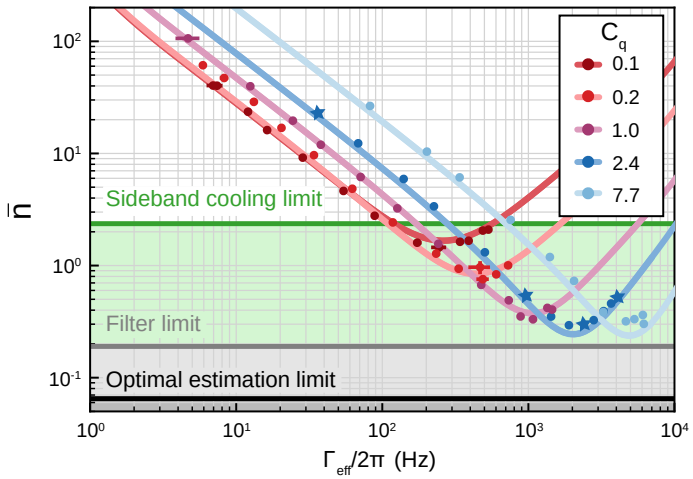

Figure 6.4: Final occupancy at different C_q A figure from [8]. The horizontal axis is the effective mechanical linewidth, a quantity proportional to feedback gain.

We conduct feedback cooling series at different C_q's, and the occupancies are shown in Fig. 6.4. All of the series can reach squashing regime, which results in the "Nike" shapes. The solid lines are independent theoretical predictions, which match the experimental results well. Generally, the lowest occupancy in one series decreases as C_q increases, as η_{meas} increases with C_q. The saturation at high C_q's is a sign of detection efficiency becoming the bottle neck of η_{meas}. The lowest occupancy is $\bar{n} = 0.29 < 1$, which is the first demonstration of feedback cooling a mechanical oscillator to its quantum ground state. All of the cooling series goes beyond the sideband cooling limit given by Ω_{m} and κ, demonstrating the distinct mechanism of feedback and sideband cooling. The filter limit corresponds to the best state estimation provided by our choice of feedback transfer function. Our result approaches this limit closely. While the optimal estimation limit corresponds to Eqn. 4.8, where the optimal estimation method is used, which is discussed in detail in reference [82]. The deviation of our result from this limit shows the room of improvement in engineering the filter.

This first demonstration of feedback cooling a mechanical oscillator to its quantum ground state opens the door to various of measurement-based quantum control protocols.

Chapter 7

Conclusion and Outlook

In this thesis, we introduced a membrane-in-the-middle system with soft-clamped Si_3N_4 membranes, which has the unique property of simultaneous satisfaction of strong backaction and high detection efficiency. This feature enables quantum limited displacement measurement of the membrane motion. Making use of this clean measurement record, we achieved first feedback cooling of a mechanical resonator to its quantum ground state. In Chapter 4 and 5, by exploiting the optomechanically induced quantum correlations, we demonstrated the first displacement and force measurement below the Standard Quantum Limit and the first mechanically induced entanglement between two optical fields. And although we have achieved a number of remarkable results, the potential of our system has not been run out yet.

As mentioned in the concluding remarks of the sub-SQL experiment, our system provides a good platform for force sensing, which is compatible with sensitivity enhancing techniques using quantum correlations, like variational readout and synodyne detection. This sensitivity can be further boosted by changing the defect of our current membrane to a ribbon to reduce mode mass, and put the system into a dilution refrigerator, which can both improve the mechanical Q factor and decrease the temperature of thermal environment. Due to low thermal conductivity at low temperature and high energy of optical photons, operating optical experiment is not trivial in a dilfridge [14]. We are currently exploring the performance of soft-clamped membranes under this condition.

In this chapter, we introduce two main outlooks based on our membrane-in-the-middle system. The first one is that of a stroboscopic measurement, an alternative backaction evading measurement compared to variational readout, while the second is entanglement between microwave and optical fields.

7.1 Stroboscopic Measurement

In all the projects discussed before, we used a continuous laser field. We know that a conventional continuous wave conventional measurement of displacement is subjected to the Standard Quantum Limit. However, from the interaction Hamiltonian of an optomechanical system (Eqn. 2.25), only the position of the mechanical oscillator is coupled to the optical field. In principle, this interaction can be used as a quantum non-demolition (QND) measurement [138] of position, where there is no limit in the precision of position measurement. As position and momentum is a pair of non-commuting variables, measurement of position will inevitably increase the uncertainty in momentum, and this momentum uncertainty is rotated into position uncertainty after a quarter mechanical period. Therefore, for a conventional continuous wave measurement, we are actually trying to measure position and momentum simultaneously [47], which destroys the QND nature of the interaction.

The key of achieving QND measurement of a mechanical resonator is to measure only one of the mechanical quadratures. This idea was first proposed in Thorne et al. and Caves et al. [139, 140]. Only quite recently were experimental demonstrations of QND measurements on mechanical oscillators realized using two-tone measurements schemes in the microwave domain [15, 16, 17], and later in the optical domain [96]. A different approach was adapted by the group of Eugene Polzik at our institute, where a "negative mass" atomic ensemble was used to realise a QND interaction [97]. QND measurement of a mechanical oscillator using other schemes has not been demonstrated yet.

The conceptually easiest scheme is stroboscopic measurement [141], where a pulsed probe with repetition rate $2\Omega_m$ and the length of each pulse much shorter than the mechanical period is used for reading out

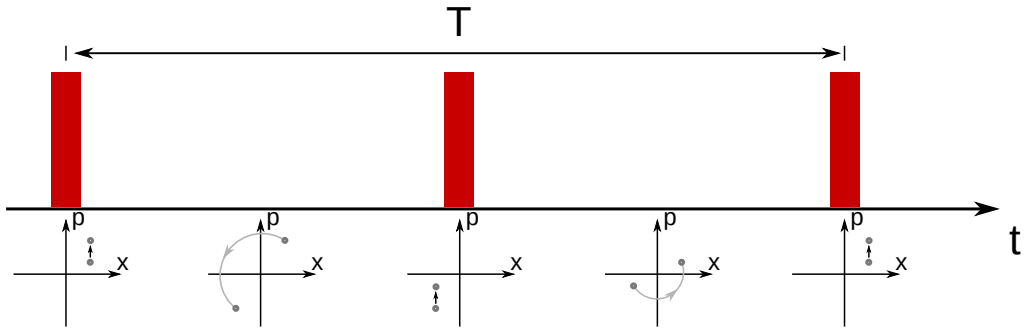

Figure 7.1: Idea of stroboscopic measurement The phase space evolution is shown in lower half of the figure.

the mechanical displacement. The scheme is illustrated in Fig. 7.1. Before the arrival of the first pulse, the average displacement of the mechanical oscillator is located at the equilibrium position with an uncertainty given by thermal noise sphere (refer to Fig. 4.4). At the moment of the arrival of the first pulse, the center of the mechanical state collapses to a random position in the phase space, with a probability distribution governed by the thermal sphere. The initial variances of position and momentum of this conditional state depends on the strength of the pulse. If the pulse is very weak, the uncertainties are roughly given by the thermal noise. The interaction between the first pulse and the mechanics transfers a momentum p to the mechanics. We assume that the coherence time of the mechanical oscillator is much longer than a mechanical period T, (thanks to the ultra-narrow mechanical linewidth, our system is deeply in this regime). After half of the mechanical period, the mechanics oscillates to a position with the same magnitude but opposite sign as the initial position, and the momentum also switches the sign. Then the second pulse decreases the total momentum by the same amount as the increase from the first pulse. After another half of a period, the mechanical state rotates back to the original position, and a new cycle starts. In this scheme, every time when a pulse arrives, the magnitude of the displacement is the same. By demodulating the signal at Ω_{m}, we can be sensitive to the magnitude of displacement only, and see no influence from momentum. Thus, this QND measurement is also called a backaction evading measurement, as backaction comes in the form of random momentum. Notice that quantum backaction still exists in this scheme, but the probe is "blind" to it. When the measured variance of displacement is below x_{zpf}^2, we get an conditional squeezed mechanical state. Stroboscopic measurement can be used to both prepare and verify this squeezing, which has been demonstrated in atomic ensembles [142]. However, this has not beem demonstrated on mechanical oscillators yet. One of the key challenges is to have stroboscopic measurement rate exceeding the decoherence rate. The large C_{q} and high detection efficiency provided by our system gives us a chance to satisfying this demanding condition.

We have tried to implement this stroboscopic measurement scheme using a fiber based amplitude modulator to generate pulses, and use a lock-in amplifier to acquire the signal. The result is shown in Fig. 7.2, where the filtered shape comes from the low-pass filter in the lock-in amplification. We notice there is some amount of backaction evasion happening at the resonance of the mechanical peak around 1.189 MHz, which proves the validity of the scheme. (The frequency of this mechanical mode is different from the one used in other projects, because this is a different membrane.) However, the more noticeable feature is the dense peaks in the stroboscopic spectrum, which make the spectrum too noisy for useful application.

After some intensive investigation, we found that these peaks are mechanical sidebands acquired by optical sidebands of the pulse sequence. When we modulate the intensity of the probe laser, depending on the pulse shape, there will be not only optical sidebands at frequency $\pm\Omega_{\mathrm{mod}}$, there will also be sidebands at $\pm n\Omega_{\mathrm{mod}}$, where n is an integer. The carrier at laser frequency and all these sidebands acquire their own mechanical sidebands, which appear around the demodulation frequency, resulting in these sharp peaks. We refer this phenomenon as "optical aliasing".

To solve this "optical aliasing", a membrane with bandgap at $n\Omega_{\mathrm{m}}$, where n is odd, will be helpful, which cleans up the main noise peak contributor.

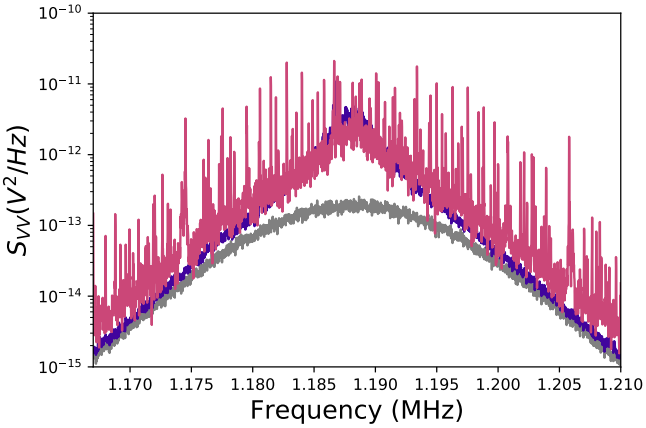

Figure 7.2: Result of stroboscopic measurement The spectrum of stroboscopic measurement (red) against the spectrum of continuous wave measurement (blue) and continuous wave shot noise (gray). The mechanical peak is centered around 1.189 MHz, highlighted by the gap between the mechanical spectra and the shot noise spectrum.

7.2 Optomechanical Interaction Induced Entanglement between Microwave and Optical Fields

Quantum internet requires high quality local quantum computation at individual nodes and high efficient distribution of quantum information among numerous distant nodes [36]. However, since no existing platform of quantum computing can satisfy these two requirements simultaneously, researchers have turned their attention to finding hybrid solutions to the problem. Among the candidates of quantum computation platforms, superconducting qubit is one of the leading choices, due to the fast operation and scalability. However, the high loss rate of microwave propagating in coaxial cables makes quantum information in microwave regime hard to be distributed to distant nodes [143]. Transducing quantum information from microwave to optical frequency, especially telecom frequencies, is a solution to this problem, as optical fields can propagate in free space or fiber with very low loss.

In Chapter 5, we mentioned that mechanical systems can couple microwave and optical fields with significant strength simultaneously, which gives mechanical systems the potential to link the drastically different frequency regimes. We introduced optomechanical coupling in the optical domain in detail in this thesis, and only briefly touched upon the coupling between mechanics and microwave fields, which plays an equally important role in a quantum transducer. There are mainly two categories of mechanics-microwave coupling. One employs piezo-electric materials based optomechanical crystals [35], where mechanical frequency typically matches that of microwaves, and can be directly coupled to superconducting qubits [18, 19, 32]. In the other category, the mechanics is a part of an LC resonator, whose resonance frequency changes with mechanical motion [21, 33, 144, 145]. The mechanical frequency in this category is typically orders of magnitudes lower than that of microwave. Among various ways of coupling, the most common design has the mechanical oscillator being a part of a capacitor. Suppose the capacitor can be approximated by a parallel plate capacitor, and one of the plates is the mechanical oscillator. In this scenario, the capacitance is given by

$$C = \frac{\epsilon A}{d + \Delta d}, \tag{7.1}$$

where ϵ is the dielectric permittivity, A is the area of the parallel plate, d is the equilibrium distance between two plates, and Δd is the displacement due to mechanical motion. Then the resonance frequency of the LC circuit is

$$\Omega_e = \frac{1}{\sqrt{LC}} = \sqrt{\frac{d + \Delta d}{\epsilon L A}} \approx \sqrt{\frac{d}{\epsilon L A}} \left(1 + \frac{\Delta d}{2d}\right), \tag{7.2}$$

where the last approximation is under the assumption $d \gg \Delta d$. Comparing this expression to $\Omega_{cav} \approx \Omega_{cav}(1 - q/L)$ for optical optomechanical cavity, we find the two cases are equivalent. Having the LC circuit

being a microwave cavity in mind, we can define the annihilation operator for intra-cavity microwave field $\hat{c}$, and the Hamiltonian of the microwave-mechanical system is given by

$$\hat{H} = \hbar\Omega_{\mathrm{e}}\hat{c}^{\dagger}\hat{c} + \hbar\Omega_{\mathrm{m}}\hat{b}^{\dagger}\hat{b} + \hbar G_{\mathrm{e}}\hat{c}^{\dagger}\hat{c}, \tag{7.3}$$

where $G_{\mathrm{e}} = \frac{\partial\Omega_{\mathrm{e}}}{\partial d}$. This is exactly the same as the Hamiltonian in optical case. In practice the assumption of parallel plate capacitor does not always hold. However, this Hamiltonian is still valid, but with modified electro-mechanical coupling G_{e}. Thus we can treat the microwave part of a transducer just as the optical part theoretically, and the derivation of microwave-optics entanglement just follows the one presented in Section 5.1.

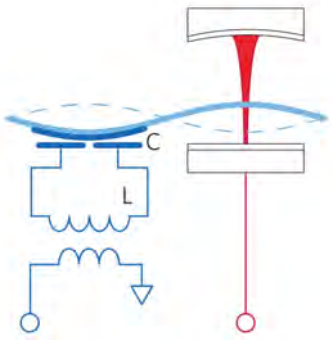

Figure 7.3: Sketch of the opto-electro-mechanics A figure from [33]. The microwave part of the membrane is metallized to enhance the electro-mechanical coupling.

As the optical part of our system is based on membrane-in-the-middle system, it is natural for us to adopt the opto-electro-mechanical design from Andrews et al. [33], as shown in Fig. 7.3. In this design a mechanical mode couples to an optical cavity and an LC circuit simultaneously, with a node in the middle to ensure maximum coupling for both parties. The microwave side of the membrane is metallized by a material (for instance Niobium), which is able to be thermalized well below its superconducting critical temperature in dilfridge. In the work by Andrews et al., the mechanical oscillator is a standard Si_3N_4 square membrane, which does not have the advantages of soft-clamped devices. To adapt soft-clamping into the node-in-the-middle requirement, we fabricate double defect membrane as shown in Fig. 7.4 [146]. The coupling between the localized modes of the two defects raises the degeneracy, and results in two normal modes with two defects moving in and out of phase. Due to the coupling, these modes are also separated in frequency space. With one defect coupled to optical cavity and the other coupled to microwave cavity, we can achieve simultaneous coupling while preserve ultra-coherent mechanical motion. With this system, we can apply similar operation as in Chapter 5, to entangle microwave and optical fields. Of course, in reality, before we can achieve this outstanding goal, we need to overcome technical challenges such as operating a high-finesse optical cavity at dilfridge temperature, operating optics close to a superconducting circuit, getting descent microwave-mechanical coupling, getting a low-loss microwave cavity etc. The path towards a quantum enabled electro-mechanical system, based on soft-clamped mechanical oscillators, is currently being pursued by a PhD student in our group, Yannick Seis.

If we can achieve entanglement between microwave and optical fields, the next step is trying to conduct entanglement swapping between two nodes composed of two opto-electro-mechanical transducers. After a successful operation, distant quantum nodes in microwave regime can be entangled. The scheme is depicted in Fig. 7.5, where a Hong-Ou-Mandel like interferometer is the key element for the swapping operation [110, 147, 148, 149]. This entanglement swapping is for continuous variables, which has the advantage of deterministic operation [147] over the probabilistic swapping for discrete variables. This advantage helps relaxing the requirements on the quantum memory, which is used to store the quantum states while waiting for success of other operations [150]. The ultra-coherent mechanical oscillator has the potential to be used as a memory as well. As a trade off, continuous variable entanglement swapping is sensitive to optical loss, because loss mixes in uncorrelated vacuum. This disadvantage, however, is controllable by using telecom wavelength [151]. Another drawback for continuous variable is the compatibility to common quantum computing platforms. We know most quantum computors are based on discrete quantum variables, especially

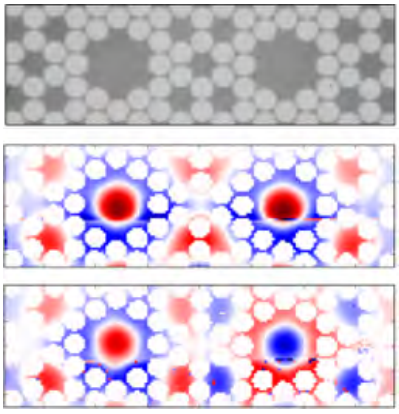

Figure 7.4: Double defect membrane A figure from [5]. Top panel: a picture of a soft-clamped double defect membrane, zoomed in around the defects. Middle and bottom panel: measured in phase and out of phase normal modes. The blue and red color represent different direction of displacements.

superconducting qubits, the primary motivator for quantum transducers. However, though a bit tedious, continuous variable schemes can be compatible with discrete variables, as entanglement swapping between continuous and discrete variables is feasible [152].

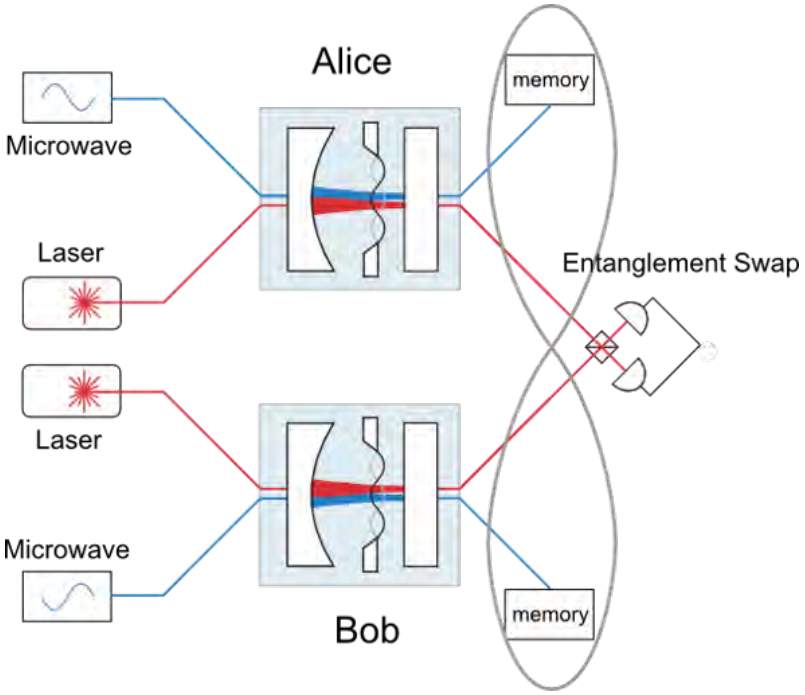

Figure 7.5: Sketch of entanglement swapping With two MIM based optical-microwave entangler, one can entangle two distant quantum nodes in microwave regime, by an entanglement swap operation on optical parts.

Appendix A

Electro Optic Components

A.1 Electro-Optic Phase Modulators

An electro-optic phase modulator (EOM) is a device modulating the phase of the input light via electro-optic (Pockels) effect. For a material with electro-optic effect, when voltage is applied on the material, its refractive index will change, thus the phase of the light passing through changes due to longer optical path length $\phi = 2\pi\delta L/\lambda$. When the applied voltage is periodic, the light is phase modulated. Suppose the original light field is given by $Ae^{i\omega t}$. If we apply a phase modulation with depth β and frequency Ω_{mod}, the modulated field is given by

$$A \exp\left(i\omega t + i\beta \sin\left(\Omega_{\text{mod}} t\right)\right). \tag{A.1}$$

This expression can be expanded using Jacobi-Anger expansion, and reads [89]

$$Ae^{i\omega t}\left(J_0(\beta) + \sum_{n=1}^{\infty} J_n(\beta) e^{in\Omega_{\text{mod}}} + \sum_{n=1}^{\infty} (-1)^n J_n(\beta) e^{-in\Omega_{\text{mod}}}\right), \tag{A.2}$$

where J_n, $n \in \mathbf{Z}$ is nth order Bessel's function of first kind. The first term in bracket determines the residual amplitude at the original (carrier) frequency, the second term represents sidebands at frequencies $n\Omega_{\text{mod}}$ higher than the carrier, and the third term represents sidebands at frequencies lower than the carrier, distributed symmetrically against higher frequency sidebands.

A.1.1 Calibration

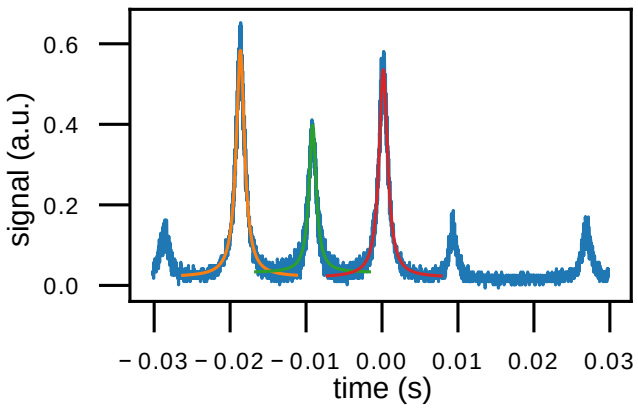

Figure A.1: Sideband calibration of V_π An example of sidebands in a sideband calibration of V_π. In this example, the peak with green fitted line is the carrier, while the right most peak belongs to the adjacent sweeping period. In this special case, due to large modulation depth, second order sidebands are visible.

When using EOMs, it is important to know the phase modulation depth β. Typically, this value is linearly proportional to the applied voltage as $\beta = g_{\mathrm{EOM}} V_{\mathrm{mod}}$, where g_{EOM} is the transition gain from voltage to phase. The voltage giving $\beta = \pi$ is usually referred as V_π, which is one of the most important parameters of an EOM. This value is expected to be given in the specification sheet of the device at a certain frequency and wavelength. However, V_π is usually not a constant at all frequencies. Thus calibrating V_π at the needed frequency is necessary. The idea of V_π calibration lies in Eqn. A.2. When $\beta = \pi$, we have the power ratio between one of the first order sidebands to the carrier to be

$$\frac{|J_1(\pi)|^2}{|J_0(\pi)|^2} \approx 0.875. \tag{A.3}$$

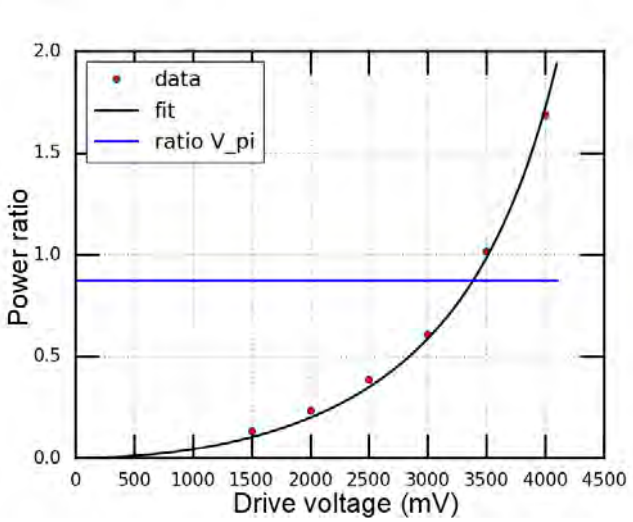

Figure A.2: Power ratio between the first sideband and the carrier The horizontal coordinate of the intersection between the ratio at V_π line and the fitting line indicates V_π of the EOM.

For frequency significantly larger than cavity linewidth $\Omega_{\mathrm{mod}} \gg \kappa$, we apply the same technique as sideband calibration of cavity linewidth described in Subsection 3.3.7. From OMIT described in Section 2.6, we notice that pure phase modulation does not appear in amplitude quadrature when there is no imbalance between the phase modulation sidebands, due to interference between the red and blue sidebands. However, in this case ($\Omega_{\mathrm{mod}} \gg \kappa$), when one sideband or the carrier is swept through the cavity, the influence from other frequency components is strongly suppressed by the cavity. Therefore, each frequency component can be treated as an independent laser tone. As a result, the area below each Lorentzian peak is proportional to the power of the tone. One of the sweeping time trace on oscilloscope is shown in Fig. A.1. We conduct sideband calibration experiment at different modulation voltages, and plot the power ratio between one of the first order sidebands to the carrier as in Fig. A.2. We fit the data with function $|J_1(g_{\mathrm{EOM}} V_{\mathrm{mod}})|^2 / |J_0(g_{\mathrm{EOM}} V_{\mathrm{mod}})|^2$, where g_{EOM} is the free parameter. Then $V_\pi = \pi / g_{\mathrm{EOM}}$.

When the modulation frequency is small $\Omega_{\mathrm{mod}} \ll \kappa$, or even just comparable to κ, the sideband way of calibrating V_π does not work anymore, because the sidebands will merge together, making a Lorentzian fit not possible. Moreover, the argument of independent sidebands is not valid anymore. In this case, we apply a phase modulation tone as what we usually do for calibration, lock the carrier on resonance with a cavity, and measure the modulation tone using balanced homodyne detector at phase quadrature. In spectrum, it is hard to get DC component, as what we can do in the sideband calibration case, instead, we make use of the fact that $|J_1(\beta)|^2$ is not a monotonic function of β. Then we can get an idea of β by just looking at the area below the first order sideband

$$A \propto |J_1(g_{\mathrm{EOM}} V_{\mathrm{mod}})|^2. \tag{A.4}$$

The transduction may be suppressed by cavity, by homodyne locking away from phase quadrature, changed by locking the laser not exactly on resonance with the cavity, but this proportional relation does not change. We take a series of spectra with different modulation voltage, with the maximum voltage as large as possible, such that the second order sideband is strong enough to decrease the increasing tendency of the first order

sideband. The experimental results and fit are shown in Fig. A.3. Notice the decreasing slope for large voltage data, which helps locating the horizontal position of the fitting curve. From this fit we can extract V_π at the modulation frequency.

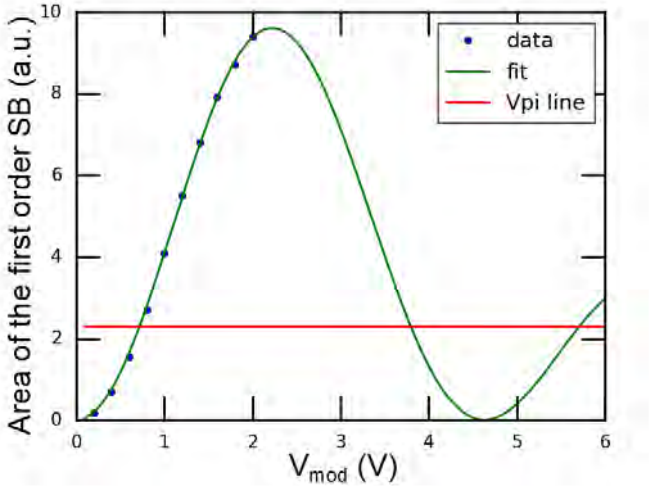

Figure A.3: Area of the first order sideband The horizontal coordinate of the first intersection between the ratio at V_π line and the fitting line indicates V_π of the EOM.

During calibration of V_π, one should pay attention to the wavelength dependence as well. As EOM modulates phase through changing optical length, even though the modulation may provide the same change of optical path length, different optical wavelength also changes phase modulation, as $\phi = 2\pi\delta L/\lambda$.

A.2 Laser Electro Optic Phase Modulators

In optical-optical entanglement experiment, we used the built-in EOMs in lasers for PDH lock and calibration tone. Unlike the fiber based EOM introduced in previous section, this built-in EOM of laser is an intra-cavity Pockels cell. Voltage applied on the EOM effectively change the optical path length of the laser cavity, which selects the laser frequency, thus the modulation is in frequency instead of phase.

For frequency modulation, a detailed introduction can be found in [153]. Here we give a brief review. For a frequency modulated signal, the instant frequency is given by

$$\Omega_i = \omega + g_{\mathrm{FM}} V_{\mathrm{mod}} \cos(\Omega_{\mathrm{mod}} t), \tag{A.5}$$

where g_{FM} is the device gain from voltage to frequency, and without loss of generality, we choose cos with zero initial phase. $g_{\mathrm{FM}} V_{\mathrm{mod}}$ determines the amplitude of the frequency modulation (how far the frequency swing around the carrier frequency), which is independent from Ω_{mod}. As the frequency is not a constant, the instant phase of the signal should be expressed as an integration

$$\omega t + g_{\mathrm{FM}} V_{\mathrm{mod}} \int_0^t \cos(\Omega_{\mathrm{mod}} t')dt' = \omega t + \frac{g_{\mathrm{FM}} V_{\mathrm{mod}}}{\Omega_{\mathrm{mod}}} \sin(\Omega_{\mathrm{mod}} t). \tag{A.6}$$

Comparing this expression to the instant phase of phase modulation $\omega t + g_{\mathrm{EOM}} V_{\mathrm{mod}} \sin(\Omega_{\mathrm{mod}} t)$, we notice that frequency modulation has the same effect as phase modulation, except the $1/\Omega_{\mathrm{mod}}$ dependence of phase modulation amplitude. Thus we can see frequency modulation tone at Ω_{mod}, and can use this modulation for PDH lock.

A.2.1 Calibration

Just as in the case of fiber based EOM, we need to calibrate g_{FM} for laser EOMs. As the Pockels cells need much higher voltage than we can apply to reach V_π at a frequency around Ω_{m}, we cannot use the calibration

methods as in the fiber based EOM case. Instead, we compare the modulation tones generated by the fiber based EOM and the laser EOMs at almost the same frequency in homodyne spectrum, and use the V_π for the fiber EOM as a benchmark. Then the extracted V_π for the EOM in Laser B is shown in Fig. A.4. V_π of laser EOM has a clear proportional dependence on Ω_{mod}, as indicated by the $1/\Omega_{\text{mod}}$ dependence in phase modulation depth. By fitting these data points with a proportional function, we can get the tendency of V_π as a function of frequency. Due to the uncertainties in the response of the Pockels cell, to get the exact V_π at a certain frequency, we need to measure V_π at that frequency.

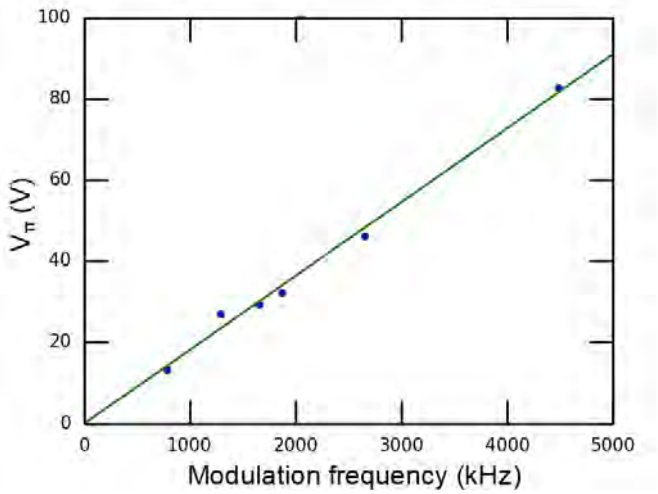

Figure A.4: V_π of Laser B EOM There is a linear dependence between V_π and modulation frequency for laser EOM.

Please notice the large values of V_π's, as a consequence, we cannot apply frequency modulation at too high frequency, if we still want reasonable modulation depth. Therefore, for PDH lock, we only use modulation frequency close to κ, and need an amplifier from the output of PI controller. With the worry seeing the effect of PDH modulation tone in spectrum (e.g. second order mechanical sidebands), we compare the spectra with laser EOM locked with a modulation frequency comparable to κ, and with fiber EOM locked with a modulation frequency much larger than κ. The spectra have no difference.

A.3 Electro-Optic Amplitude Modulators

Combining an electro-opitc phase modulator and a Mach-Zehnder interferometer, one can modulate amplitude of a light beam. The amplitude modulator used in our experiment belongs to this category.

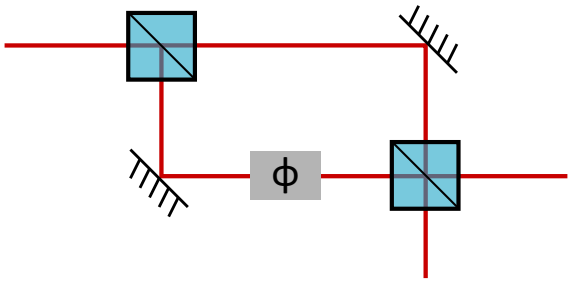

Figure A.5: Mach-Zehnder Interferometer The phase difference between the two arms can cause intensity unbalance between two output ports.

A Mach-Zehnder interferometer is composed of two beam splitters (BS). The first one splits a beam, and the two arms recombines at the second one. In one of the arms, there could be a phase shifter changing the

relative phase between the two arms. Then upon recombination, the powers in the two output ports changes according to the phase shift. Suppose we have a classical field in one of the input port, while the input of the other port is vacuum ($|\psi\rangle = (\alpha, 0)^T$). Then after the first BS, the state becomes

$$\frac{1}{\sqrt{2}}\begin{pmatrix}1 & 1\\ 1 & -1\end{pmatrix}\begin{pmatrix}\alpha\\ 0\end{pmatrix} = \frac{\alpha}{\sqrt{2}}\begin{pmatrix}1\\ 1\end{pmatrix}. \tag{A.7}$$

The phase shifter has the effect as

$$\begin{pmatrix}1 & 0\\ 0 & e^{i\phi}\end{pmatrix}\frac{\alpha}{\sqrt{2}}\begin{pmatrix}1\\ 1\end{pmatrix} = \frac{\alpha}{\sqrt{2}}\begin{pmatrix}1\\ e^{i\phi}\end{pmatrix}. \tag{A.8}$$

When the two arms are recombined at the second BS, we have

$$\frac{1}{\sqrt{2}}\begin{pmatrix}1 & 1\\ 1 & -1\end{pmatrix}\frac{\alpha}{\sqrt{2}}\begin{pmatrix}1\\ e^{i\phi}\end{pmatrix} = \frac{\alpha}{2}\begin{pmatrix}1+e^{i\phi}\\ 1-e^{i\phi}\end{pmatrix}. \tag{A.9}$$

Then the output powers at the two output ports are given by

$$\frac{|\alpha|^2}{4}(1+e^{i\phi})(1+e^{-i\phi}) = \frac{|\alpha|^2}{2}(1+\cos\phi) \tag{A.10a}$$

$$\frac{|\alpha|^2}{4}(1-e^{i\phi})(1-e^{-i\phi}) = \frac{|\alpha|^2}{2}(1-\cos\phi) \tag{A.10b}$$

respectively. Notice that by changing ϕ from 0 to π, we can turn the output power from completely on to completely off. Modulating the phase, we can modulate the output amplitude.

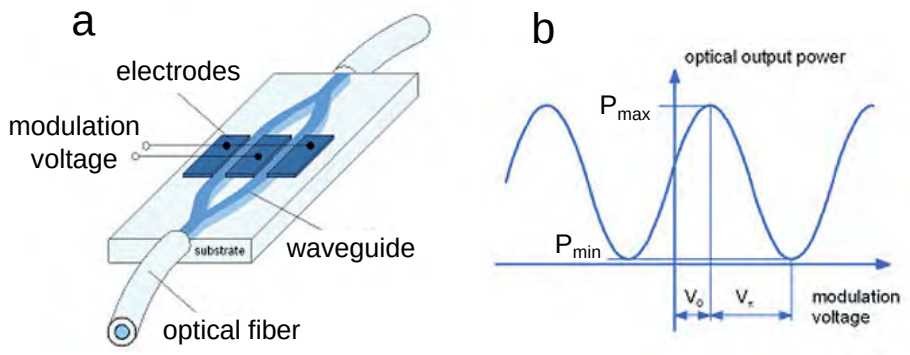

Figure A.6: Amplitude modulator Figures from [154]. **a.** The sketch of the amplitude modulator used in our experiment. **b.** Optical output power of the amplitude modulator as a function of modulation voltage. V_0 is an offset due to difference in arm lengths.

In our experiment, we use an amplitude modulator provided by Jenoptik. The sketch of the design is shown in Fig. A.6 a, where the waveguides are made of electro-optic materials. There are electrodes on both arms of the Mach-Zehnder interferometer, and the voltage on the arms are opposite. This "push-pull" design doubles the phase difference between the two arms upon the same modulation voltage. Nevertheless, the operation principle is still the same.

The output of the amplitude modulator is one of the output ports of the Mach-Zehnder interferometer. The output power as a function of modulation voltage is shown in Fig. A.6 b, and is governed by [154]

$$P = P_{\min} + \frac{P_{\max} - P_{\min}}{2}\left(1 + \cos\left(\frac{\pi(V - V_0)}{V_\pi}\right)\right), \tag{A.11}$$

where $P_{\min}$ and $P_{\max}$ are the minimum and maximum powers of the interference. Ideally, $P_{\min} = 0$, however, in practice, there is always finite $P_{\min}$ due to imperfect mode matching between the two arms and deviation of the beam splitter splitting ratio from 50 : 50. V_0 is a voltage offset caused by unequal optical path length

between the arms when the applied voltage is zero. In practice, V_0 drifts as temperature changes. This drift is more dramatic when the input optical power is large. As a result, if the phase modulation is less than 2π, the amplitude modulation depth will drift with V_0. For instance, if the initial $V_0 = 0$, and we apply a modulation voltage $V = V_\pi$, we will observe full amplitude modulation depth. If the offset drifts to $V_0 = V_\pi/2$, the modulation depth drops to 1/2. Therefore, to keep the amplitude modulation depth a constant, we need to stabilize the offset V_0.

A.3.1 Offset Lock

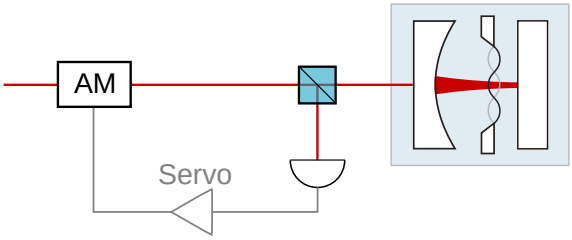

Figure A.7: Setup for amplitude modulator offset lock The beam splitter direct part of the laser beam to a photodetector, the output of which provides error signal for the amplitude modulator offset lock.

As shown in Fig. A.7, to lock the offset of the amplitude modulator, we split the optical power before the optomechanical cavity, and detected the splitted light by a photodetector. The DC output of this photodetector is input to a servo, which is used as a PI controller. The servo outputs an additional close to DC voltage to the amplitude modulator to compensate any drift in V_0.

In this lock, error signal is the difference between measured DC voltage and the set point, similar to the slope homodyne path length lock as mentioned in Subsection 3.6.4. Consequently, it is hard to have a set point very close to $P_{\max}$ or $P_{\min}$. Moreover, as we would like the lock to be stable even during ringup in ringdown experiment, the bandwidth of this lock is kept very low. After all, the usual drift happens at minute time scale. If we enlarge the bandwidth of the lock, this setup can also be used as an amplitude noise eater, which can reduce the amplitude noise in the laser beam.

A.4 Acousto-Optic Modulators

Acousto-optic modulators (AOM) are a commonly used electro-optic components used in optical experiment, which are typically used for amplitude modulation, frequency shift, and tunable wavelength filter [155]. Though we do not use AOMs in any of the projects introduced in this thesis, we used it for heterodyne measurements in membrane interferometer and mechanical performance test in dilution refrigerator to shift the LO/signal frequency and generate pulses. Therefore, it is beneficial to introduce this device here. This introduction is based on a detailed material provided by AA Opto Electronic [155].

The basic structure of an AOM is a crystal with a piezo attached to one end and an acoustic wave absorber on the other end. Driving the piezo at a certain frequency results in acoustic wave traveling through the crystal and, being absorbed by the absorber. When the absorption is nearly perfect, we can consider the acoustic wave as a traveling wave. This kind of acoustic wave is longitudinal wave in material density, therefore the refractive index of the crystal is modulated. This change of refractive index then scatters the laser beam passing through the crystal through the so called Brillouin scattering. To satisfy conservation of momentum and energy, the scattering should satisfy

$$\vec{k}_\mathrm{f} = \vec{k}_\mathrm{i} + N\vec{k}_\mathrm{a} \tag{A.12a}$$

$$\omega_\mathrm{f} = \omega_\mathrm{i} + N\omega_\mathrm{a}, \tag{A.12b}$$

where $\vec{k}_\mathrm{f}$, $\vec{k}_\mathrm{i}$ and $\vec{k}_\mathrm{a}$ are the wave vectors of the scattered optical beam, the incident optical beam and the acoustic wave respectively. The ω's are the corresponding angular frequencies. N is an integer number (could be negative) governing the order of scattering.

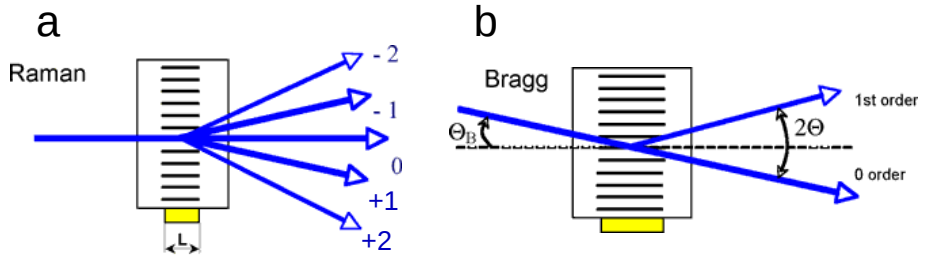

Figure A.8: Regimes of AOM operation Figures from [155]. The yellow rectangles represent the piezo used to generate acoustic wave in the crystal, and black grating represents acoustic wave. **a.** Raman-Nath regime, the laser beam incidents nearly normal to the propagation direction of acoustic wave, and there are diffracted beams on both sides of the carrier. **b.** Bragg regime, the laser beam incidents at an angle close to Bragg angle of the acoustic wave. Only one diffraction beam is visible.

There are two working regimes of AOMs. The first one is called Raman-Nath regime, as shown in Fig A.8 a, where the incident laser beam is almost perpendicular to the sound wave propagating direction. In this regime, the laser beam experience a modulation of refractive index due to the acoustic wave, and get phase modulated just as EOM. The "sidebands" appear both above and below the original frequency, and the amplitudes are governed by Bessel's function of the first kind. However, due to the requirement of conservation of momentum, these sidebands do not share the same spacial mode as the carrier, but are diffracted away as shown in the figure. Then the frequency shifts can also be understood as Doppler shifts with respect to the acoustic wave.

The second regime is referred as Bragg regime, shown in Fig. A.8 b. In this regime, the incident angle of the laser beam roughly matches Bragg's law, with the lattice spacing given by acoustic wavelength:

$$2\Lambda \sin\theta = N\lambda = \frac{N\lambda_0}{n}, \tag{A.13}$$

where Λ, λ and λ_0 are the wavelength of the acoustic wave, the optical field in crystal and the optical field in vacuum respectively. n is the refractive index, and θ is the angle between the incident beam and the normal vector of the crystal surface. In this case, only one diffracted beam is significant, others are suppressed by destructive interference. The frequency of this diffracted beam is given by $\omega_i \pm \omega_a$, where the sign depends on the incident angle and the propagating direction of acoustic wave. In the case of Fig. A.9 a, the acoustic wave is propagating "upward", and the projection of the wave vector of the incident laser on the propagating direction of the acoustic wave is "against" $\vec{k}_a$. Then the frequency of the diffracted beam is Doppler shifted "up" to $\omega_i + \omega_a$. When the incident wave vector has a component "along" the acoustic wave, i.e. negative θ, as shown in Fig. A.9 b, the diffracted beam will have a frequency $\omega_i - \omega_a$.

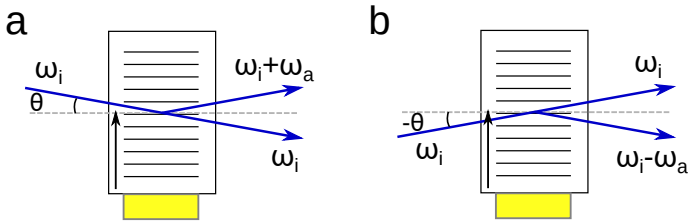

Figure A.9: Diffracted beam frequency in Bragg regime The black arrow indicates the propagation direction of the acoustic wave. **a,b.** show the cases of two optical beam incident angles and their corresponding scattered optical frequencies.

Consider a case with perfectly matched Bragg's law, the power of the diffracted beam compared to the total incident optical power is given by [155]

$$\frac{I_1}{I} = \sin^2\left(\sqrt{\frac{\pi^2}{2\lambda_0^2} M_2 \frac{L}{H} P}\right), \tag{A.14}$$

where M_2 is the figure of merit of the crystal material, L as shown in the figures is the width of the acoustic wave field, H is the height of the field, and P is the power of radio frequency (RF) drive. L is proportional to the interaction strength between the optical field and acoustic field, thus the crystal cannot to be too thin for the sake of diffraction efficiency. H together with L governs the cross section of the acousto-active part of the crystal, which is proportional to the required RF driving power for a certain acoustic wave intensity. The dependence on $\sin^2$ indicates that the efficiency is not a monotonic function of RF power, as shown in Fig. A.10, whose consequence will be discussed later. In experiment, to maximize the power of a diffracted beam, we usually set up the system in Bragg regime.

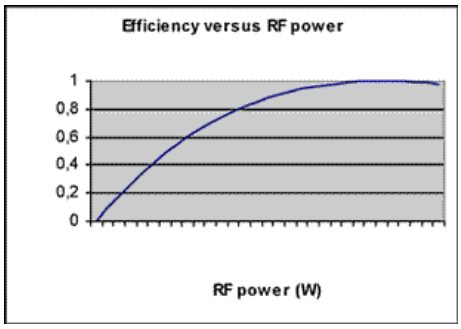

Figure A.10: Ideal AOM efficiency as a function of driving power A figure from [155]. There is a maximum diffraction efficiency as the RF power varies.

A.4.1 AOM setup for Ringdown Experiment

From Eqn. A.14, one might think the diffraction efficiency can be up to unity if the AOM is driven at optimal RF power. However, Bragg's law is derived from a plane wave, but in practice, we typically deal with Gaussian beams. If the wavefront of the Gaussian beam in the AOM is not flat, the diffraction efficiency will inevitably drop. Therefore, we would like to put the beam waist at the center of the AOM for high efficiency. However, even if the beam waist is at the center of the AOM, the finite beam width will also harm the plane wave treatment. Moreover, the finite width of the acoustic wave also results in curved wavefront at some places cross the crystal, resulting in further decrease of efficiency. As a result, the typical maximum diffraction efficiency is around 80%. Placing the beam waist at the center of the AOM and having a wider waist help getting a better efficiency (closer to plane wave at the waist, and smaller wavefront curvature).

However, diffraction efficiency is not the only parameter we should optimize. If we are using AOM for amplitude modulation, the pulse rise time is a crucial parameter, which is the time for the pulse to change from 10% of the total intensity to 90%. This paramter determines how sharp the pulse edge is, and typically we would like the rising time to be short. This quantity is simply the time for the acoustic wave passing through the laser beam. For a Gaussian it is defined by

$$T_\mathrm{r} = 0.64\frac{D}{v_\mathrm{a}}, \tag{A.15}$$

where D is the beam diameter, and v_a is the acoustic speed. In this case, we again need to put the beam waist in the AOM, but a tightly focused beam is preferred. Therefore, there is a trade off between efficiency and rise time. One should design the optical path according to the requirement.

Here, we discuss the AOM setup for amplitude modulation in ringdown experiment as an example to see the key points of designing the setup when using AOMs. We make use of the spacial separation between the zeroth order and first order diffracted beams to separate them, and couple the first order beam to a fiber, while block the zeroth order beam. As the diffraction angle is typically small, the fiber collimator should be reasonably far from the AOM (of the order 30 cm) to ensure good separation. The RF to acoustic power transduction efficiency for AOMs are usually optimized in the range from 40 MHz to 80 MHz. Therefore, the RF sources we use to drive the AOMs should have frequencies in this range. However, when do interferometric detection, the beat tone between local oscillator at the original frequency and the beam passed through AOM at the shifted frequency is also in this range, but the bandwidth of our detector is typically not as large. To solve the problem, we employ two AOMs instead of one, and arrange them such that one

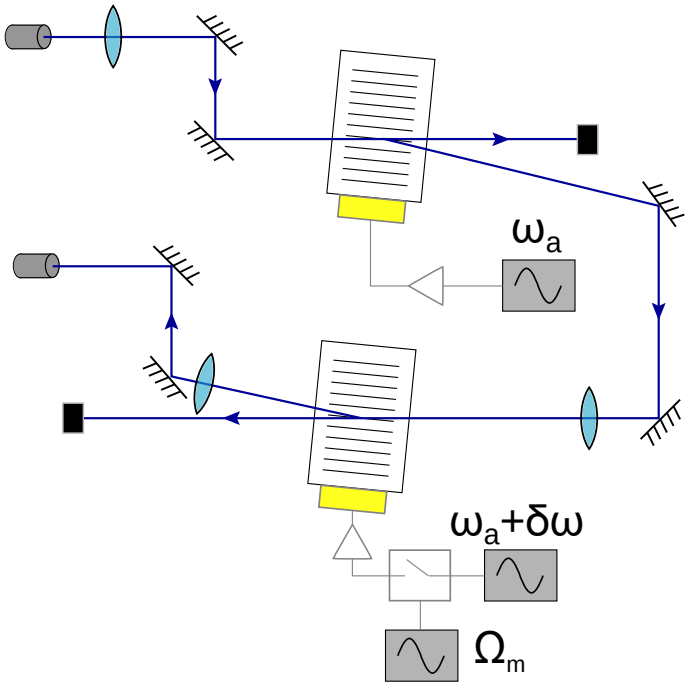

Figure A.11: AOM setup for ringdown measurement The zeroth order beams are blocked. Notice the first AOM shifts the frequency down, while the second shifts the frequency up. The switch from the RF source to the second AOM is used pulse generation.

AOM shifts frequency up while the other shifts down, then the net frequency shift can be controlled by tuning the relative frequency $\delta\omega$ between the RF sources. When $\delta\omega = 0$, the beam net frequency shift is zero, and the interferometric detection is homodyne. In this case, it is also possible to use just one AOM in a bi-passing setup, where the first order beam is reflected right back, after passing through the AOM again, been separated from the incident beam using a combination of PBS and quarter waveplate, similar to the homodyne path length lock (Subsection 3.6.4). By sending a RF tone at Ω_m to the switch, we can generate pulses to excite the mechanics.

AOMs typically need quite high RF driving powers (of the order 1 W to 5 W). Amplification of the RF drive is necessary. To reduce the amplification noise, a typical amplification chain is composed of a low noise pre-amplifier and a high power amplifier. If the total amplification exceeds the required value, an attenuator can be placed between the two amplifiers. This is better than putting it before the pre-amplifier or directly reducing drive power in terms of noise performance.

A.4.2 Effects of Noise of RF Source

For quantum measurements, we would like our optical fields to be shot noise limited. However, even though the incident light is shot noise limited, when passing through an AOM driven by an noisy RF source, the diffracted light will be noisy in both amplitude and phase quadratures. From Eqn. A.12ab, it is clear that phase noise of the RF drive leads to frequency noise of acoustic wave, thus ends up in frequency/phase noise of light. The only way to reduce optical phase noise is to use a clean RF drive.

The source of amplitude noise of a light beam diffracted by an AOM is more complicated. Both amplitude and phase noise of the RF source play a role. If the RF power is not at the optimal value, any amplitude noise in RF power will result in efficiency fluctuation of the first order diffraction, as can be seen from Fig. A.10. This efficiency change leads to amplitude fluctuation in the diffracted light. Therefore, it is crucial to drive the AOM at an RF power giving maximum diffraction efficiency, where the flat response suppresses the effect of amplitude noise. The optimal driving power can be determined from the power of the diffracted beam. On the other hand, if there is phase noise in the RF drive, this phase noise will cause frequency fluctuation of the acoustic wave, thus fluctuation in the acoustic wavelength, momentum and wave vector. From Eqn. A.13, fluctuating Λ results in fluctuating Bragg angle. However, the incident angle is

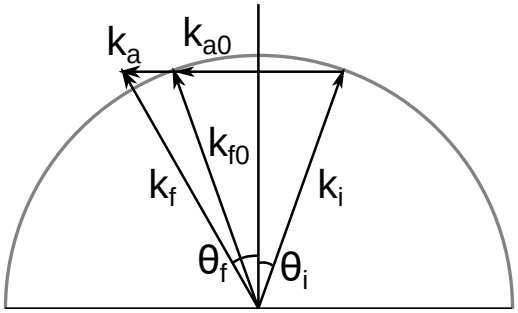

Figure A.12: Conservation of momentum in Brillouin scattering $\vec{k}_{f0}$ and $\vec{k}_{a0}$ represent the momenta of the scattered light and the acoustic wave, when the Bragg's criterion is satisfied. $\vec{k}_f$ and $\vec{k}_a$ represent the corresponding momenta when the wave vector of the acoustic wave is longer than the "Bragg" value. θ_i and θ_f represent the incident angle and the scattered angle when the acoustic wave vector is "too long". Apparently, the two angles are not equal in this case.

fixed, mismatching the Bragg criterion due to Bragg angle fluctuation leads to lower diffraction efficiency. Moreover, the mismatching between incident angle and Bragg angle leads to change in the diffraction angle of the incident beam (as a result of conservation of momentum, illustrated in Fig. A.12) [155], which mis-aligns the coupling to optical fiber, and results in optical amplitude fluctuation after the fiber (pointing noise). Optically, the pointing noise can be reduced by having the fiber coupler closer to the AOM, but this will decrease the separation between the original and diffracted beams. Therefore, optimization in RF drive is required to decrease it further.

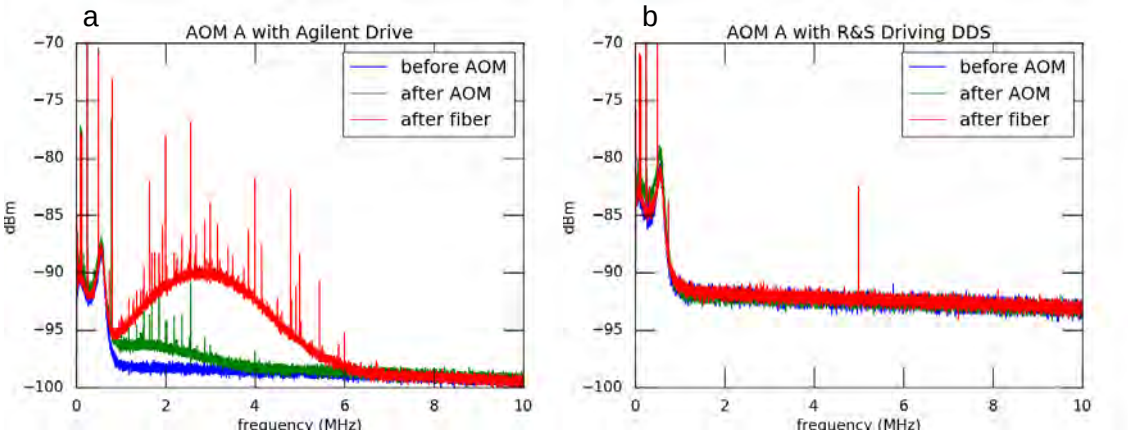

Figure A.13: Amplitude noise related to AOM a,b. Optical amplitude noises when driving an AOM with an Agilent AWG and Rohde&Schwarz spectral analyzer clocked DDS board. The common low frequency noise is relaxation oscillation noise of the Ti-Sapphire laser.

The effect of amplitude noise of RF drive can easily be suppressed below the shot noise level by using optimal driving power for most of the available RF sources. The effect of phase noise, however, strongly depends on the phase noise performance of the RF source. To test the effect, we set up an AOM similar to what is shown in Fig. A.11, but with only one AOM, and directly detect the optical fields before the AOM, the first order diffracted beam after the AOM, and also the first order diffracted beam after a fiber. The spectrum of the first measurement provides information of the original laser noise, the second provides information about the noise given by Bragg angle fluctuation, while the last measurement also includes the effect of pointing noise. To have a fair comparison, we compensate the optical power difference by recording the DC output of the photodetector, and scaling the measured spectra. The results are shown in Fig. A.13. When we are driving the AOM with an Agilent AWG (Fig. A.13 a), we can clearly observe the increased noise by Bragg angle fluctuation (green) and pointing noise (red). When the drive is changed to a quiet source, in this case, a DDS board with clock from a Rohde&Schwarz spectral analyzer (Fig. A.13), the amplitude

noise even after the fiber is the same as the original noise.

Appendix B

Lock-in Amplification

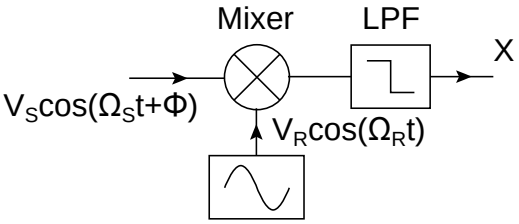

Figure B.1: Block diagram of demodulation

A signal usually contains multiple frequency components, but not all of them are of interest. Lock-in amplification is a data processing method to extract the frequency component of interest, and suppress noises at other frequencies.

The idea of lock-in amplification is based on frequency demodulation. Supposing we would like to extract a frequency component at Ω_S from a time dependent signal, we can write this component as $V_S(t)\cos(\Omega_S t + \Phi(t))$, where the amplitude and phase varies at very slow rate (Notice that all measured signals can only be real instead of complex). In a demodulation process, this signal is mixed with a reference tone $V_R\cos(\Omega_R t)$. The effect of a mixer is multiplying these two inputs, and give

$$V_m = V_S(t)\cos(\Omega_S t + \Phi(t))V_R\cos(\Omega_R t). \tag{B.1}$$

Recall the trigonometric identity

$$\cos(A+B) = \cos A\cos B - \sin A\sin B, \tag{B.2}$$

thus we have

$$\cos A\cos B = \frac{\cos(A+B)+\cos(A-B)}{2}. \tag{B.3}$$

Then we can rewrite the output signal from the mixer as

$$V_m = \frac{V_S(t)V_R}{2}\left(\cos((\Omega_S+\Omega_R)t+\Phi(t)) + \cos((\Omega_S-\Omega_R)t+\Phi(t))\right), \tag{B.4}$$

which contains two frequency components, one at $\Omega_S+\Omega_R$, and the other at $\Omega_S-\Omega_R$. The low pass filter filters out the $\Omega_S+\Omega_R$ component and leaves $\Omega_S-\Omega_R$ component, if the filter bandwidth is higher than the difference frequency. Then we have

$$V_{out} = \frac{V_S(t)V_R}{2}\cos((\Omega_S-\Omega_R)t+\Phi(t)). \tag{B.5}$$

Ideally, after the demodulation, the only time dependence comes from the fluctuation of $V_S(t)$ and $\Phi(t)$, if what we want to study is their dynamics, not the boring oscillation at $\Omega_S-\Omega_R$. Then we should choose $\Omega_R=\Omega_S$, and the demodulated signal is a very slowly changing value

$$V_{out}(t) = \frac{V_S(t)V_R}{2}\cos\Phi(t). \tag{B.6}$$

In this case, we cannot distinguish changes in signal amplitude $V_S(t)$ from those in phase $\Phi(t)$.

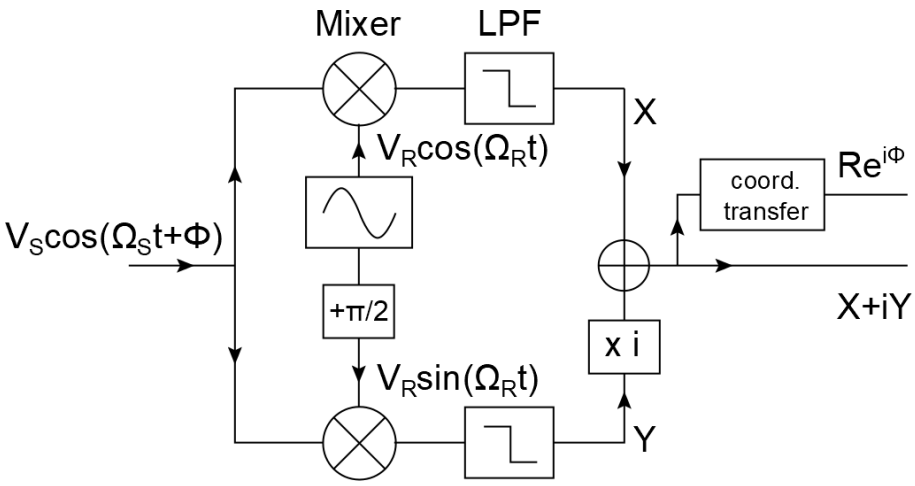

Figure B.2: Signal processing in a lock-in amplifier

To solve the problem, we need two demodulators $\pi/2$ out of phase, as shown in Fig. B.2, to reconstruct both phase and amplitude information of the input signal. The output of the mixer with $V_R \sin(\Omega_R t)$ input is given by

$$V_m = V_S(t) \cos(\Omega_S t + \Phi(t)) V_R \sin(\Omega_R t). \tag{B.7}$$

Noticing that

$$\sin(A + B) = \sin A \cos B + \cos A \sin B, \tag{B.8}$$

we have

$$\cos A \sin B = \frac{\sin(A + B) - \sin(A - B)}{2}. \tag{B.9}$$

Thus the demodulation output of this branch reads

$$V_{out,sin}(t) = \frac{V_S(t) V_R}{2} \sin \Phi(t). \tag{B.10}$$

By multiplying this expression with imaginary unit i, and summing it with the output of the other branch, we can reconstruct the complex expression of the input signal

$$V_{out} = \frac{V_S(t) V_R}{2} (\cos \Phi(t) + i \sin \Phi(t)). \tag{B.11}$$

By changing the coordinate from Cartesian to polar, we have

$$V_{out}(t) = \frac{V_S(t) V_R}{2} e^{i\Phi(t)}. \tag{B.12}$$

It is evident that the amplitude of the processed signal is proportional to the that of the original signal, and the phase is directly given by the original signal. The low-pass filter rejects additional noises, and also limits the bandwidth of fluctuations in one can observe in the original signal.

Appendix C

Possibility of determining Cavity Out-coupling Efficiency in Reflection

Cavity out-coupling efficiency η_c is an important parameter as it contributes to the total detection efficiency of the system. As mentioned in Section 2.4, transmission signal cannot provide information about relation between κ_L and κ_R. In the experiments presented in this thesis, we only apply homodyne measurement in transmission, therefore we cannot determine η_c by measurement. Instead, we estimate η_c from the mirror coating data and transfer matrix model, as explained in Subsection 3.3.4. This estimation only works well when the parameters of the system are well known, which fails in some circumstances, making direct measurement of η_c beneficial. For instance, in the highly non-degenerate optical-optical entanglement presented Subsection 5.2.2, the mirror coatings are not well known beyond 900 nm. Of course, one can disassemble an MIM cavity to measure the coating performance. However, as cavity assembly is time consuming and risky for the membrane, a non-invasive method is preferred.

As indicated by Section 2.4, to get the information of cavity out-coupling, we need to work in reflection, and make use of phase referenced measurement to acquire phase and amplitude information simultaneously, which allows us to reconstruct reflection coefficient. Here we consider a more realistic case by introducing intra-cavity loss rate κ_i and non-unity mode matching between cavity and inputting laser field described by $1-\epsilon$ as in Subsection 3.6.3, such that the amplitude of the mode matched part between cavity and input field is given by $\alpha_{in,\parallel}$, whose amplitude is $\sqrt{1-\epsilon}\alpha_{in}$. Similarly, the non-mode matched part $\alpha_{in,\perp}$ has the amplitude $\sqrt{\epsilon}\alpha_{in}$. Then the mode matched and not mode matched (classical) reflected fields are given by

$$\alpha_{r,\parallel} = \left(-1 + \frac{\kappa_L}{\kappa/2 - i\Delta}\right)\alpha_{in,\parallel} \tag{C.1a}$$

$$\alpha_{r,\perp} = -\alpha_{in,\perp}, \tag{C.1b}$$

with

$$|\alpha_{in,\parallel} + \alpha_{in,\perp}|^2 = (1-\epsilon)P_{in} + \epsilon P_{in} = P_{in}, \tag{C.2}$$

where we have used the fact that the fields are orthogonal, such that the product $\alpha_{in,\parallel}\alpha_{in,\perp} = 0$. Then the total power of the reflected beam reads

$$\begin{aligned} P_r &= |\alpha_{r,\parallel} + \alpha_{r,\perp}|^2 = \left|\left(-1 + \frac{\kappa_L}{\kappa/2 - i\Delta}\right)\alpha_{in,\parallel} - \alpha_{in,\perp}\right|^2 \\ &= \left[\left(1 - \frac{(\kappa_R + \kappa_i)\kappa_L}{\kappa^2/4 + \Delta^2}\right)(1-\epsilon) + \epsilon\right] P_{in} \\ &= \left(1 - (1-\epsilon)\frac{(\kappa_R + \kappa_i)\kappa_L}{\kappa^2/4 + \Delta^2}\right) P_{in}, \end{aligned} \tag{C.3}$$

where we have used $\kappa = \kappa_L + \kappa_R + \kappa_i$ and the orthogonal argument. Comparing this expression to Eqn. 2.62, we can see the two cases share the same background level P_{in}, but when there is mode mismatch, the depth of the Lorentzian dip is only $1-\epsilon$ of the perfect mode matching case. Thus, even when the cavity is critically coupled, the reflection dip does not go to zero.

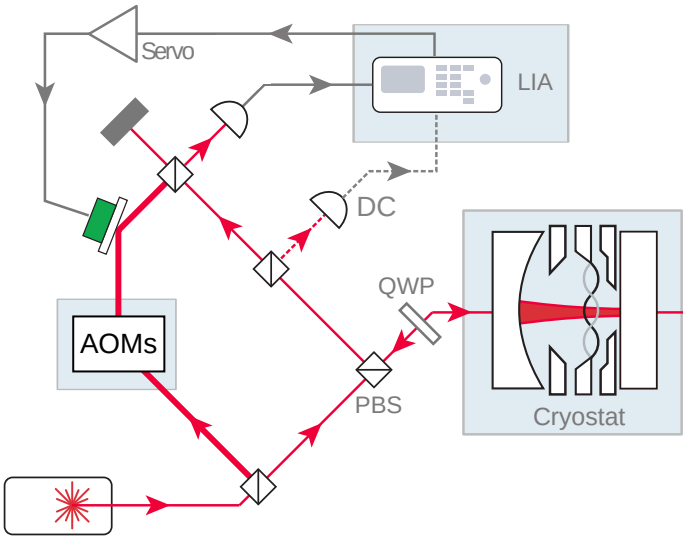

Figure C.1: Setup for η_c measurement The PBS and quarter waveplate separate the reflected beam from the cavity from the input beam. A pair of acousto-optical modulators (AOMs) shift the frequency of local oscillator (see Appendix A.4 for more information), as required by heterodyne measurement. Only a single diode is needed in this case, the other port of the final combination non-polarizing beam splitter is blocked by a beam dump. Part of the reflected light from cavity can be splitted to a photo diode, to provide information on resonance dip.

Without phase information, it is still not enough to determine η_c. To get phase information, we need phase reference measurement like homodyne and heterodyne. The optical power at DC for homodyne measurement is given by (without loss of generality, suppose α_{LO} is real)

$$\frac{1}{2}(\alpha_{LO}^2 + |\alpha_{r,\parallel}|^2 + |\alpha_{r,\perp}|^2 + 2\alpha_{LO}|\alpha_{r,\parallel}|\cos(\theta_p + \theta_c)), \tag{C.4}$$

where we assume the LO is perfectly mode matched with $\alpha_{r,\parallel}$. θ_p and θ_c are the phase difference between LO and signal due to path length difference and cavity response respectively. For simplicity, we can write the sum as $\theta = \theta_p + \theta_c$. Notice that, if we write this oscillating signal in the form of complex number, the phase is not given by θ, but by

$$\arctan\left(\frac{2\alpha_{LO}|\alpha_{r,\parallel}|\sin\theta}{\alpha_{LO}^2 + |\alpha_{r,\parallel}|^2 + |\alpha_{r,\perp}|^2 + 2\alpha_{LO}|\alpha_{r,\parallel}|\cos\theta}\right), \tag{C.5}$$

which is complicated to extract θ.

Alternatively, if we use heterodyne detection, the signal is given by

$$\frac{1}{2}(\alpha_{LO}^2 + |\alpha_{r,\parallel}|^2 + |\alpha_{r,\perp}|^2 + 2\alpha_{LO}|\alpha_{r,\parallel}|\cos(\Omega_{mod}t + \theta)), \tag{C.6}$$

where the term containing phase is at frequency of Ω_{mod}, the frequency difference between LO and input light. By feeding this signal to a lock-in amplifier (see Appendix B) with demodulation frequency Ω_{mod}, we can eliminate the complication from DC terms, and get a demodulated signal

$$V_{out}(t) = \frac{V_R\alpha_{LO}|\alpha_{r,\parallel}(t)|}{2}e^{i\theta(t)} = \frac{V_R\alpha_{LO}}{2}\left(-1 + \frac{\kappa_L}{\kappa/2 - i\Delta}\right)\sqrt{1-\epsilon}\alpha_{in}e^{i\theta_p}, \tag{C.7}$$

where the constant V_R is the amplitude of the local oscillator in the lock-in amplifier. As we always treat the far off-resonance value as the background value, we can normalize this output by dividing $\frac{V_R\alpha_{LO}}{2}\sqrt{1-\epsilon}\alpha_{in}$, and the normalized output is simply

$$V_n(t) = \left(-1 + \frac{\kappa_L}{\kappa/2 - i\Delta}\right)e^{i\theta_p}, \tag{C.8}$$

which is the same as the reflection coefficient discussed in Section 2.4, apart from a global phase θ_p. Thus, the contour is given by Fig. 2.5 up to a rotation, the angle of which can be identified by the opening of the contour, and cancelled by a rotation. From this data, we can extract cavity output-coupling efficiency, as intended.

The experimental setup of this measurement is shown in Fig. C.1. AOMs are used to shift the frequency of the local oscillator, such that the beat note of the signal and LO is not at DC. The PBS and quarter waveplate combination directs the reflected field from the cavity to the heterodyne detector. We use a 50:50 non-polarizing beams splitter to combine LO and signal, and only detect one of the output ports. This simple setup reduces the signal-to-noise ratio to half. However, this is a classical measurement, thus we are not that sensitive to detection efficiency. The heterodyne path length lock is used to stabilize the relative phase between LO and signal, which is optional. If we would like to get a proper error signal for the lock, we need to demodulate the signal from the photodiode to near DC. The output of the lock-in amplifier can serve as the error signal without additional treatment. Alternatively, we can let the heterodyne free run, and sweep the laser wavelength across the cavity resonance fast enough, such that during this time, the phase difference caused by path length fluctuation is negligible. If it is required, a BS can be insert before the heterodyne BS, to guide the beam to a detector, which provides information about reflection dip free from potential mode matching issue between LO and reflected signal, as shown in the dashed lines in Fig. C.1.

A key difference in mode matching in this setup from homodyne in transmission is that we need to optimize the mode matching between LO and $\alpha_{r,\parallel}$, the part of the reflected signal mode matched with cavity mode. If the mode matching is not perfect, the interference between the LO and $\alpha_{r,\perp}$, the non-mode-matched part of the signal beam, will make Eqn. C.7 no longer valid. Instead the amplitude will be modified a bit, and more importantly, the phase will not longer be $\theta_p + \theta_c$. Suppose the mode matching between LO and $\alpha_{r,\parallel}$ is $\iota_\parallel$, and that between LO and $\alpha_{r,\perp}$ is $\iota_\perp$ ($\iota_\parallel + \iota_\perp \leq 1$, as there can be LO part not matching any reflected signal components). Then the amplitudes of $\alpha_{LO,\parallel}$ and $\alpha_{LO,\perp}$ are given by $\sqrt{\iota_\parallel}\alpha_{LO}$ and $\sqrt{\iota_\perp}\alpha_{LO}$ respectively, and the heterodyne signal reads

$$\begin{aligned}&\frac{1}{2}(\alpha_{LO,\parallel}^2 + \alpha_{LO,\perp}^2 + (1-\iota_\parallel-\iota_\perp)\alpha_{LO}^2 + |\alpha_{r,\parallel}|^2 + |\alpha_{r,\perp}|^2 \\ &+2\alpha_{LO,\parallel}|\alpha_{r,\parallel}|\cos(\Omega_{mod}t + \theta_p + \theta_c) + 2\alpha_{LO,\perp}|\alpha_{r,\perp}|\cos(\Omega_{mod}t + \theta_p)),\end{aligned} \tag{C.9}$$

where $(1-\iota_\parallel-\iota_\perp)\alpha_{LO}^2$ is the part of LO not mode matching with either of the reflected field. Subsequently, the output of the lock-in amplifier is

$$\begin{aligned}V_{out}(t) &= \frac{V_R}{2}e^{i\theta_p(t)}\left(\alpha_{LO,\perp}|\alpha_{r,\perp}| + \alpha_{LO,\parallel}|\alpha_{r,\parallel}|e^{i\theta_c}\right) \\ &= \frac{V_R\alpha_{LO}\alpha_{in}(t)}{2}e^{i\theta_p(t)}\left(-\sqrt{\epsilon\iota_\perp} + \sqrt{(1-\epsilon)\iota_\parallel}\left(-1 + \frac{\kappa_L}{\kappa/2 - i\Delta}\right)\right).\end{aligned} \tag{C.10}$$

To normalize this signal, we divide the expression by $\frac{V_R\alpha_{LO}\alpha_{in}(t)}{2}(\sqrt{\epsilon\iota_\perp} + \sqrt{(1-\epsilon)\iota_\parallel})$, and get

$$V_n(t) = \left(-1 + \frac{1}{1 + \sqrt{\frac{\epsilon}{1-\epsilon}\frac{\iota_\perp}{\iota_\parallel}}}\frac{\kappa_L}{\kappa/2 - i\Delta}\right)e^{i\theta_p}. \tag{C.11}$$

Then the phase of this signal is given by

$$\theta_p + \arctan\left(\frac{\sqrt{(1-\epsilon)\iota_\parallel}\sin\theta_c}{-\sqrt{\epsilon\iota_\perp} + \sqrt{(1-\epsilon)\iota_\parallel}\cos\theta_c}\right), \tag{C.12}$$

which is closer to $\theta_p + \theta_c$, when the ratio $\iota_\perp/\iota_\parallel$ is closer to 0. Thus, optimizing $\iota_\parallel$ is crucial. To do this, instead of modulating path length to change relative phase between LO and signal, one can try to change phase by sweeping laser through the cavity resonance, or insert a phase modulator in the cavity. However, neither of the methods is easy to implement.

As there could always be some mode mismatch, we study the behavior of reflection coefficient in this case. Figure C.2 shows the contour of Eqn. C.11 when the mode matching between LO and $\alpha_{r,\parallel}$ is not unity. The contours are again circles, similar to Fig. 2.5. However, the diameters are given by

$$d = \frac{1}{1 + \sqrt{\frac{\epsilon}{1-\epsilon}\frac{\iota_\perp}{\iota_\parallel}}}\frac{\kappa_L}{\kappa/2} = \frac{2\eta_c}{1 + \sqrt{\frac{\epsilon}{1-\epsilon}\frac{\iota_\perp}{\iota_\parallel}}}, \tag{C.13}$$

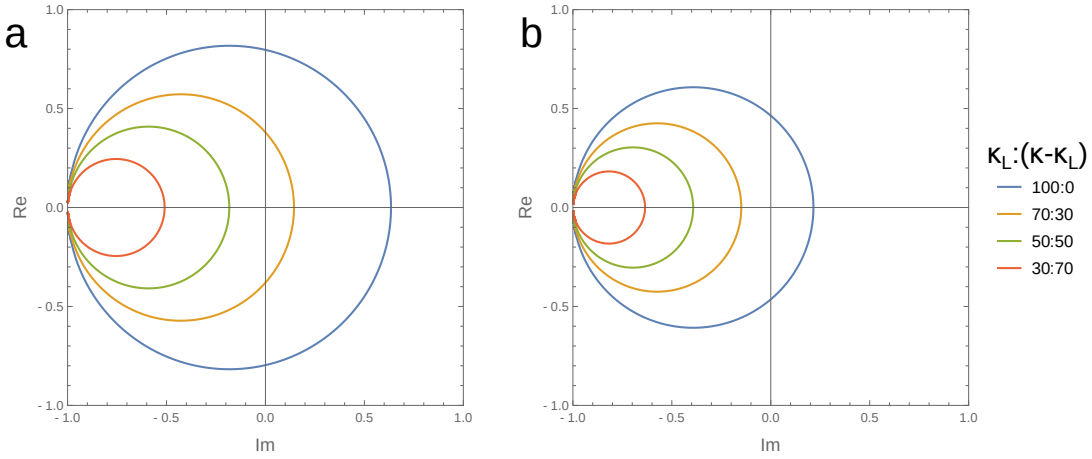

Figure C.2: Reflection coefficient with non-unity mode matching In both panels, $\epsilon = 0.2$, the ratios between κ_L and $\kappa - \kappa_L$ for different curves are shown in the legend. **a.** $\iota_\parallel = 0.5$, $\iota_\perp = 0.1$. **b.** $\iota_\parallel = 0.3$, $\iota_\perp = 0.5$.

where $\eta_c = 2\kappa_L/\kappa$ is cavity out-coupling in reflection. The same applies in the following of this chapter. Therefore, η_c, ϵ and $\iota_\perp/\iota_\parallel$ all influences the size of the contour. Moreover, the shapes are all circles, which prevent us from getting each contribution from a shape distortion. Thus, this method alone is not sufficient to determine η_c, in the case of non-unity LO-cavity mode matching. However, as finite ϵ and $\iota_\perp$ only decrease the size of the contour, if the contour encloses the origin, the cavity has to be over-coupled to reflection. This estimation can be more accurate with improved mode matching for probe-cavity and LO-signal.

One may wondering if getting the reflection dip by direct detection simulataneously with the heterodyne helps, as the reflection is free from mode matching between LO and reflected signal issue. To study this, we can write the normalized Eqn. 2.62 as

$$P_{r,n} = 1 - (1 - \epsilon)\frac{4\eta_c(1 - \eta_c)}{1 + 4\Delta^2/\kappa^2}, \tag{C.14}$$

where Δ^2/κ^2 is the self-changing parameter when we sweep through cavity resonance, which does not provide any information about the depth of the dip, mode matching or cavity out-coupling efficiency. Thus the reflection dip depth depends on ϵ and η_c. Together with Eqn. C.13, we have 2 equations and 3 unknowns, which is insufficient for solving for η_c. To get more equations, one can change laser wavelength to a different cavity mode, where η_c is significantly different, but the wavelength is not too far from the original one. In this case, we can roughly treat ϵ and $\iota_\perp/\iota_\parallel$ as constants. By conducting the same measurements, we will have 4 equations and 4 unknowns, which allows us to estimate the η_c in the first case.

Bibliography

[1] William Hvidtfelt Padkær Nielsen, Yeghishe Tsaturyan, Christoffer Bo Møller, Eugene S Polzik, and Albert Schliesser. Multimode optomechanical system in the quantum regime. *Proceedings of the National Academy of Sciences*, 114(1):62–66, 2017.

[2] VB Braginski and AB Manukin. Ponderomotive effects of electromagnetic radiation. *Sov. Phys. JETP*, 25(4):653–655, 1967.

[3] VB Braginskii, AB Manukin, and MY Tikhonov. Investigation of dissipative ponderomotive effects of electromagnetic radiation. *Soviet Journal of Experimental and Theoretical Physics*, 31:829, 1970.

[4] Albert Einstein. Näherungsweise integration der feldgleichungen der gravitation. *Albert Einstein: Akademie-Vorträge: Sitzungsberichte der Preußischen Akademie der Wissenschaften 1914–1932*, pages 99–108, 2005.

[5] David Mason. Figure credit: Dr. david mason. unpublished.

[6] BP Abbott, R Abbott, TD Abbott, MR Abernathy, F Acernese, K Ackley, C Adams, T Adams, P Addesso, RX Adhikari, et al. Observation of gravitational waves from a binary black hole merger. *Physical review letters*, 116(6):061102, 2016.

[7] VB Braginskii. Classical and quantum restrictions on the detection of weak disturbances of a macroscopic oscillator. *Soviet Journal of Experimental and Theoretical Physics*, 26:831, 1968.

[8] Massimiliano Rossi, David Mason, Junxin Chen, Yeghishe Tsaturyan, and Albert Schliesser. Measurement-based quantum control of mechanical motion. *Nature*, 563(7729):53, 2018.

[9] JD Thompson, BM Zwickl, AM Jayich, F Marquardt, SM Girvin, and JGE Harris. Strong dispersive coupling of a high-finesse cavity to a micromechanical membrane. *Nature*, 452(7183):72, 2008.

[10] Yeghishe Tsaturyan, Andreas Barg, Eugene S Polzik, and Albert Schliesser. Ultracoherent nanomechanical resonators via soft clamping and dissipation dilution. *Nature nanotechnology*, 12(8):776, 2017.

[11] Vivishek Sudhir. *Quantum limits on measurement and control of a mechanical oscillator*. PhD thesis, ÉCOLE POLYTECHNIQUE FÉDÉRALE DE LAUSANNE, 2016.

[12] JD Teufel, T Donner, D Li, JW Harlow, MS Allman, K Cicak, AJ Sirois, JD Whittaker, KW Lehnert, and RW Simmonds. Sideband cooling of micromechanical motion to the quantum ground state. *Nature*, 475(7356):359, 2011.

[13] Jasper Chan, Mayer TP Alegre, Amir H Safavi-Naeini, Jeff T Hill, Alex Krause, Simon Gröblacher, Markus Aspelmeyer, and Oskar Painter. Laser cooling of a nanomechanical oscillator into its quantum ground state. *Nature*, 478(7367):89, 2011.

[14] RW Peterson, TP Purdy, NS Kampel, RW Andrews, P-L Yu, KW Lehnert, and CA Regal. Laser cooling of a micromechanical membrane to the quantum backaction limit. *Physical review letters*, 116(6):063601, 2016.

[15] Florent Lecocq, Jeremy B Clark, Raymond W Simmonds, Jose Aumentado, and John D Teufel. Quantum nondemolition measurement of a nonclassical state of a massive object. *Physical Review X*, 5(4):041037, 2015.

[16] EE Wollman, C-U Lei, AJ Weinstein, J Suh, A Kronwald, F Marquardt, AA Clerk, and KC Schwab. Quantum squeezing of motion in a mechanical resonator. *Science*, 349(6251):952–955, 2015.

[17] J Suh, AJ Weinstein, CU Lei, EE Wollman, SK Steinke, P Meystre, AA Clerk, and KC Schwab. Mechanically detecting and avoiding the quantum fluctuations of a microwave field. *Science*, 344(6189):1262–1265, 2014.

[18] Yiwen Chu, Prashanta Kharel, Taekwan Yoon, Luigi Frunzio, Peter T Rakich, and Robert J Schoelkopf. Creation and control of multi-phonon fock states in a bulk acoustic-wave resonator. *Nature*, 563(7733):666, 2018.

[19] KJ Satzinger, YP Zhong, HS Chang, GA Peairs, A Bienfait, MH Chou, AY Cleland, CR Conner, É Dumur, J Grebel, et al. Quantum control of surface acoustic-wave phonons. *Nature*, 563(7733):661, 2018.

[20] Sungkun Hong, Ralf Riedinger, Igor Marinković, Andreas Wallucks, Sebastian G Hofer, Richard A Norte, Markus Aspelmeyer, and Simon Gröblacher. Hanbury brown and twiss interferometry of single phonons from an optomechanical resonator. *Science*, 358(6360):203–206, 2017.

[21] TA Palomaki, JD Teufel, RW Simmonds, and KW Lehnert. Entangling mechanical motion with microwave fields. *Science*, 342(6159):710–713, 2013.

[22] Ralf Riedinger, Andreas Wallucks, Igor Marinković, Clemens Löschnauer, Markus Aspelmeyer, Sungkun Hong, and Simon Gröblacher. Remote quantum entanglement between two micromechanical oscillators. *Nature*, 556(7702):473, 2018.

[23] CF Ockeloen-Korppi, E Damskägg, JM Pirkkalainen, M Asjad, AA Clerk, F Massel, MJ Woolley, and MA Sillanpää. Stabilized entanglement of massive mechanical oscillators. *Nature*, 556(7702):478, 2018.

[24] Oriol Romero-Isart. Coherent inflation for large quantum superpositions of levitated microspheres. *New Journal of Physics*, 19(12):123029, 2017.

[25] Brian Vlastakis, Gerhard Kirchmair, Zaki Leghtas, Simon E Nigg, Luigi Frunzio, Steven M Girvin, Mazyar Mirrahimi, Michel H Devoret, and Robert J Schoelkopf. Deterministically encoding quantum information using 100-photon schrödinger cat states. *Science*, 342(6158):607–610, 2013.

[26] Roger Penrose. On gravity's role in quantum state reduction. *General relativity and gravitation*, 28(5):581–600, 1996.

[27] William Marshall, Christoph Simon, Roger Penrose, and Dik Bouwmeester. Towards quantum superpositions of a mirror. *Physical Review Letters*, 91(13):130401, 2003.

[28] Oriol Romero-Isart, Anika C Pflanzer, Florian Blaser, Rainer Kaltenbaek, Nikolai Kiesel, Markus Aspelmeyer, and J Ignacio Cirac. Large quantum superpositions and interference of massive nanometer-sized objects. *Physical review letters*, 107(2):020405, 2011.

[29] Igor Pikovski, Michael R Vanner, Markus Aspelmeyer, MS Kim, and Časlav Brukner. Probing planck-scale physics with quantum optics. *Nature Physics*, 8(5):393, 2012.

[30] Gregory S MacCabe, Hengjiang Ren, Jie Luo, Justin D Cohen, Hengyun Zhou, Alp Sipahigil, Mohammad Mirhosseini, and Oskar Painter. Phononic bandgap nano-acoustic cavity with ultralong phonon lifetime. *arXiv preprint arXiv:1901.04129*, 2019.

[31] Andreas Wallucks, Igor Marinković, Bas Hensen, Robert Stockill, and Simon Gröblacher. A quantum memory at telecom wavelengths, 2019.

[32] A. Bienfait, K. J. Satzinger, Y. P. Zhong, H. S. Chang, M. H. Chou, C. R. Conner, É Dumur, J. Grebel, G. A. Peairs, R. G. Povey, and A. N. Cleland. Phonon-mediated quantum state transfer and remote qubit entanglement. *Science*, 364(6438):368–371, April 2019.

[33] Reed W Andrews, Robert W Peterson, Tom P Purdy, Katarina Cicak, Raymond W Simmonds, Cindy A Regal, and Konrad W Lehnert. Bidirectional and efficient conversion between microwave and optical light. *Nature Physics*, 10(4):321, 2014.

[34] AP Higginbotham, PS Burns, MD Urmey, RW Peterson, NS Kampel, BM Brubaker, G Smith, KW Lehnert, and CA Regal. Harnessing electro-optic correlations in an efficient mechanical converter. *Nature Physics*, 14(10):1038, 2018.

[35] Moritz Forsch, Robert Stockill, Andreas Wallucks, Igor Marinković, Claus Gärtner, Richard A Norte, Frank van Otten, Andrea Fiore, Kartik Srinivasan, and Simon Gröblacher. Microwave-to-optics conversion using a mechanical oscillator in its quantum ground state. *Nature Physics*, pages 1–6, 2019.

[36] H Jeff Kimble. The quantum internet. *Nature*, 453(7198):1023, 2008.

[37] Amir H Safavi-Naeini, Simon Gröblacher, Jeff T Hill, Jasper Chan, Markus Aspelmeyer, and Oskar Painter. Squeezed light from a silicon micromechanical resonator. *Nature*, 500(7461):185, 2013.

[38] TP Purdy, P-L Yu, RW Peterson, NS Kampel, and CA Regal. Strong optomechanical squeezing of light. *Physical Review X*, 3(3):031012, 2013.

[39] GS Agarwal and S-M Huang. Electromagnetically induced transparency in mechanical effects of light. *Physical Review A*, 81(4):041803, 2010.

[40] SP Vyatchanin and EA Zubova. Quantum variation measurement of a force. *Physics letters A*, 201(4):269–274, 1995.

[41] David Mason, Junxin Chen, Massimiliano Rossi, Yeghishe Tsaturyan, and Albert Schliesser. Continuous force and displacement measurement below the standard quantum limit. *Nature Physics*, page 1, 2019.

[42] S Barzanjeh, ES Redchenko, M Peruzzo, M Wulf, DP Lewis, and JM Fink. Stationary entangled radiation from micromechanical motion. *Nature*, 570:480–483, 2019.

[43] Warwick P Bowen and Gerard J Milburn. *Quantum optomechanics*. CRC press, 2015.

[44] Understanding the paraxial gaussian beam formula. https://www.comsol.com/blogs/understanding-the-paraxial-gaussian-beam-formula/. Accessed: 2019-09-04.

[45] Gaussian beam - wikipedia. https://en.wikipedia.org/wiki/Gaussian_beam. Accessed: 2019-09-05.

[46] William Nielsen. *Quantum Cavity Optomechanics with Phononic Bandgap Shielded Silicon Nitride Membranes*. PhD thesis, University of Copenhagen, 2016.

[47] Markus Aspelmeyer, Tobias J Kippenberg, and Florian Marquardt. Cavity optomechanics. *Reviews of Modern Physics*, 86(4):1391, 2014.

[48] King Y Fong, Wolfram HP Pernice, and Hong X Tang. Frequency and phase noise of ultrahigh q silicon nitride nanomechanical resonators. *Physical Review B*, 85(16):161410, 2012.

[49] Aijun Li, Li Ma, David Keene, Joshua Klingel, Marvin Payne, and Xiaojun Wang. Forced oscillations with linear and nonlinear damping. *American Journal of Physics*, 84(1):32–37, 2016.

[50] P Meystre, EM Wright, JD McCullen, and E Vignes. Theory of radiation-pressure-driven interferometers. *JOSA B*, 2(11):1830–1840, 1985.

[51] Albert Schliesser. *Cavity Optomechanics and Optical Frequency Comb Generation with Silica Whispering-Gallery-Mode Microresonators*. PhD thesis, Ludwig Maximilians Universität, 2009.

[52] Stefan Weis, Rémi Rivière, Samuel Deléglise, Emanuel Gavartin, Olivier Arcizet, Albert Schliesser, and Tobias J Kippenberg. Optomechanically induced transparency. *Science*, 330(6010):1520–1523, 2010.

[53] Yiqiu Ma, Shtefan L. Danilishin, Chunnong Zhao, Haixing Miao, W. Zach Korth, Yanbei Chen, Robert L. Ward, and David G. Blair. Narrowing the filter-cavity bandwidth in gravitational-wave detectors via optomechanical interaction. *Phys. Rev. Lett.*, 113:151102, Oct 2014.

[54] Jiayi Qin, Chunnong Zhao, Yiqiu Ma, Xu Chen, Li Ju, and David G. Blair. Classical demonstration of frequency-dependent noise ellipse rotation using optomechanically induced transparency. *Phys. Rev. A*, 89:041802, Apr 2014.

[55] Jiayi Qin, Chunnong Zhao, Yiqiu Ma, Li Ju, and David G. Blair. Linear negative dispersion with a gain doublet via optomechanical interactions. *Opt. Lett.*, 40(10):2337–2340, May 2015.

[56] Claude Cohen-Tannoudji and William D Phillips. New mechanisms for laser cooling. *Phys. Today*, 43(10):33–40, 1990.

[57] F Diedrich, JC Bergquist, Wayne M Itano, and DJ Wineland. Laser cooling to the zero-point energy of motion. *Physical Review Letters*, 62(4):403, 1989.

[58] AD O' Connell, M Hofheinz, M Ansmann, RC Bialczak, M Lenander, E Lucero, M Neeley, D Sank, H Wang, MS Weides, et al. Quantum ground state and single-phonon control of a mechanical resonator. *Nature*, 464(7289):697, 2010.

[59] Jeremy B Clark, Florent Lecocq, Raymond W Simmonds, José Aumentado, and John D Teufel. Sideband cooling beyond the quantum backaction limit with squeezed light. *Nature*, 541(7636):191, 2017.

[60] Massimiliano Rossi, Nenad Kralj, Stefano Zippilli, Riccardo Natali, Antonio Borrielli, Gregory Pandraud, Enrico Serra, Giovanni Di Giuseppe, and David Vitali. Enhancing sideband cooling by feedback-controlled light. *Physical review letters*, 119(12):123603, 2017.

[61] Claude Fabre, Michel Pinard, Sophie Bourzeix, Antoine Heidmann, Elisabeth Giacobino, and Serge Reynaud. Quantum-noise reduction using a cavity with a movable mirror. *Physical Review A*, 49(2):1337, 1994.

[62] Stefano Mancini and Paolo Tombesi. Quantum noise reduction by radiation pressure. *Physical Review A*, 49(5):4055, 1994.

[63] Nancy Aggarwal, Torrey Cullen, Jonathan Cripe, Garrett D Cole, Robert Lanza, Adam Libson, David Follman, Paula Heu, Thomas Corbitt, and Nergis Mavalvala. Room temperature optomechanical squeezing. *arXiv preprint arXiv:1812.09942*, 2018.

[64] Joseph F Vignola, John A Judge, Jacek Jarzynski, Maxim Zalalutdinov, Brian H Houston, and Jeffrey W Baldwin. Effect of viscous loss on mechanical resonators designed for mass detection. *Applied Physics Letters*, 88(4):041921, 2006.

[65] D. Tielbürger, R. Merz, R. Ehrenfels, and S. Hunklinger. Thermally activated relaxation processes in vitreous silica: An investigation by brillouin scattering at high pressures. *Phys. Rev. B*, 45:2750–2760, Feb 1992.

[66] René Vacher, Eric Courtens, and Marie Foret. Anharmonic versus relaxational sound damping in glasses. ii. vitreous silica. *Phys. Rev. B*, 72:214205, Dec 2005.

[67] Thomas Faust, Johannes Rieger, Maximilian J Seitner, Jörg P Kotthaus, and Eva M Weig. Signatures of two-level defects in the temperature-dependent damping of nanomechanical silicon nitride resonators. *Physical Review B*, 89(10):100102, 2014.

[68] Mingyun Yuan, Martijn A Cohen, and Gary A Steele. Silicon nitride membrane resonators at millikelvin temperatures with quality factors exceeding 108. *Applied Physics Letters*, 107(26):263501, 2015.

[69] Tom P Purdy, Robert W Peterson, and Cindy A Regal. Observation of radiation pressure shot noise on a macroscopic object. *Science*, 339(6121):801–804, 2013.

[70] BM Zwickl, WE Shanks, AM Jayich, C Yang, AC Bleszynski Jayich, JD Thompson, and JGE Harris. High quality mechanical and optical properties of commercial silicon nitride membranes. *Applied Physics Letters*, 92(10):103125, 2008.

[71] Quirin P Unterreithmeier, Thomas Faust, and Jörg P Kotthaus. Damping of nanomechanical resonators. *Physical review letters*, 105(2):027205, 2010.

[72] Gabriela I González and Peter R Saulson. Brownian motion of a mass suspended by an anelastic wire. *The Journal of the Acoustical Society of America*, 96(1):207–212, 1994.

[73] P-L Yu, TP Purdy, and CA Regal. Control of material damping in high-q membrane microresonators. *Physical review letters*, 108(8):083603, 2012.

[74] Kevin Y Yasumura, Timothy D Stowe, Eugene M Chow, Timothy Pfafman, Thomas W Kenny, Barry C Stipe, and Daniel Rugar. Quality factors in micron-and submicron-thick cantilevers. *Journal of microelectromechanical systems*, 9(1):117–125, 2000.

[75] Luis Guillermo Villanueva and Silvan Schmid. Evidence of surface loss as ubiquitous limiting damping mechanism in sin micro-and nanomechanical resonators. *Physical review letters*, 113(22):227201, 2014.

[76] Yeghishe Tsaturyan. *Ultracoherent soft-clamped mechanical resonators for quantum cavity optomechanics*. PhD thesis, University of Copenhagen, 2019.

[77] AN Cleland and ML Roukes. Noise processes in nanomechanical resonators. *Journal of applied physics*, 92(5):2758–2769, 2002.

[78] Yook Kong Yong and John R Vig. Resonator surface contamination-a cause of frequency fluctuations? *IEEE transactions on ultrasonics, ferroelectrics, and frequency control*, 36(4):452–458, 1989.

[79] YT Yang, C Callegari, XL Feng, and ML Roukes. Surface adsorbate fluctuations and noise in nanoelectromechanical systems. *Nano letters*, 11(4):1753–1759, 2011.

[80] J Atalaya, A Isacsson, and MI Dykman. Diffusion-induced dephasing in nanomechanical resonators. *Physical Review B*, 83(4):045419, 2011.

[81] WA Phillips. Tunneling states in amorphous solids. *Journal of Low Temperature Physics*, 7(3-4):351–360, 1972.

[82] Massimiliano Rossi, David Mason, Junxin Chen, and Albert Schliesser. Observing and verifying the quantum trajectory of a mechanical resonator. *Phys. Rev. Lett.*, 123:163601, Oct 2019.

[83] David Mason. *Dynamical Behavior near Exceptional Points in an Optomechanical System*. PhD thesis, Yale University, 2017.

[84] AM Jayich, JC Sankey, BM Zwickl, C Yang, JD Thompson, SM Girvin, AA Clerk, F Marquardt, and JGE Harris. Dispersive optomechanics: a membrane inside a cavity. *New Journal of Physics*, 10(9):095008, 2008.

[85] Vincent Dumont, Simon Bernard, Christoph Reinhardt, Alex Kato, Maximilian Ruf, and Jack C Sankey. Flexure-tuned membrane-at-the-edge optomechanical system. *Optics express*, 27(18):25731–25748, 2019.

[86] Geoffrey Brooker. *Modern classical optics*, volume 8. Oxford University Press, 2003.

[87] Herbert R Philipp. Optical properties of silicon nitride. *Journal of the Electrochemical Society*, 120(2):295–300, 1973.

[88] AL Campillo and JWP Hsu. Near-field scanning optical microscope studies of the anisotropic stress variations in patterned sin membranes. *Journal of applied physics*, 91(2):646–651, 2002.

[89] Electro-optic modulator. https://en.wikipedia.org/wiki/Electro-optic_modulator. Accessed: 2019-10-08.

[90] John Bechhoefer. Feedback for physicists: A tutorial essay on control. *Reviews of Modern Physics*, 77(3):783, 2005.

[91] Eric D Black. An introduction to pound–drever–hall laser frequency stabilization. *American journal of physics*, 69(1):79–87, 2001.

[92] Christoffer Møller. *Quantum Back-Action Evasion in a Hybrid Spin-Optomechanical System*. PhD thesis, University of Copenhagen, 2018.

[93] Andreas Kronwald, Florian Marquardt, and Aashish A Clerk. Arbitrarily large steady-state bosonic squeezing via dissipation. *Physical Review A*, 88(6):063833, 2013.

[94] Patricia Purdue and Yanbei Chen. Practical speed meter designs for quantum nondemolition gravitational-wave interferometers. *Physical Review D*, 66(12):122004, 2002.

[95] Klemens Hammerer, Markus Aspelmeyer, Eugene Simon Polzik, and Peter Zoller. Establishing einstein-poldosky-rosen channels between nanomechanics and atomic ensembles. *Physical review letters*, 102(2):020501, 2009.

[96] Itay Shomroni, Liu Qiu, Daniel Malz, Andreas Nunnenkamp, and Tobias J Kippenberg. Optical backaction-evading measurement of a mechanical oscillator. *Nature communications*, 10(1):2086, 2019.

[97] Christoffer B Møller, Rodrigo A Thomas, Georgios Vasilakis, Emil Zeuthen, Yeghishe Tsaturyan, Mikhail Balabas, Kasper Jensen, Albert Schliesser, Klemens Hammerer, and Eugene S Polzik. Quantum back-action-evading measurement of motion in a negative mass reference frame. *Nature*, 547(7662):191, 2017.

[98] Carlton M Caves. Quantum-mechanical noise in an interferometer. *Physical Review D*, 23(8):1693, 1981.

[99] The quantum enhanced ligo detector sets new sensitivity record. https://www.ligo.org/science/Publication-SqueezedVacuum/index.php. Accessed: 2019-09-24.

[100] Min Jet Yap, Jonathan Cripe, Georgia L Mansell, Terry G McRae, Robert L Ward, Bram JJ Slagmolen, Daniel A Shaddock, Paula Heu, David Follman, Garrett D Cole, et al. Broadband reduction of quantum radiation pressure noise via squeezed light injection. *arXiv preprint arXiv:1812.09804*, 2018.

[101] NS Kampel, RW Peterson, R Fischer, P-L Yu, K Cicak, RW Simmonds, KW Lehnert, and CA Regal. Improving broadband displacement detection with quantum correlations. *Physical Review X*, 7(2):021008, 2017.

[102] AC Doherty, A Szorkovszky, GI Harris, and WP Bowen. The quantum trajectory approach to quantum feedback control of an oscillator revisited. *Philosophical Transactions of the Royal Society A: Mathematical, Physical and Engineering Sciences*, 370(1979):5338–5353, 2012.

[103] ML Gorodetksy, A Schliesser, G Anetsberger, S Deleglise, and TJ Kippenberg. Determination of the vacuum optomechanical coupling rate using frequency noise calibration. *Optics express*, 18(22):23236–23246, 2010.

[104] Hojat Habibi, Emil Zeuthen, Majid Ghanaatshoar, and Klemens Hammerer. Quantum feedback cooling of a mechanical oscillator using variational measurements: tweaking heisenberg' s microscope. *Journal of Optics*, 18(8):084004, 2016.

[105] Martino Poggio and Christian L Degen. Force-detected nuclear magnetic resonance: recent advances and future challenges. *Nanotechnology*, 21(34):342001, 2010.

[106] LF Buchmann, S Schreppler, J Kohler, N Spethmann, and DM Stamper-Kurn. Complex squeezing and force measurement beyond the standard quantum limit. *Physical review letters*, 117(3):030801, 2016.

[107] CF Ockeloen-Korppi, E Damskägg, GS Paraoanu, F Massel, and MA Sillanpää. Revealing hidden quantum correlations in an electromechanical measurement. *Physical review letters*, 121(24):243601, 2018.

[108] Kai Stannigel, Peter Rabl, Anders S Sørensen, Peter Zoller, and Mikhail D Lukin. Optomechanical transducers for long-distance quantum communication. *Physical review letters*, 105(22):220501, 2010.

[109] Jian-Wei Pan, Dik Bouwmeester, Harald Weinfurter, and Anton Zeilinger. Experimental entanglement swapping: entangling photons that never interacted. *Physical Review Letters*, 80(18):3891, 1998.

[110] Xiaojun Jia, Xiaolong Su, Qing Pan, Jiangrui Gao, Changde Xie, and Kunchi Peng. Experimental demonstration of unconditional entanglement swapping for continuous variables. *Physical review letters*, 93(25):250503, 2004.

[111] Vittorio Giovannetti, Stefano Mancini, and Paolo Tombesi. Radiation pressure induced einstein-podolsky-rosen paradox. *EPL (Europhysics Letters)*, 54(5):559, 2001.

[112] Lu-Ming Duan, Géza Giedke, Juan Ignacio Cirac, and Peter Zoller. Inseparability criterion for continuous variable systems. *Phys. Rev. Lett.*, 84(12):2722, 2000.

[113] Vittorio Giovannetti, Stefano Mancini, David Vitali, and Paolo Tombesi. Characterizing the entanglement of bipartite quantum systems. *Phys. Rev. A*, 67(2):022320, 2003.

[114] Gerardo Adesso, Alessio Serafini, and Fabrizio Illuminati. Extremal entanglement and mixedness in continuous variable systems. *Physical Review A*, 70(2):022318, 2004.

[115] Stefano Zippilli, Giovanni Di Giuseppe, and David Vitali. Entanglement and squeezing of continuous-wave stationary light. *New Journal of Physics*, 17(4):043025, 2015.

[116] Martin B Plenio. Logarithmic negativity: a full entanglement monotone that is not convex. *Physical review letters*, 95(9):090503, 2005.

[117] Junxin Chen, Massimiliano Rossi, David Mason, and Albert Schliesser. Entanglement of propagating optical modes via a mechanical interface. *arXiv preprint arXiv:1911.05729*, 2019.

[118] MD Levenson and RM Shelby. Four-mode squeezing and applications. *J. Mod. Opt.*, 34(6-7):775–792, 1987.

[119] Silvia Giannini, Stefano Mancini, and Paolo Tombesi. Information theoretic aspects in ponderomotive systems. *arXiv preprint quant-ph/0210122*, 2002.

[120] Christopher Wipf, Thomas Corbitt, Yanbei Chen, and Nergis Mavalvala. Route to ponderomotive entanglement of light via optically trapped mirrors. *New Journal of Physics*, 10(9):095017, 2008.

[121] Spyros Tserkis and Timothy C Ralph. Quantifying entanglement in two-mode gaussian states. *Physical Review A*, 96(6):062338, 2017.

[122] G. Giedke, M. M. Wolf, O. Krüger, R. F. Werner, and J. I. Cirac. Entanglement of formation for symmetric gaussian states. *Phys. Rev. Lett.*, 91:107901, Sep 2003.

[123] ZY Ou, SF Pereira, HJ Kimble, and KC Peng. Realization of the einstein-podolsky-rosen paradox for continuous variables. *Phys. Rev. Lett.*, 68(25):3663, 1992.

[124] AS Villar, LS Cruz, KN Cassemiro, M Martinelli, and P Nussenzveig. Generation of bright two-color continuous variable entanglement. *Phys. Rev. Lett.*, 95(24):243603, 2005.

[125] JM Pirkkalainen, S Cho, J Li, GS Paraoanu, PJ Hakonen, and MA Sillanpää. Hybrid circuit cavity quantum electrodynamics with a micromechanical resonator. *Nature*, 494(7436):211, 2013.

[126] AP Reed, KH Mayer, JD Teufel, LD Burkhart, W Pfaff, M Reagor, L Sletten, X Ma, RJ Schoelkopf, E Knill, et al. Faithful conversion of propagating quantum information to mechanical motion. *Nat. Phys.*, 13(12):1163, 2017.

[127] Seán M Meenehan, Justin D Cohen, Gregory S MacCabe, Francesco Marsili, Matthew D Shaw, and Oskar Painter. Pulsed excitation dynamics of an optomechanical crystal resonator near its quantum ground state of motion. *Physical Review X*, 5(4):041002, 2015.

[128] Alexander Kubanek, Markus Koch, Christian Sames, Alexei Ourjoumtsev, Pepijn WH Pinkse, Karim Murr, and Gerhard Rempe. Photon-by-photon feedback control of a single-atom trajectory. *Nature*, 462(7275):898, 2009.

[129] Pavel Bushev, Daniel Rotter, Alex Wilson, François Dubin, Christoph Becher, Jürgen Eschner, Rainer Blatt, Viktor Steixner, Peter Rabl, and Peter Zoller. Feedback cooling of a single trapped ion. *Physical review letters*, 96(4):043003, 2006.

[130] Tongcang Li. Millikelvin cooling of an optically trapped microsphere in vacuum. In *Fundamental Tests of Physics with Optically Trapped Microspheres*, pages 81–110. Springer, 2013.

[131] Vijay Jain, Jan Gieseler, Clemens Moritz, Christoph Dellago, Romain Quidant, and Lukas Novotny. Direct measurement of photon recoil from a levitated nanoparticle. *Physical review letters*, 116(24):243601, 2016.

[132] M Poggio, CL Degen, HJ Mamin, and D Rugar. Feedback cooling of a cantilever' s fundamental mode below 5 mk. *Physical Review Letters*, 99(1):017201, 2007.

[133] Dustin Kleckner and Dirk Bouwmeester. Sub-kelvin optical cooling of a micromechanical resonator. *Nature*, 444(7115):75, 2006.

[134] MD LaHaye, O Buu, B Camarota, and KC Schwab. Approaching the quantum limit of a nanomechanical resonator. *Science*, 304(5667):74–77, 2004.

[135] Dalziel J Wilson, Vivishek Sudhir, Nicolas Piro, Ryan Schilling, Amir Ghadimi, and Tobias J Kippenberg. Measurement-based control of a mechanical oscillator at its thermal decoherence rate. *Nature*, 524(7565):325, 2015.

[136] A Vinante, M Bignotto, M Bonaldi, M Cerdonio, L Conti, P Falferi, N Liguori, S Longo, R Mezzena, A Ortolan, et al. Feedback cooling of the normal modes of a massive electromechanical system to submillikelvin temperature. *Physical review letters*, 101(3):033601, 2008.

[137] B Abbott, R Abbott, R Adhikari, P Ajith, B Allen, G Allen, R Amin, SB Anderson, WG Anderson, MA Arain, et al. Observation of a kilogram-scale oscillator near its quantum ground state. *New Journal of Physics*, 11(7):073032, 2009.

[138] Vladimir B Braginsky, Yuri I Vorontsov, and Kip S Thorne. Quantum nondemolition measurements. *Science*, 209(4456):547–557, 1980.

[139] Kip S Thorne, Ronald WP Drever, Carlton M Caves, Mark Zimmermann, and Vernon D Sandberg. Quantum nondemolition measurements of harmonic oscillators. *Physical Review Letters*, 40(11):667, 1978.

[140] Carlton M Caves, Kip S Thorne, Ronald WP Drever, Vernon D Sandberg, and Mark Zimmermann. On the measurement of a weak classical force coupled to a quantum-mechanical oscillator. i. issues of principle. *Reviews of Modern Physics*, 52(2):341, 1980.

[141] VB Braginskii, YI Vorontsov, and FY Khalili. Optimal quantum measurements in detectors of gravitation radiation. *JETP Lett*, 27(5), 1978.

[142] Georgios Vasilakis, Heng Shen, Kasper Jensen, Misha Balabas, Daniel Salart, Bing Chen, and Eugene Simon Polzik. Generation of a squeezed state of an oscillator by stroboscopic back-action-evading measurement. *Nature Physics*, 11(5):389, 2015.

[143] Amir H Safavi-Naeini and Oskar Painter. Proposal for an optomechanical traveling wave phonon–photon translator. *New Journal of Physics*, 13(1):013017, 2011.

[144] JD Teufel, F Lecocq, and RW Simmonds. Overwhelming thermomechanical motion with microwave radiation pressure shot noise. *Physical review letters*, 116(1):013602, 2016.

[145] Tolga Bagci, Anders Simonsen, Silvan Schmid, Luis G Villanueva, Emil Zeuthen, Jürgen Appel, Jacob M Taylor, A Sørensen, Koji Usami, Albert Schliesser, et al. Optical detection of radio waves through a nanomechanical transducer. *Nature*, 507(7490):81, 2014.

[146] Yeghishe Tsaturyan, Letizia Catalini, and Albert Schliesser. Manuscript in preparation. unpublished.

[147] Sze M. Tan. Confirming entanglement in continuous variable quantum teleportation. *Phys. Rev. A*, 60:2752–2758, Oct 1999.

[148] P van Loock and SL Braunstein. Unconditional entanglement swapping for continuous variables. *Phys. Rev. A*, 61(quant-ph/9906075):010302, 2000.

[149] Jing Zhang, Changde Xie, and Kunchi Peng. Entanglement swapping using nondegenerate optical parametric amplifier. *Physics Letters A*, 299(5-6):427–432, 2002.

[150] LM Duan, MD Lukin, JI Cirac, and P Zoller. Long-distance quantum communication with atomic ensembles and linear optics. *Nature*, 414(6862):413, 2001.

[151] Jiliang Qin, Jialin Cheng, Shaocong Liang, Zhihui Yan, Xiaojun Jia, and Kunchi Peng. Transferring of continuous variable squeezed states in 20 km fiber. *Applied Sciences*, 9(12):2397, 2019.

[152] Shuntaro Takeda, Maria Fuwa, Peter van Loock, and Akira Furusawa. Entanglement swapping between discrete and continuous variables. *Phys. Rev. Lett.*, 114:100501, Mar 2015.

[153] Frequency modulation. https://www.st-andrews.ac.uk/~www_pa/Scots_Guide/RadCom/part12/page1.html. Accessed: 2019-10-09.

[154] Jenoptik. *Integrated-optical modulators: Technical information and instructions for use*.

[155] Acousto optic principles. http://www.acoustooptic.com/acousto-optic-principles.html. Accessed: 2019-10-11.